

Reservoir Condition Pore-Scale Imaging of Reaction

Hannah Paris Menke

Department of Earth Science and Engineering

Royal School of Mines

Imperial College London

London SW7 2AZ

United Kingdom

A dissertation submitted in fulfillment of the requirements for the degree of

Doctor of Philosophy

of Imperial College London

April 2016

Copyright Declaration

The copyright of this thesis rests with the author and is made available under a Creative Commons Attribution Non-Commercial No Derivatives licence. Researchers are free to copy, distribute or transmit the thesis on the condition that they attribute it, that they do not use it for commercial purposes and that they do not alter, transform or build upon it. For any reuse or redistribution, researchers must make clear to others the licence terms of this work.

A handwritten signature in black ink, appearing to read 'Hannah P Menke', written in a cursive style.

Hannah P Menke
Department of Earth Science and Engineering
Imperial College London
April 2016

Declaration of Originality

I declare that this thesis, **Reservoir-Condition Pore-Scale Imaging of Reaction**, is entirely my own work under the supervision of Prof. Martin J Blunt and Dr. Branko Bijeljic. The work was performed in the Department of Earth Science and Engineering at Imperial College London. All published and unpublished material used in the thesis has been given full acknowledgment. This work has not been previously submitted, in whole or in part, to any other academic institution for a degree, diploma, or any other qualification.

A handwritten signature in black ink, appearing to read 'Hannah P Menke', written in a cursive style.

Hannah P Menke
Department of Earth Science and Engineering
Imperial College London
April 2016

Abstract

This thesis presents the first dynamic imaging of fluid/rock reaction using x-ray microtomography (μ -CT) and focuses on three series of experiments: (1) imaging a homogenous carbonate during dissolution using a laboratory scanner; (2) imaging heterogeneous carbonates at multiple flow rates using a synchrotron pink beam; (3) imaging the same rocks using a laboratory scanner at multiple reactive conditions incorporating effluent analysis.

First the *in situ* reservoir condition imaging apparatus was adapted to image Ketton carbonate dynamically using a laboratory μ -CT scanner. 10 images were acquired over 2 ½ hours. Porosity and surface area were measured from the images and permeability and connectivity were calculated using flow models. Ketton dissolved uniformly at these conditions although the effective reaction rate (r_{eff}) was 16 times lower than those measured in batch reactor experiments with no transport limitations.

Second the experimental apparatus was used with fast synchrotron-based μ -CT to image two more complex carbonates, Estailades and Portland Basebed at two different flow conditions. ~100 images were taken over 2 hours, which captured the complexity of dissolution. It was found that the type of dissolution is both pore structure and flow rate dependent. A new type of dissolution, channelling, is observed which has a r_{eff} up to 100 times lower than batch rates.

Third, effluent analysis was incorporated into the experimental apparatus. All three rocks were imaged again at two separate reactive conditions. The r_{eff} was between 10 and 100 times lower than the batch rates, with the lowest rates in samples with the most channelized flow, confirming that transport limitations are the dominant mechanism in determining r_{eff} at the fluid/solid boundary. Effluent analysis confirmed that using the *in situ*, rather than the injected pH, to determine r_{eff} is valid in the uniform regime, but overestimates r_{eff} with channelling by an order of magnitude.

List of Publications

Journal Articles

1. Menke, H.P., Bijeljic, B., Blunt, M.J., 2016b Dynamic Reservoir-Condition Microtomography of Reactive Transport in Complex Carbonates using a Laboratory Source: Effect of Initial Pore structure and Reactive Conditions. *Geochimica et Cosmochimica Acta*, In Review.
2. Menke, H.P., Andrew, M.G., Blunt, M.J., Bijeljic, B., 2016a. Reservoir Condition Imaging of Reactive Transport in Heterogeneous Carbonates Using Fast Synchrotron Tomography – Effect of Initial Pore structure and Flow Conditions. *Chemical Geology*, 2016. doi: 10.1016/j.chemgeo.2016.02.030
3. Menke, H.P., Andrew, M.G., Blunt, M.J., Bijeljic, B., 2015b. Dynamic Pore-Scale Reservoir-Condition Imaging of Reaction in Carbonates using Synchrotron Fast Tomography, *Journal of Visualized Experiments*, In Press.
4. Andrew, M.G., Menke, H.P., Bijeljic, B., Blunt, M.J. 2015a. Pore-scale dynamic drainage of CO₂ in brine at reservoir conditions using a Synchrotron Pink Beam, *Transport in Porous Media*, 2015. **110**(1): p. 1-24.
5. Menke, H.P., Bijeljic, B., Andrew, M.G., Blunt, M.J., 2015a. Dynamic Three-Dimensional Pore-Scale Imaging of Reaction in a Carbonate at Reservoir Conditions. *Environmental Science and Technology*, 2015. **49**(7): p. 4407-4414.
6. Menke, W.H., Menke, H.P., 2014. Precision of Delay Times Determined Through Cross Correlation Achieved Through Out-Member Averaging. *Jökull*, 64, 15. 2014.
7. Andrew, M.G., Menke, H.P.; Blunt, M.J, Bijeljic, B, 2015b. Dynamic Drainage and Imbibition Imaged Using Fast X-ray Microtomography. *International Symposium of the Society of Core Analysts*. St. John's, Newfoundland, 16-21 August, 2015.
8. Menke, H.P., Bijeljic, B., Andrew, M.G., Blunt, M.J., 2014. Dynamic pore-scale imaging of reactive transport in heterogeneous carbonates at reservoir conditions. *Energy Procedia*, 63, 5503. 2014.

Selected Conference Presentations

1. Menke, H., B. Bijeljic, M. G. Andrew, and M. J. Blunt. EAGE, Madrid, Spain 2015.
Oral Presentation

2. Menke, H., B. Bijeljic, M. G. Andrew, and M. J. Blunt. Interpore, Padua, Italy 2015. **Oral Presentation**
3. Reynolds, C.; Menke, HP; Andrew, M.G.; Bijeljic, B.; Blunt, M.; Krevor, S.; Interpore, Spain, 2015. **Oral Presentation**
4. Andrew, M.G., Menke, H.P., Singh, K., Blunt, M.J. Interpore, Padua, Italy 2015. **Oral Presentation**
5. Thomas Seers, Matthew Andrew, Hannah Menke, Kamal Singh, Branko Bijeljic. Imaging cross fault multiphase flow using time resolved high pressure-temperature synchrotron fluid tomography: implications for the geological storage of carbon dioxide within sandstone saline aquifers. EGU, Vienna, Austria 2015. **Oral Presentation**
6. Thomas Seers, Matthew Andrew, Hannah Menke, Kamal Singh, Branko Bijeljic. From digital outcrops to digital rocks: multi-scale characterization of structural heterogeneity within high porosity sandstone reservoirs'. EAGE, Madrid, Spain 2015. **Oral Presentation**
7. HP Menke, B Bijeljic, MG Andrew, MJ Blunt Dynamic Pore-Scale Imaging of Reactive Transport in Heterogeneous Carbonates at Reservoir Conditions Across Multiple Dissolution Regimes. AGU Fall Meeting, San Francisco, USA 2014
8. MG Andrew, HP Menke, MJ Blunt, B Bijeljic, Micro-CT imaging of reservoir condition CO₂ during multi-phase flow in natural rock AGU Fall Meeting, San Francisco, USA, 2014.
9. Menke, H. P., Branko Bijeljic, M. G. Andrew, and Martin Blunt. Gordon Conference on Flow in Permeable Media, Lewiston, ME, USA 2014.
10. Menke, H.P., Bijeljic, B., Andrew, M.G., Blunt, M.J., "Dynamic pore-scale imaging of reactive transport in heterogeneous carbonates at reservoir conditions." International Conference on Greenhouse Gas Technologies, Austin, TX, USA, 2014.
11. Menke, H. P., Branko Bijeljic, M. G. Andrew, and Martin Blunt. EGU, Vienna, Austria, 2014 **Oral Presentation**
12. Menke, H. P., Branko Bijeljic, M. G. Andrew, and Martin Blunt. UKCCSRC Annual Meeting, Cambridge, UK 2014.
13. Menke, H. P., Branko Bijeljic, M. G. Andrew, and Martin Blunt. "Dynamic Pore-scale Imaging of Reactive Transport in Heterogeneous Carbonates at

Reservoir Conditions." In *76th EAGE Conference and Exhibition 2014*. **Oral Presentation**

14. Bijeljic, B., M. G. Andrew, H. P. Menke, and M. J. Blunt. "Using pore-scale imaging and modeling to provide new insights in multi-phase flow, transport and reaction phenomena in porous media." In *AGU Fall Meeting Abstracts*, vol. 1, p. 02. 2013. **Oral Presentation**

Acknowledgements

First and foremost I would like to express my gratitude to my advisors, Professor Martin Blunt and Branko Bijeljic. This work was only possible with their advice and support and I am profusely grateful for the opportunities they have given me.

I would also like to acknowledge the Qatar Carbonates and Carbon Storage Research Centre who funded me throughout this research project.

To my advisors at the Colorado School of Mines, I give my most profound thanks; Alexis Navarre-Sitchler, John McCray, and Reed Maxwell, your steadfast patience, support, and encouragement during my time in Colorado was especially remarkable. My continued career in academia is in no small part due to your kindness - a debt, I fear, I could never hope to repay.

I must also recognise my Imperial College team members (both experimental and modelling) who include: Catriona Reynolds, Joao P. Nunes, Kamal Singh, Ali Raeini, Ali Al-Menhali, Tarik Saif, Peter Lai, and Oussama Gharbi - Your academic rigor, collaborative mindset, and generous intellectual discussions have been invaluable.

To Matthew Andrew, my unofficial advisor, frequent collaborator, mentor, and best friend. Your generosity of spirit, intellectual precision, and boundless enthusiasm are an inspiration. You have been an exceptionally positive influence on my life and it has been an honour to work with you.

And to my examiners, Dominik Weiss and Catherine Noiriél, your insightful feedback and interest have been of great assistance in the preparation of this work.

My family also deserves special mention. Bill, Dallas, Josh, Lisa, Todd, Anna, Lee, Maude, Ed, and Pam, thank you all for the numerous opportunities and years of selfless support you have given me. I could not have done this without you and I hope I have made you proud.

Lastly, to E, I am happier now than I have ever been. I feel very lucky to know you and I am excited for what our futures may hold.

Dedication

For J1 & W2

And to 🐱 and 🐱.

May the triumvirate continue to accomplish great things together.

Contents

Copyright Declaration.....	2
Declaration of Originality.....	3
Abstract.....	4
List of Publications.....	5
Selected Conference Presentations	5
Acknowledgments.....	8
Dedication	9
Contents	10
List of Figures.....	13
List of Tables	21
1 Introduction.....	22
1.1 Atmospheric CO ₂ and temperature	23
1.2 Carbon storage.....	24
1.3 CO ₂ solubility	25
1.4 CO ₂ saturated brine and pH.....	25
1.5 Scope and objectives.....	26
2 Literature review and scientific background.....	28
2.1 CO ₂ phase behavior	28
2.2 The CO ₂ -brine-calcite system	29
2.3 Flow and transport in porous media	39
2.4 Pore scale flow and transport in porous media.....	42
2.5 Measurement and prediction of reaction: a review	
2.6 Imaging.....	47
2.6.1 In situ time-resolved μ -CT measurements.....	50
2.6.2 Beer-Lambert's law.....	50
2.6.3 X-ray beam sources	51
2.6.4 Laboratory-based μ -CT.....	52
2.6.5 Synchrotron lightsources	53
2.7 Carbonate pore structure classification	55
3 Image processing techniques	57
3.1 Artefact removal	57
3.2 Filtering and denoising.....	57
3.2.1 Simple filters	57
3.2.2 Edge preserving filters	58
3.3 Image registration	58
3.4 Image resampling	58
3.5 Difference imaging	59
3.6 Segmentation.....	59
3.6.1 Global thresholding	59
3.6.2 Watershed segmentation	59
3.7 Object separation.....	60
3.8 Measurement error.....	61

4	Experimental methods.....	63
4.1	Experimental apparatus with the Versa XRM-500	63
4.2	Experimental method with the Versa XRM-500	66
4.2.1	Pre-reaction dry scan.....	67
4.2.2	Leak testing the rig	67
4.2.3	Brine pre-equilibration.....	68
4.2.4	Purging the system	68
4.2.5	Loading the core	68
4.2.6	Wetting the core.....	71
4.2.7	Brine arrival.....	71
4.2.8	Dynamic scanning	72
4.2.9	Sampling.....	73
4.2.10	Post-experimental depressurization	75
4.2.11	Unloading the core and stopping reaction	75
4.2.12	Post-reaction dry scanning.....	75
4.3	Experimental apparatus using a synchrotron lightsource	75
4.4	Experimental method using a synchrotron lightsource	77
4.5	Effluent analysis	81
4.5.1	ICP-MS methods	81
4.6	Network extraction from μ -CT images	81
4.7	Flow modelling on μ -CT images.....	83
5	Pore and rock typing	84
5.1	Ketton.....	84
5.2	Estailades.....	89
5.3	Portland Basebed.....	93
5.4	Rock summary table	97
6	Reactive-flow imaging.....	98
6.1	Image Ketton dissolution using a laboratory source	98
6.1.1	Imaging strategy	100
6.1.2	Image processing.....	101
6.1.3	Results and discussion	101
6.1.4	Conclusions.....	111
6.2	Imaging Portland and Estailades dissolution using fast tomography	113
6.2.1	Imaging strategy	114
6.2.2	Image processing.....	115
6.2.3	Results and discussion	116
6.2.4	Conclusions.....	129
6.3	Imaging dissolution using a laboratory source at multiple reactive . conditions	131
6.3.1	Imaging strategy	132
6.3.2	Image processing.....	133
6.3.3	Results and discussion	133
6.3.4	Conclusions.....	150

7 Conclusions and future work.....	151
7.1 Conclusions	151
7.2 Future work	152
8 References	154
Appendices	169

List of Figures

Figure 1.1 CO₂ concentration vs year for since 1958, showing a steady increase. Data taken from [7]23

Figure 1.2 The isobaric minimum solubilities of CO₂ in pure water. Taken with permission from [44]. CO₂ solubility increases with increasing pressure and decreases with increasing temperature.....25

Figure 1.3 pH of the CO₂ saturated 1M and 5M NaCl systems as a function of pressure p . The pH decreases with salinity and pressure and increases with temperature. Taken with permission from Peng [46].26

Figure 2.1 CO₂ phase behaviour as calculated from [53]. The triple point for carbon dioxide is -57°C at 5.2 atm, below which liquid CO₂ is not stable. The critical point is at 31.1°C and 73 atm, above which CO₂ exists as a supercritical fluid.....29

Figure 2.2 pH-pC diagram of open system at standard temperature and pressure. Concentrations of CO₂, HCO₃⁻, CO₃²⁻, H⁺, and OH⁻ as functions of pH (Bjerrum plot) calculated using thermodynamic pK values for zero ionic strength (blue solid lines) or stoichiometric pK values (pK₀) typical for seawater and used here for the simple system (red dashed lines). CO₂ dominates for pH below pK₁, CO₃²⁻ above pK₂, and HCO₃⁻ in between. The lines of [H⁺] and [HCO₃⁻] cross at pH ≈ 4.5 (fresh water pK's) and pH ≈ 4.3 (seawater pK's). Taken with permission from [78]. ...32

Figure 2.3 The concentrations of each major carbonate species vs pH for brine #1 (a) and brine #2 (b) at 1 bar and 25°C (ambient conditions) and 50°C and 100 bar (experimental conditions). Increasing temperature and pressure shifts the speciations toward a lower pH.....37

Figure 2.4 Chemical and physical processes associated with carbonate mineral dissolution in CO₂-saturated brine at the mineral surface.40

Figure 2.5 Uniform dissolution dominates at low reaction rates. High reaction rates and low flow rates cause compact dissolution. Wormholes form at intermediate flow and reaction rates when dissolution follows preferential flow paths. Dissolution figures taken with permission from [125]..44

Figure 2.6 Relationship between $\ln(r / \alpha H)$ and $1/T$ in the (CO₂ + H₂O) system : ♦ , $p = 6$ MPa; , □ $p = 10$ MPa; ▲ , $p = 13.8$ MPa. Also ● , k_1 for calcite dissolution in the (HCl + H₂O) system. The experimental uncertainties are comparable to the size of the plotting symbols. Solid lines show linear regressions. Taken with permission from Peng [46].46

Figure 2.7 Neutron radiographs of dissolution patterns with increasing Péclet number. From left to right, face dissolution, conical wormholes, dominant wormholes, ramified wormholes, and uniform dissolution. Taken with permission from Fredd [147].47

Figure 2.8 X-ray optical geometries. (A) shows a parallel x-ray beam, while (B) shows a conical x-ray beam. Parallel beams are typical of synchrotrons, while conical beams are typical of bench-top systems. Figure inspired by [96].51

Figure 2.9 The geometric and optical magnification capabilities of the Versa-XRM 500 used for our experiments. Geometric magnification allows for high resolution scans at shorter source distances than traditional optical magnification. Modified from www.zeiss.com.52

Figure 2.10 A typical synchrotron schematic consisting of an electron gun that fires electrons through a Linac and into the booster synchrotron. The accelerated beam is then injected into the storage ring to be used by the many beam lines.53

Figure 2.11 A synchrotron undulator. The periodic structure of magnets (1) bend the electron beam (2) producing intense light (3).54

Figure 2.12 The Diamond Lightsource pink beam apparatus. The beam passing through the undulator produces intense light. The spectrum is narrowed by mirrors and filters and then is transmitted through the sample. The scintillator fluoresces in the visible spectrum and the light is focused and measured by the objective lens and CCD camera array.55

Figure 2.13 The Choquette and Pray classification system, which is based on rock fabric and depositional/diagenetic environment. Taken with permission from www.wiki.aapg.org.56

Figure 3.1 A segmented 2-D slice of Ketton (a), the Euclidian distance map of the solid phase (b) where brighter colours indicate a greater distance from the solid boundary, the grains separated by watershed boundaries (c), and the grains independently coloured by label (d).60

Figure 3.2 The porosity and permeability variation with gradient magnitude during watershed segmentation for Ketton (a) and Portland (b) rock samples. The porosity and permeability change very little with Ketton, but Portland shows large changes in permeability.....61

Figure 4.1 Instrumentation outside the μ -CT consists of three ISCO pumps, a barrel wash pump, a reactor complete with heating and stirring, an ISCO pump controller and two PID heating controllers.63

Figure 4.2 The *in situ* experimental apparatus used in the Versa XRM-500. CO₂ is pressurized by the injection pump and used to equilibrate brine in the reactor. Reactive brine is pulled through core assembly by the receiving pump. The cell is confined by deionized water in the confining pump at 12MPa and heated using heating tape controlled by a thermocouple in the confining fluid. The experimental system is connected together using tubing and fluid flow is directed using Valves (V) and Unions (U)..... **64**

Figure 4.3 μ -CT working diagram. An x-ray source fires x-rays through the sample which fluoresce when they hit the scintillator. The visible light is focused by the objective lens and digitised by the CCD array. **65**

Figure 4.4 The X-ray spectra emitted by the Versa XRM-500 source at three different energies as calculated by SpekCalc [137-139]. (a) is the raw spectrum emitted from the source and (c) is the spectrum inside the core holder after lower energy x-rays have been filtered by the air, carbon fibre, and aluminium components. (b) and (d) are the total energy spectra calculated for the maximum source current available at each energy level. The flux increases with power, but decreases with added filters. **66**

Figure 4.5 The core assembly inside the core holder. (A) PEEK tubing is attached to the interior end fittings and threaded through the steel end caps. (B) The core (B) is wrapped in aluminium foil (C) and inserted into the Viton sleeve. The Viton sleeve is then stretched over the end fittings to create a watertight seal (D) and two additional layers of aluminium foil are added to hold everything in place and prevent gas diffusion (E)..... **69**

Figure 4.6 The core holder is mounted on the stage in between the source and detector (A). The source is moved as close to the core holder as possible while still allowing for free rotation (B). *Photo Credit: Matthew Andrew* **70**

Figure 4.7 The difference image of a 2-D projection before and after brine arrival. The reactive fluid arrival is easily observable as a distinct attenuation difference (black) because the undoped brine absorbs fewer x-rays. **72**

Figure 4.8 Effluent sampling valve (A) mounted to the back of the scanner and a glass sampling syringe (B) for collecting effluent from the sample loop. **74**

Figure 4.9 The two-position six-port VICI HPLC valve schematic. Position A sends the fluid through the sample loop at reservoir conditions. Position B bypasses the sample loop allowing for ambient condition effluent sample extraction. Modified from www.thamesrestek.co.uk. **74**

Figure 4.10 The *in situ* experimental apparatus used at the Synchrotron. CO₂ is pressurized by the injection pump and used to equilibrate brine in the reactor. Reactive brine is pulled through core assembly by the receiving pump. The cell is confined by deionized water in the confining pump at 12MPa and heated using heating tape controlled by a thermocouple in the confining fluid. The experimental system is connected together using tubing and fluid flow is directed using Valves (V) and Unions (U)..... **76**

Figure 4.11 A short carbon fibre core holder used for *in situ* imaging at Diamond Lightsource. Sensitive equipment is protected from fluid spills by aluminium foil. **77**

Figure 4.12 The core assembly mounted on the I-13I beamline rotation stage. Flow and electrical lines are free to rotate. *Photo credit: Catriona Reynolds*. **78**

Figure 4.13 Teledyne ISCO pump remote control software controls flow conditions inside the beamline hutch. **79**

Figure 4.14 The Diamond Lightsource I13-I beamline pink beam taken by a visible light camera. The beam is seen in the visible spectrum because the beam is powerful enough to ionize the air. **80**

Figure 4.15 The x-ray spectra of the Diamond Lightsource I-13I pink beam. Calculated by beamline scientist Christophe Rau using both the experimental Tuning curve and theoretical mirror reflectivity and filter transmission. The dotted lines indicate spectrum termination points for gold (Au) and Aluminium (Al) filters and mirrors. **80**

Figure 4.16 The extracted network of a Ketton μ -CT image. Balls that are colored according to size represent pores and pore throats are grey sticks. Larger pores are redder and represented by larger balls. **82**

Figure 4.17 Normalized flow fields in Ketton. Only velocities fast than the average velocity are depicted with brighter and redder colors indicating faster velocities. **83**

Figure 5.1 A μ -CT image of Ketton Oolite taken at approximately 4-micron resolution. **85**

Figure 5.2 The MICP (a) and Pore Throat Radii distributions (b) for Ketton Oolite. A clear bimodal pore size distribution exists. Data taken from [214]. **86**

Figure 5.3 Probability density functions (PDFs) of pore voxel velocity in Ketton calculated on all dry μ -CT images of Ketton used in this thesis. All samples show a narrow range of velocities with a single well-defined population. **87**

Figure 5.4 Thin section images of Ketton Oolite, showing grain nuclei and concentric layering (a) and the presence of angular calcitic grains along with Ooliths (b). Taken with permission from Andrew [170]. **88**

Figure 5.5 A μ -CT image of Estailades Limestone taken at approximately 4-micron resolution. **89**

Figure 5.6 The MICP (a) and Pore Throat Radii distributions (b) for Estailades Limestone. A clear bimodal pore size distribution exists. Data taken from [214]. **90**

Figure 5.7 Probability density functions (PDFs) of pore voxel velocity in Estailades calculated on all dry μ -CT images of Estailades used in this thesis. All samples show a narrow range of velocities with a single well-defined population preceded by a long tail. **91**

Figure 5.8 Microporous and non-microporous grains in Estailades limestone imaged using thin section (top) and SEM (bottom). Figure taken with permission from [170].
..... **92**

Figure 5.9 A μ -CT image of Portland Basebed taken at approximately 4- μ m resolution. Portland consists of tightly packed ooids and microporous cement. **93**

Figure 5.10 The MICP (a) and Pore Throat Radii distributions (b) for Portland Base bed showing a single well-defined population preceded by a long tail. Data taken from [62]. **94**

Figure 5.11 Probability density functions (PDFs) of pore voxel velocity in Portland Base bed calculated on all dry μ -CT images of Portland used in this thesis. All samples show a large range of velocities spanning 10 orders of magnitude with a two overlapping populations. **95**

Figure 5.12 Microporous calcite grains in Portland limestone imaged using thin section (top) and SEM (bottom). Figure taken with permission from the Qatar Carbonates and Carbon Storage Research Centre (QCCSRC) image library..... **96**

Figure 6.1 Filtered and registered horizontal slices of three-dimensional Ketton images taken in the centre of the image at time 0 (a), 17 (b) 33 (c), 50 (d), 67 (e), 83 (f), 100 (g), 116 (h), 133 (i) and 149 (j) minutes. The carbonate (grey) is shown being dissolved by the brine (black) as time progresses. **101**

Figure 6.2 The porosity (a) and change in porosity (b) is averaged across each slice perpendicular to the flow direction and shown as a function of time. As the rock dissolves, the porosity increases. **102**

Figure 6.3 Surface area to the bulk volume ratio (squares) and the imaged-averaged porosity (crosses) as a function of time measured on 10 time-evolving μ -CT images (a). Image 7 (at 100 minutes) was of poor quality due to X-ray source fluctuations, which may explain why the measured specific surface area is lower than the general trend. Permeability plotted as a function of porosity through time (b). A power-law relationship with the equation $K = 1.4 \times 10^{-7} \phi^{5.16}$ is seen between porosity and permeability as dissolution progresses. **102**

Figure 6.4 (a) The Ketton grain size frequency histogram shown at the beginning and at the end of the experiment. (b-d) The same histogram but for three 1.3 mm sections in the direction of flow. **107**

Figure 6.5 Network representations of Ketton carbonate (extracted from μ -CT images) depicted at time 0 (a), 67 (b), and 149 (c) minutes. The spheres are pores, where the smallest pores are green, the largest are red, and the pore throats are grey. **108**

Figure 6.6 Normalized flow fields in Ketton are shown at times 0 (a) and 149 (b) minutes. The ratios of the magnitude of u at the voxel centres divided by the average pore velocity U_{av} are represented by cones (too small to be seen individually) that are coloured using a logarithmic scale spanning from 2 to 20. Velocity histogram (c) sampled uniformly in 256 bins of $\log(u/U_{av})$ which calculated as the ratios of the magnitude of u at the voxel centres divided by the average pore velocity U_{av} , for the images at times 0 and 149 minutes. **110**

Figure 6.7 The image processing workflow is presented for Portland carbonate. The reference greyscale image (a), the reacted greyscale image (b), the difference image (c), the filtered difference image (d), the segmented difference image (e), and the final segmented image (f). **116**

Figure 6.8 The sliced-averaged porosity versus distance from the sample inlet for Estailades at $0.1 \text{ mL}\cdot\text{min}^{-1}$ (a) and $0.5 \text{ mL}\cdot\text{min}^{-1}$ (b) and Portland at $0.1 \text{ mL}\cdot\text{min}^{-1}$ (c) and $0.5 \text{ mL}\cdot\text{min}^{-1}$ (d) for times 0, 30, 60, 90, and 120 min. The blue, yellow and red lines denote $t = 0, 60, 90,$ and 120 minutes, respectively. **116**

Figure 6.9 The percent change in average porosity across the whole sample versus time (a), porosity versus permeability (b), the change in porosity as a function of the change in permeability (c), and the specific surface area through time (d) of Estailades and Portland carbonates during dissolution. The porosity and surface area are calculated directly from the segmented images. Permeability is found from the computed flow field. **117**

Figure 6.10 The ratios of the magnitude of u at the voxel centres divided by the average pore velocity U_{av} are coloured using a linear scale where low velocity is blue, medium velocity is yellow, and high velocity is red. **119**

Figure 6.11 Probability density functions (PDFs) of pore voxel velocity during (a) experiment 1, (b) experiment 2, (c) experiment 3, and (d) experiment 4. The velocity histogram is computed on the pore-space images and sampled uniformly in 256 bins of $\log(\mathbf{u}/U_{av})$, which are calculated as the ratios of the magnitude of u at the voxel centres divided by the average pore velocity U_{av} . The distributions are shown at times 0, 5, 12, 25, 37, 63, and 120 minutes. **120**

Figure 6.12 Normalized correlation, Eqs. (6.1) and (6.2), between the initial voxel velocities (time=0) and each those from successive image through time for each experiment..... **121**

Figure 6.13 (a) Péclet number (Pe), (b) Damköhler number (Da), (c) Péclet-Damköhler number ($PeDa$), and (d) effective reaction rates (r_{eff}) for each experiment through time. **124**

Figure 6.14 (a) Mean Péclet number (Pe), (b) maximum Péclet number (Pe), (c) standard deviation of Péclet number (Pe), and (d) fraction of void voxels with Péclet number (Pe) ≤ 1 , measured by direct simulation for each experiment through time.

Figure 6.15 A schematic of wormholing (a), uniform (b), and channel formation (c) dissolution regimes. In the wormholing regime, the reactive brine (blue) floods the pore space (black) dissolving the rock (white) as it advances. In the uniform dissolution regime, brine floods the whole pore space rapidly and the rock then dissolves across its entire surface area. During channel formation, flow is faster than in the wormholing regime: reactive brine floods the rock very quickly, but the heterogeneity of the rock allows preferential flow paths to form which then provide the majority of the reactant to a more limited portion of the surface of the rock. **128**

Figure 6.16 Sliced-averaged porosity versus distance from the sample inlet for Ketton at pH 3.6 (a) and pH 3.1 (b), Estailades at pH 3.6 (c) and pH 3.1 (d) and Portland at pH 3.6 (e) and pH 3.1 (f). The red and blue lines indicate ~ 1 and ~ 2 hours into the experiment..... **134**

Figure 6.17 The percent change in average porosity across the whole sample versus time (a), permeability versus porosity (b), the change in permeability as a function of the change in porosity (c), and the specific surface area versus time (d) of Ketton, Estailades, and Portland carbonates during dissolution. The porosity and surface area are calculated directly from the segmented images. Permeability is found from applying Darcy's Law from the computed flow field **135**

Figure 6.18 The ratios of the magnitude of u at the voxel centres divided by the average pore velocity U_{av} are coloured using a linear scale where low velocity is blue, medium velocity is yellow, and high velocity is red..... **137**

Figure 6.19 Probability density functions (PDFs) of pore voxel velocity during (a) experiment 1, (b) experiment 2, (c) experiment 3, (d) experiment 4, (e) experiment 5, (f) experiment 6. The velocity histogram is computed on the pore-space images and sampled uniformly in 256 bins of $\log(\mathbf{u}/U_{av})$, which are calculated as the ratios of the magnitude of u at the voxel centres divided by the average pore velocity U_{av} . The distributions are shown at times 0, ~60 (blue), ~120 (red), ~240 minutes **138**

Figure 6.20 Normalized correlation, Eqs. (1) and (2), between the initial voxel velocities (time=0) and each those from successive image through time for each experiment **139**

Figure 6.21 (a) Péclet number (Pe), (b) Damköhler number (Da), (c) Péclet-Damköhler number ($PeDa$), and (d) effective reaction rates (r_{eff}) for each experiment through time **143**

Figure 6.22 (a) Ca^{2+} concentration [$mol.L^{-1}$] measured in effluent and (b) pH as calculated from Ca^{2+} concentration by the method presented in Leal et al. [243] versus time [min]. The error bars represent the standard error of the concentration and pH values. **145**

Figure 6.23 A comparison of effluent measured and CT observed fluid-solid reaction plotted as the difference in dissolved solid $CaCO_3$ versus time calculated using Eq. 6.17. **146**

Figure 6.24 A schematic of the flow and transport processes through time during (a) uniform dissolution and (b) channel formation. Rock grains (grey circles) are dissolved in advectively-dominated regions of fast flow (red arrows). Ca^{2+} ions (dark blue circles) are trapped in the diffusive regions of the pore space..... **149**

List of Tables

Table 2.1: The major chemical components of each brine. Temperature and pressure conditions were held steady at 100 Bar and 50°C inside a continuously stirred reactor vessel.....	30
Table 2.2 The saturation indices of the major dissolved minerals in brine #1 and brine #2 at experimental conditions. All minerals are under-saturated and thus the solid mineral forms are not stable and all species remain in solution.	34
Table 2.3 The major species activities for brine #1 and brine #2 at experimental conditions as calculated by the program PHREEQC.....	36
Table 2.4 The major chemical reactions of the CO ₂ -rock-brine system and their typical timescales.....	38
Table 4.1 Energy limits of the Versa XRM-500.	66
Table 5.1 Summary of physical rock properties. Chemical composition was found using X-ray diffraction..	97
Table 6.1 Network properties and computed flow and reaction parameters for times 0, 67, and 149 minutes for section 6.1.....	109
Table 6.2 Experimental Parameters for section 6.2.....	114
Table 6.3 Computed Flow and Reaction Parameters for Times 0, 63, and 120 min for section 6.2.....	123
Table 6.4 Network and direct flow simulation properties for times 0, 63, and 120 min.	127
Table 6.5 Experimental Parameters for section 6.3.....	132
Table 6.6 Computed flow and reaction parameters for times 0, ~60, ~120 and ~240 min for section 6.3.....	141
Table 6.7 Network properties for the initial images in each experiment.	144
Table 6.8 Image measured vs. pH predicted reaction rates at time ~180 minutes. The error represents the standard error of the effluent calcium content.....	148

1. Introduction

Fluid-rock reaction in carbonate rocks is a process that has an extensive range of applications to energy, global climate change, and the environment. Carbon Capture and Storage (CCS) has been proposed as one of the principal solutions to combat rising anthropogenic CO₂ emissions. The most straightforward way of storing CO₂ underground is to use either saline aquifers which are unsuitable for drinking water, or producing or depleted oil reservoirs, as the infrastructure already exists for fluid injection. CO₂ has been used extensively in enhanced oil recovery applications (EOR) by pumping liquid (or supercritical) CO₂ into reservoirs to both boost reservoir pressure and use multiphase wettability changes to drive more oil out of the reservoir.

However, over half of the world's oil reservoirs are composed of carbonate rock [1]. When CO₂ fluid mixes with reservoir brine it becomes carbonic acid and can partially dissolve the host rock. The dissolution processes at reservoir conditions are poorly understood. The type of dissolution is controlled by the initial pore structure, fluid flow and reactive transport conditions. Carbonate rocks are extremely diverse and complex and thus it requires many experiments to determine the principal controls on dissolution for a range of carbonate rock types. At reservoir conditions the acidity of the brine is strongly dependent on temperature and pressure. Additionally, the acidity of the brine is partially controlled by the amount of calcium dissolved in solution. Therefore the development of a laboratory-based technique that allows for reservoir condition imaging of complex pore-structures with a temporal resolution sufficient to study dynamic processes is imperative for acquiring the breadth of data needed for complete understanding of pore-scale processes in carbonate rocks.

In this thesis we develop novel techniques for imaging and analysis of fluid/rock reaction in a range of carbonate rocks at the pore scale using X-ray microtomography. These techniques include dynamic reservoir condition imaging experiments, a range of image analysis techniques to extract key parameters including porosity, surface area, and grain size, and apply field-scale dimensionless numbers used to describe flow and reactive conditions (such as the Péclet and Damköhler numbers) to the pore-scale. We calculate effective pore-scale reaction rates from both image and effluent analysis and use pore-scale models to find permeability, connectivity, and distributions of velocity. These tools are then used to describe the observation of two distinct dissolution regimes, uniform and channelling, and the mechanisms controlling these dissolution types. These methods are applied specifically to the brine-rock system for CCS applications and a range of novel results are presented that focus on three experimental datasets:

1. We demonstrate the validity of the method using the simple rock Ketton on the laboratory scanner (section 6.1).

2. We adapt the method to study highly heterogeneous rocks at multiple flow conditions using fast synchrotron tomography (section 6.2).
3. We add effluent analysis to the laboratory method and study multiple reaction rates on rocks with increasing complexity (section 6.3).

In this introduction we explain the motivation behind this thesis. We first describe the evidence for CO₂ emissions on global climate change and the possible function that CCS will play in mitigation (section 1.1). We will then look at some of the concerns with CO₂ storage, specifically the potential difficulties with injecting CO₂-acidified brine into the subsurface (section 1.2). We then describe the behaviour of aqueous CO₂ at high temperature and pressure (section 1.3) and examine how the acidity of CO₂ changes at reservoir conditions (section 1.4). Finally, the scope and objectives of this work are defined in the context of CCS (section 1.5).

1.1 Atmospheric CO₂ and Temperature

Atmospheric CO₂ is closely correlated with global temperature. Ice core data has shown that over approximately the last million years, temperature has closely followed atmospheric CO₂ levels [2] and that in that time the CO₂ concentration in the atmosphere has never exceeded 300 ppm [3-5]. The Mauna Loa observatory in Hawaii has been tracking the concentration of CO₂ in the atmosphere since 1958 [6] and has seen a steady increase in concentration far exceeding historic levels [Figure 1.1]. As of 2015, the yearly average concentration is expected to exceed 400 ppm.

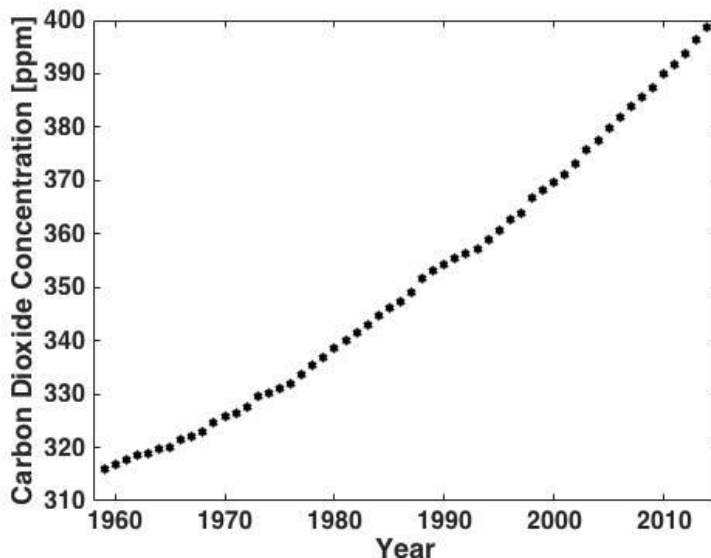


Figure 1.1: CO₂ concentration vs year for since 1958, showing a steady increase in CO₂ concentration through time. Data taken from [7].

The rising global population coupled with increasing industrialisation has driven a mounting reliance on fossil fuels that has caused the atmospheric CO₂ concentration to climb at an alarming rate [8]. Fossil fuels currently account for approximately 85% of world energy use [9]. Total energy demand is expected to rise substantially in the next 20 years as world population grows and economies continue to develop [10]. The International Energy Agency predicts that the world energy demand will continue to increase by more than 30% between 2010 and 2035 [11]. It is predicted that even with the introduction of renewable fuel sources, fossil fuels will continue to account for more than 75% of world energy consumption [12]. These continued greenhouse gas emissions resulting from the unrelenting consumption of fossil fuels represent a significant challenge to the global climate [13]. Thus, a solution to the dramatic reduction in CO₂ emissions to the atmosphere is required to mitigate the rise in global temperatures [14].

Ultimately the solution to global climate change and the world energy crises is to shift entirely to renewable energy. However, such a transformation will take many years and will require massive investment in new energy infrastructure including more competitive prices for renewable sources [15]. In the short term, Carbon Capture and Storage (CCS) is the most competitive large-scale solution that will allow us to continue to burn fossil fuels while maintaining acceptable levels of CO₂ in the atmosphere [16, 17].

1.2 Carbon Storage

Injecting carbon dioxide in carbonate reservoirs is known to induce many physical and chemical changes, including diagenetic chemical reactions [18, 19], permeability changes [20], and multiphase fluid displacement [21, 22]. The reservoir depth, temperature, fluid phases, chemical composition, brine salinity, and stored CO₂ volume, phase, and penetration distance from the injection well all affect the evolution of physical and chemical processes within the reservoir [23, 24]. Thus, long-term storage security depends on the understanding of these rock-fluid interactions.

Carbonate minerals are abundant in both oil reservoirs and saline aquifers [25-27]. When CO₂ fluid is introduced to aquifer brine it dissolves and creates a CO₂-acidified brine [28]. This brine can react with carbonate rocks and impact both the formation integrity and the flow properties. Examples of this include reports of weakening of carbonate cements and damage to injection wells [29, 30] and natural analogues where CO₂ rapidly escapes from subsurface deposits [31, 32]. Such destructive events can undermine CO₂ storage operations by causing leakage of CO₂ out of the reservoir, instigate unpredictable fluid flow, or force the termination of CO₂ injection altogether [33]. Characterizing the controls on reaction in the rock-fluid system is thus integral to the success of CO₂ storage efforts.

Brine acidity (or pH) after CO₂ injection is a crucial factor in carbonate reaction rate and equilibrium state and can trigger dissolution or precipitation of

carbonate minerals. Low pH brines have also been used in the EOR [34], CO₂-EOR [35], acid gas injection [36], and hydraulic fracturing industries [37] to stimulate carbonate reservoirs and enhance oil and gas recovery [38, 39]. A poor understanding of the mechanisms behind dissolution processes can result in poorly etched fractures, ineffective well stimulation, and added operational risk. Therefore, improved comprehension of rock-fluid interaction is of use to the CO₂ storage community as well as other energy related industries.

1.3 CO₂ solubility

CO₂ solubility in water is strongly dependent on fluid temperature and pressure [Figure 1.2]. At high temperatures and pressures inside a typical carbonate reservoir, the potential for dissolved CO₂ is substantially greater than at atmospheric conditions [40]. CO₂ solubility increases dramatically with pressure, varies considerably with temperature [41, 42] and decreases with increasing salinity [43]. Thus it is imperative to study the CO₂-brine system at reservoir conditions to form an accurate picture of the dissolution process.

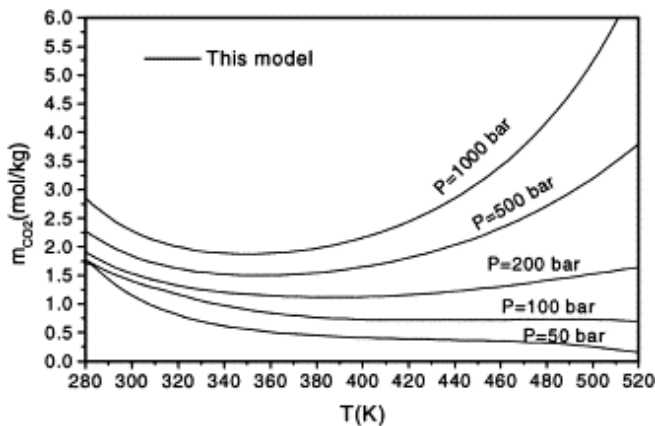


Figure 1.2 The isobaric minimum solubilities of CO₂ in pure water. Taken with permission from [44]. CO₂ solubility increases with increasing pressure and decreases with increasing temperature.

1.4 CO₂ saturated brine and pH

CO₂-saturated brine acidity, which is partially controlled by CO₂ solubility, has a large dependence on temperature, pressure, and salinity [Figure 1.3]. pH decreases with increasing salinity and pressure, and increases with increasing temperature [45]. Therefore, experiments using representative aquifer brines at reservoir conditions are required to accurately characterize the chemical conditions for dissolution.

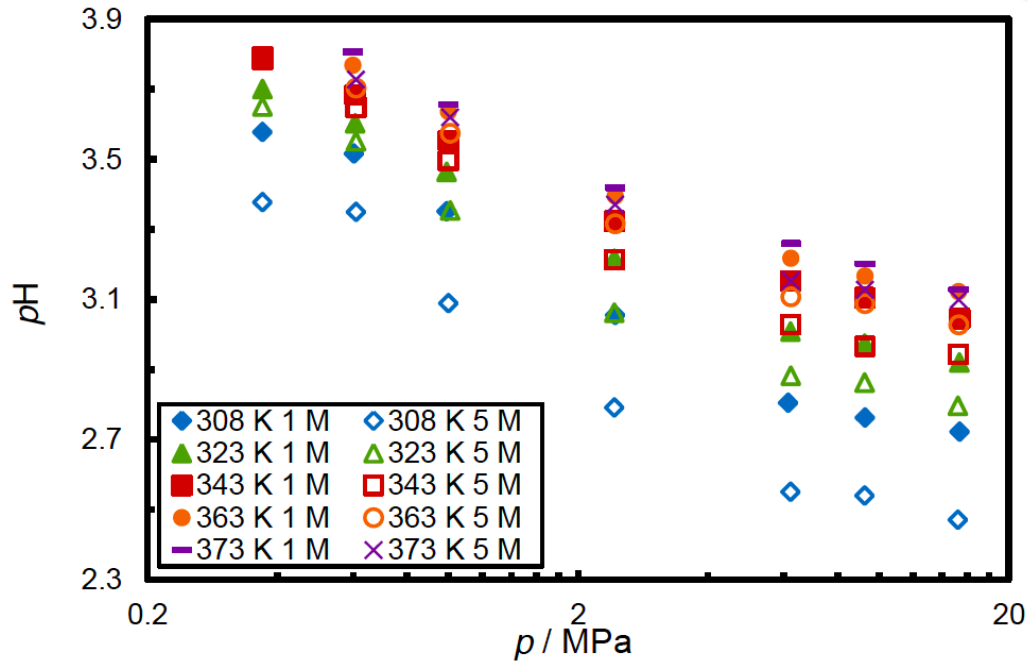


Figure 1.3 pH of the CO₂ saturated 1M and 5M NaCl systems as a function of pressure p . The pH decreases with salinity and pressure and increases with temperature. Taken with permission from Peng [46].

1.5 Scope and Objectives

The scope of the work presented in this thesis is to conduct key experiments to develop a better understanding of chemical reaction between limestone minerals and CO₂-acidified brine at the pore scale and for the purpose of 1) providing insight into the flow and transport mechanisms controlling dissolution rate in the pore-space and 2) to provide the scientific community with robust bench mark datasets for calibrating pore-scale reactive transport models. Experimental measurements were made of the location and rate of dissolution of limestone when subjected to CO₂ acidified brine at reservoir conditions. Changes in porosity, permeability and surface area were measured and new pore-scale dimensionless numbers describing reactive flow were derived providing a quantitative understanding of time-resolved reaction rates. Network extraction and flow models were used to understand localized changes in the flow field inside a porous rock. One key aspect of this work was the experimental measurement of reaction rate both using imaging and effluent analysis at conditions that are relevant to the petroleum industry which can now be employed to increase the accuracy of available theoretical modelling approaches.

The experiments conducted in this thesis focus on experimental investigations at the high temperatures and pressures representative of a deep reservoir. A new high pressure and temperature imaging apparatus was designed and constructed to accommodate the acidic reservoir fluids and control flow through a micro-core with great accuracy while allowing for the flexibility of stage rotation during flow and the

ability to extract samples of effluent without disturbing flow conditions. This apparatus was then used to examine dissolution of a simple limestone sample at reservoir conditions and the images were published and released to the modelling community for verifying pore-scale reactive transport models. These experimental techniques were then further applied to two more complex limestone samples at various flow and transport conditions to investigate the wider impact of flow and brine acidity on dissolution behavior.

There has been some debate on the validity of pore-scale experiments using microtomography with regard to representative elementary volumes (REV) [47]. The concept of REV is traditionally explained by Bear [48] and is defined as the minimum sample volume beyond which the statistically variations of a particular property become negligible. It is important to note that the REV is different for each property. For example, the REV for porosity of a rock will be different than that of permeability. In pore-scale imaging, the calculated properties are meaningful for upscaling only if the image volume is larger than the REV. In microtomography, the detector has a fixed number of pixels and thus there is a trade off between resolution and scale: the larger the volume scanned, the poorer the image resolution and the larger each voxel. The volume and resolution of the experiments must be calibrated to be able to capture the process of interest while maintaining the volume to be larger than the REV. Bijeljic et al. [49] has calculated variograms showing the normalized functions for porosity and velocity in the direction of flow for a range of carbonate rocks. Mostaghimi et al. [50] investigated the pore scale changes in permeability for beadpack, sandstones, and carbonates using increasing long images up to 3 mm in length and found that the existence and size of an REV increases with sample complexity and that the carbonate variation in permeability can vary by up to 50%, but that this variation stabilizes well before the total sample length. This thesis focuses on high resolution images of around 5 microns which with current detector technology limits the volume of each image to around 5 mm x 5 mm x 5 mm. This total volume is above the REV measured for porosity, velocity, and permeability and the resolution is adequate for observing pore-scale dissolution. Furthermore, the images acquired during this study and the properties measured are intended as benchmark experiments to validate pore-scale reactive transport models. They are not intended to deliver complete upscaled descriptions of flow and transport in heterogeneous media, only to provide insight into the possible controls on dissolution under various conditions.

Overall, the goal of this study is to enable more rigorous modelling of limestone dissolution in deep saline aquifers used for carbon storage and in oil reservoirs when EOR is performed. The application of the results can also help identify some of the complexities in pore-scale reactive transport phenomena and increase the accuracy of representative reservoir simulation models to mitigate the risks associate with the CCS, acid well stimulation, and EOR operations that they are designed to simulate and control.

2 Literature Review and Scientific Background

In this section we will examine some of the scientific concepts behind reactive flow in porous media, and how experiments can address these matters. We examine the phase relationships of pure CO₂ at reservoir conditions (section 2.1). Then we examine the chemistry behind dissolution in CO₂-brine-rock system and use our experimental brines and the program PHREEQC as examples to show how to verify chemical speciation and equilibrium of the initial fluids before using them during experimentation (section 2.2). Bulk flow properties in porous media (section 2.3) are discussed followed by an examination of dimensionless numbers describing pore-scale flow (section 2.4). Previous studies of reaction are examined at various scales with an emphasis on the state of pore-scale understanding of reaction in porous media. Additionally previous studies of reaction rate are reviewed (section 2.5) and x-ray micro-tomography is described for both laboratory and synchrotron applications (section 2.6). Finally, geological methods of charactering pore and rock structures are explicated (section 2.7).

2.1 CO₂ Phase Behavior

A phase diagram for CO₂ is shown in Figure 2.1. Below the triple point, CO₂ exists as three distinct phases with chemical and physical properties that vary slowly and have discrete phase boundaries. Above the critical point the gas-vapor boundary disappears and CO₂ behaves with the viscosity of a vapor and the density of a liquid. In CCS, for a given increase in reservoir pressure a greater amount of CO₂ can be injected. However, as the petrophysical and solubility relationships of supercritical CO₂ are a strong function of reservoir temperature, pressure, and salinity [51, 52] it is thus required to study the CO₂-brine-calcite system at reservoir conditions.

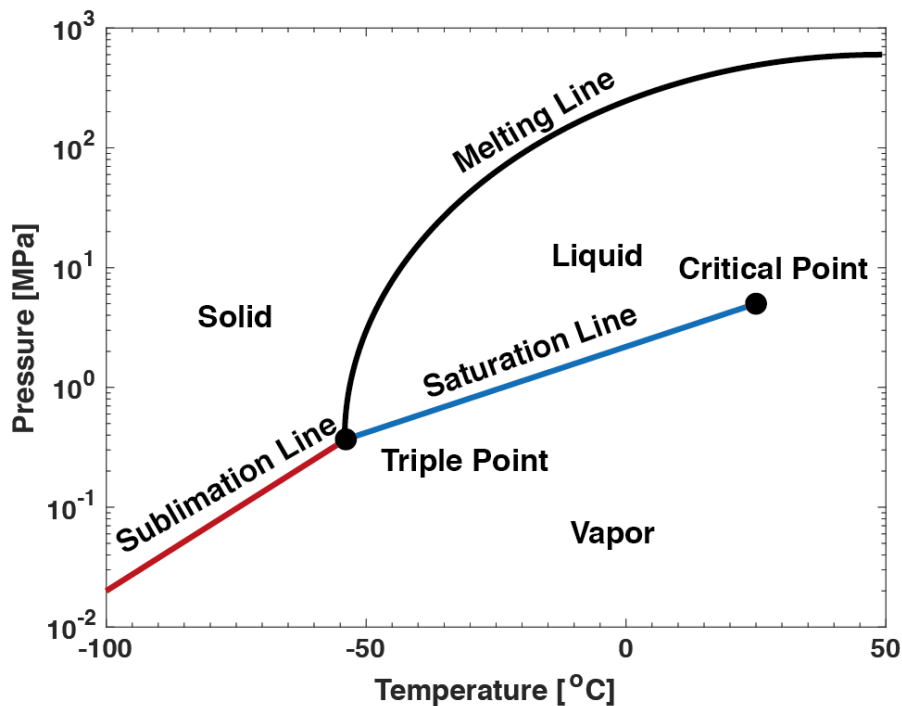


Figure 2.1 CO₂ phase behaviour as calculated from [53]. The triple point for carbon dioxide is -57°C at 5.2 atm, below which liquid CO₂ is not stable. The critical point is at 31.1°C and 73 atm, above which CO₂ exists as a supercritical fluid.

2.2 The CO₂-brine-calcite system

The chemistry behind calcite dissolution in the presence of CO₂-saturated brine has several variables to consider: the chemical constituents of the rock, the equilibrium between CO₂ and highly saline brine, the effect on pH of dissolved calcite, and the timescales associated with equilibrium. In this section we will discuss the interplay between these processes and how they affect the equilibrium calculations of our experimental brines.

For the purposes of calculation in this section we use the program PHREEQC and make several assumption. We assume our rock is pure calcite (CaCO₃) – and indeed all of the rocks reacted in this study are exceptionally pure (>97.2% calcite with the remaining fractions being quartz). We also assume that all reaction takes place at the representative reservoir conditions of our experiments (10MPa and 323.15 K) and that brine is made of pure (deionized) water in which 1% *wt.* KCl (0.14 M) and 5% *wt.* NaCl (0.91 M) are dissolved.

In this thesis we use two separate solutions in a closed system. Both solutions have the same elevated temperature and pressure with the same salinity brines and are equilibrated with super critical CO₂. The first solution, hereafter called ‘Brine #1’ is designed to represent a system very near the well bore where injection of CO₂ saturated brine is very recent and does not initially have any carbonate rock present.

The second solution, hereafter called 'Brine #2', is designed to be representative of a pore fluid farther away from the well-bore where some reaction has taken place and thus has some carbonate rock dissolved in the brine. Both of these equilibrated brines are then used in the subsequent flow experiments (sections 6.1-6.3) to dissolve three porous mediums made of calcite at various flow conditions.

In this section we will discuss chemical speciation and equilibrium and how these concepts are applied to Brine #1 and Brine #2.

Table 2.1 The major chemical components of each brine. Temperature and pressure conditions were held steady at 100 Bar and 50°C inside a continuously stirred reactor vessel.

	Component	Amount / Condition
Brine #1 pH \cong 3.1	$H_2O_{(l)}$	940 g
	$CO_{2(sc)}$	100 Bar
	$NaCl_{(s)}$	50 g
	$KCl_{(s)}$	10g
Brine #2 pH \cong 3.6	$H_2O_{(l)}$	940 g
	$CO_{2(sc)}$	100 Bar
	$NaCl_{(s)}$	50 g
	$KCl_{(s)}$	10 g
	$CaCO_{3(s)}$	0.16 g

The acidity of CO₂-brine solution dictates how it chemically interacts with the solid mineral. A standard way to describe a solution's acidity is with pH [54], which is defined as:

$$pH = -\log \alpha_{H^+} \quad (2.1)$$

Where α is the activity of the proton. The pH of the solutions will directly impact the rate of dissolution of the porous medium and thus is of considerable interest to the carbon capture and storage industries[41, 55-62]. Activity can be related to concentration [63] in species I using the activity coefficient γ_i :

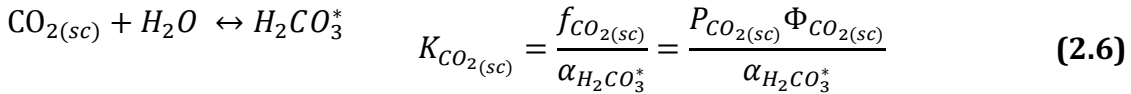
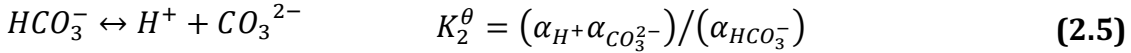
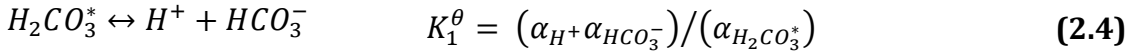
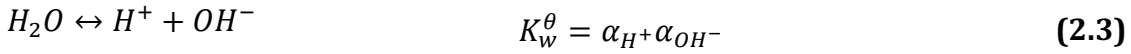
$$\alpha_i = \gamma_i [i] \quad (2.2)$$

In an ideal solution, the activity coefficient is 1. However, in a non-ideal system such as the one studied here, the activity is controlled by the interaction between the dissolves species and is less than 1.

The chemical components of a fluid will partition into multiple species, the distribution of which can be described by the equilibrium constant, K . The equilibrium constant of a gas dissolving into a liquid is controlled by the gas phases fugacity and partial pressure and the activities of the dissolved species [64] while the equilibrium constant of chemical speciation within a liquid is only controlled by the species activities.

The solubility of CO₂ in water has important implications for contaminant transport and carbon capture and storage [41, 65-68]. The CO₂ solubility affects CO₂ reactivity with the pore structure [69-71] and thus determines both the sealing capacity of the aquifer [20, 58, 72, 73] and the total potential CO₂ reservoir capacity [74-76].

When CO₂ dissolves in water there are four reactions that take place, each with their own equilibrium equation.



Where $P_{CO_{2(sc)}}$ is the total pressure of the supercritical phase, $\Phi_{CO_{2(sc)}}$ is the fugacity coefficient, $K_{CO_{2(sc)}}$ is the equilibrium constant of CO_{2(sc)} and $H_2CO_3^*$ is defined as concentration of aqueous CO₂ in solution. K_w^θ is the equilibrium constant for water dissociation and K_1^θ and K_2^θ are the first and second carbonic acid dissociation constants. The activity, activity coefficient, molality, and fugacity of species I are given by α_i , γ_i , and f_i respectively. K_w^θ has been calculated semi-theoretically by Bandura and Lvov [77] for a wide range of temperatures and densities. Spycher and Pruess [64] give estimations of activity and equilibrium constants for carbonate speciation at high temperatures and pressures.

An easy way to visualise the interaction between species concentration and pH is using a Bjerrum plot. The blue lines in Figure 2.2 illustrate how the speciation of CO₂ changes with pH in an open system at standard temperature and pressure. In such a system, where pure water is exposed to the atmospheric forcing of a partial pressure of CO₂ of 400ppm at 1 bar, the pH of the water is around 5.59 and thus the major carbonate species is $H_2CO_3^*$.

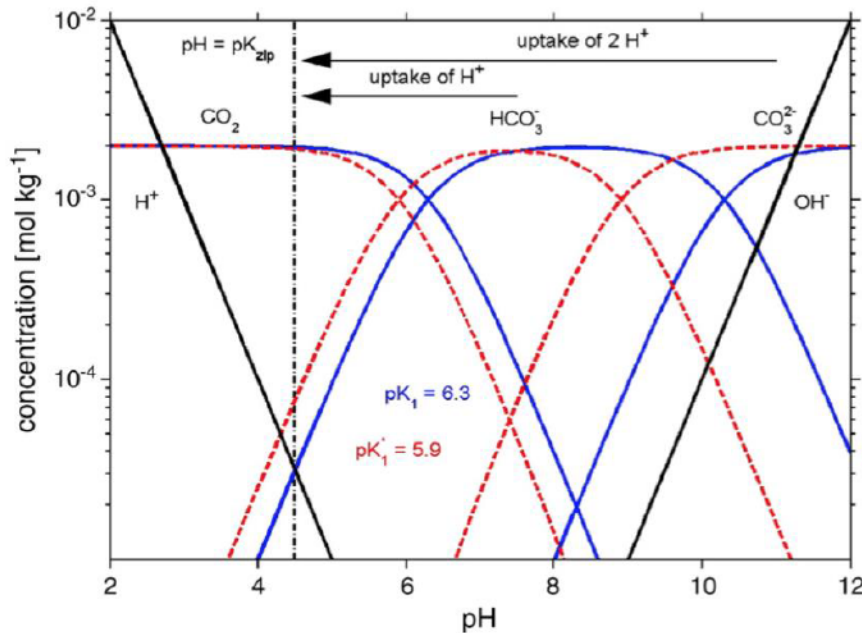


Figure 2.2 pH-pC diagram of open system at standard temperature and pressure. Concentrations of CO_2 , HCO_3^- , CO_3^{2-} , H^+ , and OH^- as functions of pH (Bjerrum plot) calculated using thermodynamic pK values for zero ionic strength (blue solid lines) or stoichiometric pK values (pK') typical for seawater and used here for the simple system (red dashed lines). CO_2 dominates for pH below pK_1 , CO_3^{2-} above pK_2 , and HCO_3^- in between. The lines of $[\text{H}^+]$ and $[\text{HCO}_3^-]$ cross at $\text{pH} \approx 4.5$ (fresh water pK's) and $\text{pH} \approx 4.3$ (seawater pK's). Taken with permission from [78].

In our system, which is closed to the atmosphere, it is exposed to a partial pressure of pure CO_2 at 100 bar. The equilibrium pH is thus much lower (~ 3) but the dominant CO_2 species remains H_2CO_3^* .

However, as illustrated by the red lines in Figure 2.2, salinity also affects the chemical speciation and thus both the total amount of dissolved salt species and the activity of our brine needs to be calculated. In our reservoir systems, the halite (NaCl), sylvite (KCl), and calcite (CaCO_3) minerals are added to the liquid solution and equilibrated. We must first confirm that all of the mineral dissolves into solution and then calculate the activities of the dissolved species.

When a mineral and fluid interact, the equilibrium state is what controls whether dissolution or precipitation occurs. For example, when halite (NaCl) is added into pure water, chemical equilibrium is reached with the following:



The chemical equilibrium constant, K_{eq} , of halite is:

$$K_{eq} = \frac{\alpha_{\text{Na}^+} \alpha_{\text{Cl}^-}}{\alpha_{\text{NaCl}}} \quad (2.4)$$

where α_i is the activity of species i . For most solids, the activity at equilibrium is 1, and therefore:

$$K_{eq} = (\alpha_{\text{Na}^+})_{\text{equilibrium}} (\alpha_{\text{Cl}^-})_{\text{equilibrium}} = K_{sp} \quad (2.5)$$

where K_{sp} is the solubility product. However, most real solutions are out of equilibrium and thus a new term, Q , is introduced as the ion activity product at disequilibrium.

$$Q = (\alpha_{\text{Na}^+})_{\text{disequilibrium}} (\alpha_{\text{Cl}^-})_{\text{disequilibrium}} \quad (2.6)$$

We can then use the ratio of Q to K_{eq} to define two new terms called the saturation index, SI , and Ω , the saturation state, to describe the impact of ion activity product on disequilibrium.

$$SI = \log \Omega = \log \left(\frac{Q}{K_{sp}} \right) \quad (2.7)$$

When $SI = 0$ the solution is said to be at equilibrium, while if it is greater or less than 0, the solution is either under or super saturated, respectively, and thus dissolution (when under-saturated) or precipitation (when super-saturated) is favourable.

The Gibbs free energy of reaction is another way of stating reaction potential. We can equate the change in Gibbs free energy (ΔG) to the saturation state as:

$$\Delta G = -RT \ln \left(\frac{Q}{K_{sp}} \right) \quad (2.8)$$

where R is the universal gas constant and T is the temperature. Thus, when $\Delta G=0$ the system is said to be at equilibrium at a given temperature T .

We calculate our the saturation indices of our solids in Table 2.2 and find them all to be much less than zero and thus the minerals are very under saturated and all of the mineral that is present in the system dissolves and remains in solution. Note that we report the aragonite saturation index even though it is not initially present as it is a possible mineral form of calcium carbonate.

Table 2.2 The saturation indices of the major dissolved minerals in Brine #1 and Brine #2 at experimental conditions. All minerals are under-saturated and thus the solid mineral forms are not stable and all species remain in solution.

	Mineral	Saturation Index
Brine #1 pH \cong 3.1	<i>Halite</i>	-1.99
	<i>Sylvite</i>	-2.32
Brine #2 pH \cong 3.6	<i>Halite</i>	-1.99
	<i>Sylvite</i>	-2.32
	<i>Calcite</i>	-4.54
	<i>Aragonite</i>	-4.66

We must then calculate the activities of the dissolved species in order to accurately characterise their speciation. The Debye-Hückle Equation is the predominant method of calculating activity coefficient of relatively dilute electrolytic solutes [79-81] (<0.01mol.kg⁻¹).

$$\log \gamma = \frac{-A|Z_+Z_-|\sqrt{I}}{1 + \alpha^\circ B\sqrt{I}} \quad (2.14)$$

where α° is the ion size parameter and Z^+ and Z^- are the charges of the cations and anions in solution. The molecular strength of the system, I , and parameters A and B are calculated using the equations:

$$I = \frac{1}{2} \sum_i m_i Z_i^2 \quad (2.15)$$

$$A = \frac{1.824863 \cdot 10^6 \cdot \rho_0^{0.5}}{(\epsilon_0 T)^{3/2}} \quad (2.16)$$

$$B = \frac{50.292 \cdot \rho_0^{0.5}}{(\epsilon_0 T)^{1/2}} \quad (2.17)$$

where ρ_0 is the density and ϵ_0 is the dielectric constant of pure water at set temperature and pressure, and T is set temperature in Kelvin.

However in a system such as ours where the salt concentrations are above 0.1 mol.kg⁻¹, there is experimental evidence that the activity coefficient first decreases, but then increases with increasing ionic strength. Thus the equation must be modified with a correction factor. We use an extension to the Debye-Hückle called the B-dot equation that, depending on the type of ion, does a reasonable job of predicting activity coefficients of salt in solutions at concentrations between 0.3 to 1 mol.kg⁻¹ [82, 83].

$$\text{Log } \gamma_{\pm} = \frac{-A|Z_+Z_-|\sqrt{I}}{1 + \alpha^{\circ}B\sqrt{I}} + \dot{B}I \quad (2.18)$$

\dot{B} is an empirical correction factor derived experimentally from the difference between measured and predicted activity coefficients using the rearranged formula:

$$\dot{B} = \log(\gamma_{observed} - \gamma_{D-H}) = \frac{1}{I} \cdot \left[\log \gamma_{\pm} + \frac{-A|Z_+Z_-|\sqrt{I}}{1 + \alpha^{\circ}B\sqrt{I}} \right] \quad (2.19)$$

where $\gamma_{observed}$ is the experimentally derived activity coefficient and γ_{D-H} is the Debye-Hückle calculated coefficient. However, it should be noted that experimental observations of the activity coefficient at high temperatures and pressures with complex ionic components are sparse.

We now have all of the tools necessary to calculate the activities of the chemical species in our first system. Table 2.3 shows the activities for Brine #1 and Brine #2 as calculated by the program PHREEQC [84].

Table 2.3 The major species activities for Brine #1 and Brine #2 at experimental conditions as calculated by the program PHREEQC.

	Species	Activity
Brine #1		
pH \cong 3.1		
	H^+	8.7×10^{-4}
	$H_2O_{(l)}$	9.5×10^{-1}
	Cl^-	6.2×10^{-1}
	K^+	8.2×10^{-2}
	Na^+	6.6×10^{-1}
	$H_2CO_3^*$	1.0×10^0
Brine #2		
pH \cong 3.6		
	H^+	2.5×10^{-1}
	$H_2O_{(l)}$	9.5×10^{-1}
	Cl^-	6.2×10^{-1}
	K^+	8.2×10^{-2}
	Na^+	6.6×10^{-1}
	$H_2CO_3^*$	1.0×10^0
	Ca^{2+}	3.9×10^{-4}

Figure 2.3 illustrates the carbonate speciation with respect to pH for Brine #1 and Brine #2 at ambient conditions and at experimental conditions as calculated by the program PHREEQC and Phreeplot [85]. An increase in pressure shifts the speciation towards the left, but at our conditions (pH 3.1 and 3.6) the dominant ion in our system remains $H_2CO_3^*$.

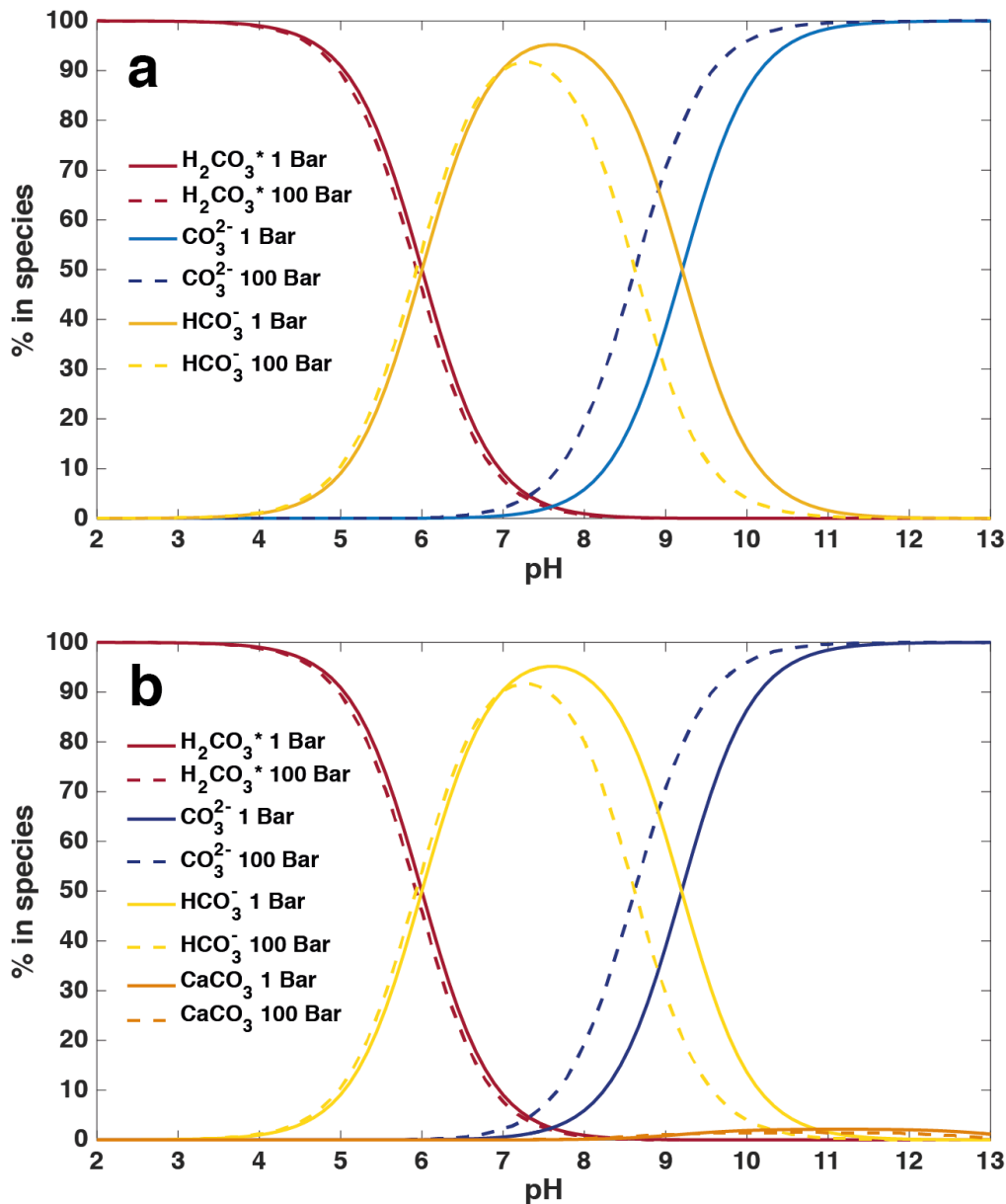


Figure 2.3 The concentrations of each major carbonate species vs pH for Brine #1 (a) and Brine #2 (b) at 1 bar and 25°C (ambient conditions) and 50°C and 100 bar (experimental conditions). Increasing temperature and pressure shifts the speciations toward a lower pH.

However, in order to be sure our initial system has equilibrated before starting the flow experiments we must investigate the timescales in which equilibrium is reached for each reaction. Chemical reactions vary in speed by orders of magnitude and can be classified by the controlling mechanism [86]. Slow reactions are generally kinetically controlled while fast reactions are controlled by equilibrium. For example, most heterogeneous mineral reactions are very slow (on the order of

weeks at low temperature) and kinetically controlled while acid-base reactions involving solutes are fast (seconds or less) and equilibrium controlled. Table 2.4 lists the reactions in our system along with typical timescales reported in the literature.

Table 2.4 The major chemical reactions of the CO₂-calcite-brine system and their typical timescales.

Reactions	Timescale
$H_2O_{(l)} \leftrightarrow H^+ + OH^-$	picoseconds [87-89]
$H_2CO_3^* \leftrightarrow HCO_3^- + H^+$	milliseconds [90]
$CO_{2(aq)} + H_2O \leftrightarrow H_2CO_3^*$	seconds [90]
$CO_3^{2-} + H^+ \leftrightarrow HCO_3^-$	milliseconds [90]
$CaCO_{3(s)} + H^+ \leftrightarrow HCO_3^- + Ca^{2+}$	days – years [90]
$NaCl_{(s)} \leftrightarrow Na^+ + Cl^-$	milliseconds – hours [91]
$KCl_{(s)} \leftrightarrow K^+ + Cl^-$	milliseconds – hours [92]

The reaction rate of salts and gases in our system are orders of magnitude faster than mineral dissolution and thus will not be considered as the rate limiting control on chemical equilibrium. Additionally, all experiments in this thesis are at done at equilibrium with respect to gas and salt species. However, the importance of mineral dissolution in the CO₂-brine system cannot be understated, as it has the potential to impact the integrity of both formations and geologic seals [20, 58]. Carbonate dissolution is kinetically controlled and thus rate must be taken into account.

Carbonate dissolution is traditionally described by [93]:

$$r = -\frac{dm_{mineral}}{dt} = r_{surface}(1 - \Omega)^n \quad (2.20)$$

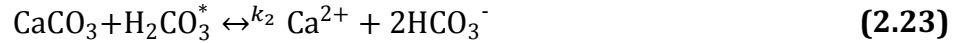
where the rate of reaction, r , is the change in the amount of mineral m in time t . The total rate is controlled by the reaction rate at the mineral surface, $r_{surface}$, the saturation state of the bulk fluid, Ω , and an empirical factor, n .

Transitional State Theory (TST) [94] has been proposed to integrate the kinetics of dissolution with traditional thermodynamics and provide insight into the rate limiting mechanism(s). The TST equation for calcite dissolution is:

$$r = \frac{S}{V}k(1 - \Omega) \quad (2.21)$$

where S is the mineral surface area, V is the bulk volume of the fluid, and k is the reaction rate constant.

It is well established that a chemical reaction can be divided into different steps in kinetic theory [93, 95]. Busenberg and Plummer [96] have investigated calcite dissolution at near equilibrium for at ambient conditions at a range of salinities. They divide mineral dissolution into three parallel reactions that describe the chemical interaction involved in carbonate dissolution for CO₂ acidified systems [97-99].



H_2CO_3^* represents the sum of dissolved molecular CO₂(aq) and H₂CO₃ in the aqueous system. The rate coefficients for each reaction are k_1 , k_2 , and k_3 . Plummer [99] suggests that the kinetics can be divided into three regimes. In the first regime the dissolution is only dependent on the partial pressure of CO₂. In the second regime the partial pressure of CO₂ and pH both play a role. While in the third regime, calcite precipitation is also important. We can thus write the overall rate equation for carbonate dissolution as a combination of all three.

$$r = k_1\alpha_{\text{H}^+} + k_2\alpha_{\text{H}_2\text{CO}_3^*} + k_3 \quad (2.25)$$

This model has been used in numerous reservoir simulators. However, uncertainty remains regarding the validity of this model at the temperatures, pressure, and salinities of CO₂ sequestration sites due to the difficulties in measuring reaction rate at these conditions. To date only Peng [46] has measured the pH and reaction rate of calcite in reservoir fluids at *in situ* conditions and we use these rates for all rate calculations in this study.

In order to equilibrate our fluids, we use a high temperature batch reactor, a powdered mineral phase with a very high surface area, and continuously mix the fluids. Thus there are plentiful surface sites, easily available energy, and fast diffusion of reaction products away from the solid surface, meaning that our system approaches equilibrium relatively quickly (on the order of minutes to hours). Given 48 hours to mix, we can ensure that our initial system is fully equilibrated and indeed this is confirmed by the identical experimental apparatus and conditions of Gharbi [62] and by the elemental analysis of the reactor fluid discussed in section 6.3.

2.3 Flow and transport in porous media

Acid-induced dissolution during carbon sequestration is a dynamic process that cannot be explained fully by either static modelling or batch reactor experiments [48]. When acid brine is flowed through a porous medium mixing is incomplete and

reaction rate is controlled by the interplay between advection and diffusion and coupling flow and transport and chemical reaction provide greater insight into these processes[100]. Figure 2.4 shows the rock-brine system at the mineral surface. When a miscible reactive fluid is injected into a porous medium inside a bulk solution, it will be transported and spread, react with a mineral surface, and the products will then also be transported [101].

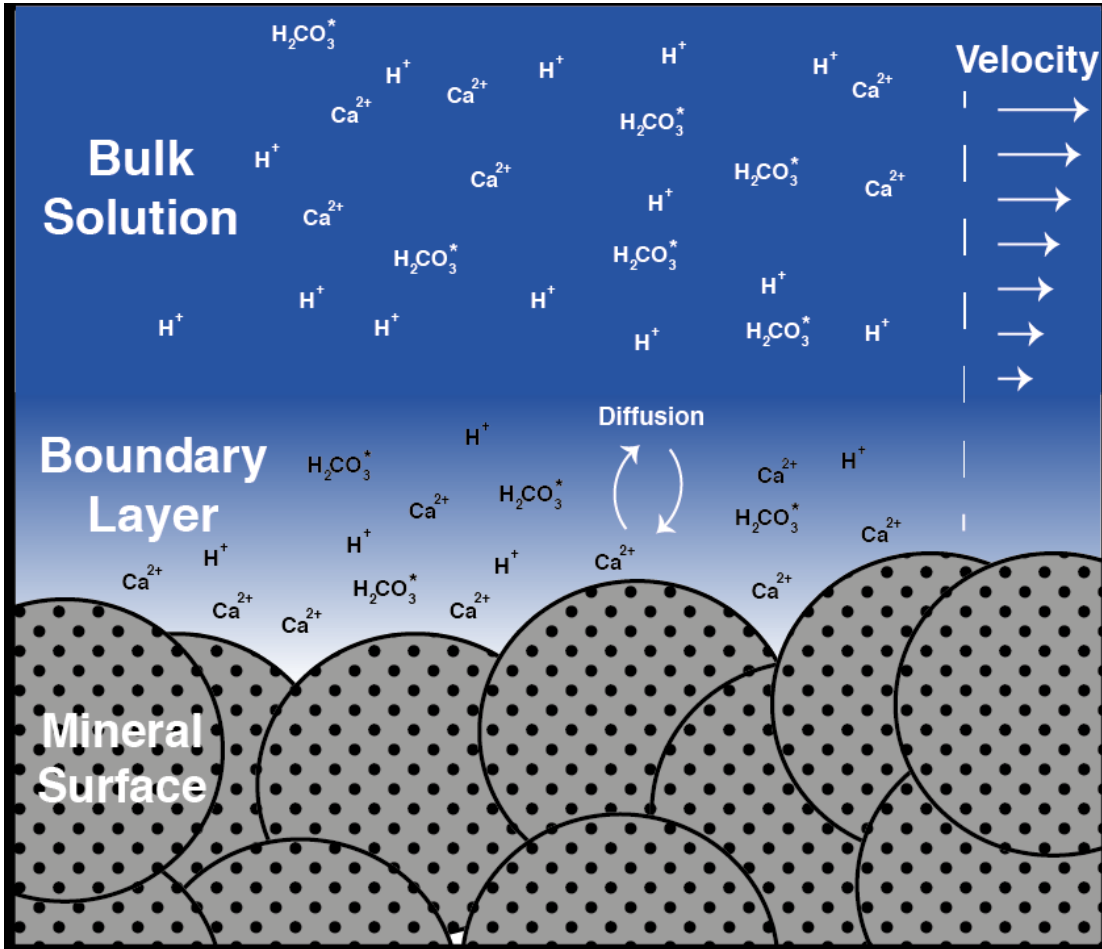


Figure 2.4 Chemical and physical processes associated with carbonate mineral dissolution in CO₂-saturated brine at the mineral surface.

Reaction at the mineral surface is controlled not only by the surface area of the mineral and the reaction rate constant but also by the transport of chemical constituents onto and away from the mineral surface within the boundary layer [102]. The boundary layer is defined as the layer of fluid in the immediate vicinity of the mineral surface where the effects of viscosity are great and the fluid velocity is small enough that diffusion is the dominant transport regime. The transport in the bulk fluid can be either advection or diffusion dominated depending on the local fluid velocity and the topology of the porous media [103]. Thus, to fully understand reaction in a heterogeneous system, it is imperative to first describe the distribution and magnitude of fluid movement within the porous medium.

In an advectively well-mixed batch reactor, transport by advection is fast so that boundary layer diffusion effects are minimised. Hence, the measured reaction rate under these conditions approaches the intrinsic reaction rate of the fluid/solid system. However in fluid/solid reactive transport in subsurface porous media, due to solid surface irregularities, diffusive layers always exist and the reaction is expected to occur at the rates slower than in the batch reactor, as we show later in section 6.

The Navier-Stokes equation [104] is traditionally used to describe viscous fluid flow:

$$\rho_{fluid} \left(\frac{\partial U_{av}}{\partial t} + U_{av} \nabla U_{av} \right) = -\nabla P + \mu \nabla^2 U_{av} \quad (2.26)$$

where ρ_{fluid} is the fluid density, U_{av} is the bulk fluid velocity, μ is viscosity, and P is pressure. The steady flow conditions in subsurface rock are commonly found to be such that viscous forces dominate inertial forces resulting in a Reynolds number much less than 1, so the Navier-Stokes equation simplifies to steady-state Stokes flow:

$$0 = -\nabla P + \mu \nabla^2 U_{av} \quad (2.27)$$

The macroscopic description of flow at the continuum scale is commonly described by Darcy's Law [105] which linearly relates flow rate to the pressure gradient through a permeability constant:

$$\frac{Q}{A} = q = \frac{-k}{\mu} \frac{dP}{dx} \quad (2.28)$$

where Q is the bulk flow rate, A is the surface area perpendicular to flow, q is the average flux (termed the Darcy velocity), and k is the permeability of the porous medium. This equation is often rearranged and used to solve for permeability from experimental flow and pressure measurements such that:

$$k = -\mu \frac{Q}{A} \frac{dx}{dP} \quad (2.29)$$

Solute migration within a bulk fluid can be split into two regimes: advection and diffusion. Advection is the fluids bulk motion and diffusion causes the displacement of particles due to their kinetic energy of random motion. They are together described by the advection-diffusion equation shown in one dimension for incompressible flow [106]:

$$\frac{\partial C}{\partial t} = D_m \frac{\partial^2 C}{\partial x^2} - U_{av} \frac{\partial C}{\partial x} \quad (2.30)$$

where C_i is the concentration of species i (write the equation as C_i), t is time, x is distance, D_m is the molecular coefficient of the solute, and U_{av} is the bulk fluid pore velocity equal to q/ϕ where ϕ is porosity. The concentration profile of the solute is dependent on whether advection or diffusion is the dominant mass transport mechanism. In the literature there are many papers that study the relative importance of advection and diffusion over multiple length scales from the pore [107] to the core [108, 109] to the reservoir [110-112]. This equation can apply within the pore space at the microscopic scale and this pore scale has been shown to be of great importance in controlling these mixing and reaction processes [62, 107, 113].

2.4 Pore scale flow and transport in porous media

Reactive transport has been widely investigated in the context of acid stimulation of oil wells both experimentally and numerically [107, 114, 115]. When describing advection, diffusion, and reaction in porous media, it is useful to use dimensionless numbers to compare different systems. Three common terms used to describe these phenomena are the Péclet, Damköhler, and Péclet-Damköhler numbers [116].

The Péclet number Pe [-] is a dimensionless number used to describe transport conditions and is defined as the amount of time needed for a particle to travel a characteristic length L by advection over the time needed for that particle to travel that same length by diffusion [117]:

$$Pe = \frac{\text{advection rate}}{\text{diffusion rate}} = \frac{U_{av} L}{D} \quad (2.31)$$

where U_{av} [$\text{m}\cdot\text{s}^{-1}$] is the average pore velocity, L [m] is the characteristic length (typically related to an average pore diameter) and D [$\text{m}\cdot\text{s}^{-1}$] is the molecular diffusion coefficient. Based on the Péclet number it is possible to separate the behaviour of coupled advection and diffusion in a porous media into four categories: restricted diffusion, transition, power law, and mechanical dispersion [48, 101, 118].

Reactive conditions in relation to advection are characterised by the Damköhler number Da [-] defined as:

$$Da = \frac{\text{reaction rate}}{\text{advection rate}} = \frac{kL}{U_{av}} \quad (2.38)$$

where k is a reaction rate constant [s^{-1}]. Physically this represents the ratio of the time for advection to the time for reaction over a characteristic length L . We interpret the reaction time to be the time taken to dissolve a section of the rock of length L .

Both the Damköhler and Péclet numbers are dependent on an advective term, therefore it is often useful to multiply them together to create the Damköhler-Péclet number that is dependent only on reaction and diffusion. The Péclet-Damköhler number $PeDa$ [-] defined as:

$$PeDa = \frac{\text{advection rate}}{\text{diffusion rate}} \frac{\text{reaction rate}}{\text{advection rate}} = \frac{\text{reaction rate}}{\text{diffusion rate}} = \frac{L^2 k}{D} \quad (2.43)$$

Dissolution patterns are traditionally characterized by five dissolution regimes: compact dissolution, conical wormhole, dominant wormhole, ramified wormholes, and uniform dissolution [119-121] [Figure 2.5]. Dissolution can occur in each regime when a rock undergoes specific reactive-flow conditions [122-125]. The reactive conditions are characterised using the Damköhler number and the flow conditions are characterised using the Péclet number [116, 126].

Compact (or face) dissolution occurs with a high Damköhler number and a low Péclet number, where the reaction front advances along the direction of flow and dissolution takes place as a thin front where all of the rock is dissolved [127]. Conical wormholes take place under similar reactive conditions, but intermediate Péclets where the reaction front becomes unstable especially in heterogeneous porous media. Dominant wormholes occur under high Péclet conditions where dissolution is concentrated along the preferential flow path and the high velocities mean that the residence time is minimal so the wormholes do not become very large. This is the optimum dissolution for producing oil using well acidization [128, 129]. Ramified wormholes occur when advection is the dominant mechanism and reaction is not very rapid leading to longer residence times where spreading and branching can occur. Uniform dissolution is observed when porosity increases along the length of the sample uniformly and typically occurs when the reaction rates are very low and the acid has time to access the entire pore space. The boundaries between the dissolution regimes are controlled by pore-space heterogeneity, which differs considerably between carbonate rock types [130]. Thus accurate prediction of the dissolution regime requires reservoir condition experiments with realistic flow and reactive conditions in real rocks with representative aquifer brine.

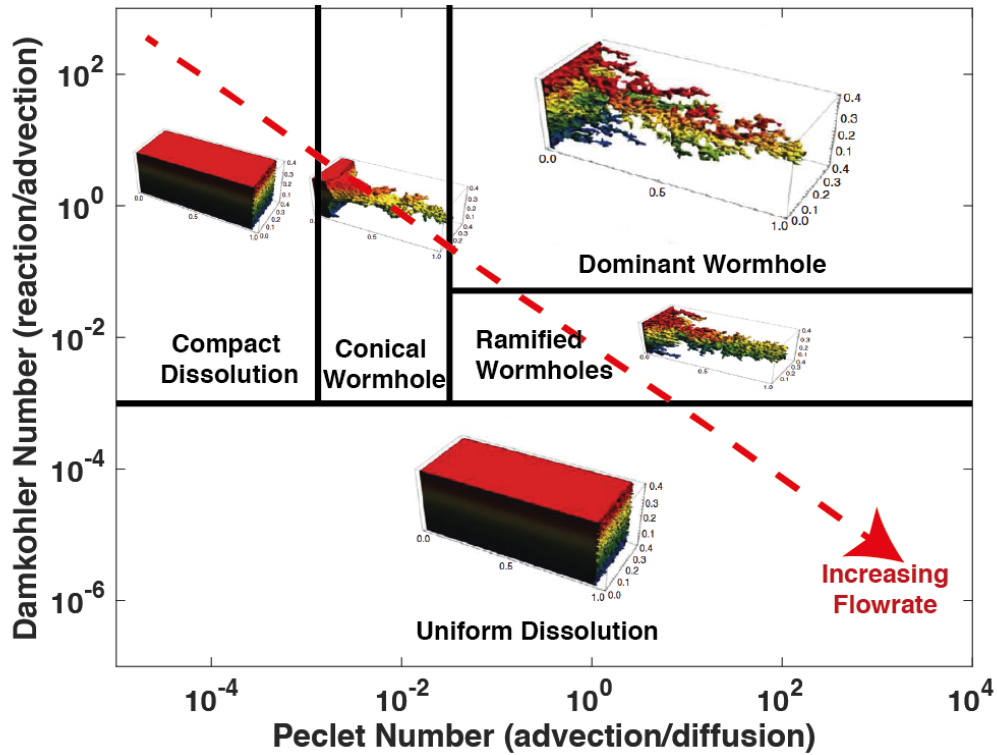


Figure 2.5 The Damköhler-Péclet Space with dissolution regimes. Uniform dissolution dominates at low reaction rates. High reaction rates and low flow rates cause compact dissolution. Wormholes form at intermediate flow and reaction rates when dissolution follows preferential flow paths. Dissolution figures taken with permission from [125].

2.5 Measurement and Prediction of Reaction: A Review

Reaction in a porous medium is a coupled dynamic process. Reaction induces changes in the characteristics of both the physical and chemical characteristics of the rock. Increases in porosity can change permeability, surface area, and composition and thus alter the flow behaviour. Such changes make it possible for the dissolution regime to evolve as the reaction takes place and for the Péclet and Damköhler numbers to change with them. For example, flow instabilities during compact dissolution can cause formation of a conical wormhole.

A number of experimental and numerical studies have described the rate limiting mechanisms associated with carbonate dissolution that include pH, ionic strength, temperature, pressure, saturation, and structural heterogeneity [93, 131]. Batch reactor experiments using a rotating disk have found that the dissolution of calcite is dependent both on the pH of the solution and on the chemical composition and that the reaction rate coefficients increase substantially with temperature [46, 52, 132]. Arvidson et al. [131] found that the published calcite dissolution rates showed over an order of magnitude in variation. Lund et al. [133] found that as

temperature increased the reaction rate shifted from surface to entirely mass transport limited.

The ultimate goal of studying flow and transport in porous media is to be able to accurately predict field scale observations using first principles. However, reactive transport model results and experimental datasets rarely agree on dissolution rates [131-137]. In fact, the predicted and observed rates often vary by orders of magnitude in the literature [138-140]. Large-scale models use average rates over an entire grid block, which can be kilometers across. They do not provide a rigorous way of relating macro-scale reactivity and instead assume that the permeability changes exponentially with porosity [141]. These estimates do not take into account local processes such as diffusion and mass transfer which occur on the micron scale and are dependent on equilibrium [142]. Additionally, changes in redox states [143], variation in residence times [144], and physical and chemical heterogeneities such as pore size distribution [49], changes in reactive surface area [145], mineralogy [46], the presence of organics and bacterial life [146], and weathering [138, 142] are also known to increase complexity. It is not currently possible to interpret field-scale observations in terms of the manifestations of all applicable heterogeneities across different scales. In addition, field-scale models rarely incorporate the time dependent coupling of these many intertwined processes. Thus, it is desirable to study these reactive-flow and transport processes reproducibly in a laboratory setting using time-dependent measurement techniques in order to provide robust datasets for pore – and eventually field – scale models.

Batch experiments are one method of experimentally measuring reaction rate. Peng [46] did an extensive number of rotating-disk batch reactor experiments and found that carbonate mineral dissolution rates at reservoir conditions could be categorised into two regimes, a pH controlled regime and an regime where both pH and $CO_2(aq)$ concentration can influence the dissolution rate. Mineral type, pressure and temperature conditions, and pH control the boundary between these regimes. Furthermore, the dissolution rates in the pH-controlled regime in HCl systems was similar to that of CO_2 -acidified systems and that it was possible to discriminate the contribution of CO_2 to the dissolution rate based on these results. Moreover, that the surface morphology of the sample had a substantial impact on dissolution rate. Batch experiments provide valuable insight into reaction rate where the dissolution is surface limited, but lack the ability to account for the complexity of transport limitations in the subsurface.

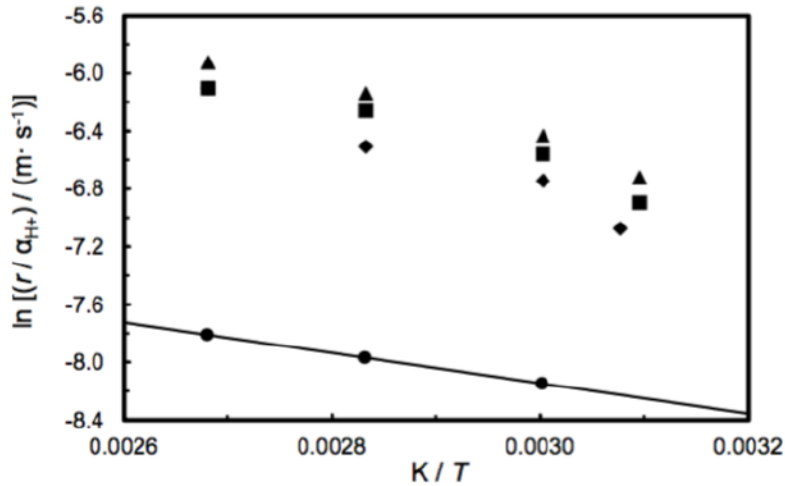


Figure 2.6 Relationship between $\ln(r / \alpha_H)$ and $1/T$ in the $(CO_2 + H_2O)$ system : ◆ , $p = 6$ MPa; □ $p = 10$ MPa; ▲ , $p = 13.8$ MPa. Also ● , k_1 for calcite dissolution in the $(HCl + H_2O)$ system. The experimental uncertainties are comparable to the size of the plotting symbols. Solid lines show linear regressions. Taken with permission from Peng [46].

Variations in dissolution rate and regime are critical for the oil and gas industry in order to optimize injection conditions for higher oil recovery. Many experiments have investigated different conditions to quantify the mechanisms that control boundaries between regimes. Fredd and Folger [119] used EDTA and HCl to dissolve limestone and imaged the resulting dissolution patterns using neutron radiography. They then classified the dissolution patterns into the five dissolution regimes [Figure 2.7]. They found that the Damköhler and Péclet numbers could be used to control the optimum breakthrough times of wormholes in carbonate reservoirs. The neutron radiography method gives insight into the various complexities of the pore space, but only in two dimensions and also lacks the resolution to make quantitative statements about the spatial and temporal distribution of reaction rate.

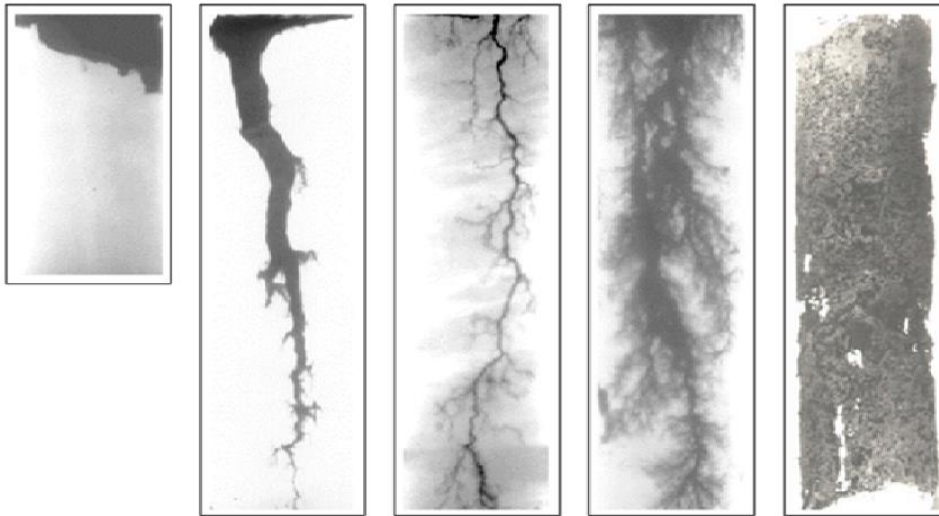


Figure 2.7 Neutron radiographs of dissolution patterns with increasing Péclet number. From left to right, face dissolution, conical wormholes, dominant wormholes, ramified wormholes, and uniform dissolution. Taken with permission from Fredd [147].

Some column experiments have been designed to replicate field conditions in a more carefully controlled laboratory setting in order to produce repeatable results [148, 149]. Singurindy and Berkowitz [148, 150] have done extensive work with carbonates in columns to investigate dissolution and precipitation of carbonates in response to acid injection. They found that when hydrochloric acid was injected into sieved sucrosic dolomite samples that the pH of the acid and the flowrate had strong impacts on precipitation. Additionally, when injecting acid into calcium carbonate samples they saw dissolution-induced changes in porosity and permeability. They identified the need to study the impact of structural heterogeneity, especially with regards to changes in acid injection rate. Column experiments provide valuable insight into dissolution rates in homogeneous mediums, but do not incorporate the inherent physical complexities of real reservoir rocks.

2.6 Imaging

In subsurface research, it is common to use core-flooding techniques coupled with three-dimensional imaging techniques (e.g. computed tomography) to investigate reaction at the fluid/solid boundary. Computed tomography is the process of using differences in material density or transparency to resolve the interior structure of an object as if it had been sliced, but without physically interfering with the sample. There are many different types of computed tomography including seismic [151], medical [152], and micro [153]. Seismic tomography typically uses sound waves and is widely used by geophysicists to gain insight into subsurface topology and fluid movement. Medical CT scanners use x-rays to resolve the inside of humans and are now in most hospitals to help diagnose illnesses and is

commonly paired with core-flooding to image rocks. X-ray microtomography (μ -CT) works on the same principals as a medical CT scanner, but is higher resolution than a medical scanner and is ideal for resolving micron scale processes. μ -CT is used extensively in semiconductor industries and is currently being developed for the oil and gas industry.

Imaging of dissolution in limestone rock has been performed at the core ($\sim cm$) scale using both CT scanning and NMR. Ott et al [108] investigated dissolution at using core flooding and CT scanning where, for several rock types and flow regimes, it was found that reaction of the dissolved CO_2 with the solid matrix increases physical heterogeneity. Ellis et al. [154] used core-scale imaging to show that exposure to CO_2 progressively reduced the sealing capacity of fractured claystone caprocks. Smith et al. [155] imaged dissolution of a dolomitic subcore before and after reaction with CO_2 acidified brine. Ziauddin and Bize [135] investigated the impact of pore-scale heterogeneities on acid stimulation treatments using NMR. Dissolution of carbonate core-plugs was carried out on several rock types grouped by the spatial distribution of porosity. It was shown that the type of dissolution was dependent on initial pore structure. Benoit Lamy-Chappuis et al. [156] used CT scanning to measure calcite dissolution in calcareous gritstone and found that the permeability increase with porosity did not agree with classical models and that the dissolution rate was largely due to the acid supply.

Core –scale imaging is valuable because it is three-dimensional and can be temporally resolved. However, it has a maximum resolution of $\sim 50 \mu m$ and thus can only resolve the fluid/solid boundary of large features such as fractures and wormholes. The greater portion of the pore space is only resolved as an average greyscale value that blurs or eliminates the solid/liquid interface thus making segmentation and analysis of local changes in connectivity and reaction rate very difficult. There are relatively few experiments that investigate the impact of coupled dissolution and flow phenomena at the micron scale – observations that are necessary for the digitisation of the pore network for direct numerical simulations of both flow and transport.

μ -CT has existed since the 1980's and was pioneered by Flannery et al. [157] who used it to look at 3-D images of sandstones and coal beds. Since then both the image resolution and acquisition times have improved and high resolution scanning of the pore-space is now routinely used to characterize and model the petrophysical properties of sedimentary rocks. μ -CT has recently become an established experimental method for studying pore-scale processes for both petroleum and carbon storage applications [113, 158, 159]. μ -CT offers several advantages: it is non-invasive, achieves high spatial resolutions, and provides three-dimensional images relatively quickly.

Image processing has been developed to binarize grey-scale images into discrete values that can be used in conjunction with network extraction and direct

simulation to extract and examine a myriad of petrophysical properties [50, 113, 160, 161]. Bijleijc et al. [162] used μ -CT images to predict solute transport using direct simulation and found that the transport in heterogeneous samples had a much larger proportion of stagnant flow than homogenous samples. Raeini et al. [163] extracted pore networks from μ -CT images to predict two-phase flow and snap-off capillary pressures. These studies represent excellent approaches to studying fluid flow at the pore-scale. However, without experimental observations of fluid distribution and reaction-induced changes in pore-space topology with which to compare, it is very difficult to validate the numerical results of such simulations.

Coupling the core-holder with imaging techniques has added the capability to image the distribution of pore fluids [164] and time resolved changes in pore topology [165, 166]. Imaging *in situ* flow and reactive transport at realistic conditions is challenging. Iglaur et al. [167] were the first to use μ -CT to image supercritical CO₂ at realistic conditions. Andrew et al. [168-170] have designed an experimental apparatus to image pore-scale multi-phase displacement for the determination of residual saturation, contact angle, and interfacial curvature at elevated temperatures and pressures. These studies were performed at low flow rates and in the absence of chemical reaction to isolate the impact of capillary forces.

Qajar et al [165, 166] provided a robust experimental methodology for measuring pore-scale porosity changes using high-resolution imaging. Acidic EDTA was injected into Savonniere limestone at ambient temperatures and 1-2.6 atm. The pre and post dissolution images were registered and then compared, showing particle mobilization and increased porosity. Carroll et al [171] reacted two carbonate cores with CO₂ saturated brine and used the changes in porosity and permeability to calibrate rate laws that were dependent on initial pore structure and reactive surface area. Smith et al. [172] and Hao et al., [173] combined μ -CT and modelling of samples from the Weyburn Oil field in Saskatchewan, Canada. Multiple dolomitic cores were imaged before and after core flooding with CO₂-saturated brine at 60°C and 12.4 MPa. The results were subsequently used to validate a continuum-scale reactive transport model. Additionally, Luquot & Gouze [174] and Gouze et al. [124] performed flow experiments with a CO₂-rich brine on limestone reservoir samples at 100°C and 12 MPa. Samples were analysed with μ -CT prior to and after dissolution and changes in the permeability, porosity, tortuosity, and hydraulic radius were characterized according to dissolution regime. Gharbi et al. [175] investigated changes in rock structure with increasing Damköhler number in two heterogeneous carbonates at reservoir conditions and observed two distinct dissolution regimes, wormholing and uniform dissolution.

Although these experiments have provided valuable information on pore-space geometry and flow, such as the porosity-permeability relationship, the analysis was limited to comparisons between pre- and post- reaction images of the rocks studied, some were not conducted at representative subsurface conditions, while others did not have the resolution required for pore-scale predictive modelling. It is

only recently that the technology has evolved – both from a resolution and data processing standpoint - to the point where studying time-resolved pore-scale processes *in situ* at reservoir conditions has been possible.

2.6.1 *In situ* time-resolved μ -CT measurements

Studies of time-resolved imaging of fluid flow in porous media at high temporal resolutions are sparse. Berg et al. [176] and Andrew et al. [177] both used a synchrotron light source to look at dynamic pore-scale displacement events between multiple fluid phases with around ~ 1 min temporal resolution. Armstrong et al. [178] used fast tomography and advanced image processing techniques to observe fluid displacement at the timescale of ~ 1 s. Noiriél et al. [179] used μ -CT to measure the three-dimensional changes in a limestone fracture at several points during acid dissolution at ambient conditions. Additionally, Noiriél et al. [180] showed a power law relationship between porosity and permeability during limestone dissolution by scanning the rock periodically *ex situ*. However, to date no studies exist that incorporate *in situ* dynamic tomography and geochemical reaction.

Measuring dynamic reaction-induced changes in pore-space geometry, topology and flow in subsurface rock systems at reservoir temperatures and pressures furthers our understanding of how different transport and reaction conditions alter the complex solid and pore structures [181], and is the main goal this thesis. Moreover, our aim is to provide a series of time-evolving x-ray image based datasets that can serve as a benchmark experimental study to calibrate pore-scale reactive transport models.

2.6.2 Beer-Lambert's law

When an x-ray beam passes through an object, a fraction of the x-rays are attenuated and the beam loses intensity. Beer-Lambert's Law states that in a homogenous sample the change in beam intensity with time is equal to the negative intensity multiplied by the linear attenuation coefficient [182-184].

$$\frac{dI}{dx} = -\mu I \quad (2.55)$$

where I is the transmitted intensity, x is the optical length of the sample, and μ is the linear attenuation coefficient. When integrated this becomes:

$$I(x) = I_0 e^{-\mu x} \quad (2.56)$$

The transmission factor, T , corresponds to the proportion of x-rays that are not absorbed by the sample:

$$T = \frac{I(x)}{I_0} = e^{-\mu x} \quad (2.57)$$

It is important to note that with a multiple component materials, the attenuation is additive:

$$I = I_0 e^{-\sum_i x_i \mu_i} \quad (2.58)$$

where x_i and μ_i are specific to the thickness and intrinsic properties of material i .

2.6.3 X-ray beam sources

There are two common types of x-ray beams, the parallel beam and the conical beam [Figure 2.8]. The parallel beam is typical of high-energy light sources such as synchrotrons, while conical beams are usually bench-top based lab sources. Parallel beams are more difficult to create and require more specialised equipment, but the spectrum is more adaptable and the beam can be much more powerful than conical sourced beams.

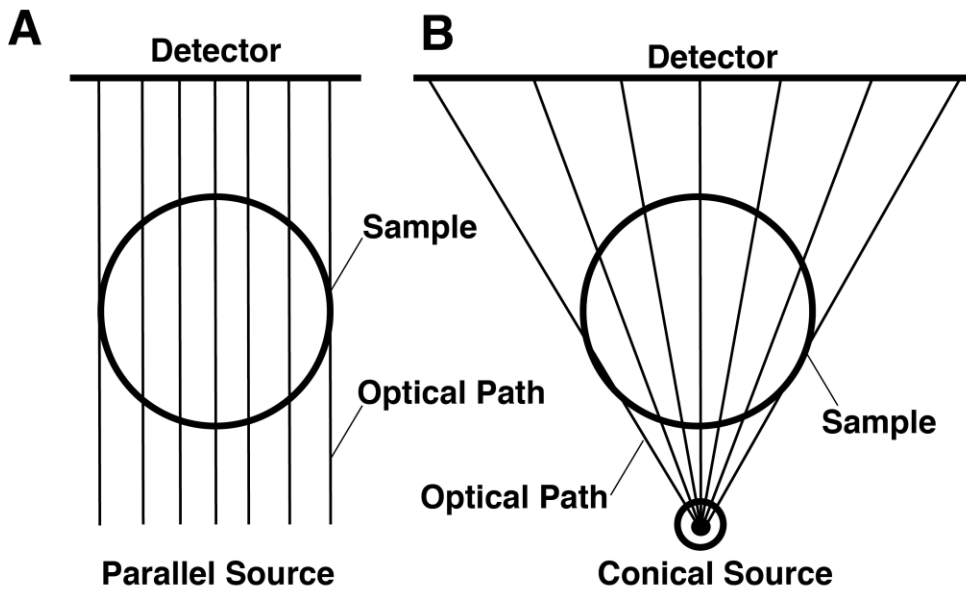


Figure 2.8 X-ray optical geometries. (A) shows a parallel x-ray beam, while (B) shows a conical x-ray beam. Parallel beams are typical of synchrotrons, while conical beams are typical of bench-top systems. Figure inspired by [170].

2.6.4 Laboratory-based μ -CT

The source inside of the Zeiss Versa XRM-500 bench-top scanner consists of a tungsten target and a linear electron accelerator. Electrons are fired at the target and the Bremsstrahlung radiation [185] produced by the energy of charged particle deceleration when deflected by the target charge particle is directed through the sample in a conical beam. The x-rays transmitted through the sample hit the iodine scintillator and give off visible light, which is then focused by the optical objective lens and converted into a digital image by the visible light charge-coupled device (CCD).

A series of images (projections) is taken at incrementally spaced angles from 0° to 180° +fan angle or 360° as the sample is rotated. The fan angle is a small number of degrees needed to compensate for the edges of the cone beam which changes depending on magnification and source-detector distance. This set of $[x,y]$ projections is then converted to sinograms $[x, \theta]$, where theta is the rotation angle, and back projected into the 3-D intensity map using a suite of transformation algorithms including the Radon Transform [186] that are beyond the scope of this thesis, but are discussed in detail in the *ASTM Standard Guide for Computed Tomography (CT) Imaging* [187].

One benefit of using a cone beam is that it is possible to magnify the image both optically and geometrically. Geometric magnification makes high-resolution scans possible at long sample distances [Figure 2.9]. Optimal sample placement depends on desired magnification and acquisition time.

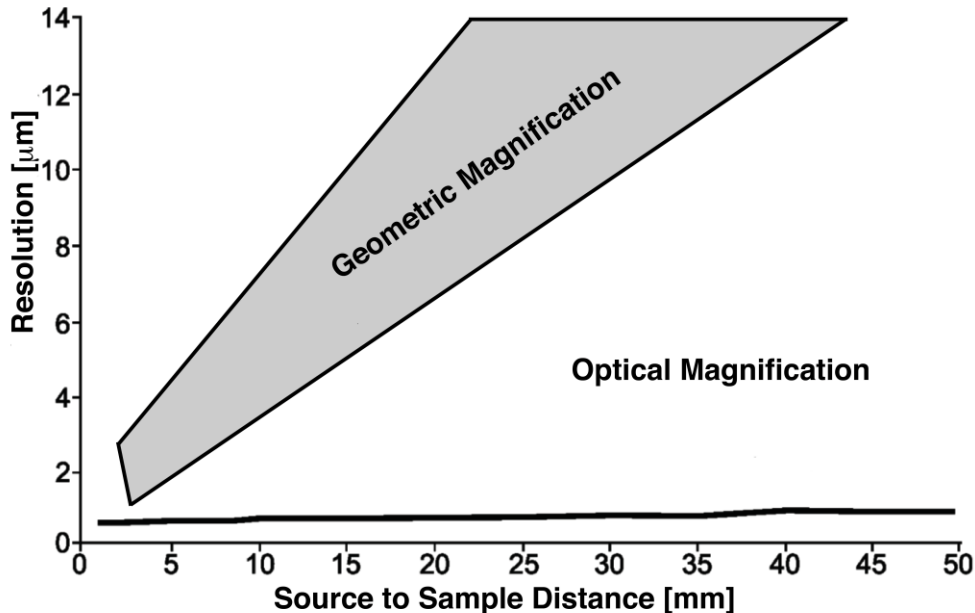


Figure 2.9 The geometric and optical magnification capabilities of the Versa-XRM 500 used for our experiments. Geometric magnification allows for high resolution

scans at shorter source distances than traditional optical magnification. Modified from www.zeiss.com.

2.6.5 Synchrotron lightsources

A synchrotron is circular particle accelerator that uses a guiding magnetic field to accelerate, direct, focus, and synchronize charged particles into a particle beam of increasing kinetic energy [188]. Synchrotrons typically consist of an electron gun that fires electrons through a linear acceleration (or linac) and into a booster ring. The booster ring speeds up the electron beam and then injects the electrons into a larger storage ring. The storage ring typically has many separate branching beam lines [Figure 2.10] that extract small quantities of energy and manipulate them to suite different experimental needs.

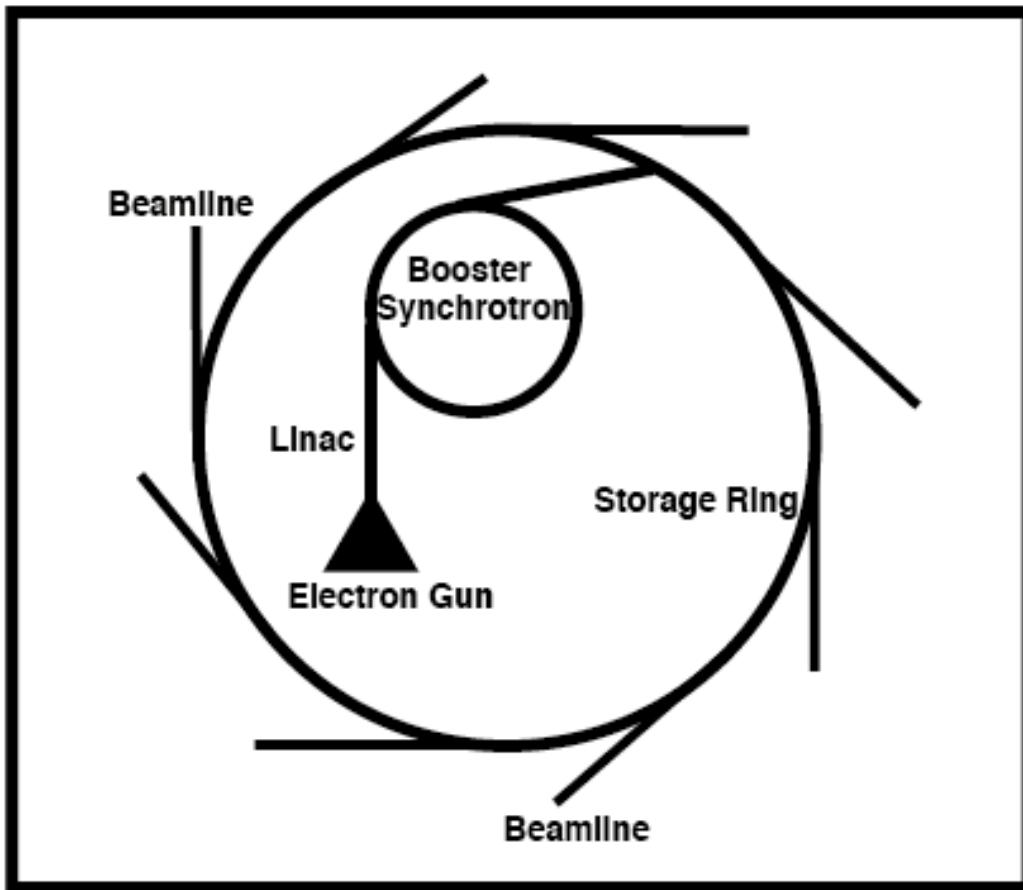


Figure 2.10 A typical synchrotron schematic consisting of an electron gun that fires electrons through a Linac and into the booster synchrotron. The accelerated beam is then injected into the storage ring to be used by the many beam lines.

One such manipulation is to use an undulator [Figure 2.11] that consists of a periodic structure of dipole magnets. The electron beam is forced to undergo

oscillations as it traverses the magnets and thus radiates energy [189]. The energy produced is concentrated to narrow energy bands and is very intense.

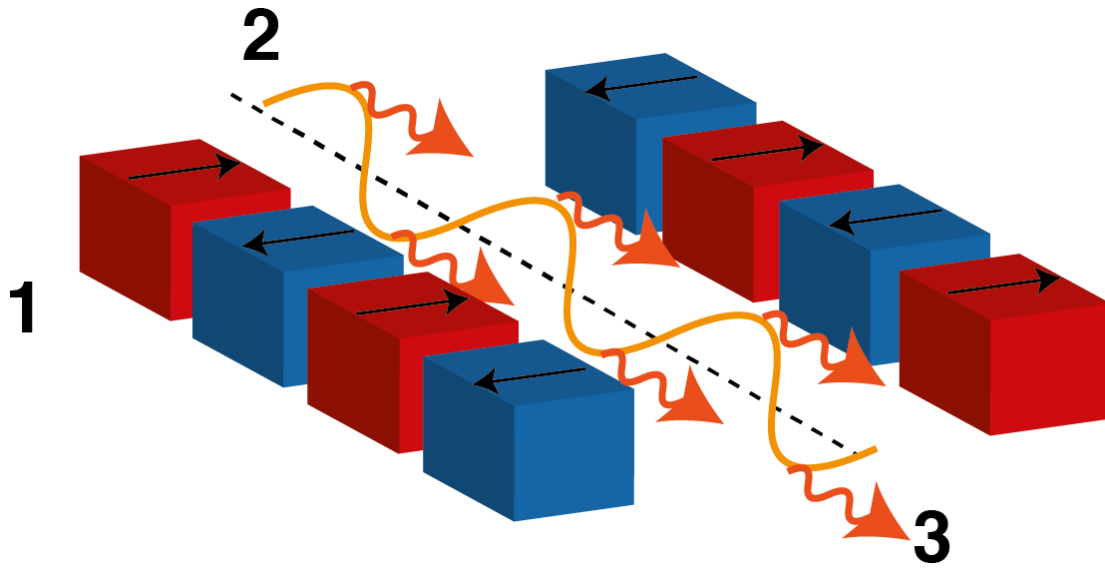


Figure 2.11 A synchrotron undulator. The periodic structure of magnets (1) bend the electron beam (2) producing intense light (3).

Mirrors and filters [Figure 2.12] are then used to narrow the spectrum of light to suit experimental needs. Mirrors absorb the high-energy spectrum while filters absorb the lower energies. Therefore it is possible to narrow the spectrum to the desired band of radiation using only these tools.

Once the beam passed through the sample the unabsorbed light is picked up by the detector assembly. The detector of a synchrotron is much the same as a laboratory source detector assembly except that the scintillator must be able to handle higher energy fluxes and the camera must be able to take and transmit images at high rates.

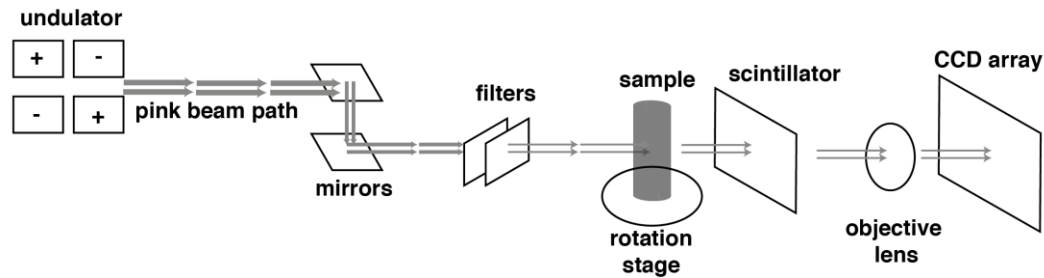


Figure 2.12 The Diamond Lightsource pink beam apparatus. The beam passing through the undulator produces intense light. The spectrum is narrowed by mirrors and filters and then is transmitted through the sample. The scintillator fluoresces in the visible spectrum and the light is focused and measured by the objective lens and CCD camera array.

2.7 Carbonate pore structure classification

Carbonate rocks have widely varying pore structures and grain size distributions [26, 190, 191]. The Choquette and Pray system of porosity classification based on rock fabric has been widely used by petroleum geologists [Figure 2.13]. This method takes into account the depositional environment of the carbonate to help predict pore evolution [192]. However, the Choquette and Pray method does a poor job of including microporosity, which can have a large effect on permeability and flow conditions [193]. Cantrell and Hagerty [193] classify microporosity into four archetypes: microporous equant cement, microporous matrix, microporous grains, and microporous fibrous to bladed cement.

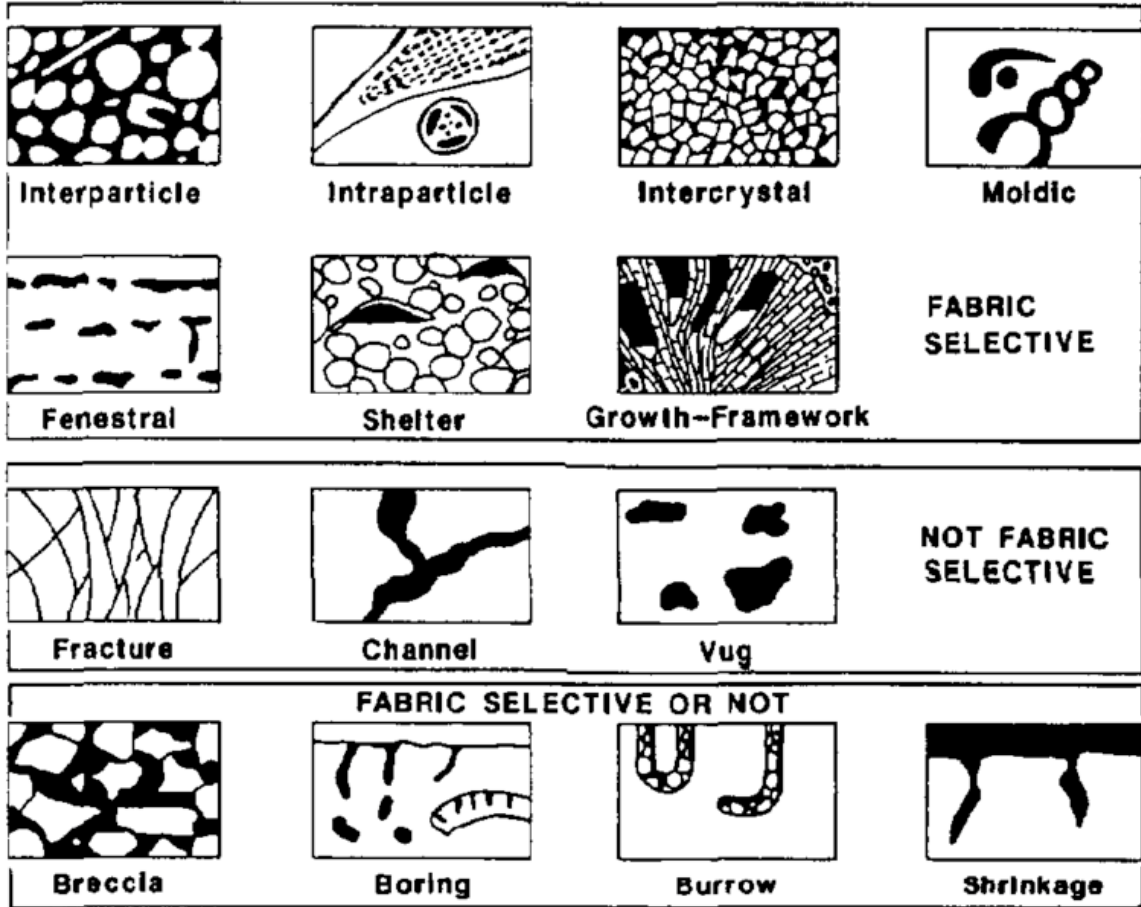


Figure 2.13 The Choquette and Pray classification system, which is based on rock fabric and depositional/diagenetic environment. Taken with permission from [194].

3 Image Processing Techniques

After image acquisition there are many image processing steps required before the image is fully analysed and key properties can be extracted. These steps include removal of image artefacts, increasing signal to noise by use of denoising filters, registration, resampling, difference imaging, phase segmentation, and object separation. Techniques available for image processing and their effectiveness are discussed below. The program Avizo 9 (www.vsg.com) was used for image processing. Novel results and image processing techniques developed during this PhD study will be examined in the results section of this thesis (section 6).

3.1 Artefact removal

Defects in the detector array of an x-ray imaging apparatus can cause ring artefacts, which manifest as voxel intensity change as a function of distance from the centre of rotation. These can be removed either pre-imaging by moving the sample by a small known amount perpendicular to the beam during acquisition and then realigning the projections during reconstruction – a process known as dynamic ring removal - or post-imaging by renormalizing the reconstructed image at the sinogram stage using Fourier filtering [195].

Beam hardening in a polychromatic beam is caused by different absorption spectra of the different wavelength of light. These can be removed by assuming they are radially symmetric Gaussian functions and fitting a trigonometric [196] or quadratic function to correct the intensity bias. Streaking due to beam hardening remains an unsolved problem [197].

3.2 Filtering and denoising

Along with the discrete image artefacts discussed above, image acquisition is fraught with random noise. The signal to noise ratio can be improved by filtering the image. Several types of filters exist that can be applied appropriately given image quality, available computing power, and time constraints.

3.2.1 Simple filters

The simplest filter is the mean filter, which replaces each voxel's greyscale value with the mean value of its neighbours [198]. The Gaussian filter works in the same way using the Gaussian weighted mean. These filters work well for reducing noise. However, they tend to blur phase boundaries and, given adequate time and computational power, should not be used when the image will be segmented into multiple discrete phases. Simple filters were used in this study for quality verification during experimental times when time was of the essence.

3.2.2 Edge preserving filters

The simplest edge-preserving filter is the median filter, which replaces the greyscale voxel value with the median value of the local group. The greyscale value is associated with the initial voxel location, and thus edges are preserved with conservative local groups. However, the edges can degrade when the local group is increased.

A new algorithm called non-localized means (NLM) has been developed to combat the limitations of local filters [199, 200]. NLM takes the mean of all voxels in the search window (which could conceivably be as large as the entire image) and then weights them using a Gaussian function by how similar they are to the target pixel. In this way edges are preserved. However, the filter is very computationally expensive and is typically only used in two-dimensions and with a relatively small search window.

3.3 Image registration

Small movements of the sample and imaging equipment may cause subsequent image grids in a sequence to be misaligned by a small amount. Thus, all images must be registered to a reference image of choice (usually a dry scan or the first image in a sequence). The most robust registration technique is normalized mutual information. The registration starts with a user-supplied initial guess. The algorithm then weights the mutual information by similarity and uses the closest values to align the image [201].

3.4 Image resampling

After image registration, the image must be resampled if it is in any way going to be compared to other images in the time series. A registered image is realigned to a reference image. During this process the voxels are translated, rotated, scaled such that the transformed image grid is no longer aligned to the grid of the reference image. In order to realign the grid, the registered image is resampled along the reference grid.

There are three main types of resampling techniques: nearest neighbour, standard, and Lanczos. Nearest neighbour simply chooses the voxel value closest to the reference image grid point and is the fastest and least computationally expensive resampling method. The standard method does a simple algebraic interpolation between adjacent voxels and assigns this value to the new voxel. However, both of these methods tend to lose vital image information.

The Lanczos method performs a multivariate interpolation of the registered image by mapping each sample point to a translated and scaled copy of the Lanczos kernel which is then evaluated at the new grid point [202, 203]. Lanczos resampling

is by far the most robust resampling method and is recommended given adequate processing time constraints.

3.5 Difference imaging

Many images do not have the edge gradients usable for segmentation. However, by analysing the change in greyscale value in each successive image in a time series it is possible to discern changes in structure and fluid arrangement that would not otherwise be quantifiable. The images are first registered together and resampled. Then the difference between the images is calculated to find the positive and negative change. This method has been used for subvoxel analyses of data sets with changes that are not segmentable at the resolution of a μ -CT such as salt precipitation [204] and microporosity [166].

3.6 Segmentation

Prior to extracting many of the petrophysical properties of a rock image, the phases within the image must be correctly identified. The best-known segmentation tool is the human eye, which uses texture, colour, gradients, and other clues to discern phases. However, it would not be possible to manually segment an image containing millions of voxels. Several segmentation algorithms exist to help automate the segmentation process. These methods include global thresholding and watershed segmentation.

3.6.1 Global thresholding

The simplest method of segmentation is global thresholding whereby all greyscale values within a range are segmented as a particular phase. This method is reasonably effective with an image with a high signal-to-noise ratio that contains only two phases. However, in a noisy image, voxel misidentification is common, particularly at the phase boundary where the voxel greyscale values are the most similar. Additionally, in an image where there are more than two phases, the boundary voxels between the high and low greyscale phases is often misidentified as the intermediate value phase due to voxel averaging – errors known as partial volume effects. Thus global thresholding was only used for qualitative preliminary analysis of images and not used for quantification purposes.

3.6.2 Watershed segmentation

The watershed method of segmentation does considerably better at identifying phase boundaries than global thresholding [205]. The term watershed is used because the gradient image calculated on the image is analogous to the height map of a catchment basin. First the gradients between neighbouring voxels are computed and a new gradient image is created. Areas of high gradient that correspond to the phase boundaries are eliminated from the region seeding. The user then seeds the areas of low gradient by eye and identifies the range of greyscale

values corresponding to each phase. The algorithm then grows the user-defined seed basins successively up the intensity map into the high gradient regions. In this way voxel misidentification due to noise is minimized and the phase boundaries are created using only the user defined phase seeds, thus reducing partial volume effects and producing clear phase boundaries.

3.7 Object separation

The generic watershed algorithm can be applied to any voxel value and is extremely useful in teasing out other physical and morphological properties such as pore or grain size distributions [Figure 3.1]. After segmentation, a label image is created with the values of each phase. A single phase can be extracted using logical arithmetic. The Euclidian distance map of the phase can then be calculated on the single-phase label image by measuring the distance of each voxel from the phase boundary. The centroids of the distance map can then be used to seed the watershed algorithm to find and separate different objects (be that grains or pores) within an image. Once different objects have been labelled in the image it is then possible to calculate various statistical parameters based on their morphology.

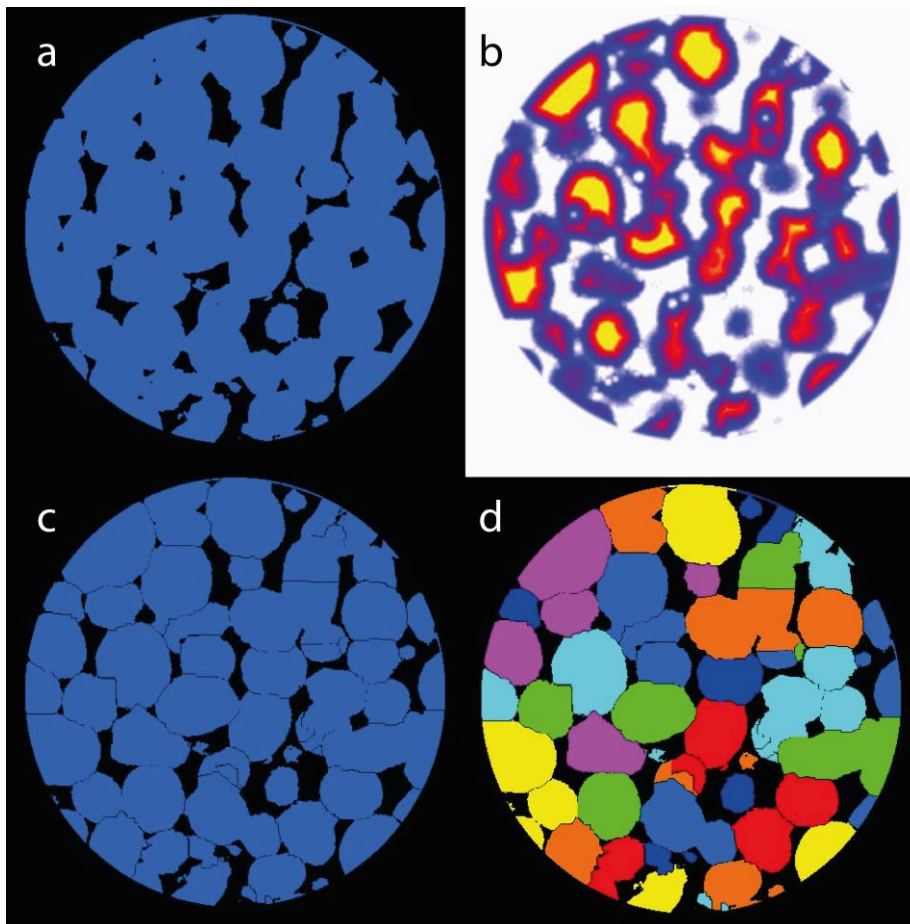


Figure 3.1 A segmented 2-D slice of Ketton (a), the Euclidian distance map of the solid phase (b) where brighter colours indicate a greater distance from the solid

boundary, the grains separated by watershed boundaries (c), and the grains independently coloured by label (d).

3.8 Measurement error

To quantitatively address potential measurement error for the image analysis process we conducted a sensitivity analysis of porosity and permeability on two of our sample rocks. First we address the impact of gradient threshold in watershed segmentation on porosity identification and then we assess how permeability changes as a result of these differences.

We have chosen two samples of varying physical heterogeneity, Ketton and Portland. Ketton has a homogenous pore-structure with large pores and Portland has heterogeneous pore-structure with small pores. The grayscale images are segmented using a watershed segmentation using Avizo 9 (www.vsg.com) to create a reference image. The images are then segmented again an additional four time with the gradient magnitude varied by -20%, -10%, 10%, and 20%. The porosity is then calculated for all ten segmented images by counting the ratio of the number of void voxels to total voxels. Furthermore the images are run through a Navier-Stokes flow solver (methods discussed in section 4.7) to assess changes in permeability.

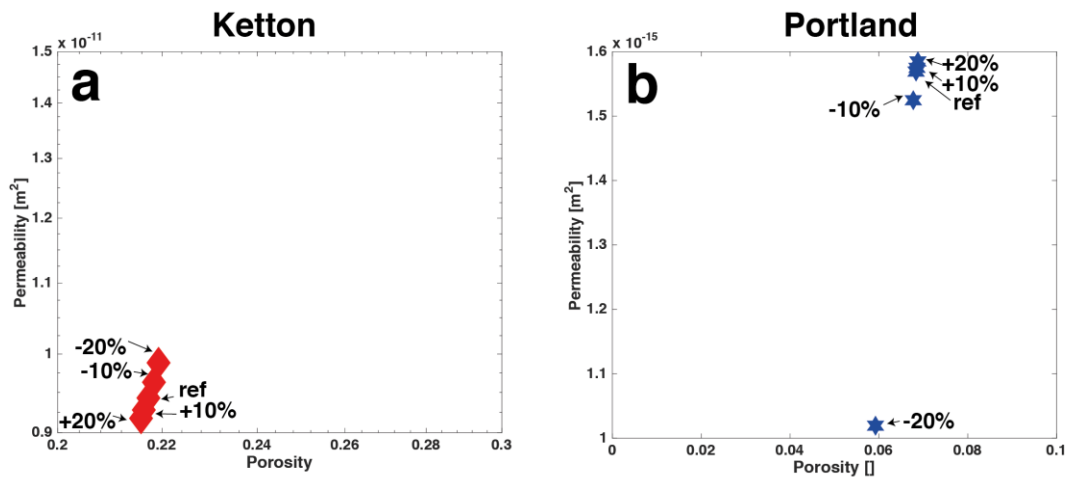


Figure 3.2 The porosity and permeability variation with gradient magnitude during watershed segmentation for Ketton (a) and Portland (b) rock samples. The porosity and permeability change very little with Ketton, but Portland shows large changes in permeability.

Figure 3.2 depicts the variation in porosity and permeability with gradient magnitude. There is little variation of porosity in the homogenous Ketton sample. However, in the Portland sample the porosity increases with increasing gradient magnitude. There is a half order of magnitude change in the permeability with Portland. This is expected because the pore sizes are small and thus a small change in

the gradient magnitude may cause the watershed algorithm to identify small pore throats as solid. In Ketton, the changes in permeability are smaller due to the large and well-connected pores.

From this analysis we can conclude that the measurement error associated with segmentation using watershed is largest with more complex samples. However, the error is not so large as to deter the use of the watershed module, which is still the predominant method of pore-scale image binarization [159]. Segmentation is by nature subjective and care must always be taken in choosing gradient magnitudes to accurately reflect the rock properties of interest in the final image.

4 Experimental Methods

4.1 Experimental apparatus with the Versa XRM-500

The experimental apparatus [Figure 4.1] consists of a Zeiss Versa XRM-500 μ -CT, three 260D Teledyne ISCO syringe pumps, a batch reactor, a carbon fibre coreholder, a lab alliance barrel wash pump, 2 PID controllers with associated heating wraps and thermocouples, a lab computer, an Isco-pump controller, and a range of high pressure valves, fittings, and tubes of both stainless steel and PEEK construction.



Figure 4.1 Instrumentation outside the μ -CT consists of three ISCO pumps, a barrel wash pump, a reactor complete with heating and stirring, an ISCO pump controller and two PID heating controllers.

These components are connected in a flow loop [Figure 4.2] where reactive fluid is pulled through a core assembly and imaged *in situ* at high temperatures and pressures.

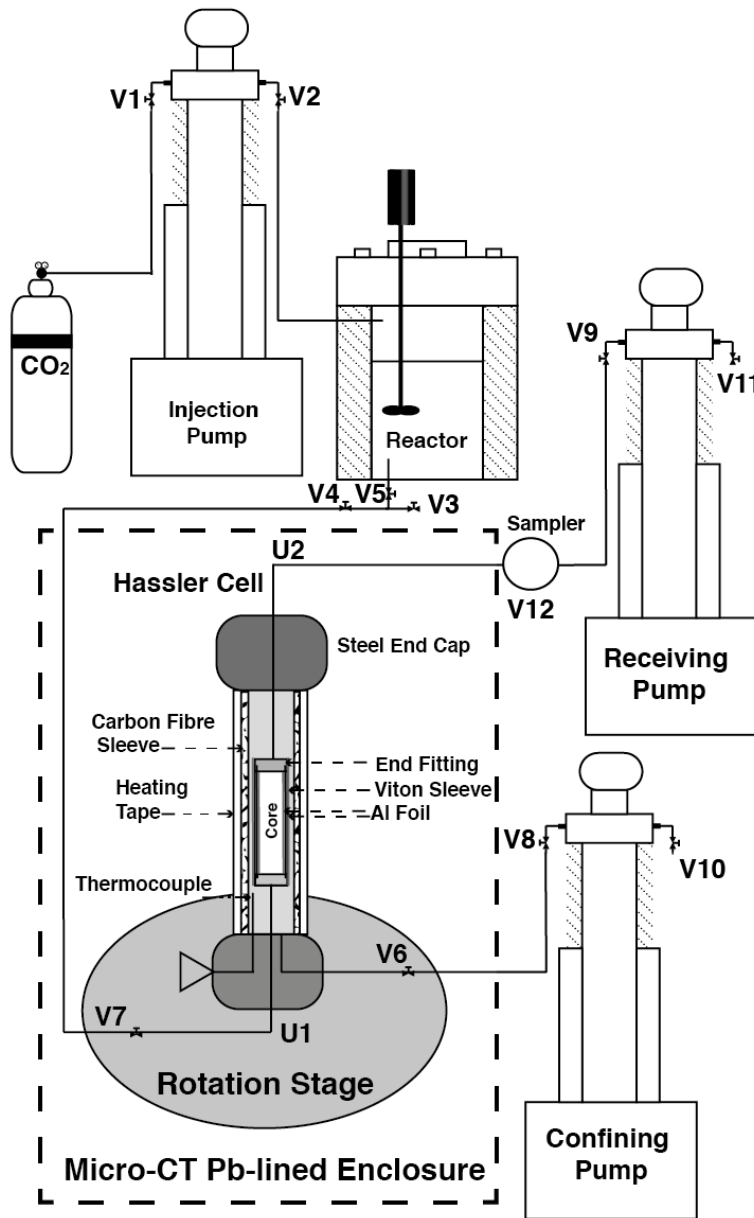


Figure 4.2 The *in situ* experimental apparatus used in the Versa XRM-500. CO₂ is pressurized by the injection pump and used to equilibrate brine in the reactor. Reactive brine is pulled through core assembly by the receiving pump. The cell is confined by deionized water in the confining pump at 12MPa and heated using heating tape controlled by a thermocouple in the confining fluid. The experimental system is connected together using tubing and fluid flow is directed using Valves (V) and Unions (U).

The Zeiss Versa XRM-500 μ -CT consists of an x-ray source, scintillator, objective lens and a camera centred around a rotation stage that is encompassed by a lead x-ray enclosure and controlled by Zeiss proprietary imaging software [Figure 4.3]. X-rays are generated by the source and directed through a sample mounted on the rotation stage. A portion of the x-rays are absorbed by the sample while the rest pass through the sample and hit the scintillator which fluoresces in the visible spectrum. This visible light is then focused by the objective onto the CCD, which translates that light into a pixelated digital image where the pixel intensity value is a function of the number of x-rays that absorbed by the scintillator.

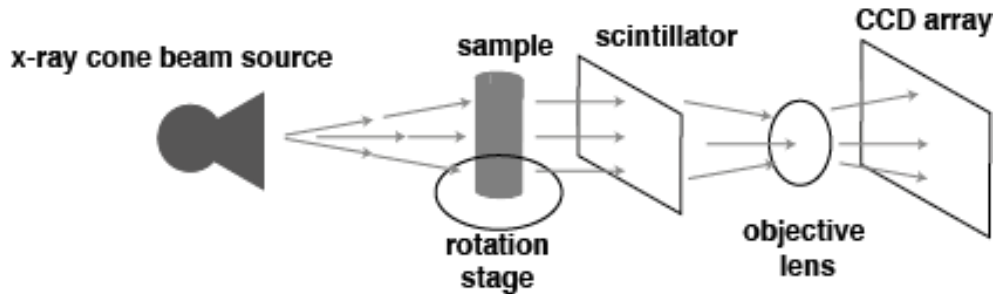


Figure 4.3 μ -CT working diagram. An x-ray source fires x-rays through the sample which fluoresce when they hit the scintillator. The visible light is focused by the objective lens and digitised by the CCD array.

The Versa-XRM 500 is capable of running at energies between 20-160 KeV. However, at the lowest energies the sample will absorb the majority of the x-rays and image acquisition will take a very long time. Thus, with dynamic imaging we focus only on the highest energies between 80 and 160 KeV. Figure 4.4a shows the x-ray spectrum emitted by the source at 80, 120, and 160KeV. At the lowest energy much of the spectrum is in the lower energy range and the characteristic (bremsstrahlung) x-rays are barely visible. However, at higher energies the characteristic x-rays are very distinct. The x-rays emitted by the source pass through - and thus filtered by - several different layers that are highly absorbing at lower energies before contacting the sample including air, brine, aluminium, and the carbon fibre sleeve of the core holder. Figure 4.4c shows the energy spectrum that reaches the sample where the much of the lower energy x-rays have been filtered out.

The Versa XRM-500 has a maximum power of 10W at high energies and 7W at medium energies. According to the standard definition of electrical power:

$$P = IV \quad (4.1)$$

where power, P [watts], is equal to current, I [amps], multiplied by voltage, V [volts]. Table 4.1 shows the maximum current available at each energy level. The maximum x-ray flux is dependent on the current of the source, which changes depending on the energy, therefore the flux must be recalculated by maximum current. Figure 4.4b is the spectrum maximum source current at the source and Figure 4.4d is the spectrum

the reaches the sample after passing through the core assembly. There is very little difference between 120 and 160 KeV inside the core holder at maximum power. As the source is more reliable at 120 KeV, this energy is chosen for dynamic scanning.

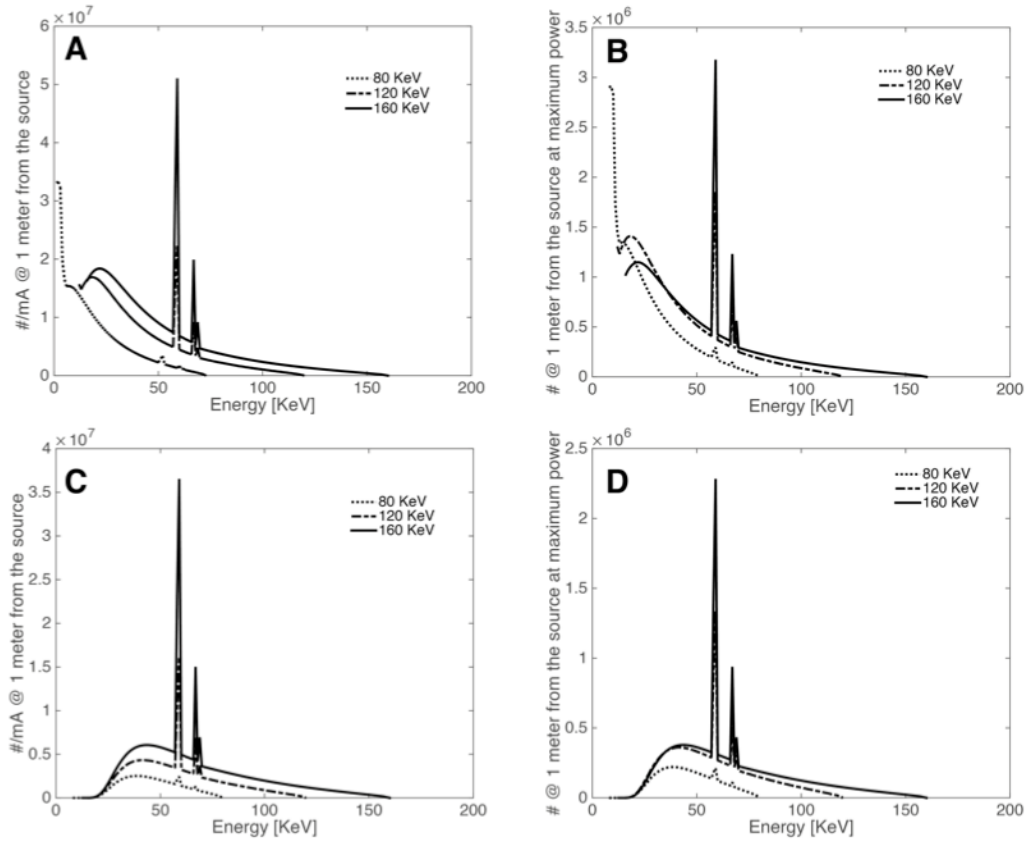


Figure 4.4 The X-ray spectra emitted by the Versa XRM-500 source at three different energies as calculated by SpekCalc [206-208]. (a) is the raw spectrum emitted from the source and (c) is the spectrum inside the core holder after lower energy x-rays have been filtered by the air, carbon fibre, and aluminium components. (b) and (d) are the total energy spectra calculated for the maximum source current available at each energy level. The flux increases with power, but decreases with added filters.

Table 4.1 Energy limits of the Versa XRM-500.

Source Energy [KeV]	Maximum Source Power [W]	Maximum Source Current [mA]
80	7	0.0875
120	10	0.0833
160	10	0.0625

4.2 Experimental method with the Versa XRM-500

Dynamic *in situ* imaging experiments are difficult and require a precisely followed method both for successful experimental completions and to ensure user safety. The procedure for *in situ* imaging includes the following steps:

1. Pre-reaction dry scan
2. Leak testing the rig

3. Brine pre-equilibration
4. Purging the system
5. Loading the core
6. Wetting the core
7. Beginning reactive flow and brine arrival
8. Dynamic scanning
9. Sampling
10. Post experiment depressurization
11. Unloading the core and stopping reaction
12. Post reaction dry scan

4.2.1 Pre-reaction dry scan

A dry scan of the entire core is taken prior to beginning the experiment. A cylindrical carbonate core sample 4 mm in diameter and approximately 1 cm in length is wrapped in a layer of adhesive aluminium foil. This layer of aluminium protects the core sample from damage during mounting and loading, thus ensuring that the dry scan will be an accurate representation of initial rock. The core is mounted on the stage and scanned in overlapping sections around 4 mm in width and length. The scan energy is chosen based on an ideal transmittance of around 0.2-0.3 and the exposure time is calibrated to an average count value of around 10,000, which ensures a high signal to noise ratio without over-saturating the detector. Each dry scan was taken with around 2400+ projections to maintain phase contrast and edge sharpness. No filters are used during image acquisition because the goal of the dry scan is met without a filter and the use of a filter would dramatically increase the time needed for scanning. However, this would not be the case with a chemically heterogeneous rock that required contrast between different mineral phases.

4.2.2 Leak testing the rig

Prior to connecting the core holder, the rig must be tested for leaks to ensure that it holds pressure. This is especially important for all parts of the apparatus between where the core holder sits on the stage and the receiving pump. During brine flow, the fluid is pulled through the core from the receiving pump. Should there be a leak, the flow rate through the core would not be accurately represented by the pump flow rate. Thus, all leaks must be sealed effectively to an acceptable leakage rate of at least one order of magnitude below the flow rate being used in the experiment (e.g. if the experiment will be carried out at 0.1 mL/min, the leakage rate in the system must be no higher than 0.01 mL/min at reservoir conditions). The rest of the system should also be tested to minimize leaks and maintain pressure to avoid unnecessary loss of brine from the system.

Additionally, the receiving pump must be constantly washed with a barrel wash. Any pump that contains highly saline brine has the potential to become damaged if salt crystals precipitate inside the barrel, which will scratch the interior of the pump and cause fluid leakage along the seals. Thus, deionized water is

constantly circulated along the outer edge of the barrel to keep any potential precipitates in solution.

4.2.3 Brine pre-equilibration

A 1% *wt* KCl 5% *wt* NaCl brine is loaded into the disassembled reactor. Powdered Ketton rock may also be added depending on the desired brine acidity. The reactor is then reassembled. CO₂ is loaded into the injection pump through valve 1, valve 1 is then closed and the injection pump is pressurized to 100 bar. Valve 2 is then opened and floods the reactor with CO₂. The reactor is heated using a PID controlled heating wrap in combination with a temperature probe and is continuously stirred with an entrainment stirrer driven by an external electric motor. The brine is equilibrated with CO₂ at 10 MPa and 50°C for between 2 and 6 hours to ensure that the brine is completely saturated with CO₂ and the carbonate is fully dissolved [45, 62, 175, 177, 209].

4.2.4 Purging the system

Prior to connecting the coreholder the system must be completely purged of air and possible precipitants in the lines from previous experiments. The lines above and below the core holder are connected together to bypass the core holder (U1 and U2). Deionised water is then loaded into the receiving pump through valve 11. Valves 7, 4, and 3 are opened and the receiving pump is used to drive DI water backwards through the system and out of the valve 3 below the reactor. Approximately 10 system volumes are used to ensure the lines are clear of air and rinsed clean.

4.2.5 Loading the core

The core is loaded into the cell in preparation for core flooding. The core wrapped in one layer of aluminium foil is inserted into a Viton sleeve [Figure 4.5]. The sleeve is cut to size so that it is 2mm shorter than the combined length of core and interior end fittings. The end fittings are 1/16" NPT to swagelock union fittings that have been machined to 5mm in exterior diameter while the Viton is 4mm in interior diameter. This 4mm Viton is then stretched over the 5mm end fittings to create a tight seal. There must not be any space between the end fittings and the core to ensure that the confining pressure does not over compress the Viton and pinch off flow. The fittings and Viton sleeve are then wrapped in two additional layers of aluminium both to prevent gaseous CO₂ from diffusing into the confining fluid and to keep the Viton sleeve in place on the fittings and prevent a hydraulic pathway from connecting the confining and pore fluids. The core holder is then put back together and the end caps and end fittings sealed.

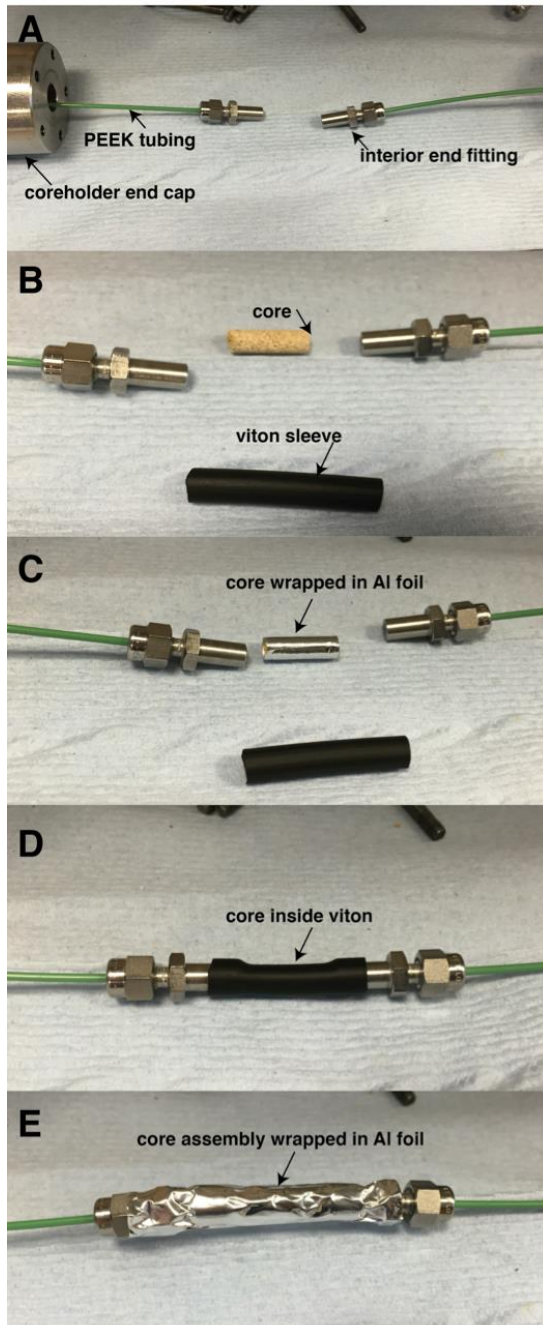


Figure 4.5 The core assembly inside the core holder. (A) PEEK tubing is attached to the interior end fittings and threaded through the steel end caps. (B) The core (B) is wrapped in aluminium foil (C) and inserted into the Viton sleeve. The Viton sleeve is then stretched over the end fittings to create a watertight seal (D) and two additional layers of aluminium foil are added to hold everything in place and prevent gas diffusion (E).

The core holder is then mounted on the stage [Figure 4.6]. The flow lines are connected and the electrical lines for heating control are attached. One must take care to make sure the core holder is completely vertical to allow the μ -CT source to be positioned as close as possible. At this stage it is also prudent to test the stage rotation and ensure that all flow and electrical lines are free to rotate from -108° to 108° (the typical $180^\circ+$ fan angle).

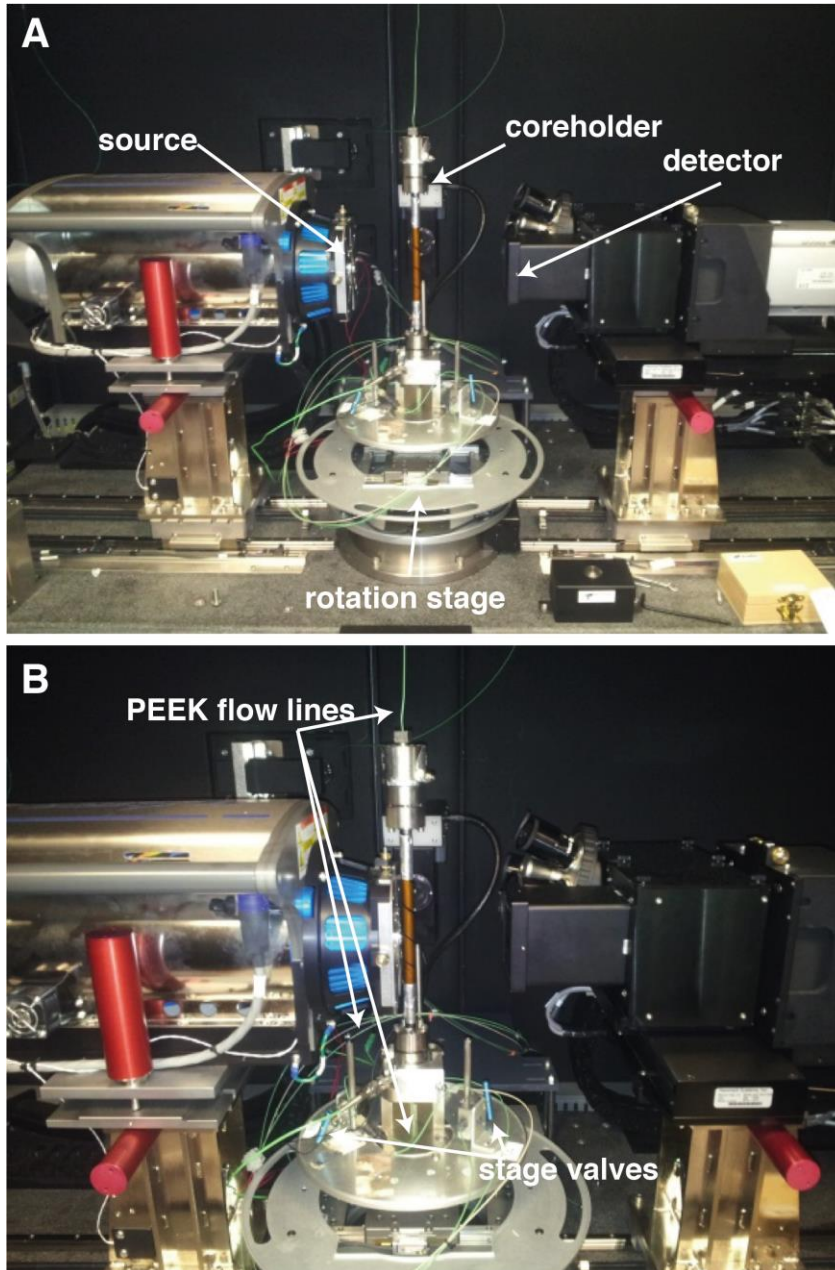


Figure 4.6 The core holder is mounted on the stage in between the source and detector (A). The source is moved as close to the core holder as possible while still allowing for free rotation (B). *Photo Credit: Matthew Andrew*

4.2.6 Wetting the core

A brine of 20% *wt* KI is loaded into the receiving pump through valve 11 and DI water is loaded into the confining pump through valve 10. Valve 10 is closed and valves 8 and 6 are opened. The confining pump is then used to confine the core at 2 MPa. Valve 11 is closed and the receiving pump is pressurized to 10 Bar. Valves 9, 7, 4, & 3, Fig. 4.1.2, are opened and the resulting pressure drop is used to drive KI doped brine through the core for wetting. The confining and pore pressures are stepped up incrementally until a reasonable flow rate is established. Approximately 20 mL of brine is driven through the core and drained through valve 3 below the reactor. In this way all air is purged from the system and the core is flooded with high contrast brine that makes the arrival of undoped reactive brine easy to observe. Valve 3 is then closed and the confining and pore pressures are increased incrementally until the core is confined at 12 MPa and the pore pressure is 10 MPa. The PID controller is then switched on to bring the core to 50°C. The receiving pump is then stopped, valve 3 is closed, and valve 5 at the base of the reactor is opened so that the reactor system is connected to the core.

The μ -CT is then turned on and the core holder is centred in the field of view at the point in which dynamic scans will be taken. A reference scan is taken at 120 KeV and 10 Watts using the negative x-direction. Additionally, a 2-D snapshot image is taken as a pre-flooding image for later comparison. Finally, a 2-D video is taken continuously as the core is flooded to track the core flooding progress.

4.2.7 Brine arrival

The receiving pump is then set to refill at the desired flow rate thus pulling fluid from the reactor through the core at the desired flow conditions while the injection pump regulates pressure from the front end. The 2-D projections are monitored for changes in attenuation that signal the arrival of reactive brine [Figure 4.7].

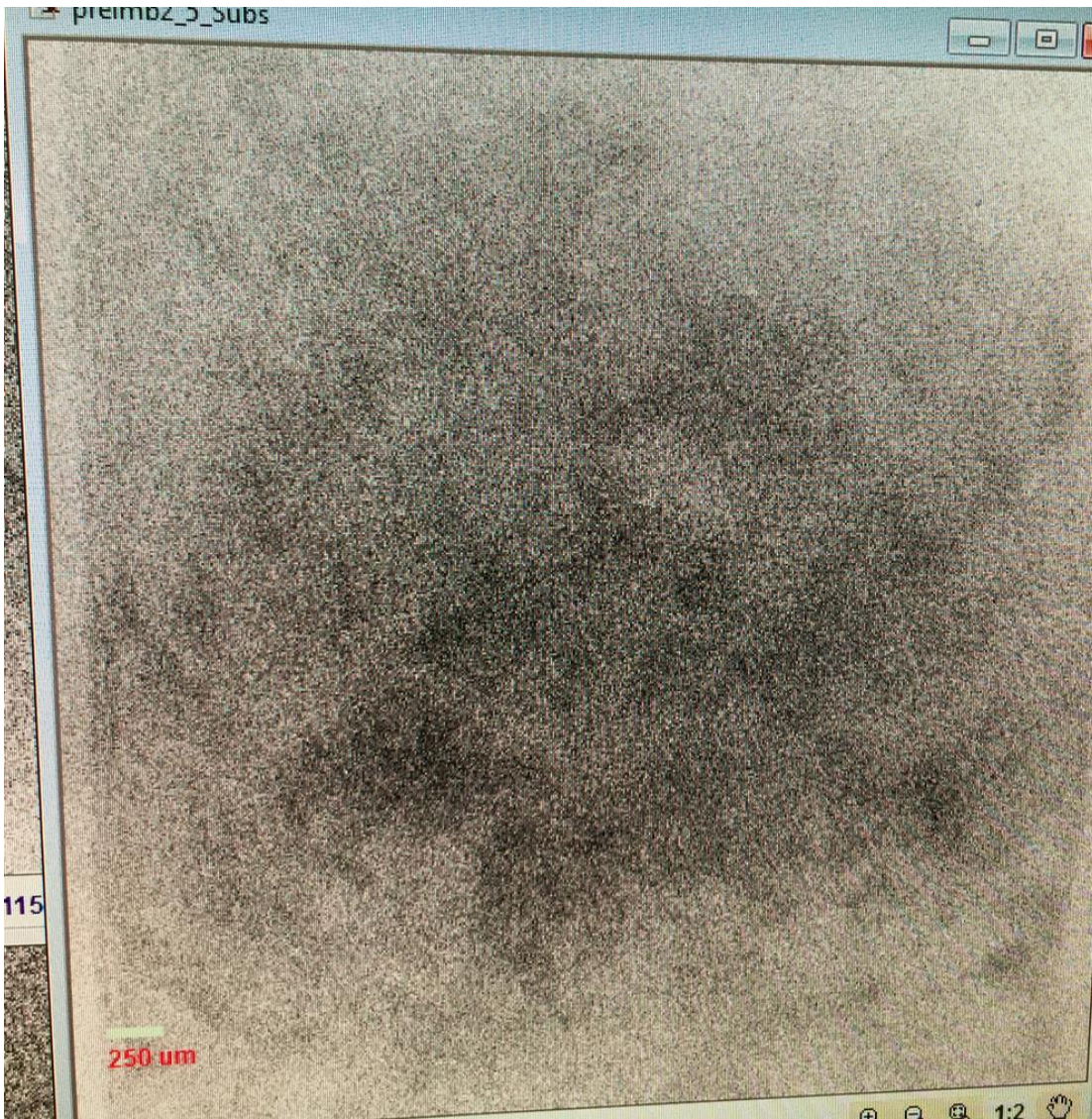


Figure 4.7 The difference image of a 2-D projection before and after brine arrival. The reactive fluid arrival is easily observable as a distinct attenuation difference (black) because the undoped brine absorbs fewer x-rays.

4.2.8 Dynamic scanning

When reactive brine arrives the transmission of the core will increase as the doped brine is displaced with the highly x-ray transparent reactive fluid. 2-D scans are stopped and 3-D tomographic scans are taken successively as fast as the scanner allows. The total scan time depends on several factors and must be optimized. All dynamic scans are run at the highest available and most reliable energy throughput – for our instrument this is 120 KeV and 10 W. While this is not the optimum energy for scanning carbonate (the transmission is slightly higher than ideal), scanning at a lower energy would mean sacrificing time and thus a fewer number of tomographic scans could be taken within a set time period. Additionally, while scanning at 160 KeV would produce faster scans, we found the instrument to be most reliable at 120

KeV. The exposure time is adjusted to get at least 8000 counts so that there is an adequate signal to noise ratio and between 400 and 800 projections are used per tomography. Homogenous carbonates with larger pores require fewer projections than heterogeneous carbonates with smaller and more complex pore structures. This should be tested before the experiment on sample rocks. The core is scanned using only 180 + fan angle to avoid stretching and tangling the flow and electrical lines.

To reduce scan time further, auto referencing is disabled and the only reference used is the one taken during the wetting the core phases. Additionally, sample drift correction is disabled as the time and spatial resolution of these scans is such that drift correction does not improve quality. To avoid source - core holder collision, the reference axis is set to -X and the 'sample too large for auto ref' box is ticked. One must be sure to follow these steps for every tomography in the recipe as the default settings are not ideal for dynamic scanning with a core holder and can indeed be dangerous if used improperly.

3-D scans are taken until either the time limit is reached or the core looks sufficiently dissolved that there is an imminent danger of internal structural collapse (and thus causing the loss of both the confining pressure and later whole core scan data).

4.2.9 Sampling

An effluent sampling valve is mounted to the back of the scanner that allows for effluent sampling at reservoir conditions without disturbing flow or pressure conditions in the flow cell [Figure 4.8]. The valve is mounted as close as possible to the outlet lines passing through the top baffles of the μ -CT to reduce the dead volume between the core and the sampler (to decrease lag time between starting flow and the first sample) while not being inside the μ -CT (which would inhibit *in situ* sampling whilst scanning).

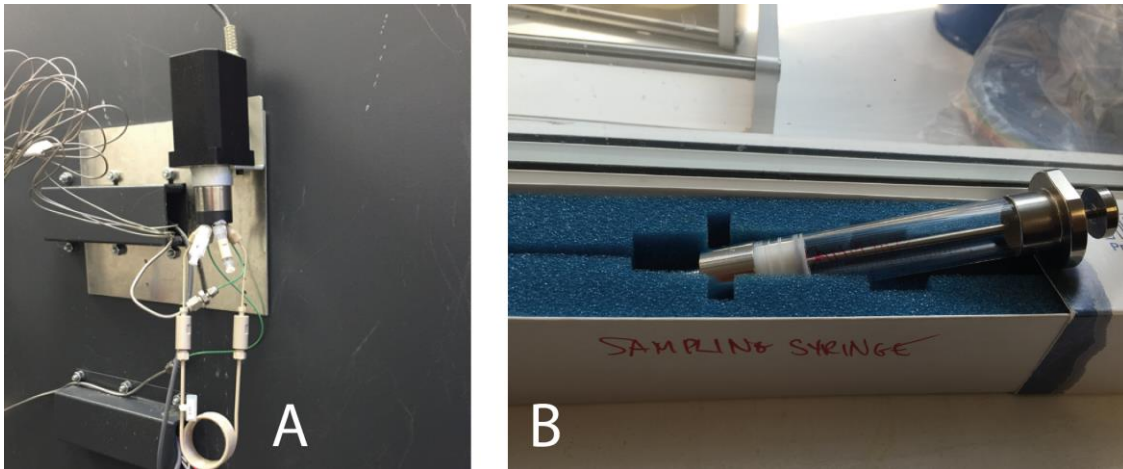


Figure 4.8 Effluent sampling valve (A) mounted to the back of the scanner and a glass sampling syringe (B) for collecting effluent from the sample loop.

The sampling valve is a VICI electronically actuated 2-position 6-port high-temperature high-pressure valve designed for high performance liquid chromatography and adapted for our use [Figure 4.9]. In position A, fluid from the core goes through port 3, out port 2 and into a 2 mL sample loop in port 5 and then out port 4 to the receiving pump. Meanwhile DI water is flushed through port 1 and 6 using a syringe to both clean the interior of the valve and provide an incompressible fluid for when the valve is actuated and the internal fluid is quickly pressurized to 100 bars. To extract a 2 mL sample the valve is electronically rotated to position B. In this position the core fluid goes in port 3 and straight out port 4 to the receiving pump thus bypassing the sample loop. The effluent sample can then be extracted from the sample loop using port 1 and a sampling syringe.

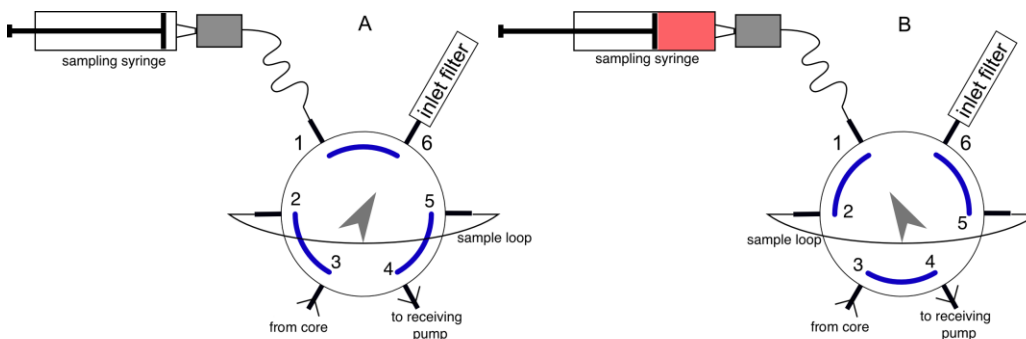


Figure 4.9 The two-position six-port VICI HPLC valve schematic. Position A sends the fluid through the sample loop at reservoir conditions. Position B bypasses the sample loop allowing for ambient condition effluent sample extraction. Modified from www.thamesrestek.co.uk.

The addition of an effluent sampler to the *in situ* rig provides the capability of analysing cation concentrations throughout our dissolution experiments. Effluent samples are extracted and then analysed on an ICP-MS. Non-reactive salt components are used as tracers to account for any dilution. Cation analysis is used both to confirm dissolution rates and pH, and in the future to provide insight into the dissolution dynamics of chemically heterogeneous samples.

4.2.10 Post-experimental depressurization

After the last scan and effluent sample are taken, the system must be efficiently depressurized in order to avoid reacting the core any further. First the receiving pump is stopped. Then valve 5 connecting the reactor to the rest of the system is closed. The system pressure is then stepped down using the confining and receiving pumps keeping around 1MPa more pressure on the confining fluid. Once within 1 MPa of atmospheric pressure is reached, the confining and receiving pumps are opened to atmosphere using valves 10 and 11 to drain any remaining fluid.

The PID controlled is shut off and the 4-way union (U2) is opened at the top of the core holder to release any remaining system pressure. The top valve is chosen to avoid spilling fluid on the sample stage and the union is opened using the plug and not the fitting as PEEK fittings under pressure have a tendency to explosively decompress when loosened. The confining line is slowly loosened and removed while excess DI confining water is caught with absorbent paper. Valves 6 and 7 are close and union 1 and the electric lines are then disconnected, the clamp loosened and the core holder is removed from the μ -CT.

4.2.11 Unloading the core and stopping reaction

The core is then carefully removed from the core holder and the Viton disconnected from the interior end fittings. The core is not removed from the Viton because Viton is x-ray transparent and doing so may damage the fragile reacted core. The Viton covered core is then placed in a beaker full of DI water to dilute any potentially reactive brine and stop all reaction.

4.2.12 Post-reaction dry scanning

The entire core is then air dried overnight, mounted on the stage, and scanned again at the same energies as the initial dry scan.

4.3 Experimental apparatus using a synchrotron lightsource

The experimental apparatus used at the Diamond Light Source [Figure 4.10] is nearly the same as the one used inside the μ -CT. The main difference is that a special core holder has been designed to sit on the rotation stage that is much shorter than the one used inside the μ -CT. The stage at Diamond synchrotron rotates much more

quickly than the one in the μ -CT and the sleeve core holder is made of carbon fibre that is relatively flexible. Thus, possible motion effects must be minimized and we have designed a new, shorter core holder [Figure 4.11] that is less prone to bend and flex during rotation and cause image blurring.

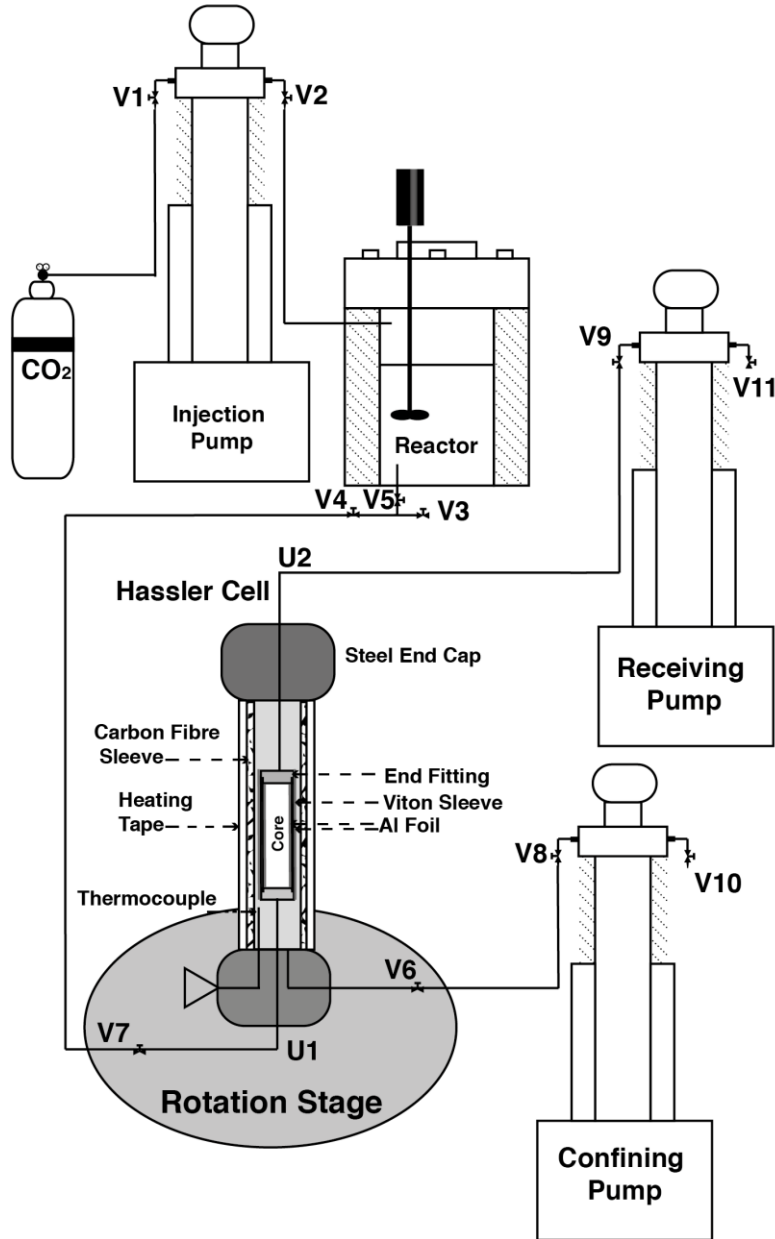


Figure 4.10 The *in situ* experimental apparatus used at the Synchrotron. CO₂ is pressurized by the injection pump and used to equilibrate brine in the reactor. Reactive brine is pulled through core assembly by the receiving pump. The cell is confined by deionized water in the confining pump at 12MPa and heated using heating tape controlled by a thermocouple in the confining fluid. The experimental system is connected together using tubing and fluid flow is directed using Valves (V) and Unions (U). Taken with permissions from Menke et al. [210].

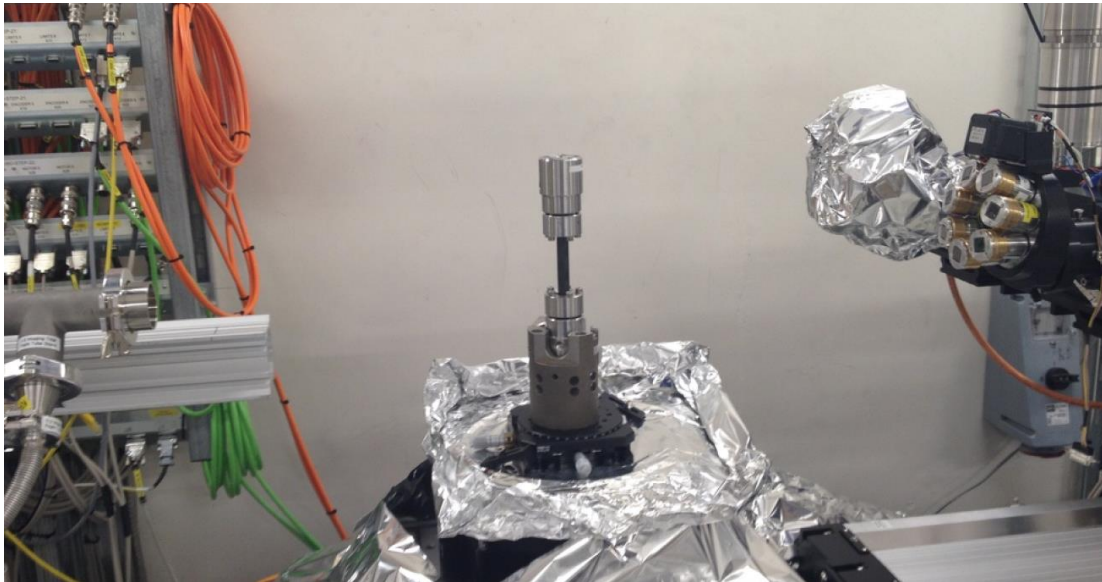


Figure 4.11 A short carbon fibre core holder used for *in situ* imaging at Diamond Lightsource. Sensitive equipment is protected from fluid spills by aluminium foil.

4.4 Experimental method using a synchrotron lightsource

The reservoir condition experimental apparatus used at Diamond synchrotron is nearly identical to that used in the μ -CT. The only difference is that the apparatus itself must be inside the x-ray enclosure [Figure 4.12]. This means that effluent sampling is not possible with the method employed for μ -CT scanner and that all pumps must be controlled remotely with the lab computer Isco software [Figure 4.13]. The system is monitored using a series of cameras inside the beamline hut.

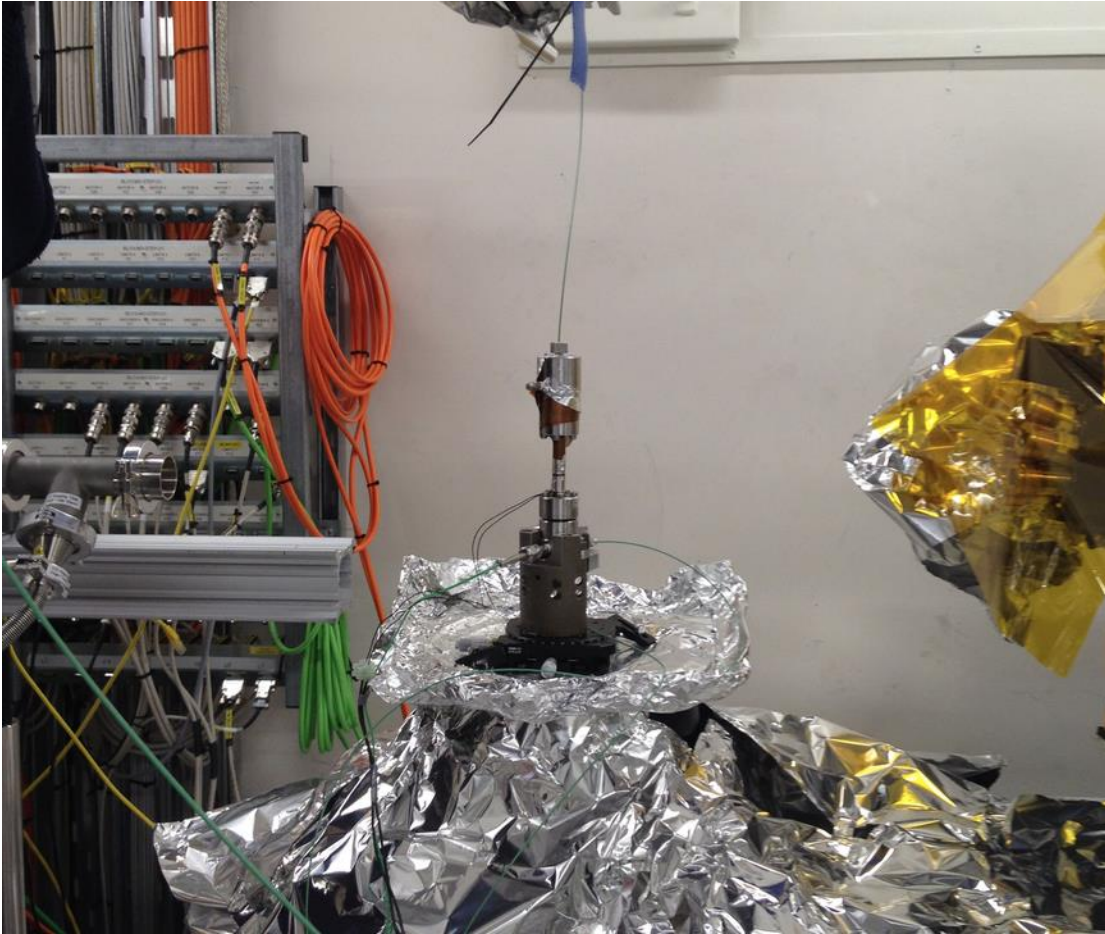


Figure 4.12 The core assembly mounted on the I-131 beamline rotation stage. Flow and electrical lines are free to rotate. *Photo credit: Catriona Reynolds.*

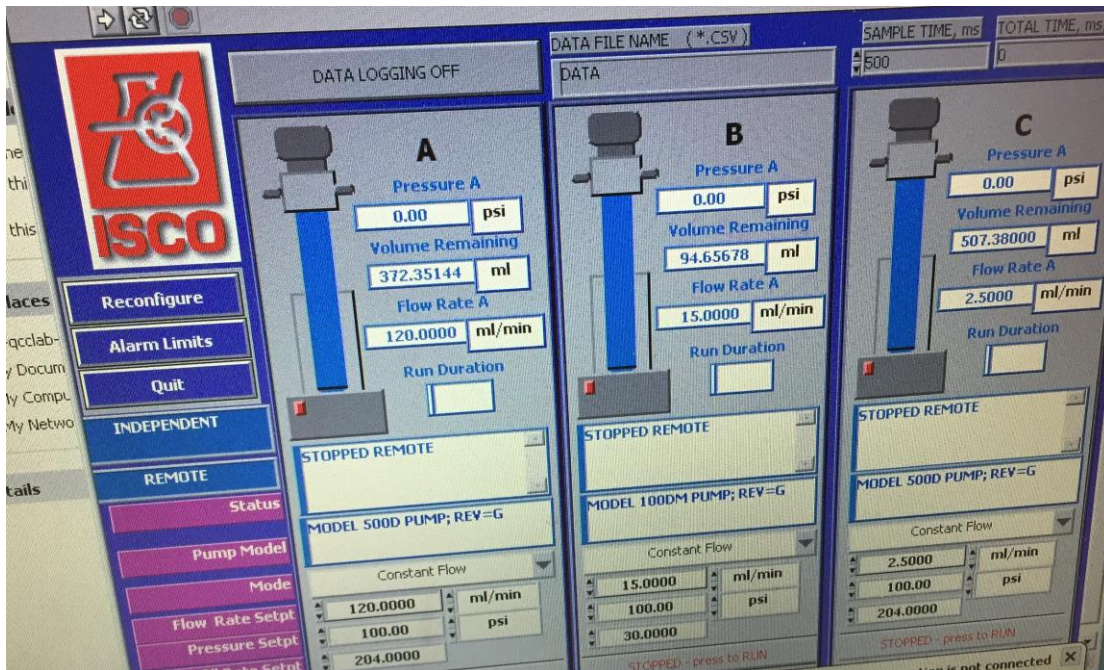


Figure 4.13 Teledyne ISCO pump remote control software controls flow conditions inside the beamline hutch.

There are two main differences between scanning at Diamond and scanning in the μ -CT: energy quantity and energy type. The total energy flux using the Diamond pink beam is much greater than that of the μ -CT and thus a tomography that would take 35 minutes in the Versa only takes 35 seconds at Diamond [Figure 4.14]. This allows for a much better time resolution and to some extent, a better quality image. The imaging apparatus at Diamond consists of a polychromatic x-ray beam produced by an undulator. Thus, the flux is highly quantized [Figure 4.15] over a narrow spectrum.

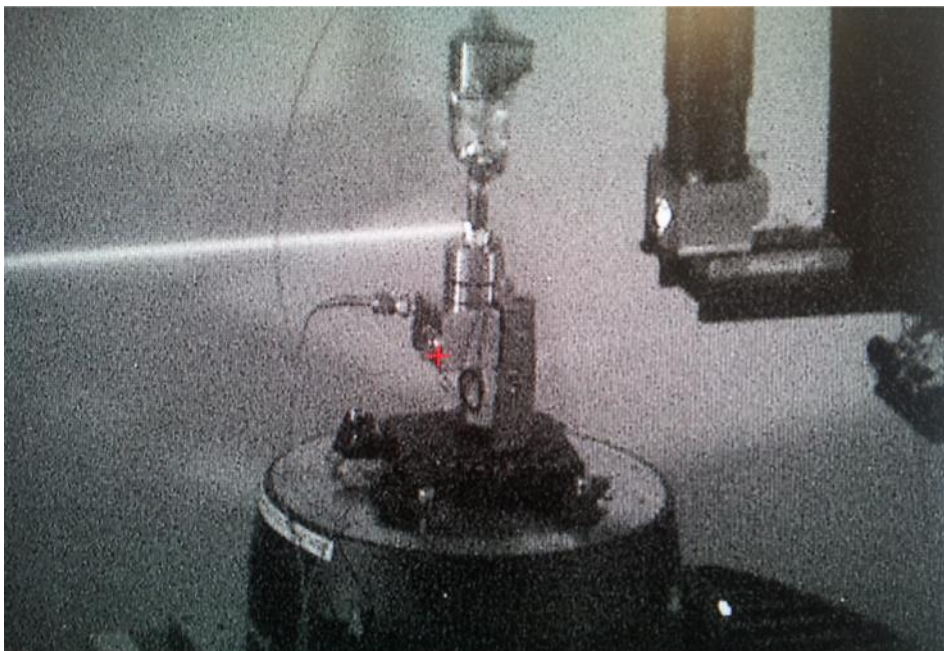


Figure 4.14 The Diamond Lightsource I13-I beamline pink beam taken by a visible light camera. The beam is seen in the visible spectrum because the beam is powerful enough to ionize the air.

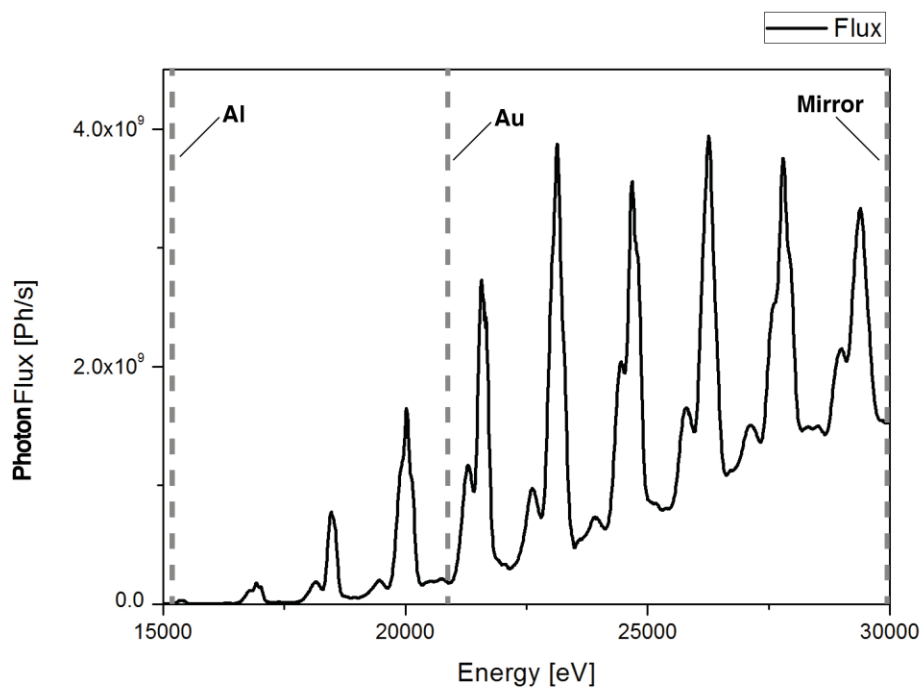


Figure 4.15 The x-ray spectra of the Diamond Lightsource I-13I pink beam. Calculated by beamline scientist Christophe Rau using both the experimental Tuning curve and theoretical mirror reflectivity and filter transmission. The dotted lines indicate spectrum termination points for gold (Au) and Aluminium (Al) filters and mirrors.

Different detectors scintillate at different intensities for different energy light. The Versa XRM-500 has a detector made of iodine. The scintillator used at Diamond Lightsource beamline I13-I is made of cadmium tungstenate (CdWO_4). We have found experimentally that the CdWO_4 detector is ideal for our applications because it scintillates abundantly at our available light frequencies and flux. A 1.25x objective lens coupled with a PCO EDGE camera were used in these experiments.

4.5 Effluent analysis

Measurement of major cation concentrations in experimental effluent samples is typically carried out using an inductively coupled plasma mass spectrometry, known colloquially as ICP-MS [211]. ICP-MS has been used widely to study mineral equilibrium concentrations at raised temperatures and pressures [99, 212]. A small amount of liquid sample is extracted from the system and acidified to keep soluble ions in solution. The concentrations of major cations are then measured at ambient conditions. The measured ion concentrations along with mass conservation and other known chemical equilibrium values are then used to calculate chemical equilibrium state of reactions taking place in the closed system.

4.5.1 ICP-MS methods

Once the sample has been removed from the effluent sampler and placed in a clean container it must be acidified to keep all the cations in solution until they can be measured by using mass-spectrometry (discussed in section 2). Steps in sample preparation are listed below:

1. The sample (~ 2 mL) is pushed out of the sampling loop using ambient air from a syringe and captured in a clean test tube.
2. 0.5 mL of sample is quickly transferred to three clean test tubes.
3. 4.5 mL of 2% HNO_3 is added to each sample container to acidify the sample.
4. The samples are analyzed for Ca^{2+} and K^+ using the ICP-MS and calibrated using solutions of known concentration.

4.6 Network extraction from μ -CT images

We use the segmented images to model pore space connectivity. Our network extraction method is based on the maximal ball algorithm [213] which provides a topological representation of the pore space as wide pores connected by throats. The algorithm grows spheres in the pore space of a segmented image to identify location and size of the pores and pore throats [Figure 4.16].

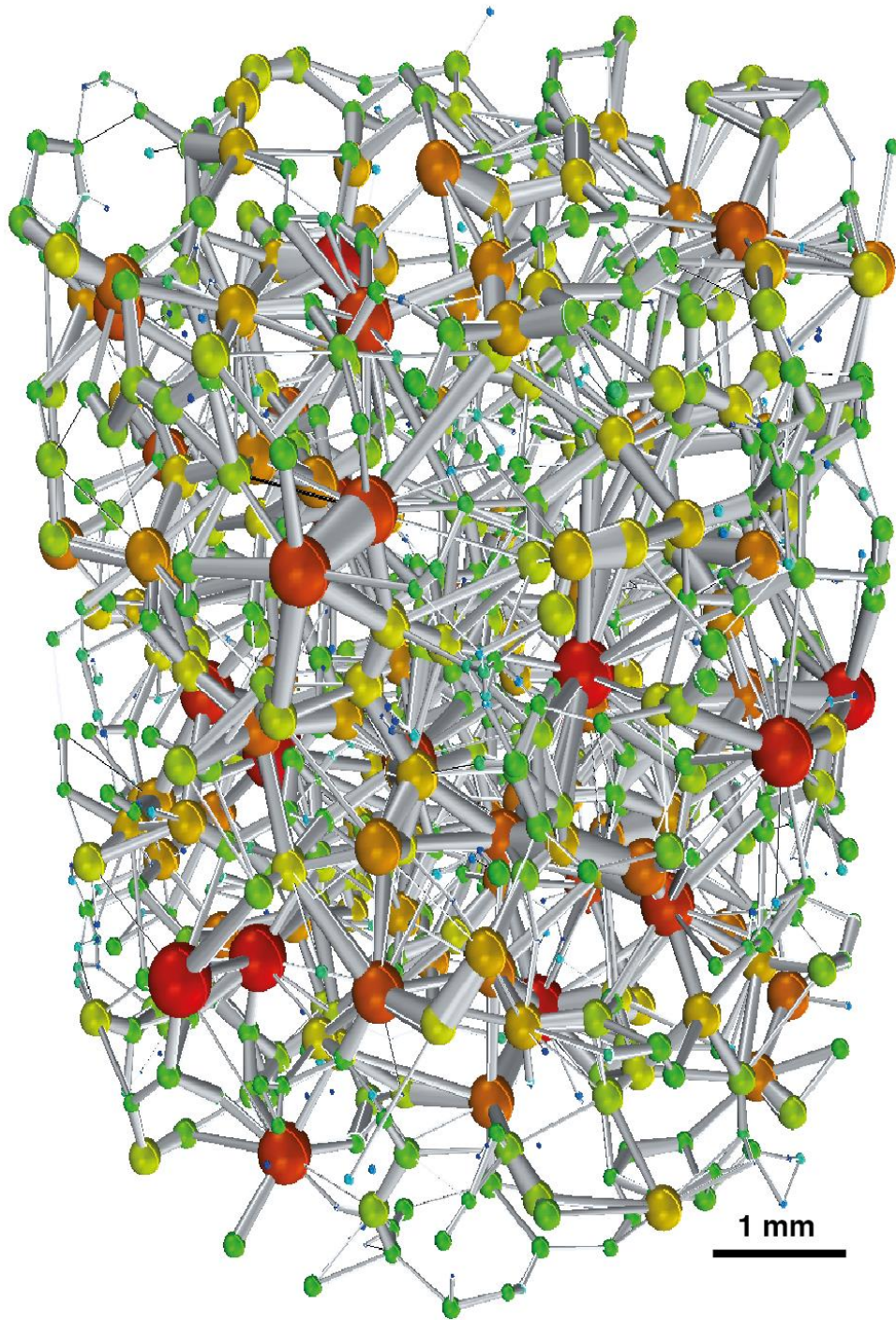


Figure 4.16 The extracted network of a Ketton μ -CT image. Balls that are colored according to size represent pores and pore throats are grey sticks. Larger pores are redder and represented by larger balls.

4.7 Flow modelling on μ -CT images

The distribution of flow speed [Figure 4.17] is calculated in accordance with the method presented in [49, 162]. A finite volume mesh is created by converting each image voxel into a grid block. We apply constant pressure boundary conditions at the inlet and outlet faces and a zero-gradient boundary condition for velocity on the lateral sides, while a no-flow boundary condition is used at solid voxel boundaries. The velocities and pressures are obtained for each voxel, and absolute permeability K [m²] is then calculated from Darcy's law: $K = -\frac{\mu q}{\nabla P}$ where μ is the viscosity, ∇P is the imposed pressure gradient between the inlet and outlet image faces and q is the computed Darcy velocity (volume flowing per unit area per unit time).

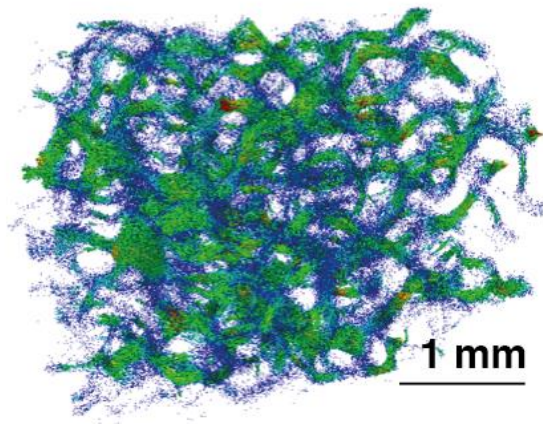


Figure 4.17 Normalized flow fields in Ketton. Only velocities fast than the average velocity are depicted with brighter and redder colors indicating faster velocities.

5 Pore and Rock Typing

To investigate the effect of pore-scale heterogeneity three limestone carbonates are examined in this thesis: Ketton, Estailades, and Portland Basebed. We chose these samples because they were readily available, relatively chemically pure, and diverse in pore structure. The rocks were characterised using the Choquette and Pray description for macro-porosity and the Cantrell description for microporosity. Scanning electron microscope and thin sections were used to examine crystallisation and surface characteristics. Core plugs used for bulk scale measurements and optical thin sections were drilled from the same 1 m³-block of rock as experimental samples to minimize local heterogeneity. The Mercury Intrusion Capillary Pressure (MICP) curves are reported and the pore throat radii is then calculated using the capillary tube form of the Young-Laplace equation:

$$P_c = \frac{2\sigma}{r} \quad (5.1)$$

where r is throat radius [m] , σ is surface tension [J.m²]and P_c is capillary pressure [Pa]. The porosity was measured using helium pycnometry or nitrogen porosimetry and the bulk absolute permeability was measured at the core-scale using a pressure drop and Darcy's Law.

Additionally, the pore-scale PDFs of velocity are calculated from the segmented dry sample images to assess the behaviour of fluid flow at the resolution of μ -CT scanning. Ketton has been shown to have homogeneous flow characteristics, in that the distribution of velocity computed on an image before reaction is narrower than observed for Estailades and Portland [49, 162].The velocity histogram is computed on the pore-space images and sampled uniformly in 256 bins of $\log(|\mathbf{u}|/U_{av})$, which are calculated as the ratios of the magnitude of u at the voxel centres divided by the average pore velocity U_{av} . Permeability was also computed using the flow solver on all dry scan images. Bulk and pore-scale values along with the chemical composition derived from x-ray diffraction are reported in Table 5.1.

5.1 Ketton

Ketton is a limestone oolite quarried in Ketton, Rutland, UK [Figure 5.1]. It was deposited 169-176 million years ago. It is an almost pure calcite medium-grained oolite with microporous cement with a standard micritic texture. Ketton has a helium porosity of 0.2337 and a core-scale permeability of 2.807×10^{-12} m² (measured at Weatherford Laboratories, East Grinstead, UK).

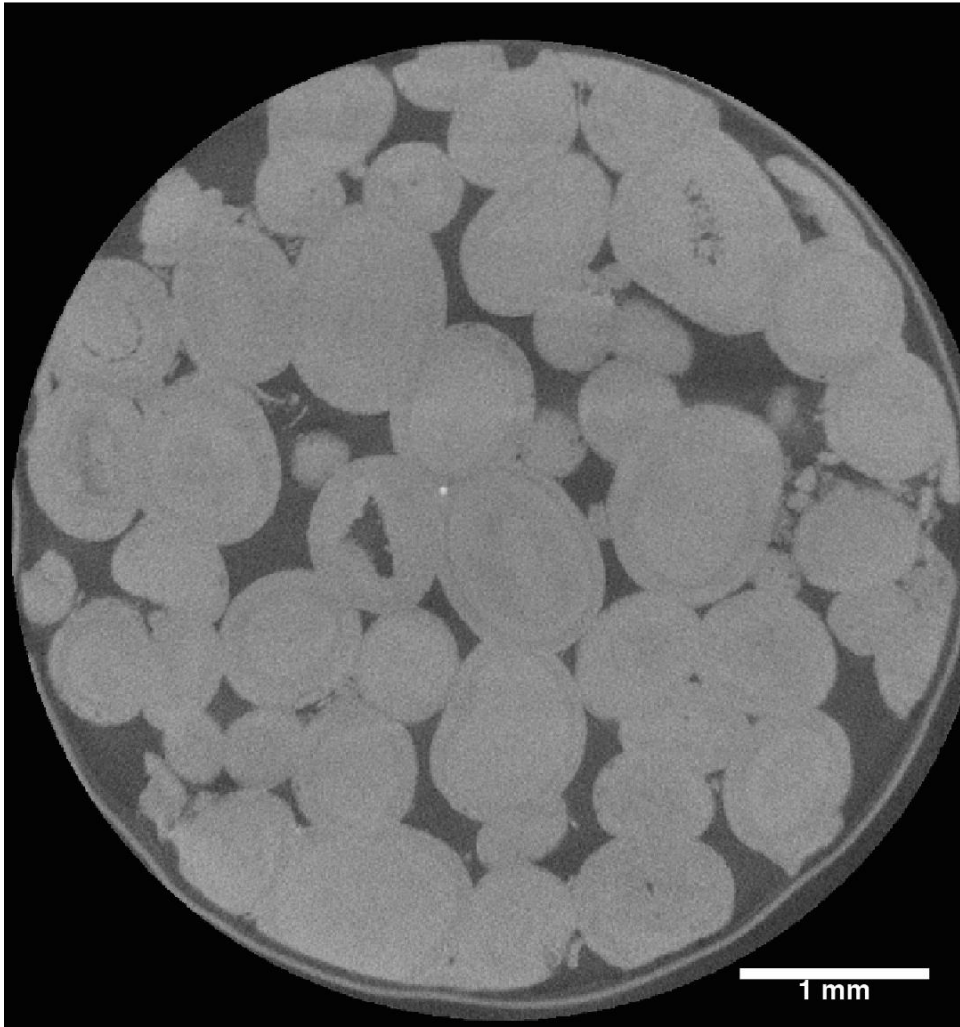


Figure 5.1 A μ -CT image of Ketton Oolite taken at approximately 4-micron resolution.

Ketton is a well-connected homogenous carbonate. The MICP curve and pore-throat distribution [Figure 5.2] show a clear bimodal population of pore throats. However, only the larger population of throats is accessible to μ -CT imaging as seen in the velocity distributions [Figure 5.3]. The grain population is divided between spherical oolites and smaller grain fragments and peloids [Figure 5.4].

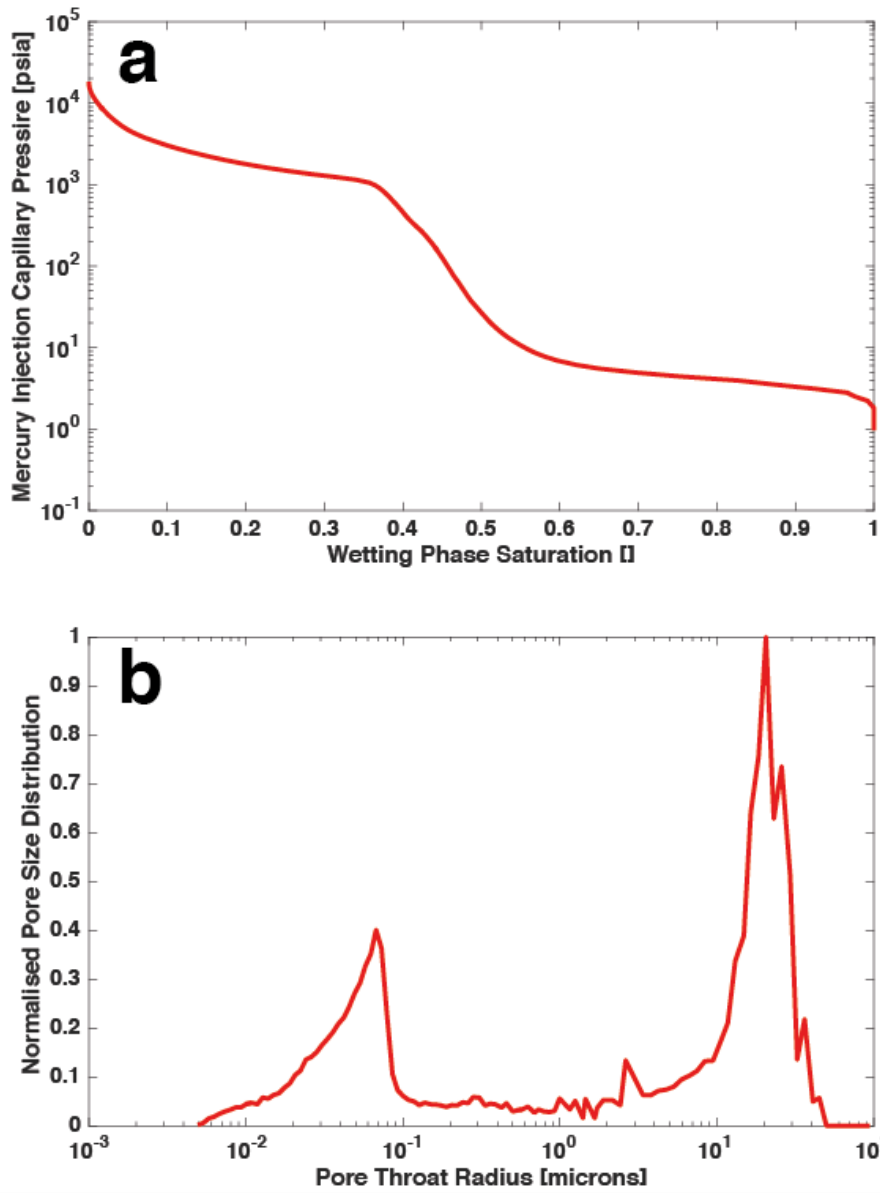


Figure 5.2 The MICP (a) and Pore Throat Radii distributions (b) for Ketton Oolite. A clear bimodal pore size distribution exists. Data taken from [214].

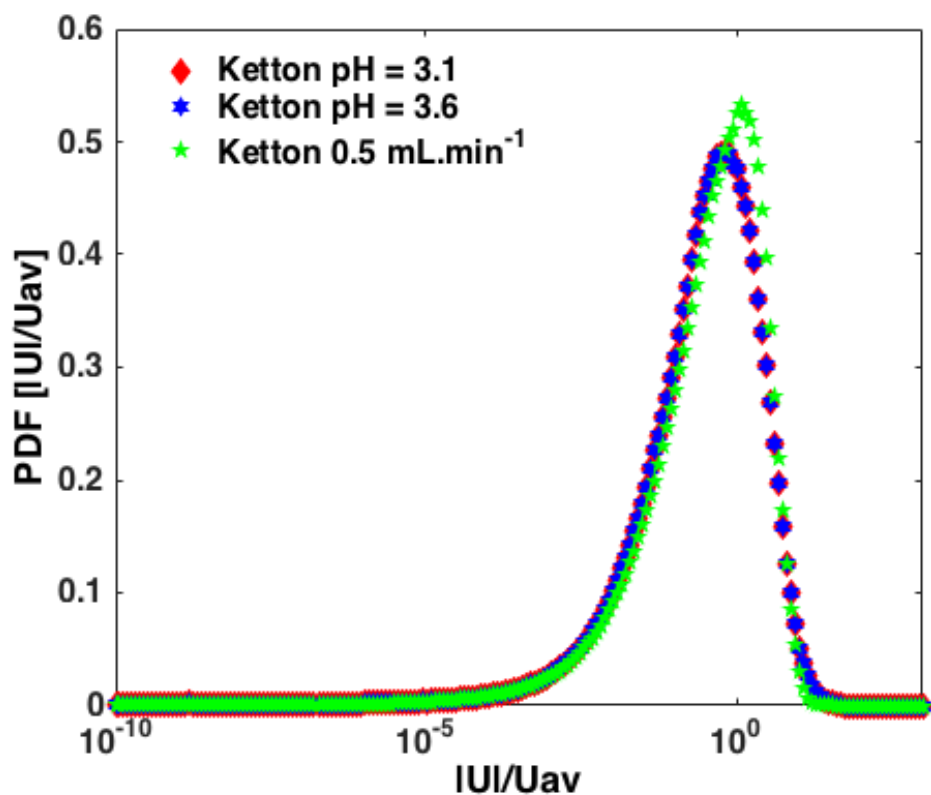


Figure 5.3 Probability density functions (PDFs) of pore voxel velocity in Ketton calculated on all dry μ -CT images of Ketton used in this thesis. All samples show a narrow range of velocities with a single well-defined population.

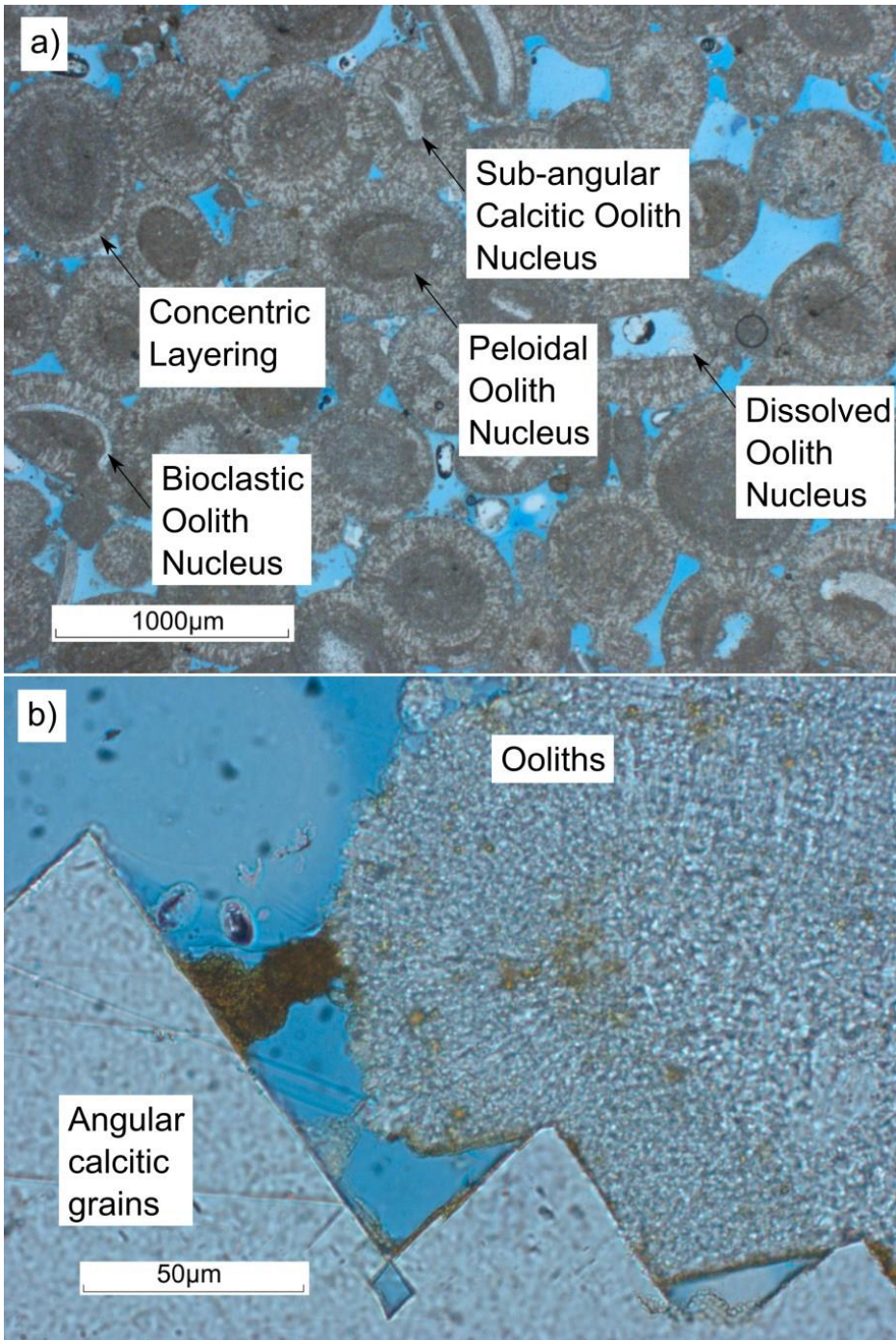


Figure 5.4 Thin section images of Ketton Oolite, showing grain nuclei and concentric layering (a) and the presence of angular calcitic grains along with Oolites (b). Taken with permission from Andrew [170].

5.2 Estailledes

Estailledes is a limestone quarried at Oppede, France [Figure 5.5]. It was deposited 22 million years ago. It is an almost pure calcite with a minor quartz component and is a medium to coarse-grained bioclastic grainstone with microporous bioclast grains. The Estailledes samples we used had a helium porosity of 0.295 and a bulk-scale absolute permeability of $1.490 \times 10^{-12} \text{ m}^2$ (measured at Weatherford Laboratories, East Grinstead, UK).

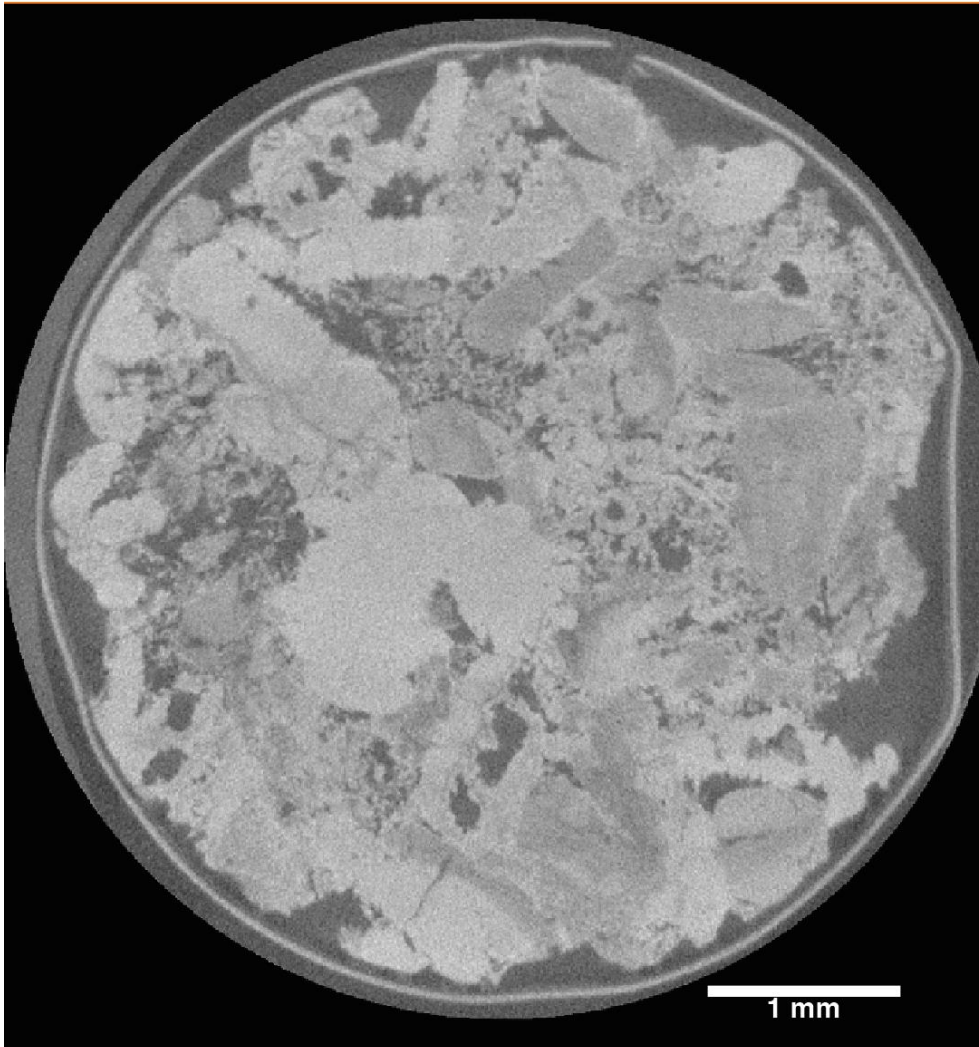


Figure 5.5 A μ -CT image of Estailledes Limestone taken at approximately 4-micron resolution.

Estailledes is a well-connected heterogeneous carbonate. The MICP curve and pore-throat distribution show [Figure 5.6] a clear bimodal population of pore throats. However, only the larger population of throats is fully accessible to μ -CT imaging as seen in the velocity distributions [Figure 5.7]. The intragranular macroporosity contributes to around half of the total porosity with the remainder residing in the microporous bioclasts [Figure 5.8].

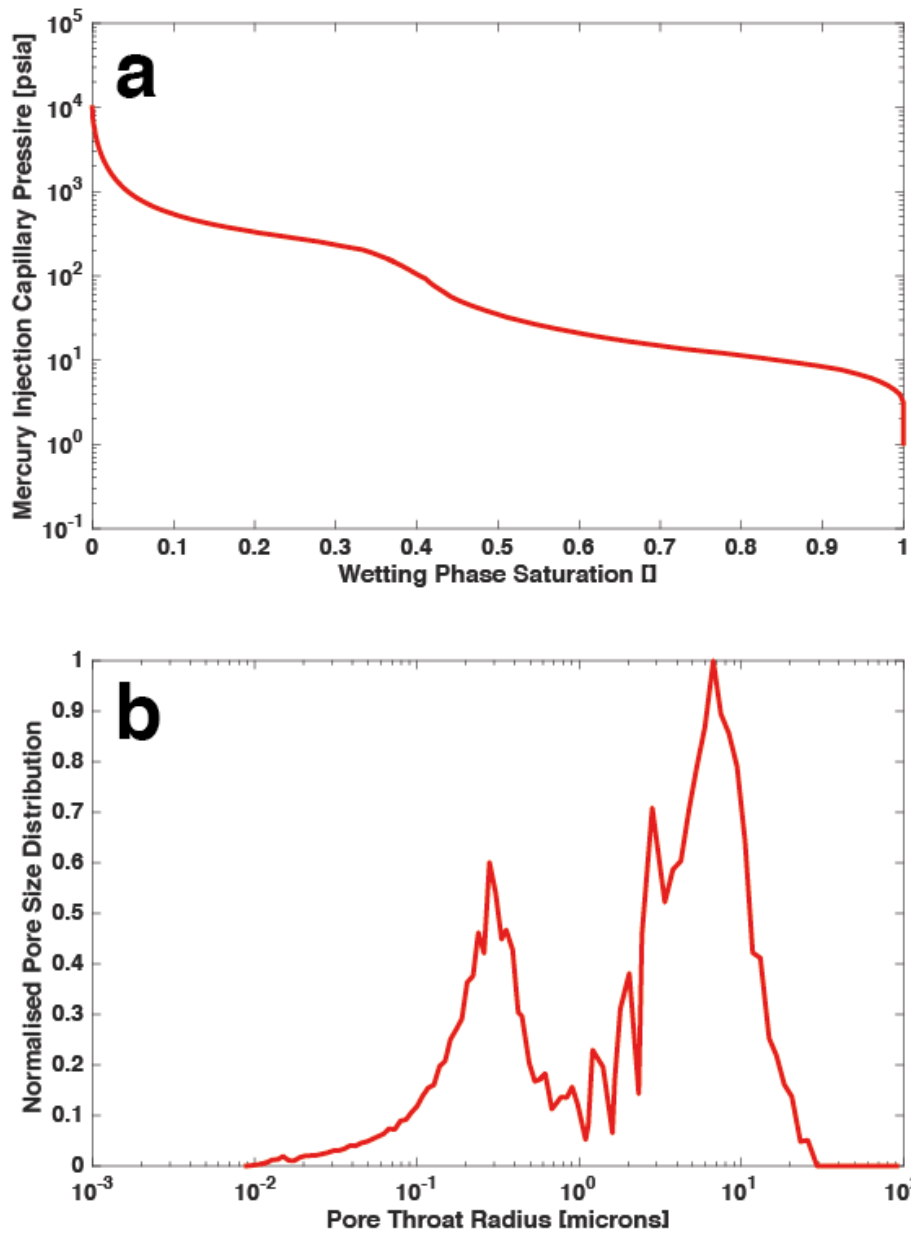


Figure 5.6 The MICP (a) and Pore Throat Radii distributions (b) for Estailades Limestone. A clear bimodal pore size distribution exists. Data taken from [214].

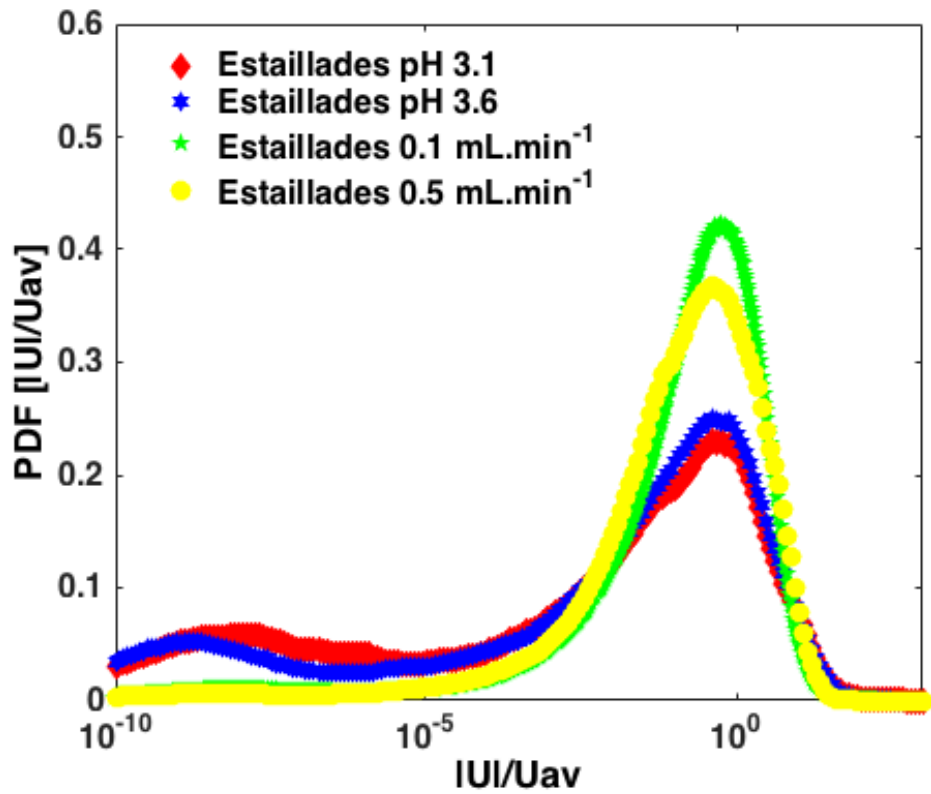


Figure 5.7 Probability density functions (PDFs) of pore voxel velocity in Estailades calculated on all dry μ -CT images of Estailades used in this thesis. All samples show a narrow range of velocities with a single well-defined population preceded by a long tail.

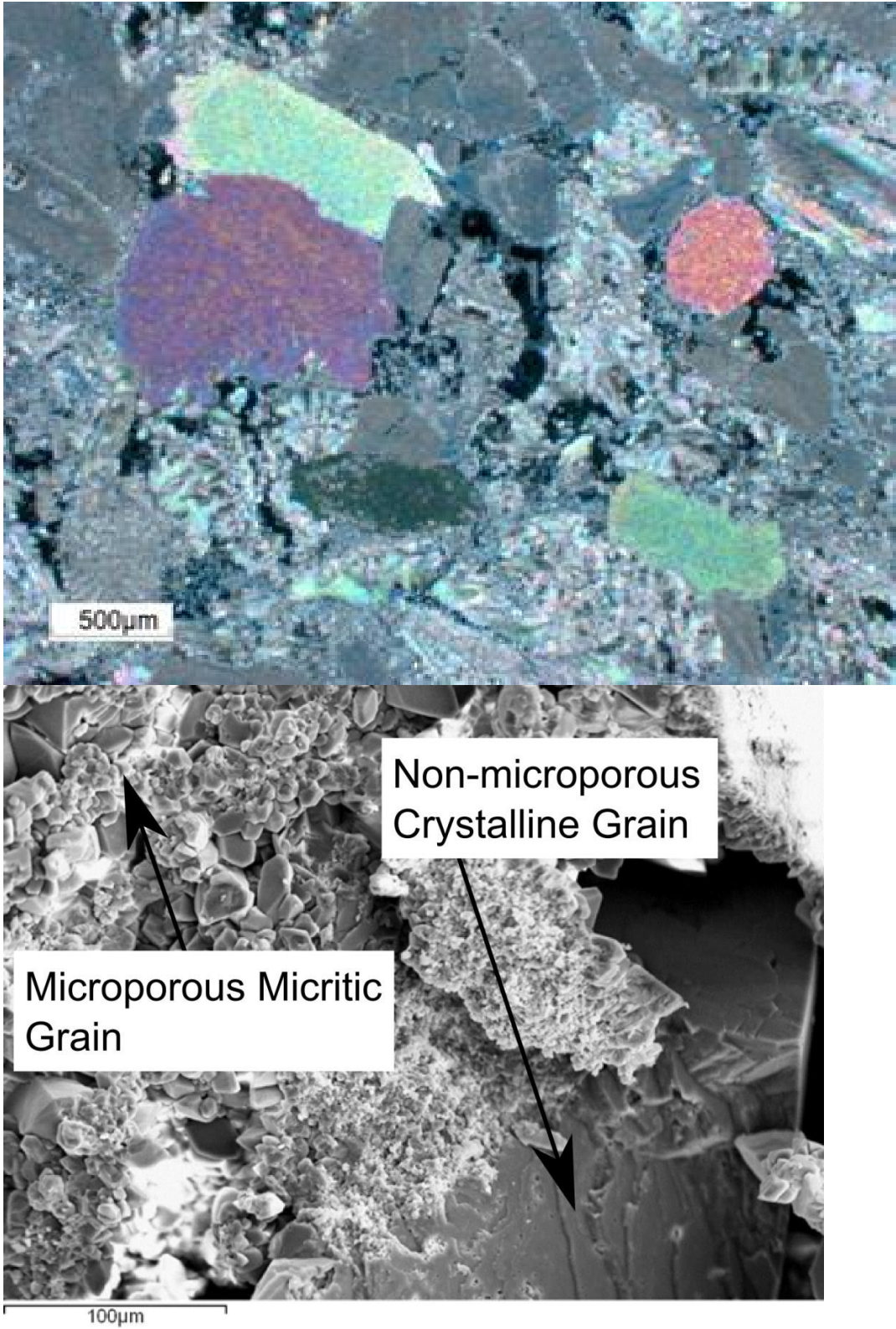


Figure 5.8 Microporous and non-microporous grains in Estailades limestone imaged using thin section (top) and SEM (bottom). Figure taken with permission from [170].

5.3 Portland Basebed

Portland Basebed is a limestone quarried in Portland, UK and was deposited during the Jurassic age [Figure 5.7]. It is an almost pure calcite with a minor quartz component and is a fine-grained grainstone containing tightly packed ooids with interparticular porosity and microporous cement. Portland has a porosity of 0.213 measured using nitrogen porosimetry and a core-scale permeability of 1.45×10^{-16} m².

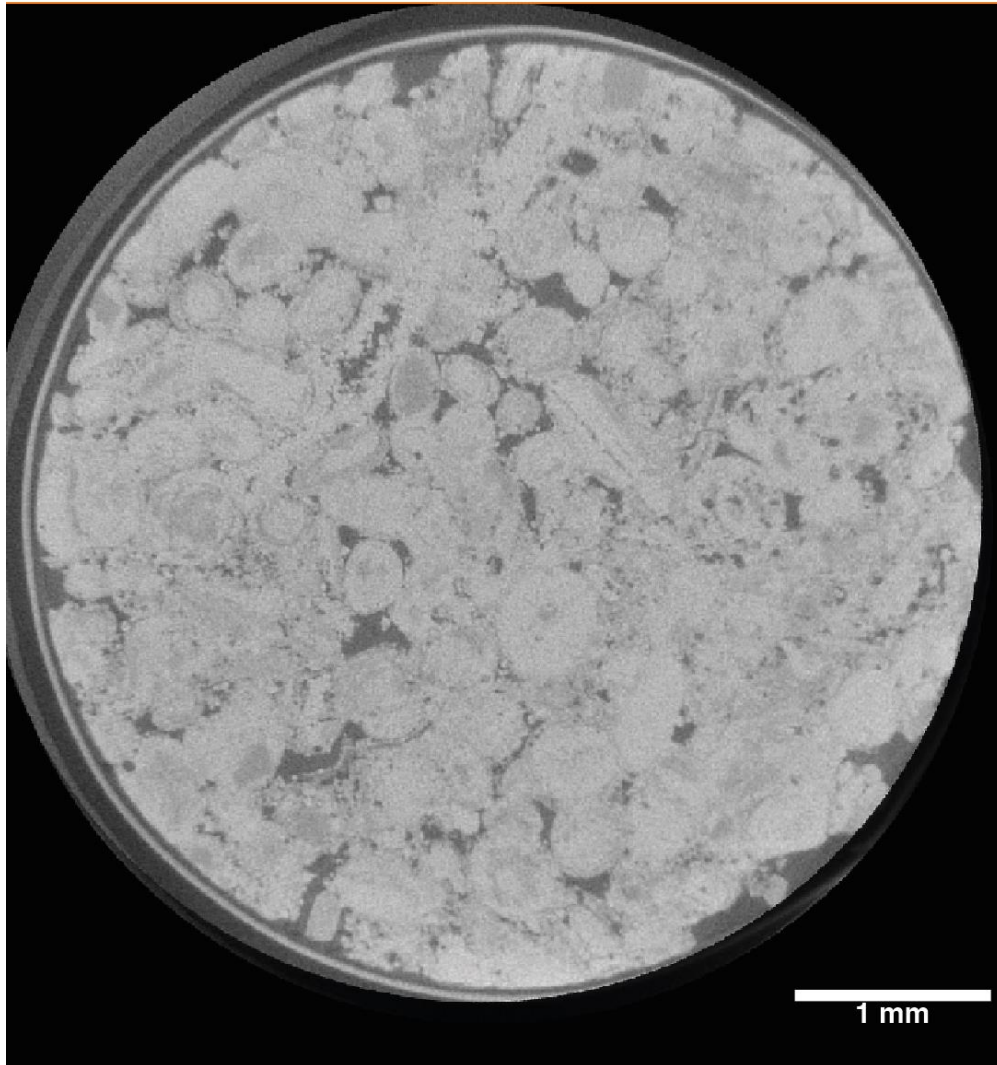


Figure 5.9 A μ -CT image of Portland Basebed taken at approximately 4- μ m resolution. Portland consists of tightly packed ooids and microporous cement.

Portland Basebed is a poorly connected heterogeneous carbonate. It has a wide pore size distribution characterized [Figure 5.8] by a few fast flow regions and abundant regions of stagnant flow as seen in the velocity distributions [Figure 5.9].

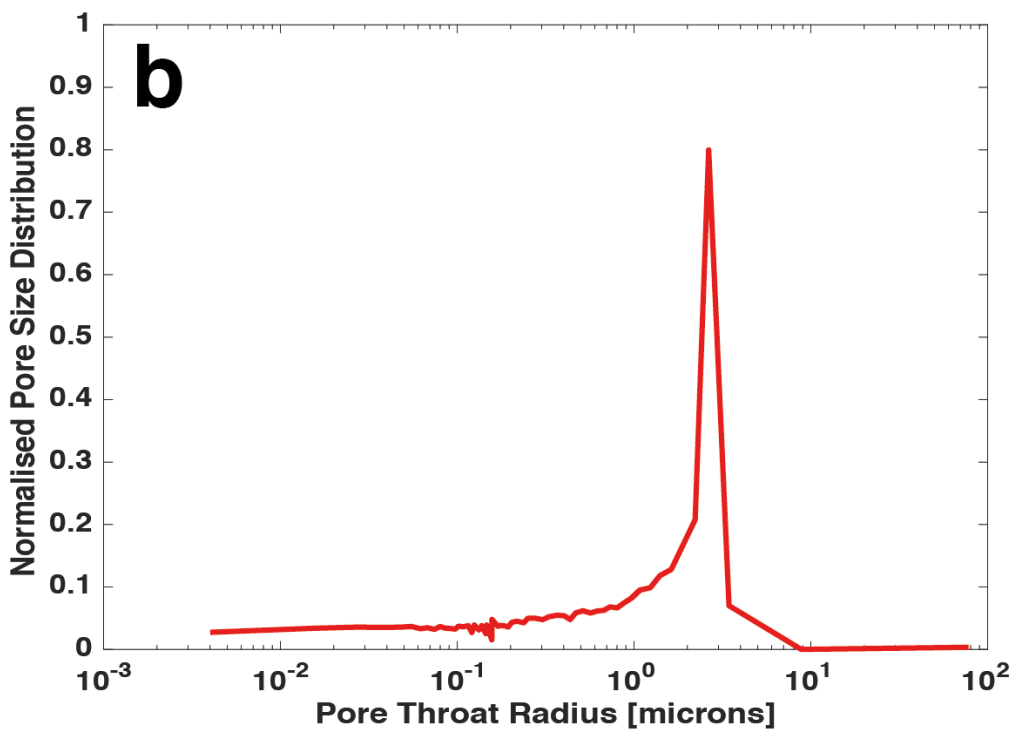
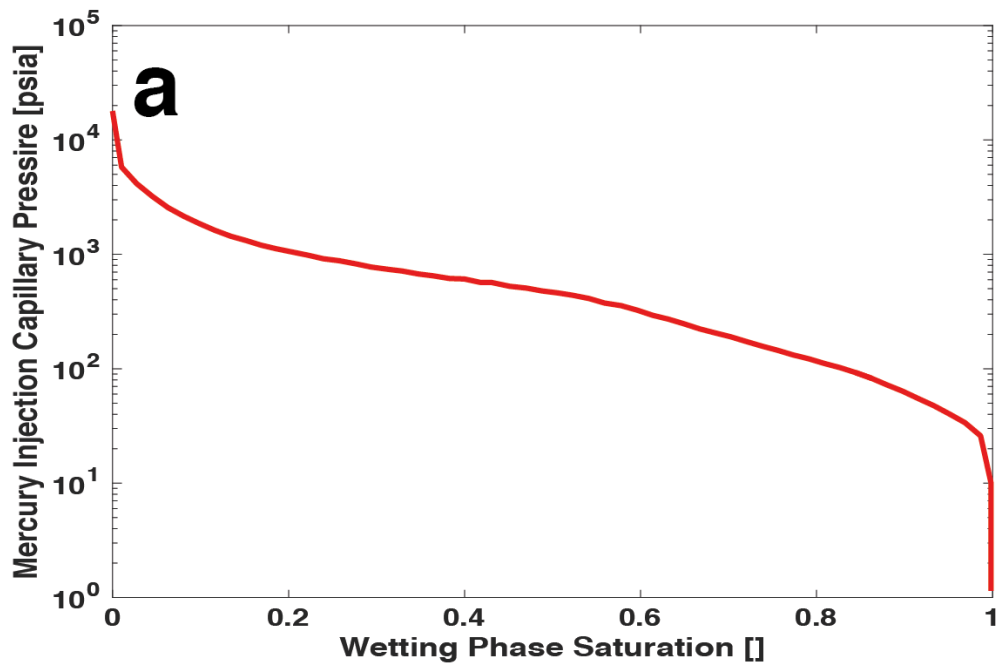


Figure 5.10 The MICP (a) and Pore Throat Radii distributions (b) for Portland Base bed showing a single well-defined population preceded by a long tail. Data taken from [62].

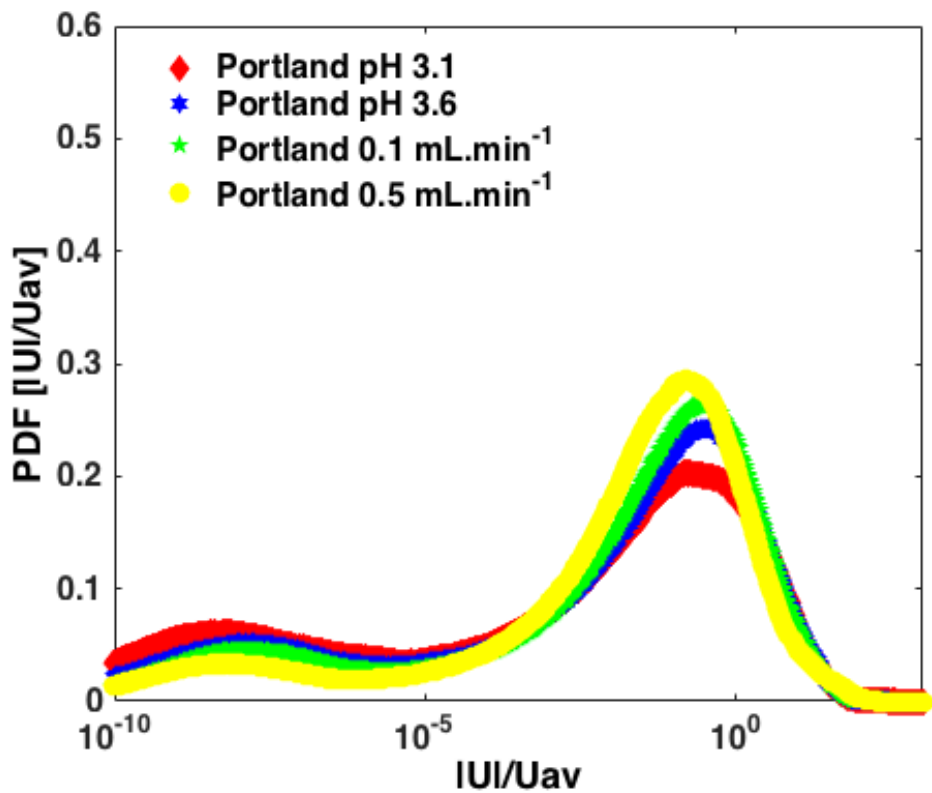


Figure 5.11 Probability density functions (PDFs) of pore voxel velocity in Portland Base bed calculated on all dry μ -CT images of Portland used in this thesis. All samples show a large range of velocities spanning 10 orders of magnitude with a two overlapping populations.

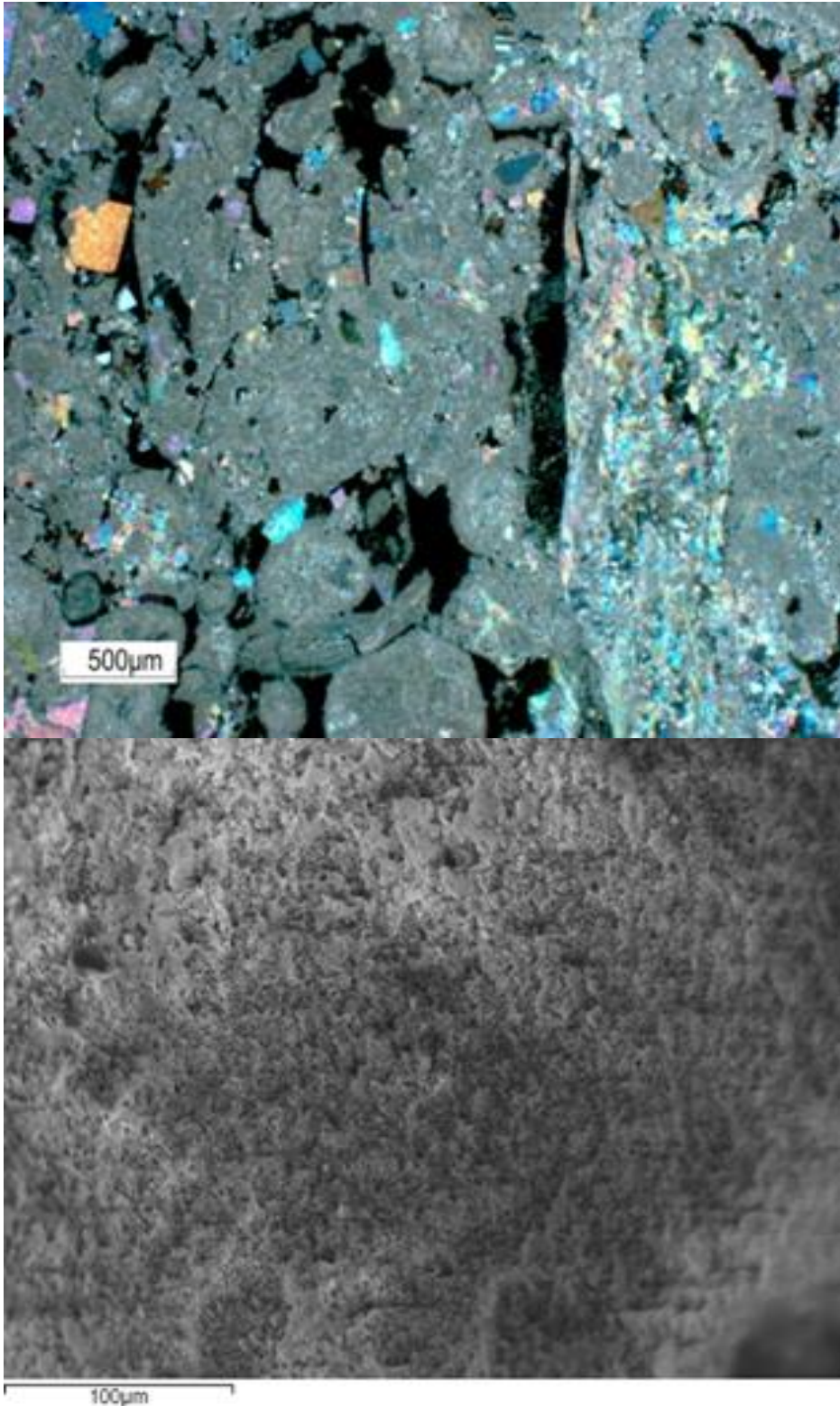


Figure 5.12 Microporous calcite grains in Portland limestone imaged using thin section (top) and SEM (bottom). Figure taken with permission from the Qatar Carbonates and Carbon Storage Research Centre (QCCSRC) image library.

5.4 Rock summary table

Table 5.1 Summary of physical rock properties. Chemical composition was found using X-ray diffraction.

	<u>Ketton</u>	<u>Estailades</u>	<u>Portland Basebed</u>
Rock type	Limestone	Limestone	Limestone
Origin	Ketton, Rutland, UK	Oppede, France	Portland, UK
Age	169-176 million Years	22 million years	150-190 million years
Bulk-measured total porosity ϕ_T []	0.2337	0.295	0.213
Bulk-measured absolute permeability [m²]	2.81×10^{-12}	1.490×10^{-12}	5.24×10^{-15}
Image-calculated permeability range [m²]	4.81×10^{-13} - 1.66×10^{-11}	1.53×10^{-14} - 1.57×10^{-13}	2.67×10^{-14} - 1.25×10^{-16}
Image-calculated porosity range ϕ_{CT} []	0.110 – 0.172	0.102 – 0.140	0.060 – 0.101
% Calcite	99.1	97.2	97.9
% Quartz	0.9	2.8	2.1
% Clay	0	0	0
% Feldspar	0	0	0

6 Reactive Flow Imaging

In this section we will describe the results of three sets of reactive flow imaging experiments.

- 1) Laboratory *in situ* dynamic imaging of reaction in a homogeneous carbonate (section 6.1).
- 2) Fast synchrotron *in situ* dynamic imaging of reaction in two heterogeneous carbonates at multiple flow conditions (section 6.2).
- 3) Laboratory *in situ* dynamic imaging of reaction in three carbonates at multiple reactive conditions (section 6.3).

6.1 Imaging Ketton dissolution using a laboratory Source

The first experiment was designed to test the methodology described in section 4. We examined dissolution in an easily imaged homogeneous rock dynamically at reservoir conditions using a laboratory μ -CT. These results are published in Menke et al. [215].

Reactions at the fluid-rock interface play a large role in many of the processes associated with fluid flow in porous media, including diagenesis, contaminant transport, and well acidization [216-218]. The focus of this paper is on reaction in carbon capture and storage (CCS), where a major concern is long-term storage security [219, 220]. The injected carbon dioxide, CO₂, will dissolve in the host brine, forming an acidic solution [45, 95, 221]. This acid in turn may react with the host rock, causing dissolution, particularly in carbonates, and – over longer time-scales – precipitation of carbonate [56]. Dissolution may compromise the integrity of geologic seals, allowing CO₂ to escape to the surface, while precipitation leads to long-term storage security [222].

Understanding dissolution in the rock-brine system, and the magnitude and distribution of fluid movement within the reservoir, is therefore imperative for accurate predictive modelling [121, 122, 125, 223, 224]. However, the rate and nature of carbonate dissolution are dependent on both the intrinsic properties of the rock such as porosity, permeability, and pore-size distribution [130], as well as the properties of the brine [119, 174, 175, 209]. In particular, the dissolution rates are strong functions of fluid temperature and pressure, making it crucial to develop accurate experimental techniques capable of measuring complex time-dependent physical and chemical phenomena at representative reservoir conditions.

One key observation of reactive transport experiments is that the average effective reaction rates measured in the field are typically several orders of magnitude lower than implied from batch reactor laboratory measurements [139, 225]. Many reasons have been advanced to explain this, including mineral

heterogeneity, weathering, and incomplete mixing in a heterogeneous flow field. However, without direct observation of pore-scale reaction it is difficult to assess which of these effects is most significant. Thus, time resolved experiments are needed to provide both the insights into dynamic interplay between transport and reaction and to validate reactive transport models.

X-ray microtomography (μ -CT) is now an established experimental method for studying pore-scale processes for both petroleum and carbon storage applications [113, 158, 159]. μ -CT offers several advantages: it is non-invasive, achieves high spatial resolutions of down to around 1 μm , gives good contrast between fluid and solid phases, and provides three-dimensional images relatively quickly.

Imaging of dissolution in limestone rock was performed at the core ($\sim\text{cm}$) scale [108] where, for several rock types and flow regimes, it was found that reaction of the dissolved CO_2 with the solid matrix increases physical heterogeneity. Ellis et al. [154] used core scale imaging to show that exposure to CO_2 progressively reduced the sealing capacity of fractured claystone caprocks. Smith et al. [172] and Hao et al., [173] combined μ -CT and modelling of samples from the Weyburn Oil field in Saskatchewan, Canada. Multiple dolomitic cores were imaged before and after core flooding with CO_2 -saturated brine at 60°C and 12.4 MPa. The results were subsequently used to validate a continuum-scale reactive transport model. Additionally, Luquot & Gouze [174] and Gouze et al. [124] performed flow experiments with a CO_2 -rich brine on limestone reservoir samples at 100°C and 12 MPa. Samples were analysed with μ -CT prior to and after dissolution and changes in the permeability, porosity, tortuosity, and hydraulic radius were characterized according to dissolution regime. Noiriél et al. [179] used μ -CT to measure the three-dimensional changes in a limestone fracture at several points during acid dissolution at ambient conditions. Although these experiments have provided valuable information on pore-space geometry and flow, such as the porosity-permeability relationship, the analysis was limited to comparisons between pre- and post-reaction images of the rocks studied, some were not conducted at representative subsurface conditions, while others did not have the resolution required for pore-scale predictive modelling. Measuring dynamic reaction-induced changes in pore-space geometry, topology and flow in subsurface rock systems at reservoir temperatures and pressures furthers our understanding of how different transport and reaction conditions alter the complex solid and pore structures, and is the main goal of our study. Moreover, our aim is to provide a series of time-evolving X-ray image based datasets that can serve as a benchmark experimental study to calibrate pore-scale reactive transport models.

Studying in-situ reactive transport at reservoir conditions is challenging. Andrew et al. [168, 169] have designed an experimental apparatus to image pore-scale multi-phase displacement for the determination of residual saturation, contact angle, and interfacial curvature at elevated temperatures and pressures. These studies were performed at low flow rates and in the absence of chemical reaction to

isolate the impact of capillary forces. Since CO₂ dissolves in water creating acid, it is also of interest to examine the dynamic nature of chemical reaction between the acid and the host rock at elevated temperatures and pressures [226].

Therefore, in this study we examine reactive dissolution processes and focus on measuring the time-dependent reaction rate between the CO₂-acidified brine and limestone rock. We select this fluid/solid system since it is important in several environmental applications including subsurface contaminant transport, geological CO₂ storage, well acidization, and ocean acidification [110, 227, 228]. We perform dynamic *in situ* imaging of reaction between a CO₂-acidified brine and Ketton limestone at the pore scale at an initially fixed Péclet, Pe , and Damköhler, Da , numbers over a period of several hours and at a temperature and pressure representative of an aquifer at approximately 1 km depth. We then use pore-scale modelling methods on μ -CT images to characterize the evolving geometrical, topological and flow features, providing physical insights into the dynamics of dissolution, and specifically how to relate average effective reaction rates to pore-scale flow and transport.

6.1.1 Imaging strategy

We injected unbuffered CO₂-saturated brine at 0.5 mL.min⁻¹ through a 4-mm diameter, 1.2-cm long core of Ketton Oolite at reservoir conditions. 10 scans were taken over a period of 2.5 hours. The full experimental protocol is described in section 4.

We imaged dynamic changes in the fluid/solid interface during reaction between unbuffered CO₂-saturated brine and Ketton (see section 5.1). The images were taken at a 3.8 μ m spatial resolution with 400 projections. A 4 mm vertical section of the core was imaged, starting 2 mm away from the inlet. This location was chosen to avoid boundary effects. This 4 mm section will hereafter be referred to as the sample. The pressure drop across the sample was not measured because the sample field of view was much smaller than the overall core, and the pressure drops in any event were very small. In complex carbonate pore structures there is always a trade-off between the sample size and resolution, and we have designed the experiment to maximize the reactive transport information available from the experiment at the μ m to mm scale. Images were taken successively as fast as our scanner allowed, with \sim 15 minutes between the start of each scan [Figure 6.1]. The images are thus the time-averaged change over a single scanning period.

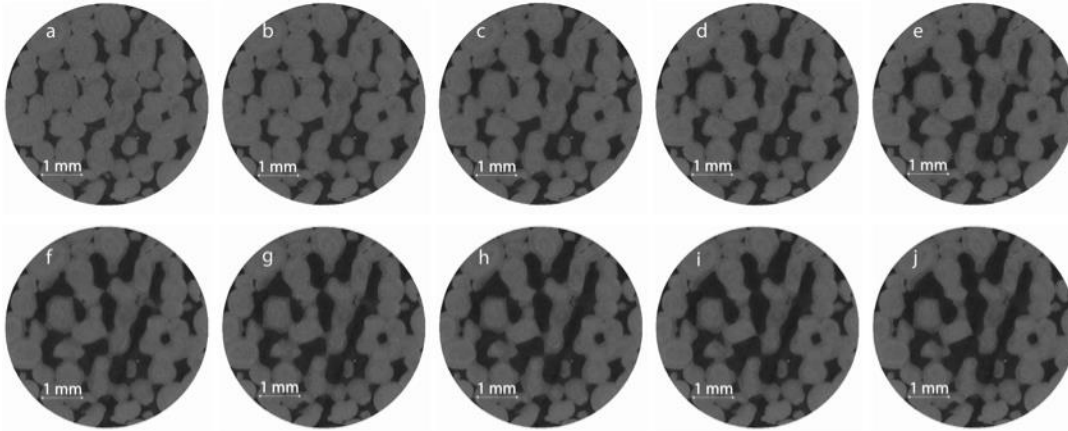


Figure 6.1 Filtered and registered horizontal slices of three-dimensional Ketton images taken in the centre of the image at time 0 (a), 17 (b) 33 (c), 50 (d), 67 (e), 83 (f), 100 (g), 116 (h), 133 (i) and 149 (j) minutes. The carbonate (grey) is shown being dissolved by the brine (black) as time progresses.

6.1.2 Image processing

We then reconstructed, filtered, and segmented the images to generate a binarized representation of the pore space. Raw reconstructed images were filtered using the non-local means edge-preserving filter [199, 200] and segmented them with a watershed algorithm in Avizo Fire 8.0 (www.vsg3d.com) using the greyscale gradient magnitude and a user-defined seed. Seed values were the same for each successive time step to avoid segmentation bias. We then used the separate objects module (discussed in section 4) in Avizo 8.1 to separate different grains within the segmented image and measure the change in grain size.

6.1.3 Results and discussion

Figure 6.2a depicts the porosity averaged over each two-dimensional slice of the image along the main flow direction as a function of time; Figure 6.2b shows corresponding change in porosity for each slice. Porosity is determined by the ratio of the number of ‘pore voxels’ to total voxels in the segmented slices. Figure 6.2b shows that a change in porosity occurs throughout the sample, which eliminates the possibility of face dissolution as the dominant dissolution regime for which the change would occur only at the inlet. The imaged-based average porosity increases from 17 to 32%, as seen in Figure 6.2b; we see no significant difference in dissolution rate over the length of the sample.

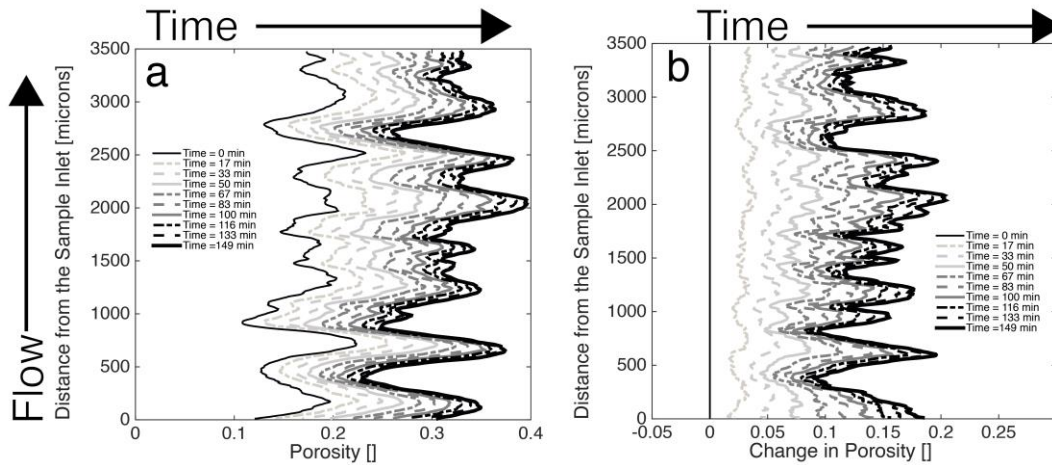


Figure 6.2 The porosity (a) and change in porosity (b) is averaged across each slice perpendicular to the flow direction and shown as a function of time. As the rock dissolves, the porosity increases.

We initially see a rapid increase in porosity, which slows with time; similarly we see a fast increase in the surface area to volume ratio, followed by a more gradual decline at later times, Figure 6.3a. Small fluctuations in the porosity change could be due to depositional layering. It also possible that the slowing could be due to the preferential dissolution of cement between grains, rather than the grains themselves (see Figure 6.4) or simply because dissolution forms new flow paths, resulting in an increasingly heterogeneous flow field, with diffusive transport further limiting the average effective reaction rate.

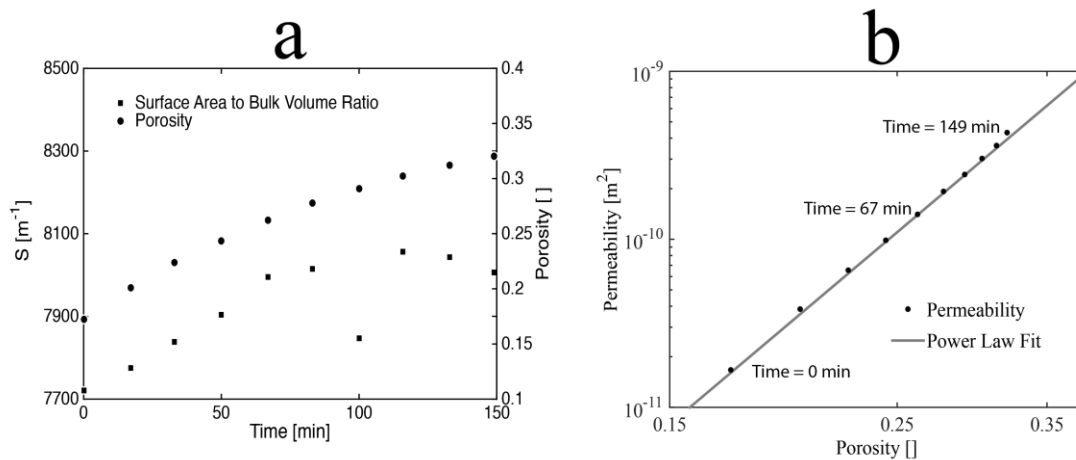


Figure 6.3 Surface area to the bulk volume ratio (squares) and the imaged-averaged porosity (crosses) as a function of time measured on 10 time-evolving μ -CT images (a). Image 7 (at 100 minutes) was of poor quality due to X-ray source fluctuations, which may explain why the measured specific surface area is lower than the general trend. Permeability plotted as a function of porosity through time (b). A power-law

relationship with the equation $K = 1.4 \times 10^{-7} \phi^{5.16}$ is seen between porosity and permeability as dissolution progresses.

We calculate Pe , Da , Pe , and r_{eff} according to the methods presented below.

Transport conditions are often characterised by the ratio of advective to diffusive rates (or the ratio of diffusive to advective time scales) with the Péclet number Pe [-] defined as:

$$Pe = \frac{\text{advection rate}}{\text{diffusion rate}} = \frac{U_{av} L}{D} \quad (6.1)$$

where U_{av} [m.s⁻¹] is the average pore velocity, L [m] is the characteristic length and D [m.s⁻¹] is the molecular diffusion coefficient.

Porosity is defined as the ratio of the volume of void space, V_{void} , to total volume V_B :

$$\phi_{Total} = \frac{V_{void}}{V_B} \quad (6.2)$$

At the pore scale, the average pore velocity can be calculated from the image measured macro-porosity ϕ_{CT} , and the Darcy velocity q :

$$U_{av} = \frac{q}{\phi_{CT}} \quad (6.3)$$

The characteristic length, L , is defined from Mostaghimi et al. [161]. In a porous medium it is often impossible to separate individual grains to derive a traditional characteristic length from a grain diameter. Thus, the pore structure is considered to correspond to a cubic packing of regular spherical grains and L becomes:

$$L = \frac{\pi}{S} \quad (6.4)$$

where the specific surface area, S [m⁻¹] is:

$$S = \frac{A_S}{V_B} \quad (6.5)$$

The pore-scale macroscopic surface area A_S [m²] can be computed on each image by adding the number of voxel faces separating void (pore) from grain or

estimated by similar geometric methods [145, 165, 229, 230]. However, this surface area is only the surface area measurable at the resolution of μ -CT image because the μ -CT cannot fully resolve surface roughness down to the molecular scale [231] and different methods of surface area measurement lead to different estimates [232] because μ -CT resolution is insufficient to capture the complete feature geometries. Therefore measuring surface area at the resolution of μ -CT is most useful when comparing surface area measurements in the same sample during dynamic processes. Moreover, it is beneficial to couple image-measured surface area with more precise surface area measurement methods to generate a greater understanding of the macro and micro porosity of a rock sample.

The BET surface area (A_{BET}) is a traditional experimental measurement method whereby nitrogen gas adsorption is measured at incremental pressures to derive total specific surface area. Using the determination from Andrew et al. [168] we can resolve the intra-granular (micro) porosity of a porous medium:

$$\phi_{Total} = \phi_{grain}[1 - \phi_{CT}] + \phi_{CT} \quad (6.6)$$

where ϕ_{grain} is the micro porosity and ϕ_{total} is the total sample porosity. This determination can then be used to find the total BET measured specific surface area S_{BET} :

$$S_{BET} = \rho_{rock}[1 - \phi_{Total}] A_{BET} \quad (6.7)$$

where ρ_{rock} is the rock density [kg.m⁻³]. The specific surface area, measured at the resolution of the μ -CT scan, is often orders of magnitude smaller than the molecular-level BET measured value; the large difference is due to the inclusion of the area of the micro-porosity in the BET measurement.

Reactive conditions in relation to advection are characterised by the Damköhler number Da [-] defined as:

$$Da = \frac{\text{reaction rate}}{\text{advection rate}} = \frac{kL}{U_{av}} \quad (6.8)$$

where k is a reaction rate constant [s⁻¹]. Physically this represents the ratio of the time for advection to the time for reaction over a characteristic length L . We interpret the reaction time to be the time taken to dissolve a section of the rock of length L . If we assume that the rock is pure then an estimate of the reaction rate constant is:

$$k = \frac{rS}{n} = \frac{\rho r}{nL} \quad (6.9)$$

where n is the number of moles of calcite per unit volume of rock. n is calculated using:

$$n = \frac{\rho_{rock}[1 - \phi_{Total}]}{M_{rock}} \quad (6.10)$$

where M_{rock} is the molecular mass of the rock. We can therefore write the Damköhler number as:

$$Da = \frac{\pi r}{U_{av} n} \quad (6.11)$$

Both the Damköhler and Péclet numbers are dependent on an advective term, therefore it is often useful to multiply them together to create the Damköhler-Péclet number that is dependent only on reaction and diffusion. The Péclet-Damköhler number $PeDa$ [-] defined as:

$$PeDa = \frac{\text{advection rate}}{\text{diffusion rate}} \frac{\text{reaction rate}}{\text{advection rate}} = \frac{\text{reaction rate}}{\text{diffusion rate}} = \frac{L\pi r}{Dn} \quad (6.12)$$

Using the specific surface area from the μ -CT scan, the characteristic length $L = 407 \mu\text{m}$ with $Pe = 2100$ at the start of the experiment; at the end $L = 392 \mu\text{m}$ and $Pe = 1100$. The high Pe number means that, on average, advection occurs much faster than diffusion at the pore scale, providing fresh reactant throughout the core.

Our estimated Da increases from approximately 3.3×10^{-5} to 7.6×10^{-5} during the experiment (U_{av} decreases as the porosity increases for a fixed Darcy flow rate) – however, it is always much less than 1. This represents the conditions at which reaction rate is slow compared to the advection rate and is thus representative of the uniform dissolution regime [108]. We only see significant dissolution once several hundreds of pore volumes have been injected, consistent with the low value of Damköhler number. In total, ~ 2000 pore volumes were injected through the core in our experiment.

Over the scale of a characteristic length, the advective time is smaller than the diffusive time ($Pe \gg 1$), while the ratio of reaction rate to diffusion $PeDa$ increases slightly from 7.0×10^{-2} to 8.2×10^{-2} during the experiments. This implies that at the pore scale, reaction is still slow compared to diffusion. However, as we discuss later, diffusion may limit the average effective reaction rate through delaying the transport of reactants to and from the solid surface.

To derive a pore scale effective reaction rate for μ -CT images we assume that chemical conditions inside the rock are relatively constant such that fresh reactant is continuously provided. It is then possible to estimate the reaction rate from the

change in porosity during an experiment. We calculate an average effective reaction rate, r_{eff} :

$$r_{eff} = \frac{\rho_{rock}(1 - \phi_{grain}) \Delta\phi_{CT}}{M_{rock} S \Delta t} \quad (6.13)$$

As discussed in the results, pore-scale average effective reaction rates tend to be orders of magnitude lower than either the batch measured reaction rates or field scale reaction rates due to diffusion-limited transport of reactants to or away from the surface in stagnant regions of the pore-space where the local Péclet number is low.

Initially $r_{eff} = 8.8 \times 10^{-5} \text{ mol.m}^{-2}\text{s}^{-1}$ (measured between scans 1 and 2), which decreases to $2.3 \times 10^{-5} \text{ mol.m}^{-2}\text{s}^{-1}$ (measured between scans 9 and 10) by the end of the experiment. The average reaction rate over the life of the experiment is $5.0 \times 10^{-5} \text{ mol.m}^{-2}\text{s}^{-1}$. This reaction rate is approximately 16 times lower than the laboratory-measured batch reaction rate of $8.1 \times 10^{-4} \text{ mol.m}^{-2}\text{s}^{-1}$ measured at the same temperature and pressure and at the injection pH of 3.1 the equilibrated fluids as measured by Peng et al. [52].

Lai et al. [233] measured a BET surface area (A_{BET}) value of $2.5 \times 10^3 \text{ m}^2.\text{kg}^{-1}$ on a similar Ketton core before reaction. The specific surface area, measured at the resolution of the μ -CT scan is approximately 650 times smaller than the molecular-level BET measured value; the large difference is due to the inclusion of the area of the micro-porosity in the BET measurement and because the μ -CT cannot fully resolve surface roughness down to the molecular scale. Had instead we used the BET-measured surface area to define r_{eff} , our average effective reaction rate would be around four orders of magnitude lower than the batch reactor value. It is evident from the constant greyscale in the grains (even as they shrink) that there is no discernable reaction in the micro-porosity and so it is inappropriate to use the BET area. However, even at a pore-scale resolution of $3.8 \mu\text{m}$, the effective surface area for reaction is considerably lower than that measured using the μ -CT scan. As discussed further below, we suggest that this is caused by diffusion-limited transport of reactants to and away from the surface in relatively stagnant regions of the pore space where the local Péclet number is low. It should be noted that, although we did not analyse the effluent, some fine particle movement could be present [120, 166] that would further decrease the measured reaction rate.

The grain size distribution over the course of the experiment is studied to test how dissolution affects characteristic length – this is presented in Figure 6.4. The grain diameter is calculated by performing a watershed segmentation of the three-dimensional distance map of the pore space using the separate object module in Aviso 8. Features with a diameter smaller than $100 \mu\text{m}$ are not included in the analysis because this method of segmentation is less accurate with very small objects, which are unlikely to be whole grains of Ketton. We see that for large grains the

average grain diameter decreases in size from 650 μm to 500 μm [Figure 6.4a] implying dissolution. Note that the grain diameter is similar to the characteristic length used to define Pe , which decreases from around 410 to 390 μm during the experiment. Additionally, we see that there is no discernable difference in the change in grain diameter over the length of the sample (each section changes by approximately 10%) confirming that – at the core scale – dissolution is uniform [Figure 6.4b-d].

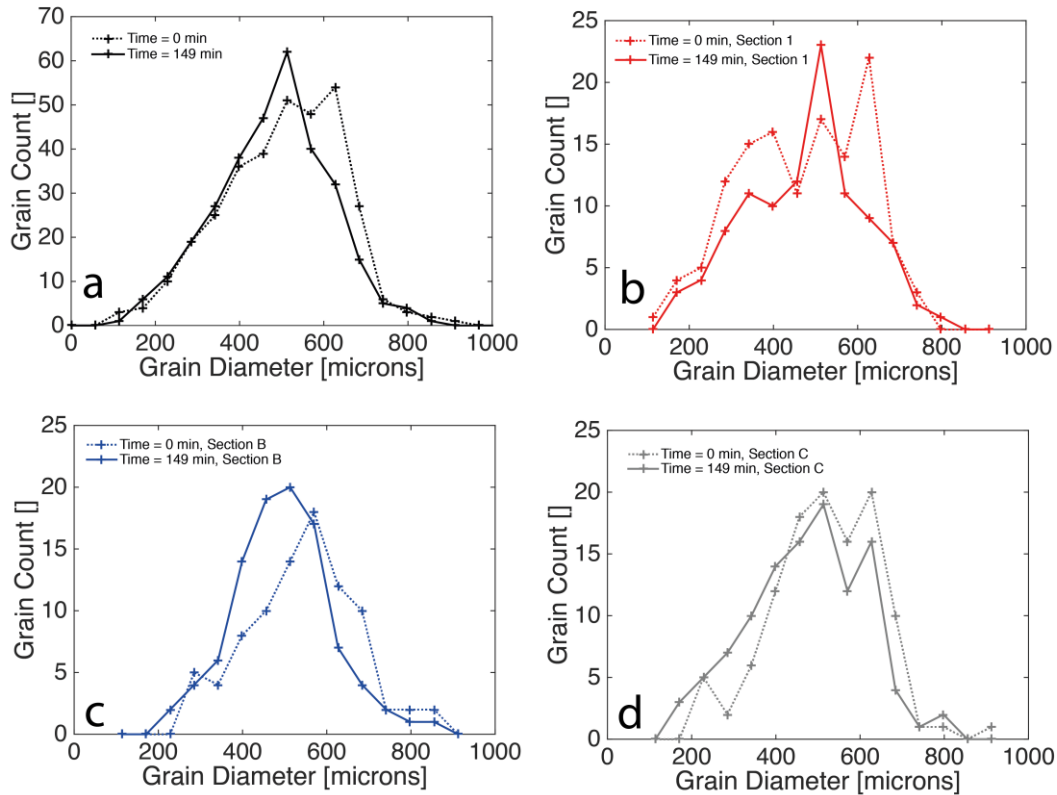


Figure 6.4 (a) The Ketton grain size frequency histogram shown at the beginning and at the end of the experiment. (b-d) The same histogram but for three 1.3 mm sections in the direction of flow.

Figure 6.5 depicts the pore-networks extracted from the images acquired at time 0 (a), 67 (b), and 149 (c) minutes. The pore size and throat diameter all increase with time, while the total number of pores and throats decreases [Table 6.1]. The coordination number (representing the connectivity) increases slightly.

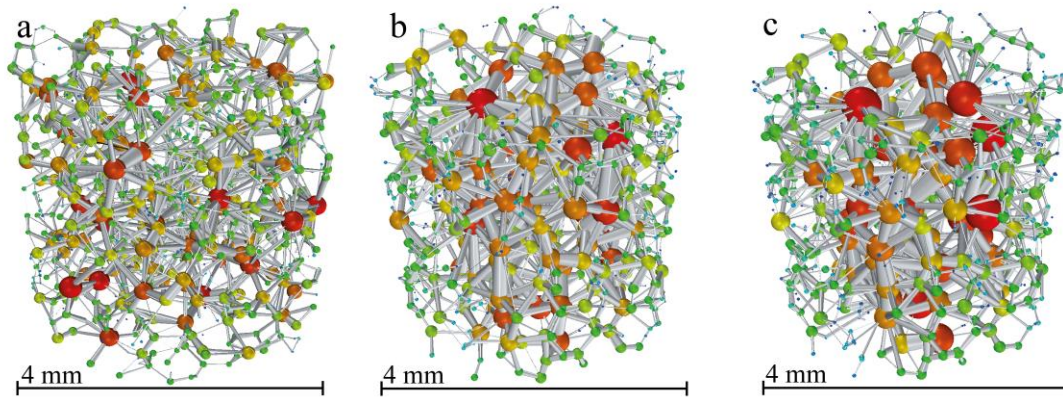


Figure 6.5 Network representations of Ketton carbonate (extracted from μ -CT images) depicted at time 0 (a), 67 (b), and 149 (c) minutes. The spheres are pores, where the smallest pores are green, the largest are red, and the pore throats are grey.

Table 6.1 Network properties and computed flow and reaction parameters for times 0, 67, and 149 minutes for section 6.1.			
Dissolution time [min]	0	67	149
Number of pores	1143	867	817
Number of throats	2229	1803	1729
Average pore radius [m] (volume-weighted)	8.1×10^{-5}	1.2×10^{-4}	1.4×10^{-4}
Average throat radius [m] (volume-weighted)	3.5×10^{-5}	5.7×10^{-5}	6.9×10^{-5}
Pore-throat contraction ratio	0.52	0.52	0.50
Average coordination number	3.8	4.0	4.1
Absolute permeability (direct simulation) [m ²]	1.66×10^{-11}	1.41×10^{-10}	4.33×10^{-10}
Image measured porosity ϕ []	0.172	0.262	0.320
Image measured specific surface area S [m ⁻¹]	7.72×10^3	8.00×10^3	8.01×10^3
Calculated L [m]	4.07×10^{-4}	3.92×10^{-4}	3.92×10^{-4}
Calculated Pe [] [Equation 6.1]	2100	1300	1050
Calculated Da [] using batch reaction rate [Equation 6.11]	3.3×10^{-5}	5.7×10^{-5}	7.6×10^{-5}
Calculated $PeDa$ [] [Equation 6.12]	7.0×10^{-2}	7.6×10^{-2}	8.2×10^{-2}
Calculated reaction rate [mol.m ⁻² .s ⁻¹] [Equation 6.13]	8.8×10^{-5}	4.6×10^{-5}	2.3×10^{-5}

We simulated flow directly on the voxels of the segmented images to quantify changes in porosity, permeability, and the flow field. From Figure 6.3b we see an increase in porosity and permeability at each measured time as the reaction progresses. Permeability increases by almost 1.5 orders of magnitude due to dissolution, which makes the pores larger and better connected [Table 6.1]. The relationship between permeability and porosity can be fitted to a power law with an equation of $K = 1.4 \times 10^{-7} \phi^{5.16}$. We observe that the permeability increases with no stepwise jumps that would be expected in the wormhole regime at the times when a wormhole breaks through the outlet [62]; this, together with the earlier observation eliminating face dissolution (which would give more dissolution at the entrance of the sample), leads us to infer that we observe the uniform dissolution regime.

In Figure 6.6a-b we assess the changes in velocity in fast flow channels by plotting the velocity fields in the pore voxels where advection is dominant for times 0 (a) and 149 (b) minutes. It can be observed in Figure 6.6a-b that, as the reaction evolves, the fast flow paths become less tortuous as a consequence of consumption of the spherically-shaped grains of Ketton and surrounding cement. The flow also tends to become concentrated through the centre of the core; this may be explained by the non-reactivity of the confining Viton sleeve driving flow towards the centre as the carbonate reacts and forms larger flow paths. However, there is still observable dissolution near the boundaries of the core.

The distribution of flow speed for the first and last acquired image is shown in Figure 6.6c, as in the analysis by Bijeljic et al. [49, 162] in which the ratios of the magnitude of u at the voxel centres divided by the average pore velocity $U_{av}=q/\phi$ are presented. Note that the normalised average pore velocity decreases with time, since the porosity increases.

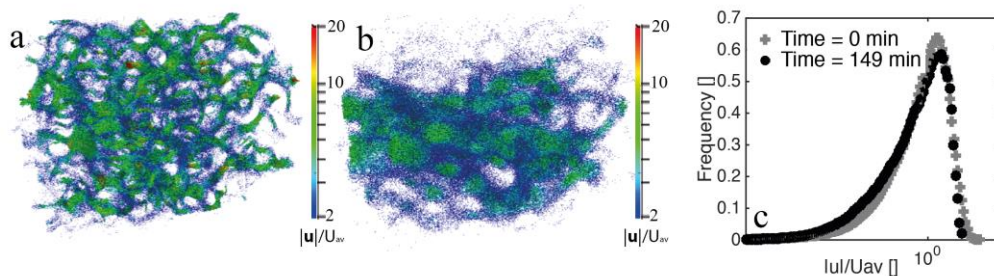


Figure 6.6 Normalized flow fields in Ketton are shown at times 0 (a) and 149 (b) minutes. The ratios of the magnitude of u at the voxel centres divided by the average pore velocity U_{av} are represented by cones (too small to be seen individually) that are

coloured using a logarithmic scale spanning from 2 to 20. Velocity histogram (c) sampled uniformly in 256 bins of $\log(|\mathbf{u}|/U_{av})$ which calculated as the ratios of the magnitude of u at the voxel centres divided by the average pore velocity U_{av} , for the images at times 0 and 149 minutes.

As suggested by Figure 6.6a-b, the fast flow paths become more uniform; this is demonstrated in Figure 6.6c, which shows that the spread in velocity distribution for the fastest voxels ($|\mathbf{u}|/U_{av}>1$) becomes narrower over time. However, the more significant finding is that the focussing of the flow paths leaves an increasing fraction of the pore space with much lower flow speeds: the tail of the velocity distribution becomes more spread. In these regions, at the micron scale, diffusion may limit the transport of reactants to and from the solid surface. As a consequence, the average effective reaction rate is lower than that seen in the batch reactor, with advectively well-mixed fluids. Furthermore, the spatial distribution of stagnant regions – for instance neighbouring fast channels – may be such to suppress transport to and from other portions of the pore space with faster flow speeds. As discussed above (see Table 6.1), this is a significant effect, with a decrease in the reaction rate by a factor of 3.8 during the experiment and an overall rate approximately sixteen times lower than measured in the batch reactor. Explicit reactive transport modelling in the pore space, which is beyond the scope of this work, is necessary to quantify the impact of transport limitations on reaction and to determine if this is indeed the reason for the low average effective reaction rates encountered in this system [234, 235].

6.1.4 Conclusions

Our approach allows us to integrate experimental *in situ* reactive transport measurements with corresponding modelling analysis on a voxel by voxel basis for scCO₂-brine-rock systems at elevated temperatures and pressures. We find an increase in porosity and permeability due to fluid/solid reaction that is more rapid at the initial stage of the experiment. Permeability increases with increasing porosity as a power law, with a flow field that shows a decrease in tortuosity and flow focusing of the fast flow channels. Analysis of the reaction-induced changes in the experimental porosity profiles and grain distribution indicate that at the flow conditions studied, Ketton dissolved predominantly in the uniform dissolution regime. Detailed analysis of the flow fields revealed that, as the fluid/solid reaction progresses, the flow becomes more focused in fast regions; a large fraction of the pore space then experiences lower flow speeds. We suggest that this leads to diffusion-limited transport of reactants to the surface and explains the 16-fold decrease in the average effective reaction rate compared to measurements in the batch reactor at the same conditions. This decrease uses the reaction rate for the injected pH: as we show later in section 6.3, the actual pH in the rock is higher.

This *in situ* experimental method for dynamic reservoir condition μ -CT imaging could be extended to study the impact of heterogeneity, flow rate, and reaction rate on the mechanisms controlling dissolution. The applications of this technique are far reaching in the petroleum, CCS, and subsurface hydrology areas

including subsurface contaminant transport [110], ocean acidification [227], and well acidization [228]. Moreover, the results from this study can serve as a benchmark for fluid/solid reaction (similar to Gramling et al. [107] for fluid/fluid reaction) in the verification of pore-scale reactive transport models [234] and elucidate potential scaling factors for resolving the discrepancy between laboratory and field reaction rates in continuum scale simulations.

6.2 Imaging Portland and Estailades dissolution using fast tomography

The second experiment was designed to adapt the methodology to fast synchrotron tomography to be able to image heterogeneous rocks extremely quickly. We examined dissolution in two complex heterogeneous rocks, Estailades and Portland Basebed, dynamically at reservoir conditions using the ‘pink beam’ of the I-13I beam line branch of Diamond Lightsource at multiple flow conditions. These results are published in Menke et al. [210].

This paper describes a method of studying dynamic reactive dissolution processes in rock with complex pore structures and with a focus on measuring the time and spatially dependent reaction rate between a CO₂-acidified brine and limestone rock at reservoir conditions. We observe a distinct dissolution regime, channelling, whose emergence is dependent on initial pore structure and flow conditions.

Several studies have investigated reaction in complex carbonates at the pore scale [62, 172, 173, 175, 179], but due to experimental or imaging constraints they have been either limited to pre and post reaction images, or were not completed at representative subsurface conditions. Menke, Bijeljic [215] performed dynamic *in situ* imaging of reaction between a CO₂-acidified brine and Ketton limestone at the pore scale over a period of several hours and at a temperature and pressure representative of an aquifer at approximately 1 km depth. However, Ketton is a relatively homogenous carbonate rock that is easy to image in very little time (~17 mins) with traditional μ -CT methods. Many carbonate rocks have complex pore structures that require more detail to accurately resolve, which can be a very time intensive process using traditional μ -CT, either with a monochromatic beam at a synchrotron source, or with bench-top x-ray scanners. Thus, a fast method of tomography is required to see dynamic reaction-induced changes in heterogeneous carbonates.

Fast synchrotron tomography has been previously used by Berg, Ott [176] to study image Haines jumps in two-phase flow, and by Andrew, Menke [177] to study the dynamic capillary pressure changes during a reservoir condition CO₂-brine drainage on the pore-scale. We present a method that uses fast synchrotron tomography to study the effect of initial pore structure and flow conditions on the dynamics of fluid/solid reaction in two highly heterogeneous rocks at reservoir conditions. The dynamic image sequence is first analysed for porosity changes and then used as inputs into flow simulations that can elucidate changes in permeability and pore-scale velocity fields. Additionally, effective reaction rates are calculated and the reactive flow dynamics is compared in terms of the initial structure and flow conditions, demonstrating both uniform and channelled dissolution structures.

6.2.1 Imaging strategy

Many carbonate rocks have complex pore structures that require many projections to accurately resolve, which can be a very time intensive process using traditional μ -CT, either with a monochromatic beam at a synchrotron source, or with bench-top x-ray scanners. Thus, a fast method of tomography is required to see dynamic reaction-induced changes in heterogeneous carbonates. The photon flux and energy of the x-ray source controls the image acquisition time of the sample. Use of the polychromatic beam of a synchrotron source is one method of scanning quickly [170, 176, 177]. This so-called ‘Pink Beam’ provides orders of magnitude more intense light than bench-top sources and images can therefore be taken on the tens-of-second rather than hour time scale.

We study the impact of initial pore structure and flow conditions on dissolution for two types of carbonate cores: Estailades and Portland Basebed [Table 6.2]. Reaction was imaged between calcite and unbuffered scCO_2 saturated brine using fast synchrotron tomography in 4mm-diameter 1.2cm-long carbonate cores. In experiments 1 and 2, we react an Estailades core at a low ($0.1 \text{ mL}\cdot\text{min}^{-1}$) and high ($0.5 \text{ mL}\cdot\text{min}^{-1}$) flow rate to gain insight into the impact of flow conditions. Then in experiments 3 and 4 we use the same high and low flow rates to react cores of Portland to investigate the impact of pore space heterogeneity. The full experimental protocol is described in section 4.

Using image analysis we first investigate changes in porosity and surface area. Then we input the images into a flow solver to study changes in permeability and velocity fields. Furthermore, we investigate the dynamic changes in the dimensionless numbers describing flow and reaction conditions and the effective reaction rates.

Table 6.2 Experimental Parameters for section 6.2.

Experiment Number	1	2	3	4
Rock type	Estailades Limestone	Estailades Limestone	Portland Basebed	Portland Basebed
Flow rate [mL/min]	0.1	0.5	0.1	0.5
Brine pH	3.1	3.1	3.1	3.1
Temperature [°C]	50	50	50	50
Pressure [MPa]	10	10	10	10
Number of Scans	51	83	71	94
Resolution [μm]	4.76	4.76	4.76	4.76
Projections	1000	1000	1000	1000

Estailades and Portland Basebed carbonates were fully scCO_2 saturated 1% KCl 5% NaCl brine was pulled through the core at flow rates of 0.1 and 0.5 mL/min at 50°C and 10MPa: these flow rates were maintained throughout the experiment. Tomographic scans were taken successively for 2 hours at the centre point of the core with a 5 mm by 4 mm field of view. The dynamic scans had 1000 projections each with an exposure time of 0.04s. Total acquisition time was ~45 seconds per scan with between 51 and 94 scans taken over a period of 2 hours. The time between

scans was controlled by the data read-off speed of the camera, which varied between experiments.

6.2.2 Image processing

The raw projections were reconstructed and artefacts were removed using the Diamond Lightsource proprietary python code. Each image consists of 2000^3 voxels, which were then binned to increase signal to noise resulting in an image of 1000^3 voxels at a resolution of 4.76 microns. The images were then cylindrically cropped to the core dimensions and converted to 16-bit from 32-bit to further decrease size using ImageJ (<http://imagej.nih.gov/ij/>). The images were then further processed using the image processing modules in Avizo 9.1 program (www.vsg.com).

The image processing workflow is presented for Portland carbonate in Figures 6.7a-f. First the raw images [Figure 6.7a-b] are filtered. The first scan in the series will hereafter be called the reference scan. All scans were registered to the reference scan and resampled. The resampled data was then subtracted from the reference scan to measure the change in the pore space as dissolution takes place [Figure 6.7c]. These 'difference images' were then filtered using non-local means to increase signal to noise [Figure 6.7d]. The reference scan and filtered difference images were then segmented using a watershed segmentation [196] [Figure 6.7e]. Finally, the segmented difference image was subtracted from the segmented reference scan to achieve segmented images for each time step [Figure 6.7].

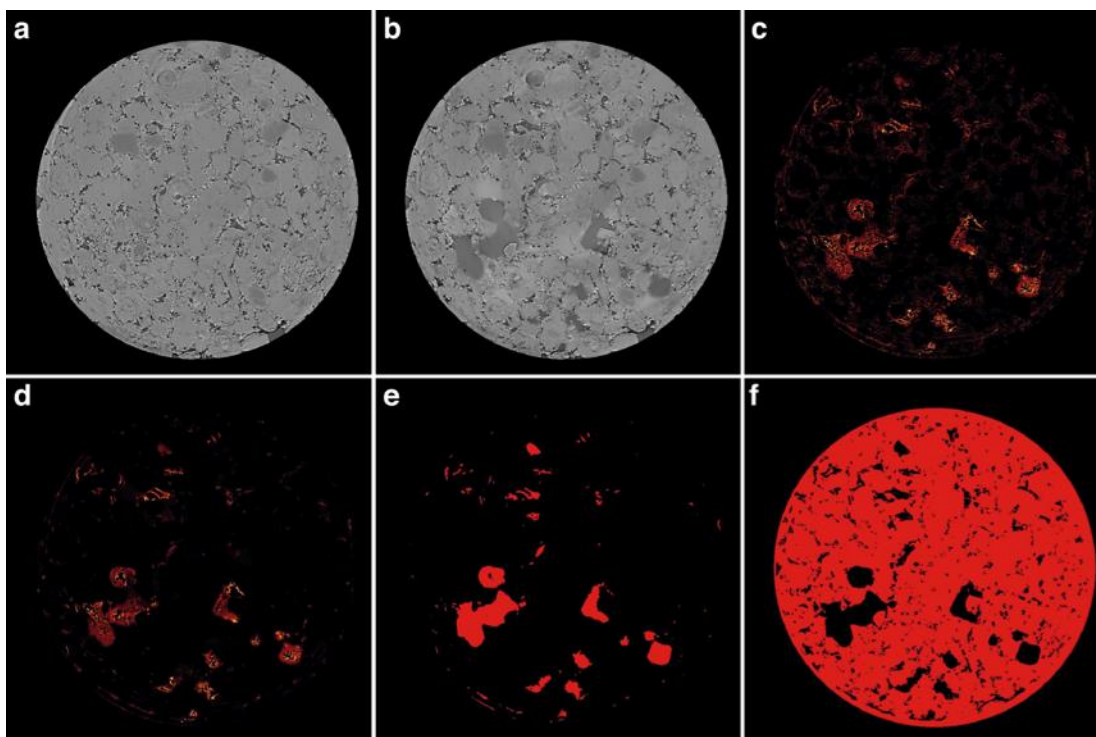


Figure 6.7 The image processing workflow is presented for Portland carbonate. The reference greyscale image (a), the reacted greyscale image (b), the difference image (c), the filtered difference image (d), the segmented difference image (e), and the final segmented image (f). The darker grey is pore while the lighter grey is rock.

6.2.3 Results and discussion

The segmented images were analysed as a time series for porosity changes by counting the number of voxels of pore and rock. During dissolution, porosity increased with time. Figure 3 depicts porosity averaged over each two-dimensional slice of the three-dimensional image along the axis of flow for each experiment at 30-minute intervals. In all four experiments porosity changed uniformly in the direction of flow. For experiment 1, the porosity also increased uniformly through time. However, in experiments 2, 3, and 4 the majority of the porosity increase occurred during the first 30 minutes with a slower rise at later times. Experiments 1 and 3 had a total increase in porosity of 6.6% and 5.5% respectively, which is smaller than the total porosity increase in the higher-rate experiments 2 and 4 (11.5% and 12.7%).

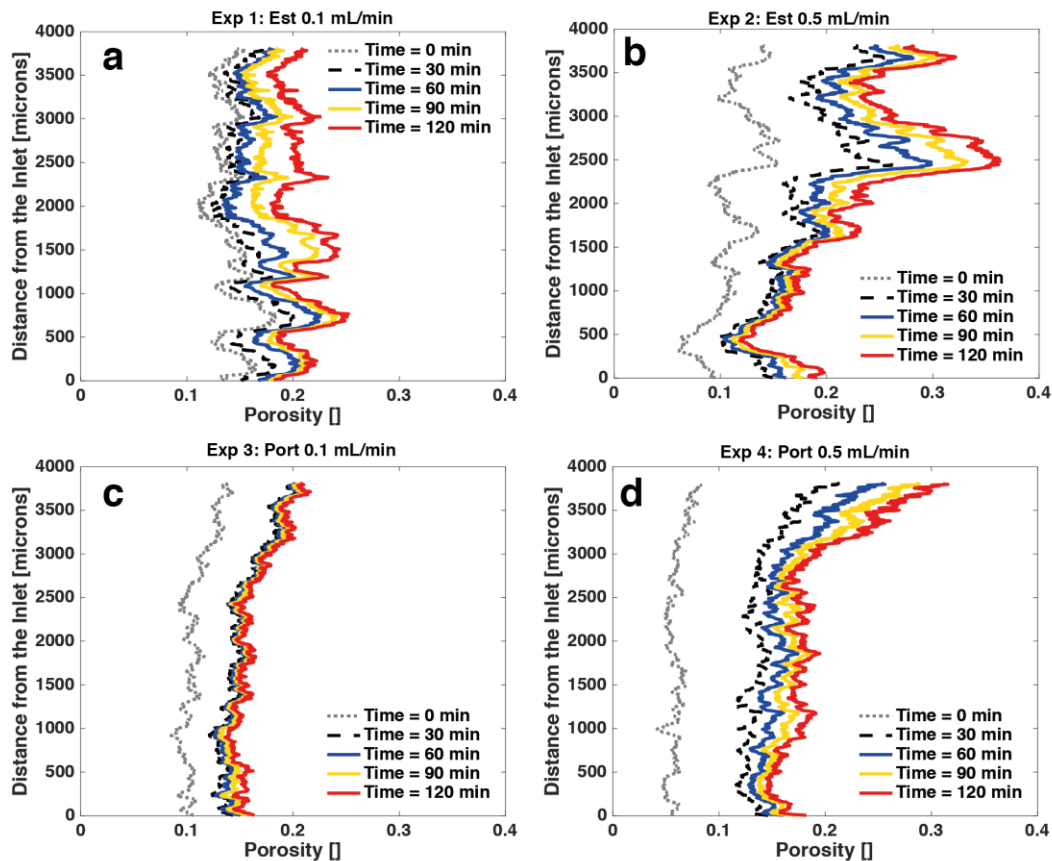


Figure 6.8 The sliced-averaged porosity versus distance from the sample inlet for Estailades at 0.1 mL.min⁻¹ (a) and 0.5 mL.min⁻¹ (b) and Portland at 0.1 mL.min⁻¹ (c) and 0.5 mL.min⁻¹ (d) for times 0, 30, 60, 90, and 120 min. The blue, yellow and red lines denote t = 0, 60, 90, and 120 minutes, respectively.

Permeability was calculated directly on the segmented images using a Navier-Stokes solver that computes voxel centre velocities. The permeability was found from the ratio between the total flow rate across the whole sample to the average pressure gradient multiplied by fluid viscosity, from Darcy's law.

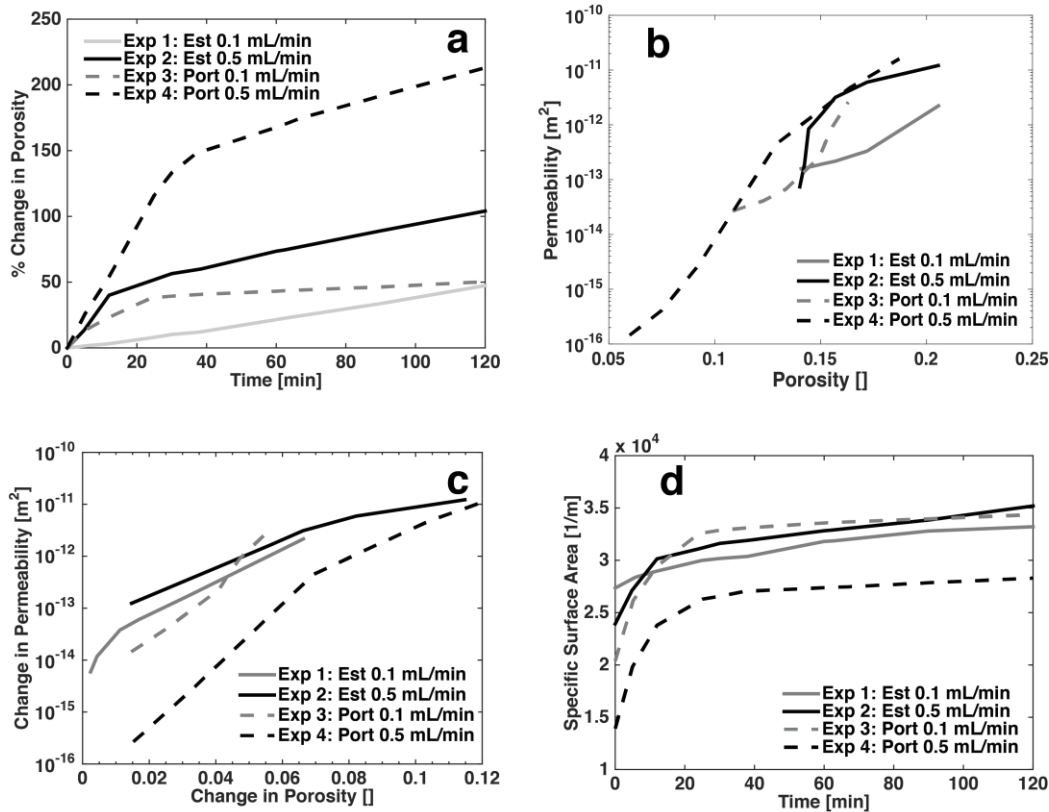


Figure 6.9 The percent change in average porosity across the whole sample versus time (a), porosity versus permeability (b), the change in porosity as a function of the change in permeability (c), and the specific surface area through time (d) of Estailades and Portland carbonates during dissolution. The porosity and surface area are calculated directly from the segmented images. Permeability is found from the computed flow field.

Figure 6.9 depicts the dynamic changes in porosity and permeability for Estailades and Portland carbonate images at flow rates of $0.1 \text{ mL}\cdot\text{min}^{-1}$ and $0.5 \text{ mL}\cdot\text{min}^{-1}$. The change in total image porosity is plotted as a function of time in Figure 6.9a. Experiment 1 had a steadily increasing porosity throughout the experiment. Experiments 2, 3, and 4 increased in porosity quickly at first and then more slowly, as evident from Figure 6.8.

Permeability increases rapidly as a function of porosity [Figure 6.9b]. The greatest change in permeability with porosity was in experiment 4, which had the highest flow rate and the lowest initial permeability [Figure 6.9c]. The low flow rate experiments 1 and 3 showed the least change in permeability with porosity, while experiment 2, which had a very high initial permeability had large changes in porosity with a smaller permeability increase. We fit the data to an empirical power-law relationship between porosity and permeability. The best fit to the Estailades experiments 1 and 2 were $K = 7 \times 10^{-8} \phi^{6.74}$ and $K = 1 \times 10^{-6} \phi^{7.52}$ respectively. For the Portland experiments 3 and 4 we found $K = 5 \times 10^{-4} \phi^{10.9}$ and $K = 1.9 \times 10^{-3} \phi^{11.0}$ respectively. The exponents, around 7 to 11, are larger than the value of approximately 5 observed for dissolution of a homogeneous limestone, Ketton [215] and much higher than a power of approximately 3 used in the Kozeny-Carman relation to predict the permeability of granular packings. This suggests that we see a very rapid rise in permeability with porosity for more heterogeneous samples.

The specific surface area, S , [Figure 6.9d], was computed on the images by adding the number of voxel faces separating grain from void. S is the surface area A_s [m²] divided by the bulk (total) volume. S showed an approximately linear increase with time for experiment 1, and a sharp initial increase for experiments 2, 3, and 4, with less change at later times. There was no clear trend with flow rate for experiments 3 and 4.

In Figure 6.10 we visualise the ratios of the magnitude of u at the voxel centres divided by the average pore velocity \bar{u} for Portland and Estailades carbonate images. U_{av} [m.s⁻¹] is calculated from the Darcy velocity q divided by the scan porosity ϕ_{CT} taken from the segmented image. The Darcy velocity is constant throughout each experiment: it is imposed by the flow rate of the pumps.

The flow fields developed preferential flow paths at early times in experiments 2, 3, and 4, which then widened later. In experiment 1 the pore space dissolved more uniformly with less evident preferential flow pathways, except possibly at the latest times.

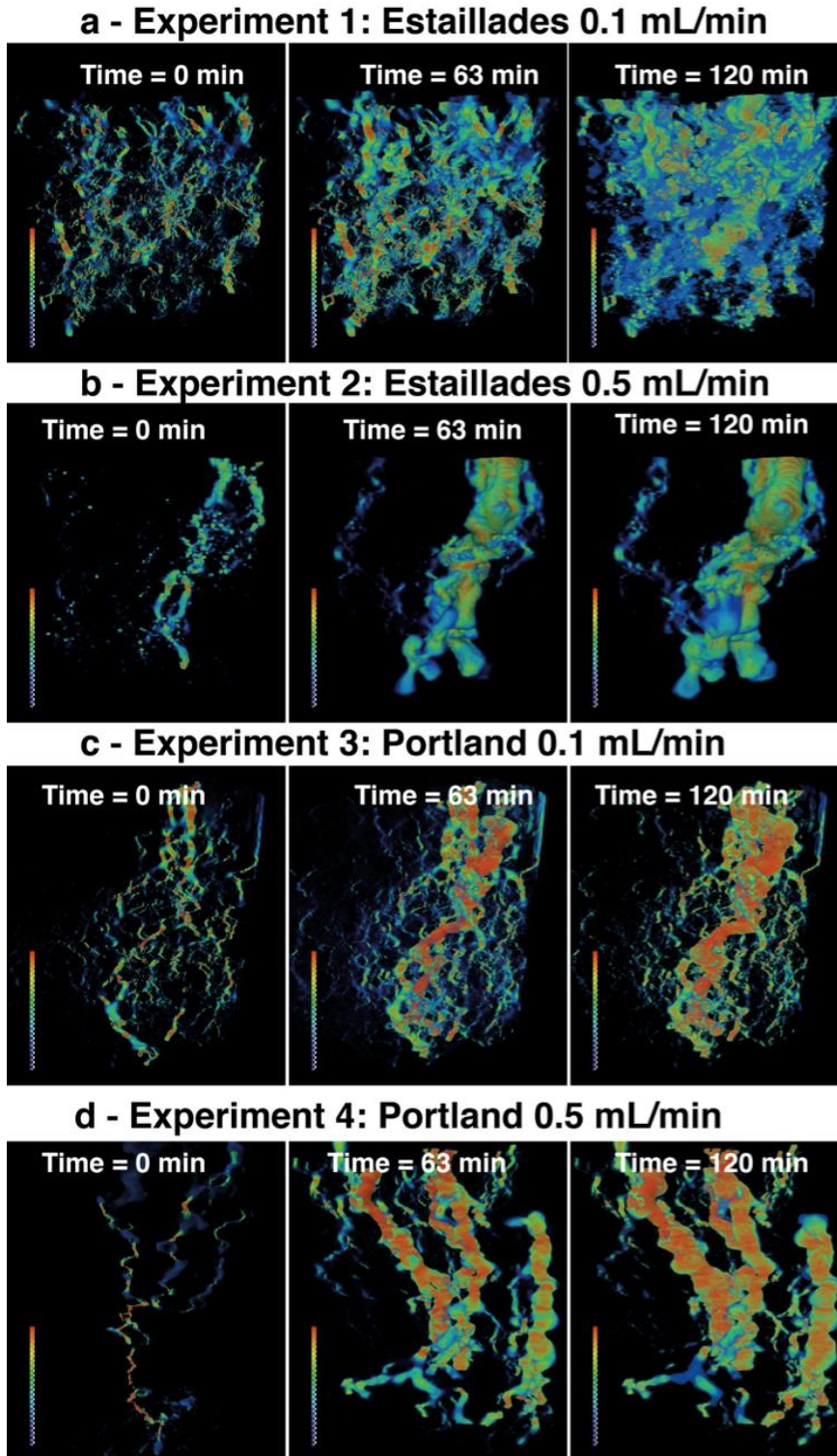


Figure 6.10 The ratios of the magnitude of u at the voxel centres divided by the average pore velocity U_{av} are coloured using a linear scale where low velocity is blue, medium velocity is yellow, and high velocity is red.

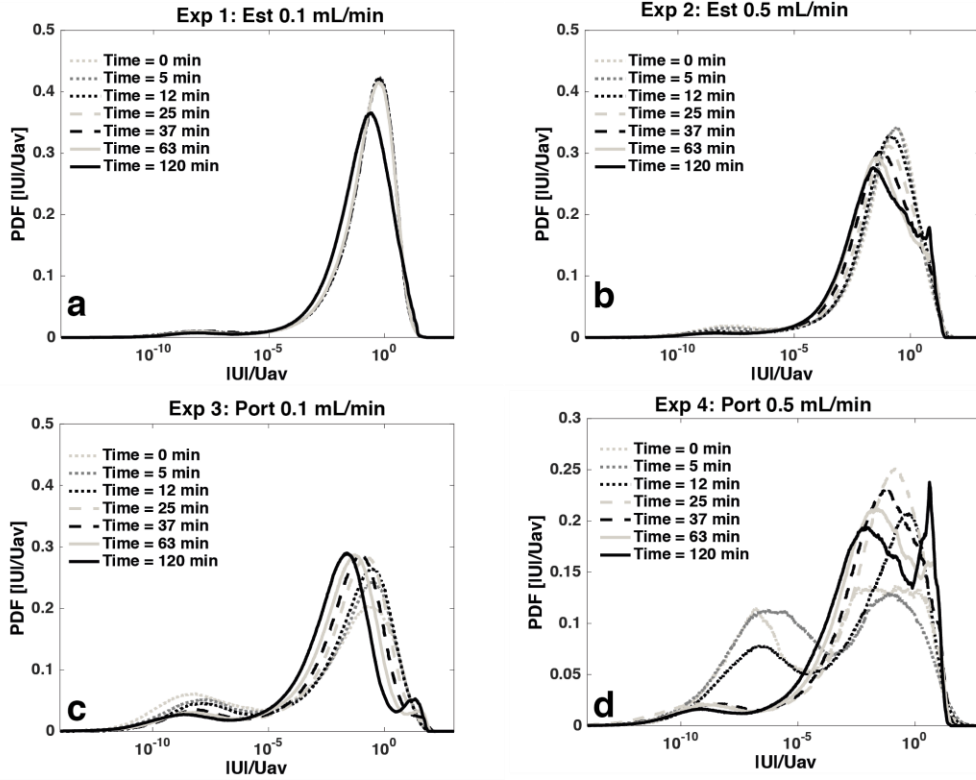


Figure 6.11 Probability density functions (PDFs) of pore voxel velocity during (a) experiment 1, (b) experiment 2, (c) experiment 3, and (d) experiment 4. The velocity histogram is computed on the pore-space images and sampled uniformly in 256 bins of $\log(|u|/U_{av})$, which are calculated as the ratios of the magnitude of u at the voxel centres divided by the average pore velocity U_{av} . The distributions are shown at times 0, 5, 12, 25, 37, 63, and 120 minutes.

The probability density functions of velocity, Figure 6.11, show a very wide range of flow speed, over around 8 orders of magnitude for Estailades and over 10 orders of magnitude for Portland. For Estailades there is no significant change in the distribution, normalized by the average velocity, over time, indicative of a relatively uniform dissolution. In contrast, in Portland, we initially observe a significant fraction of the pore space in stagnant regions; with flow velocities that are several orders of magnitude lower than the average [Figure 6.11c,d]. As dissolution proceeds, the flow becomes concentrated in fast flowing regions and the stagnant regions disappear. In experiment 4, the extra peaks at later times are due to competition between multiple preferential flow paths as seen in Figure 6.10d.

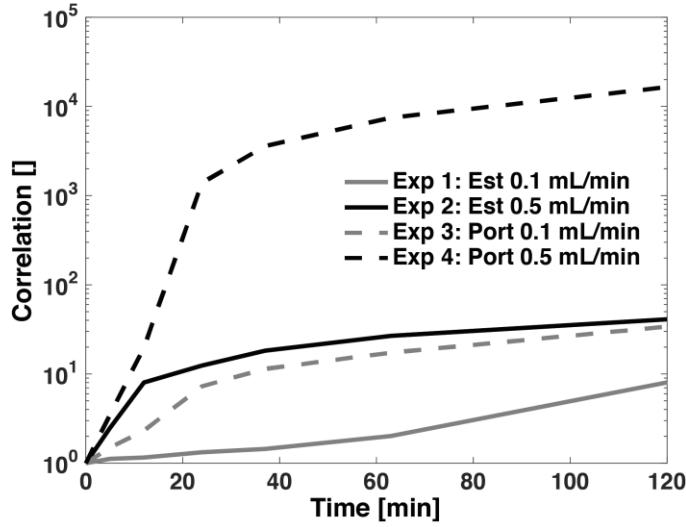


Figure 6.12 Normalized correlation, Eqs. (6.14) and (6.15), between the initial voxel velocities (time=0) and each those from successive image through time for each experiment.

Our hypothesis, discussed further below, is that in experiments 2, 3 and 4, the fast flow channels, present initially, dissolve more quickly than the stagnant regions. This causes channels to form through the pore space located in regions where the flow was initially fast. This is distinct from wormholing, since the reactant moves in advance of the channel formation. We test this quantitatively by studying the correlation of velocity in time. This is defined as:

$$C(t) = \frac{\sum_{i=1}^n v_i(0)v_i(t)}{n} - \frac{\sum_{i=1}^n v_i(0)}{n} \frac{\sum_{i=1}^n v_i(t)}{n} \quad (6.14)$$

with a normalized function:

$$\bar{C}(t) = \frac{C(t)}{C(0)} \quad (6.15)$$

where $v_i(t)$ is the velocity in voxel i at time t . The calculation is only performed on voxels that are void in the reference (initial) image at time $t=0$. $C(0)$ is the variance of the velocity initially. If dissolution proceeds randomly throughout the pore space, we would expect $C(t)$ to decline over time, as there is no correlation between the velocity in a particular voxel at time t and the same voxel originally. If the dissolution is uniform, expanding existing flow channels, then $C(t)$ may retain an approximately constant value, since we keep the same flow paths. However, if we form channels, then we see the largest flow speeds in those regions of the initial image that were flowing fastest. Since the channels focus the flow, $C(t)$ may increase over time, as the velocities located where there was void originally sample the high end of the velocity distribution.

Figure 6.12 shows the normalized correlation, Eq. (6.15). In all the experiments $C(t)$ increases with time, although there is a more marked initial rise for experiments 2, 3 and 4. We see an extraordinary one to four order-of-magnitude growth of the correlation function which provides compelling quantitative evidence that the channels which form, see Figure 6.10, are located in regions where the flow was initially fastest and where, as a consequence, dissolution was most rapid.

We use the definitions for Pe , Da , and r_{eff} defined in section 6.1. Using the flow rates established by the pumps and the surface area from the scans, the characteristic length L is between 115 μm and 226 μm for the four samples, while Pe has a value between 145 and 3040 at the start of the experiments [Table 6.3]. At high Péclet numbers, pore-scale advection is, on average, much faster than diffusion and fresh reactant is available throughout the core.

Table 6.3 Computed flow and reaction parameters for times 0, 63, and 120 min for section 6.2.

Time [min]	Property	Experiment 1: Estallades 0.1 [mL/min]	Experiment 2: Estallades 0.5 [mL/min]	Experiment 3: Portland 0.1 [mL/min]	Experiment 4: Portland 0.5 [mL/min]
0					
	absolute permeability (direct simulation) [m ²]	1.57×10^{-13}	6.90×10^{-14}	2.67×10^{-14}	1.45×10^{-16}
	image measured porosity ϕ []	0.140	0.110	0.101	0.060
	image measured specific surface area S [m ⁻¹]	2.73×10^4	2.39×10^4	2.04×10^4	1.40×10^4
	calculated L [m]	1.15×10^{-4}	1.31×10^{-4}	1.54×10^{-4}	2.26×10^{-4}
	calculated Pe [] [eq 6.1]	1.45×10^2	1.05×10^3	2.52×10^2	3.34×10^3
	calculated Da [] using batch reaction rate [eq 6.11]	1.41×10^{-4}	2.19×10^{-5}	9.78×10^{-5}	1.07×10^{-5}
	calculated PeDa []	2.04×10^{-2}	2.31×10^{-2}	2.46×10^{-2}	3.58×10^{-2}
	calculated reaction rate r_{eff} [mol.m ⁻² s ⁻¹] [eq 6.13]	5.35×10^{-6}	4.08×10^{-5}	4.32×10^{-5}	5.65×10^{-5}
63					
	absolute permeability (direct simulation) [m ²]	3.31×10^{-13}	6.00×10^{-12}	9.44×10^{-13}	4.88×10^{-12}
	image measured porosity ϕ []	0.172	0.193	0.156	0.164
	image measured specific surface area S [m ⁻¹]	3.19×10^4	3.29×10^4	3.36×10^4	2.75×10^4
	calculated L [m]	9.86×10^{-5}	9.55×10^{-5}	9.34×10^{-5}	1.14×10^{-4}
	calculated Pe [] [eq 6.1]	1.01×10^2	4.39×10^2	1.06×10^2	6.15×10^2
	calculated Da [] using batch reaction rate [eq 6.11]	1.79×10^{-4}	4.22×10^{-5}	1.48×10^{-4}	3.31×10^{-5}
	calculated PeDa []	1.82×10^{-2}	1.85×10^{-2}	1.57×10^{-2}	2.04×10^{-2}
	calculated reaction rate r_{eff} [mol.m ⁻² s ⁻¹] [eq 6.13]	7.01×10^{-6}	7.32×10^{-6}	1.52×10^{-6}	8.56×10^{-6}
120					
	absolute permeability (direct simulation) [m ²]	2.31×10^{-12}	1.23×10^{-11}	2.60×10^{-12}	1.60×10^{-11}
	image measured porosity ϕ []	0.201	0.225	0.163	0.187
	image measured specific surface area S [m ⁻¹]	3.32×10^4	3.52×10^4	3.44×10^4	2.83×10^4
	calculated L [m]	9.46×10^{-5}	8.93×10^{-5}	9.14×10^{-5}	1.11×10^{-4}
	calculated Pe [] [eq 6.1]	8.11×10^2	3.51×10^2	9.92×10^1	5.24×10^2
	calculated Da [] using batch reaction rate [eq 6.11]	2.24×10^{-4}	5.14×10^{-5}	1.57×10^{-4}	3.88×10^{-5}
	calculated PeDa []	1.82×10^{-2}	1.80×10^{-2}	1.55×10^{-2}	2.04×10^{-2}
	calculated reaction rate r_{eff} [mol.m ⁻² s ⁻¹] [eq 6.13]	6.72×10^{-6}	5.81×10^{-6}	1.49×10^{-6}	5.41×10^{-6}

Both Da and $PeDa$, the ratio of the diffusion rate to the reaction rate, are much less than one throughout the experiments, representing conditions at which the reaction rate is slow compared to both the advection and diffusion rates.

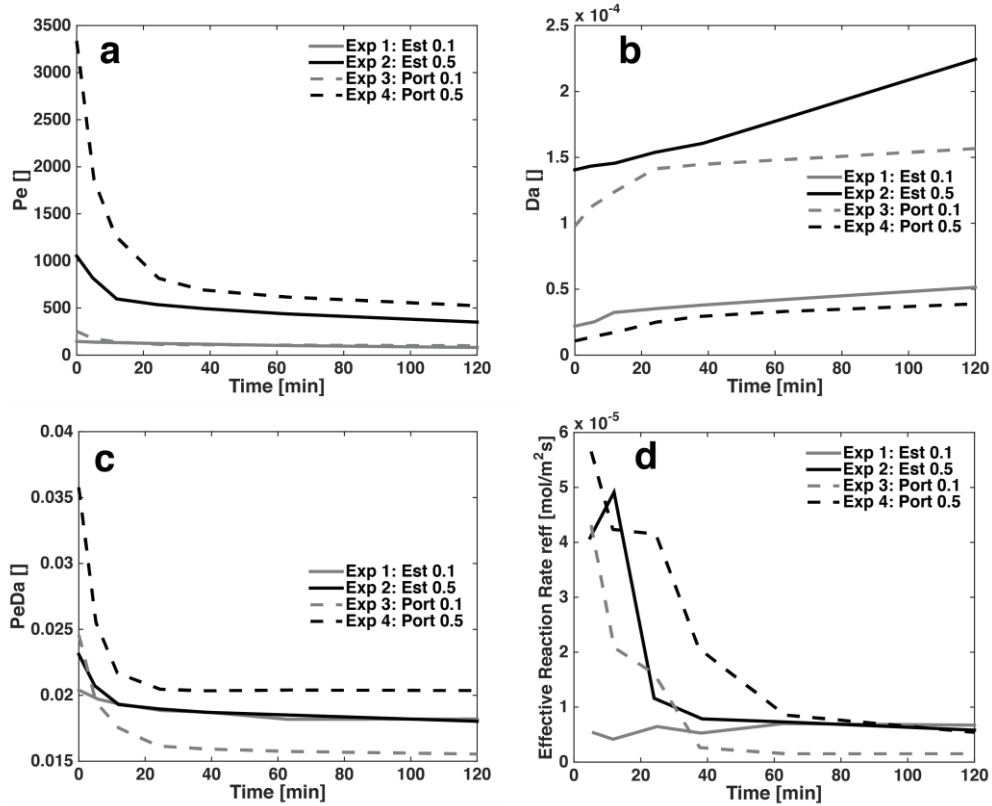


Figure 6.13 (a) Péclet number (Pe), (b) Damköhler number (Da), (c) Péclet-Damköhler number ($PeDa$), and (d) effective reaction rates (r_{eff}) for each experiment through time.

Our computed values of Pe , Da , $PeDa$, and r_{eff} are shown in Table 6.3 and displayed graphically in Figure 6.13. In experiment 1, Pe remains approximately constant with a slow decrease consistent with an increase in porosity leading to a decrease in average velocity. In the other experiments, the initial drop in Pe is more dramatic, but is again followed by a slow, almost linear, decrease with time, again consistent with the evolution of porosity [Figure 6.9a]. The magnitude of Pe in experiments 1 & 3 is lower than in 2 & 4 because of the lower imposed flow rate.

Da increases for all the experiments [Figure 6.13b], consistent with the decrease in average velocity. Both $PeDa$ and r_{eff} remain steady for experiment 1, but showed a sharp decrease for experiments 2, 3, and 4 followed by steady rates [Figures 6.13-d]. At late time, the reaction rate of experiment 1 remained higher than experiment 3 despite having the same flow rate, while experiments 2 and 4 showed similar effective reaction rates. The most significant feature is that the reaction rates are much lower than the value of $8.1 \times 10^{-4} \text{ mol.m}^{-2}\text{s}^{-1}$ measured on a flat surface with no transport limitations: initially the effective rates are at least ten times lower,

declining to 100 times lower at late times. This demonstrates that reaction is severely limited by the rate of transport of reactant to the solid surface: when channels form, these dominate the flow and limit reaction to the sides of the channels themselves; in comparison the transport of reactant and products in the pore space away from these channels is very slow. This discrepancy between intrinsic and effective rates is larger than the 16-fold variation observed in the more homogeneous Ketton sample in section 6.1.

Local Péclet statistics generated from the velocity distributions of the direct simulations are shown in Table 6.4 and displayed graphically in Figure 6.14. Each void voxels velocity is normalised to the experimental Darcy velocity and then used with equation 3 to calculate a local Péclet number. The mean local Péclet number (Figure 6.14a) decreases almost linearly through time for experiment 1 and has a sharp decrease at earlier times for experiments 2-4 which then become nearly linear at later times. The maximum local Péclet number (Figure 6.14b) follows a similar trend with the highest values at the beginning of the experiments and then decreasing in accordance with the constant experimental flow rate and the increase in porosity. The standard deviation of the local Péclet number decreases sharply for experiments 2, 3, and 4, but remains relatively constant for experiment 1 and is consistent with the PDFs of velocity in Figure 6.11.

Figure 6.14d depicts the fraction of void voxels that have a local Péclet number of ≤ 1 and have diffusion-dominated flow. Portland has a larger portion of diffusion-dominated voxels than Estailades – this is consistent with the lower permeability found in Portland as seen in Figure 6.9b. In experiment 1 the fraction of voxels with diffusion-dominated flow is small and the fraction steadily increases with time. However, in experiments 2, 3, and 4 there is a decrease in the number of diffusion-dominated voxels in the first 30 minutes of the experiment followed by a steady increase at later times. We believe this demonstrates that during the formation of the channels there is competition between preferential flow paths and as a consequence more of the pore space is advection dominated. After the channels are formed the majority of flow is directed through these mobile paths which also leaves larger immobile regions in which the number of diffusion-dominated voxels increases.

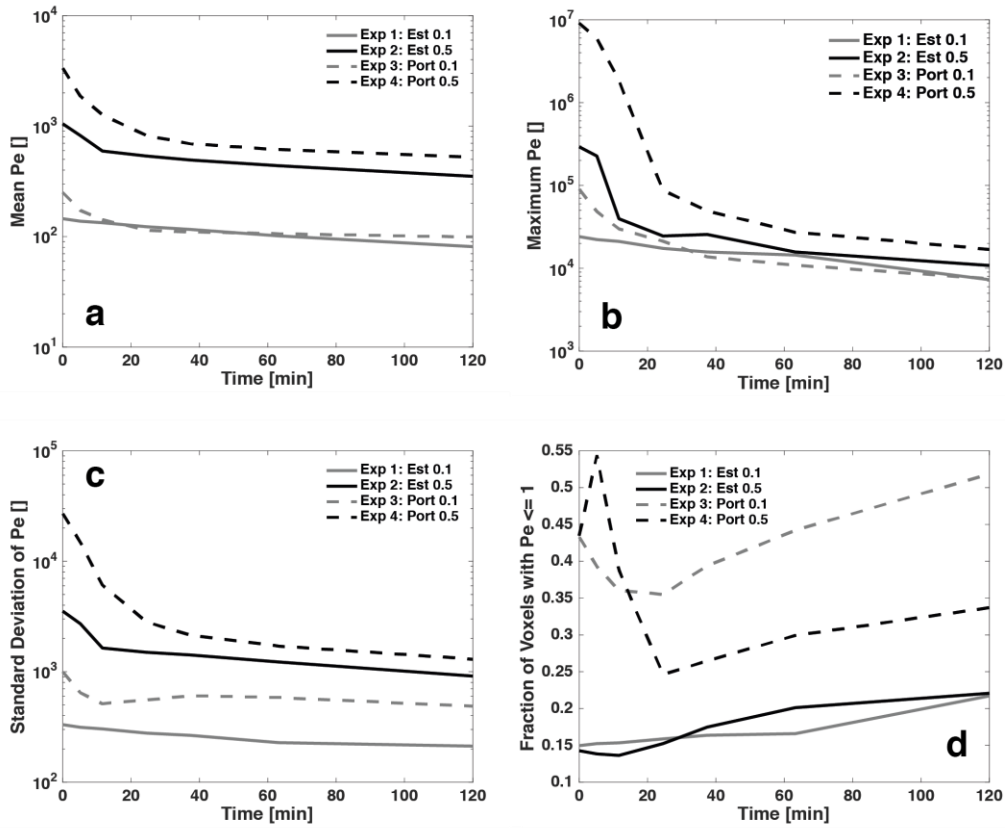


Figure 6.14 (a) Mean Péclet number (Pe), (b) maximum Péclet number (Pe), (c) standard deviation of Péclet number (Pe), and (d) fraction of void voxels with Péclet number (Pe) ≤ 1 , measured by direct simulation for each experiment through time.

Network extraction [Table 6.4] indicates that the pore size and throat diameter all increase with time, while the total number of pores and throats decrease. The coordination number (representing the connectivity) is highest initially for the Estailades samples and increases slightly through time for experiment 1 and dramatically at first for experiments 2, 3, and 4 and then stabilizes at later times.

Table 6.4 Network and direct flow simulation properties for times 0, 63, and 120 min.

Time [min]	Property	Experiment 1: Estailades 0.1 [mL/min]	Experiment 2: Estailades 0.5 [mL/min]	Experiment 3: Portland 0.1 [mL/min]	Experiment 4: Portland 0.5 [mL/min]
0					
	mean Pe [] (direct simulation)	1.45×10^2	1.05×10^3	2.51×10^2	3.34×10^3
	maximum Pe [] (direct simulation)	2.41×10^4	2.92×10^5	9.01×10^4	9.09×10^6
	standard deviation of Pe [] (direct simulation)	3.32×10^2	3.53×10^3	9.98×10^2	2.70×10^4
	fraction of voxels with $Pe < 1$ (direct simulation)	0.14	0.15	0.43	0.43
	number of pores	44878	33048	73115	28424
	number of throats	119071	81297	62365	28537
	average pore radius [m] (volume-weighted)	2.44×10^5	2.29×10^5	1.75×10^5	1.56×10^5
	average throat radius [m] (volume-weighted)	7.86×10^6	3.74×10^6	7.29×10^6	5.28×10^6
	pore-throat contraction ratio (volume-weighted)	0.30	0.30	0.34	0.33
	average coordination number	5.31	4.91	1.71	2.01
63					
	mean Pe [] (direct simulation)	1.01×10^2	4.38×10^2	1.06×10^2	6.14×10^2
	maximum Pe [] (direct simulation)	1.44×10^4	1.57×10^4	1.09×10^4	2.72×10^4
	standard deviation of Pe [] (direct simulation)	2.28×10^2	1.22×10^3	5.85×10^2	1.71×10^3
	fraction of voxels with $Pe < 1$ (direct simulation)	0.20	0.17	0.44	0.30
	number of pores	42360	31423	67312	37936
	number of throats	119462	84334	115701	60381
	average pore radius [m] (volume-weighted)	2.90×10^5	3.62×10^5	2.00×10^5	3.81×10^5
	average throat radius [m] (volume-weighted)	9.06×10^6	1.06×10^6	6.63×10^6	1.11×10^6
	pore-throat contraction ratio (volume-weighted)	0.28	0.27	0.29	0.25
	average coordination number	5.64	5.37	3.44	3.18
120					
	mean Pe [] (direct simulation)	8.11×10^1	3.51×10^2	9.92×10^1	5.24×10^2
	maximum Pe [] (direct simulation)	7.28×10^3	1.08×10^4	7.49×10^3	1.69×10^4
	standard deviation of Pe [] (direct simulation)	2.12×10^2	9.13×10^2	4.87×10^2	1.30×10^3
	fraction of voxels with $Pe < 1$ (direct simulation)	0.22	0.22	0.52	0.34
	number of pores	37873	30712	66508	36989
	number of throats	106680	80867	116476	58987
	average pore radius [m] (volume-weighted)	4.06×10^5	4.80×10^5	2.23×10^5	5.80×10^5
	average throat radius [m] (volume-weighted)	1.15×10^6	1.38×10^6	7.55×10^6	1.59×10^6
	pore-throat contraction ratio (volume-weighted)	0.25	0.24	0.28	0.21
	average coordination number	5.63	5.27	3.50	3.19

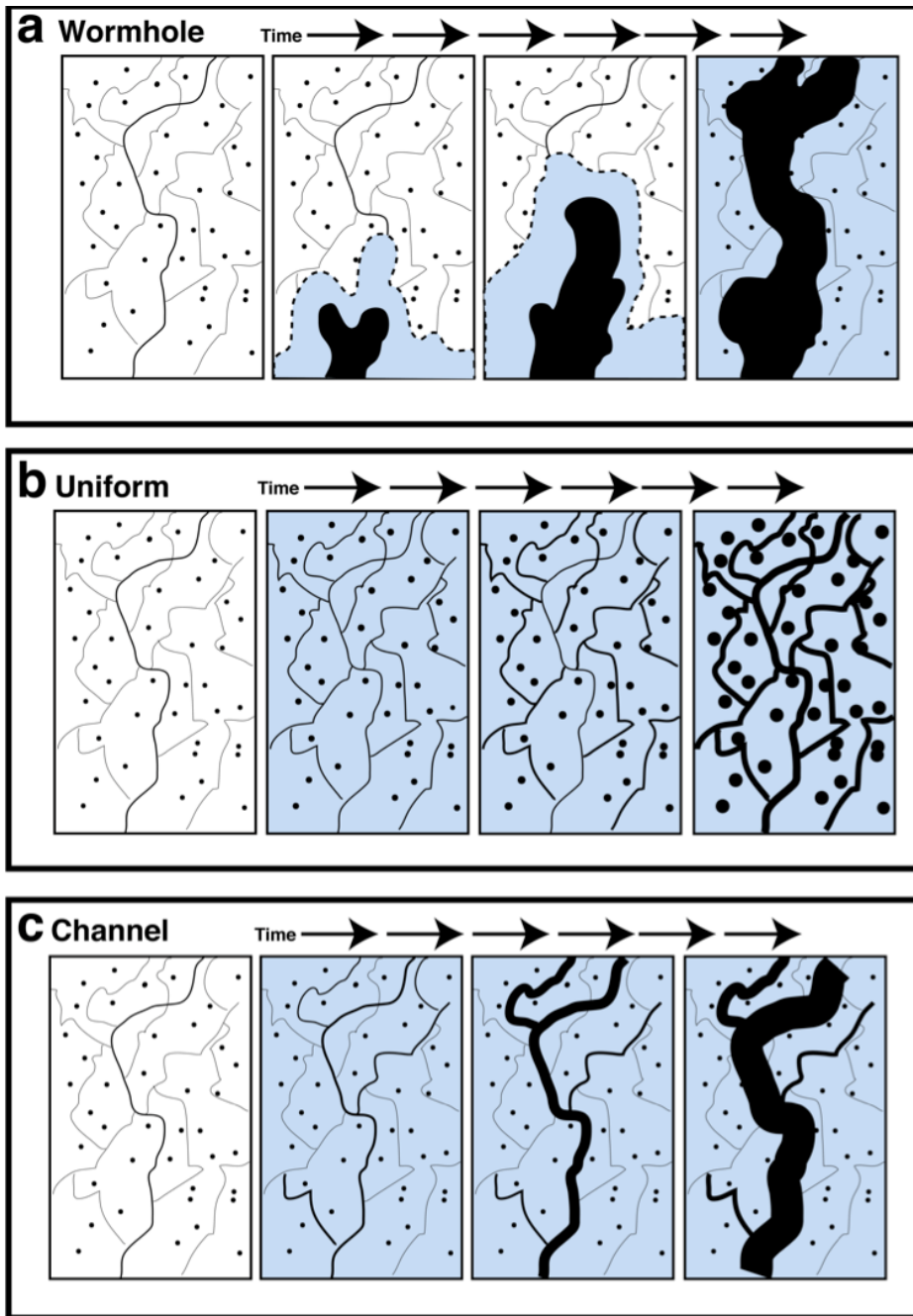


Figure 6.15 A schematic of wormholing (a), uniform (b), and channel formation (c) dissolution regimes. In the wormholing regime, the reactive brine (blue) floods the pore space (black) dissolving the rock (white) as it advances. In the uniform dissolution regime, brine floods the whole pore space rapidly and the rock then dissolves across its entire surface area. During channel formation, flow is faster than in the wormholing regime: reactive brine floods the rock very quickly, but the heterogeneity of the rock allows preferential flow paths to form which then provide the majority of the reactant to a more limited portion of the surface of the rock.

Traditionally dissolution has been studied experimentally and numerically in relatively homogeneous systems, for which there is a Pe and Da -dependent transition from uniform to wormholing patterns [108, 123, 129, 236]. In our experiments, we are in what would be considered to be the uniform regime, where the reaction rate is relatively low in comparison to the flow rate, allowing reactant to penetrate the whole sample. Indeed, under the same conditions, uniform dissolution was observed in a relatively homogeneous Ketton limestone [Menke et al, 2015]. However, the dissolution patterns we have observed are not always uniform, but clearly show the emergence of preferential flow paths. This is not the same as wormholing, where the acid etches an advancing channel through the rock, but channelling, where the acid rapidly flows throughout the sample and then widens the fast flow pathways, as illustrated schematically in Figure 10 and confirmed quantitatively through the increase in the velocity correlation function over time, Figure 6.12, and through the examination of local Péclet numbers in Figure 6.14.

In wormholing, we see a sudden and very significant increase in permeability when the hole spans the core: this is not observed in our experiments, with a smoother increase in permeability with time, as shown in Figure 6.9. Instead, in experiments 2, 3, and 4, the changes in porosity and permeability along with the evolution of the velocity fields (see, for instance, Figure 6.10d.) are indicative of channel formation [Figure 6.15b] rather than wormholing [Figure 6.15a]. In experiment 1, the steady increase in porosity and permeability coupled with the steady reaction rate is similar to uniform dissolution. The lower flow rate combined with the initial high porosity, connectivity, and permeability of Estailades means that advection dominates in the majority of the pore space and fresh reactant is continuously provided to most areas of the pore space preventing the formation of obvious preferential flow channels [Figure 6.15c].

6.2.4 Conclusions

We have found a clear impact of initial structure on the changes in porosity and permeability due to fluid/solid reaction in carbonate rocks. We see the emergence of a new type of dissolution pattern in heterogeneous systems: channelling, where preferential paths widen and dominate the flow and the dissolution process. The effective reaction rates in the channelling regime are up to two orders of magnitude smaller than that measured on flat substrates with no transport limitations, implying that transport of reactant and products in regions of the pore space away from the channels is significantly impeded.

Fast synchrotron tomography coupled with a reservoir-condition flow apparatus is a powerful experimental tool that can be adapted to explore a range of applications including multiphase flow processes [204], advection-dispersion, and transport in chemically heterogeneous media. Such an approach allows for

integration of experiment and modelling at reservoir conditions in complex systems, elucidating dynamic reaction processes on a pore-by-pore basis.

6.3 Imaging dissolution using a laboratory source at multiple reactive conditions

The third experiment was designed to adapt the laboratory methodology to include effluent analysis and to incorporate the capability to examine heterogeneous rocks at multiple reactive conditions. We examined dissolution in three rocks of increasing complexity Ketton, Estailades and Portland Basebed, dynamically at reservoir conditions using a laboratory source at two initial brine pH's. These results are in review in the Journal *Geochimica et Cosmochimica Acta*.

Carbonate dissolution by CO₂ acidified brine is controlled by many factors including pore space heterogeneity, initial pH, and flow conditions [116, 129, 209]. At reservoir conditions the acidity of the brine is strongly dependent on temperature and pressure [45]. Additionally, the acid pH changes depending on the amount of calcium dissolved in solution [52, 237].

X-ray microtomography (μ -CT) is an accepted method of studying pore-scale processes [113, 229]. μ -CT creates three-dimensional images with a high spatial resolution ($\sim 1 \mu\text{m}$) non-invasively. Two types of light sources are used for μ -CT imaging: synchrotron and laboratory. Synchrotron light sources are only sporadically accessible, but have powerful x-ray beams that can take images very quickly. Laboratory scanners are less expensive and more widely available, but have a weaker x-ray source that must be carefully fine-tuned to study dynamic processes. Carbonate rocks are extremely diverse and complex [190] and thus it requires many experiments to determine the principal controls on dissolution for a range of carbonate rock types. Therefore the development of a laboratory-based technique that allows for reservoir condition imaging of complex pore-structures with a temporal resolution sufficient to study dynamic processes is imperative for acquiring the breadth of data needed for complete understanding of pore-scale processes in carbonate rocks. In an imaging experiment, the reaction rate can be calculated from the measured change in porosity. However, it is not possible to assess the accuracy of this approach without effluent analysis. Thus it is also important to complement image-based measurements with more conventional geochemical sampling.

There have been several studies that have successfully used μ -CT to study dynamic pore-scale processes. Berg et al. [176] and Andrew et al. [177] both used a synchrotron light source to look at dynamic pore-scale displacement events between multiple fluid phases with around ~ 1 min temporal resolution. Other work has looked at fluid/solid reaction in complex carbonates, but were either not performed at reservoir conditions, or were limited to pre and post reaction images [120, 172, 173, 179]. Menke et al. [215] imaged the dissolution dynamics of carbonate at reservoir conditions. However, neither set of experiments included effluent analysis, while the samples were either limited to homogenous rocks that were relatively easy to image, or were performed using a synchrotron light source with specialized equipment.

This section describes a method to study reactive dissolution processes at reservoir conditions at the pore-scale in both homogenous and heterogeneous carbonates using a laboratory scanner. We will focus on measuring pore-scale effective reaction rates between two CO₂-acidified brines of pH 3.1 and 3.6 and limestone rock. We observe two distinct dissolution regimes – uniform and channelling – whose emergence and rate of development are dependent on initial structural heterogeneity and reactive conditions.

To investigate the effect of pore-scale heterogeneity we select three limestones: Ketton, Estailades and Portland. Ketton has been shown to have homogeneous flow characteristics, in that the distribution of velocity computed on an image before reaction is narrower than observed for Estailades and Portland [49, 162]. We present a dynamic *in situ* study of carbonate dissolution at reservoir conditions with effluent sampling to track the calcium concentration. Image sequences are binarized and then analysed for porosity and surface area changes. Furthermore, the images are used as input into flow models to elucidate the evolution of permeability and pore-scale velocity fields and initial connectivity are assessed through network extraction. Additionally, effective reaction rates are calculated for both effluent samples and CT images and compared, demonstrating both the accuracy of CT imaging of fluid-rock reaction and the formation process of different dissolution structures.

6.3.1 Imaging strategy

We study the impact of reaction rate and initial pore structure on dissolution for three limestones: Ketton, Estailades, and Portland Basebed [Table 6.5]. First, in experiments 1 and 2, brines of pH 3.1 and 3.6 are injected into Ketton limestone to investigate the impact of reaction rate on dissolution. Then in experiments 3-6 the more heterogeneous limestones, Estailades and Portland, are reacted using the same conditions to study the impact of physical heterogeneity.

Table 6.5 Experimental parameters for section 6.3.

Experiment Number	1	2	3	4	5	6
Rock type	Ketton Limestone	Ketton Limestone	Estailades Limestone	Estailades Limestone	Portland Basebed	Portland Basebed
Flow rate [mL/min]	0.1	0.1	0.1	0.1	0.1	0.1
Brine pH	3.6	3.1	3.6	3.1	3.6	3.1
Temperature [°C]	50	50	50	50	50	50
Pressure [MPa]	10	10	10	10	10	10
Number of Scans	6	10	6	6	6	6
Resolution [µm]	4.15	4.07	4.15	4.07	4.15	4.59
Projections	800	400	800	800	800	800

The images are first binarized and analysed for changes in porosity and surface area. Then a flow solver is run on the segmented images to examine the dynamic changes in permeability and pore velocity and network extraction is used to assess pore-space connectivity. Additionally, we calculate the time-resolved changes in the dimensionless numbers, which are traditionally used to describe flow and reactive conditions. Moreover, we examine the predicted overall reaction rate from effluent analysis versus the reaction rate observed by dynamic x-ray microtomography.

6.3.2 Image processing

Dynamic scans of highly heterogeneous rocks during dissolution are very difficult to segment because the rock-fluid boundaries are not sharp and the low projection rate means that the small pores are not clearly resolved. Thus, we use the difference image approach to segmentation [210]. A difference image was computed between the greyscale reference and reacted scans that was then filtered and segmented by watershed created a segmented version of the changing pore space. The segmented difference image was then subtracted from the segmented dry scan to achieve a segmented image for each time step. Flow through the pore space of the segmented images was then computed using the finite-volume code OpenFoam [238] that uses both Navier-Stokes and the volume conservation equations and employs the numerical methods presented in Raeini et al. [239] and Bijeljic et al. [49].

6.3.3 Results and discussion

Each segmented image series was analysed for changes in porosity by counting the number of voxels of pore and rock. Figure 2 depicts the slice-averaged porosity along the axis of flow for each image through time. Porosity increases with time during dissolution and in all six experiments the porosity increased relatively uniformly along the axis of flow with the exception of Estailades, which showed slightly more dissolution near the inlet. In experiment 1 the porosity also increases uniformly through time. Conversely, in experiments 2 - 6 the majority of the porosity increase occurs in the first 120 minutes. As expected, the porosity increases faster with a lower pH when experiments 3, 4, 5, and 6 are compared. However, the total increase in porosity is highest for experiment 1 (24%) and lowest for experiment 6 (6%) and thus the total amount of dissolution does not appear to be strongly correlated with the pH of the reactive fluid.

Permeability was calculated directly on the segmented images using Darcy's law: we use the fluid viscosity, the average pressure gradient across the sample, and the average flow speed at the outlet computed using the Navier-Stokes solver.

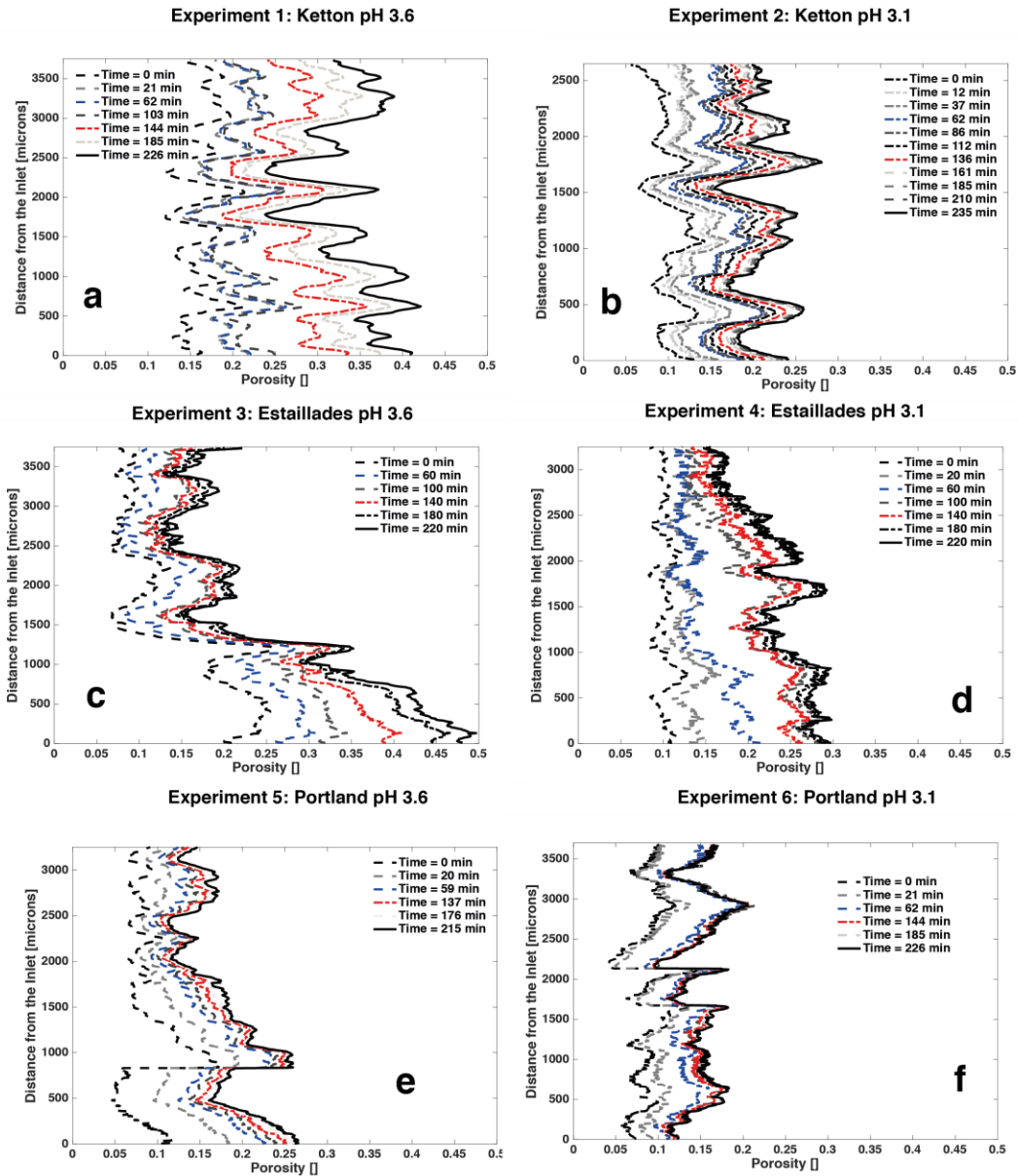


Figure 6.16 Sliced-averaged porosity versus distance from the sample inlet for Ketton at pH 3.6 (a) and pH 3.1 (b), Estailades at pH 3.6 (c) and pH 3.1 (d) and Portland at pH 3.6 (e) and pH 3.1 (f). The red and blue lines indicate ~1 and ~2 hours into the experiment.

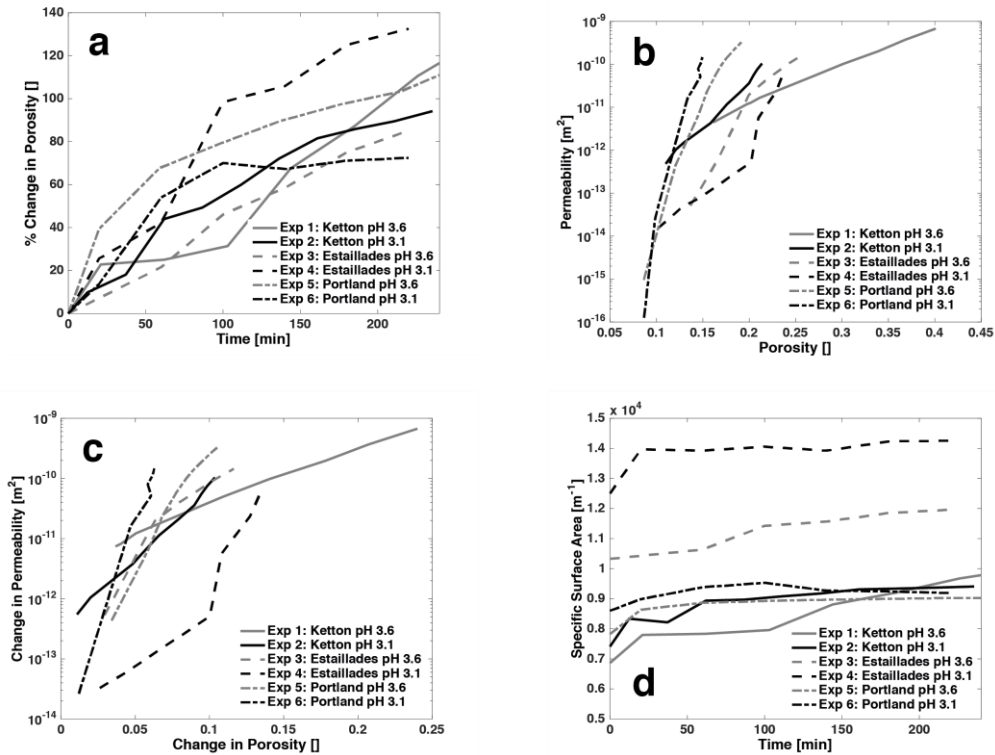


Figure 6.17 The percent change in average porosity across the whole sample versus time (a), permeability versus porosity (b), the change in permeability as a function of the change in porosity (c), and the specific surface area versus time (d) of Ketton, Estailades, and Portland carbonates during dissolution. The porosity and surface area are calculated directly from the segmented images. Permeability is found from applying Darcy's Law from the computed flow field.

Figure 6.17 depicts the evolution of porosity and permeability for Ketton, Estailades, and Portland carbonates at an injected brine pH of 3.1 and 3.6. The change in porosity with time is relatively steady for Experiment 1 [Figure 6.17a]. However, there are dramatic decreases in the porosities change at later times for experiments 2 -6 with the greater decreases with increasing initial pore-space heterogeneity.

We fit the data to an empirical power-law relationship between permeability and porosity. The best fit to the Ketton experiments 1 and 2 were $K = 8 \times 10^{-8} \phi^{5.45}$ and $K = 4.00 \times 10^{-6} \phi^{6.93}$. For the Estailades experiments 3 and 4 the best fits were $K = 2.36 \times 10^{-2} \phi^{13.42}$ and $K = 5.00 \times 10^{-5} \phi^{9.99}$ respectively. For the Portland experiments 5 and 6 we found $K = 2.17 \times 10^2 \phi^{16.16}$ and $K = 6.00 \times 10^{-9} \phi^{23.8}$, respectively. The exponents are higher than the exponent of 3 used in the Kozeny-Carmen relationship and the exponents reported in Menke et al. [215], but are similar to those reported in Noiriel et al. [180] for limestone dissolution and Smith et al. [172] for dissolution of low permeability carbonates. The porosity-permeability relationship follows a trend of increasing exponents with increasing initial

heterogeneity. The pH of the injected brine is observed to be a poor predictor of the permeability change. However, the exponents rise with decreasing initial permeability, which suggests a strong correlation between pore-space heterogeneity and the total permeability change.

Figure 6.17d depicts evolution of the specific surface area, S during dissolution. S was calculated by summing the number of void voxels faces adjacent to grains on the segmented images. S [m^{-1}] is the surface area [m^2] divided by the bulk volume [m^3]. S initially increases sharply for all experiments, and then remains relatively steady at later times for experiments 2-6, but continues on an upward trend for experiment 1. We note that the initial specific surface area is almost two times higher for Estailades, which may partially explain the increased dissolution at the sample inlet as there are more reactive surface sites to encourage dissolution along major flow paths.

The pore-scale velocity fields are visualised for Ketton, Estailades, and Portland carbonates [Figure 6.18] by calculating the ratios of the magnitude of u at the voxel centres divided by the average pore velocity, U_{av} [$\text{m}\cdot\text{s}^{-1}$], which is the Darcy velocity q divided by the scan porosity ϕ_{CT} taken from the segmented image. As the flow rate is held constant by the pumps throughout the experiment, the Darcy velocity is also constant. In experiment 1, there are many flow paths through the rock that widen through time. Conversely in experiments 2, 3, 4 there are many flow paths that consolidate to a single preferential pathway. In experiments 5 & 6, there are initially a small number of pathways that widen at later times.

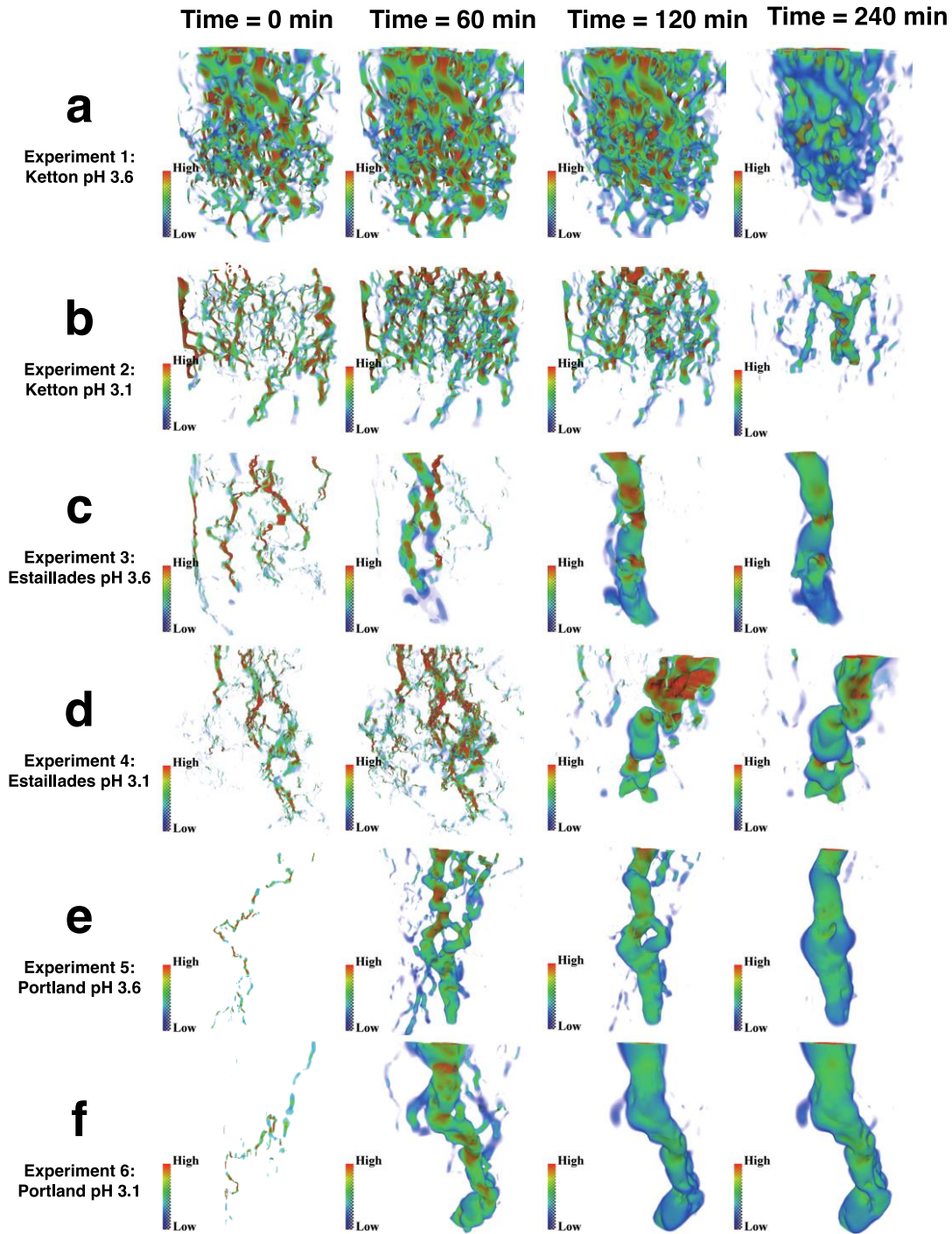


Figure 6.18 The ratios of the magnitude of u at the voxel centres divided by the average pore velocity U_{av} are coloured using a linear scale where low velocity is blue, medium velocity is yellow, and high velocity is red.

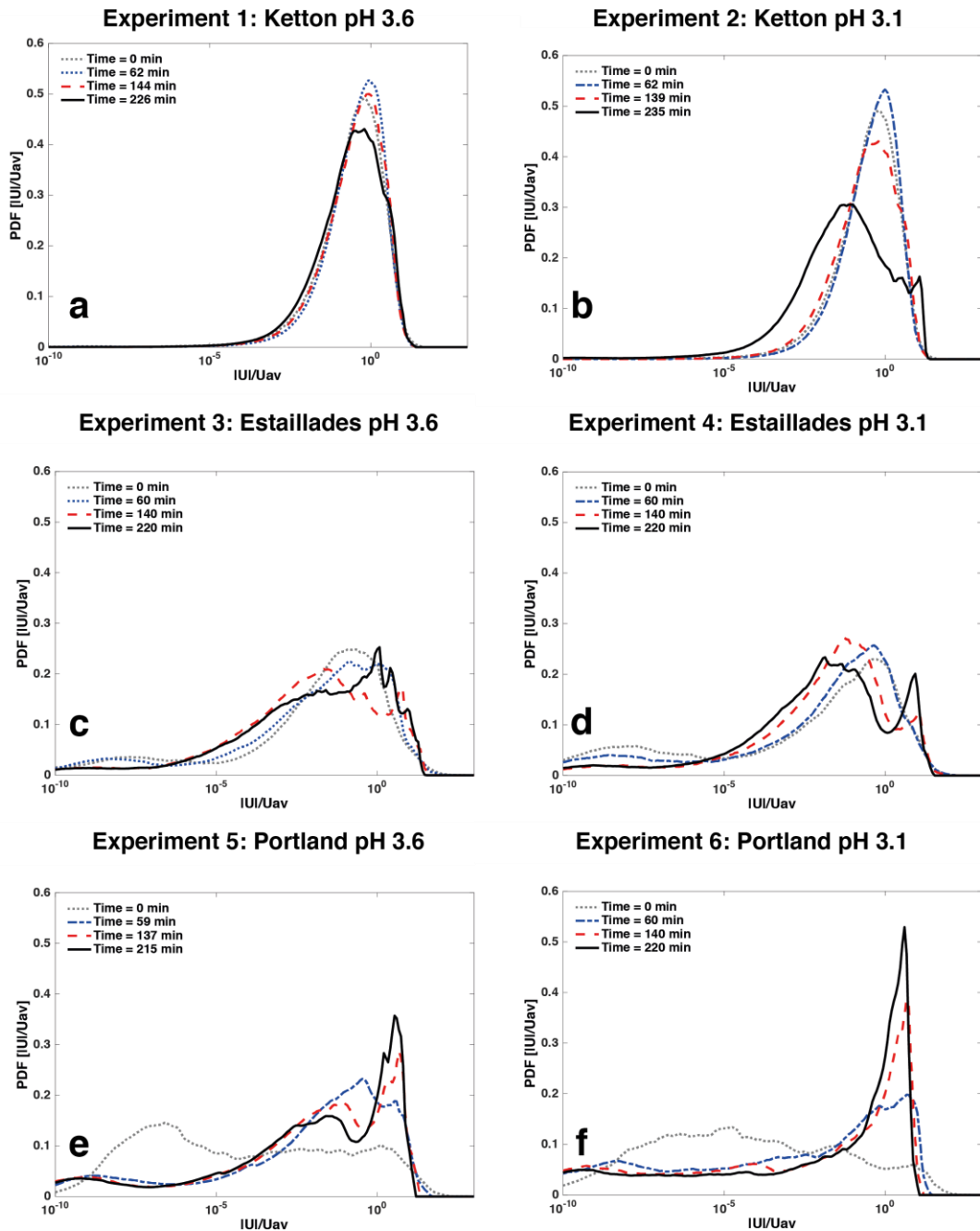


Figure 6.19 Probability density functions (PDFs) of pore voxel velocity during (a) experiment 1, (b) experiment 2, (c) experiment 3, (d) experiment 4, (e) experiment 5, (f) experiment 6. The velocity histogram is computed on the pore-space images and sampled uniformly in 256 bins of $\log(|\mathbf{u}|/U_{av})$, which are calculated as the ratios of the magnitude of \mathbf{u} at the voxel centres divided by the average pore velocity U_{av} . The distributions are shown at times 0, ~60 (blue), ~120 (red), ~240 minutes.

Figure 6.19 depicts the probability density functions (PDFs) of velocity. Ketton has the narrowest distribution, but this still spans approximately 5 orders of magnitude. With increasing heterogeneity, we see a wider distribution for Estailades, while for Portland we see voxel velocities over 10 orders of magnitude. For experiment 1, in Ketton, there is very little change in the velocity distribution, which indicates that the dissolution is relatively uniform. However, by the end of experiment 2 there is evidence of a sharp peak at high velocity and a rounded peak at lower velocities that suggests a preferential flow path and regions of stagnant flow. In experiments 3-6 [Figure 6.19c-f], the PDFs initially show two distinct regions of stagnant and high velocity flow. However, as dissolution progresses the greater proportion of velocities gradually shift to the high velocity region and the stagnant region diminishes. At lower pH this shift toward higher velocity happens more quickly.

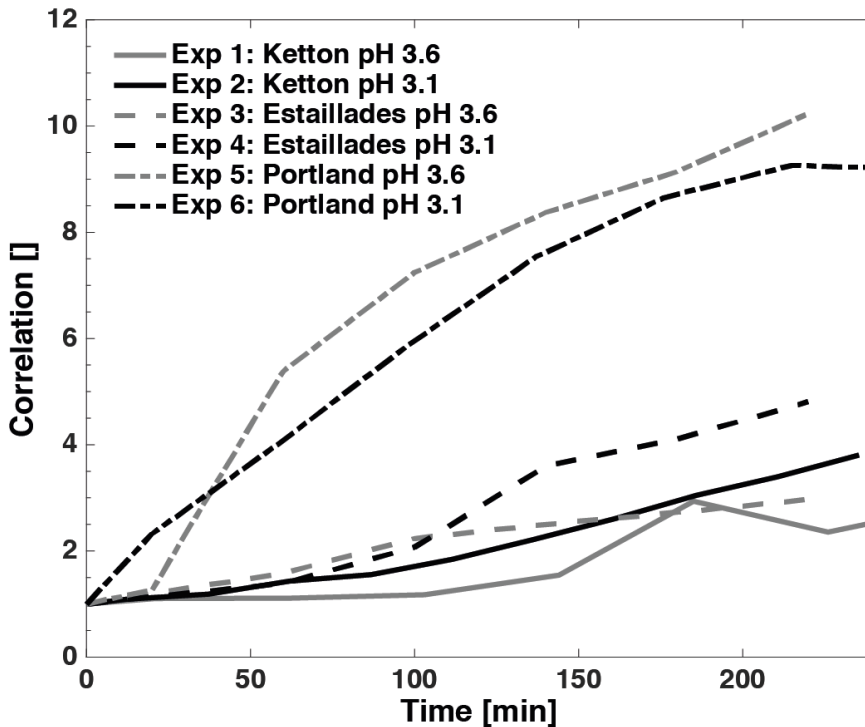


Figure 6.20 Normalized correlation, Eqs. (1) and (2), between the initial voxel velocities (time=0) and each those from successive image through time for each experiment.

To test our hypothesis that initially present fast flow paths dissolve more quickly than stagnant regions, we use the correlation coefficient presented in section 6.2.3. Figure 6.20 depicts the normalised correlation for all experiments: in all cases this increases over time, indicating that dissolution preferentially occurs in those regions of the pore space that initially had high flow speeds. If instead we had truly

uniform dissolution, with reaction occurring at the same rate everywhere, we would expect the correlation function to decline over time. Experiment 1 has the slowest rise in the correlation function and thus is closest to uniform dissolution. Experiments 2-6 show a dramatic rise in C , which provides a quantitative signature for channel formation in regions of the pores space with the highest velocities initially. Additionally, the correlations are in good agreement with the experiments performed at the same conditions in Menke, Bijeljic [210]. We also observe that injected pH is a poor predictor of the correlation in all cases except perhaps in experiments 1 and 2 where the pH changes the dissolution regime and thus the concentration of channelized flow paths.

We use definitions of Pe , Da , and r_{eff} presented in section 6.1. The flow rate of $0.1 \text{ mL}\cdot\text{min}^{-1}$ and the imaged measured specific surface area measured are used to calculate a characteristic length L of between $251 \mu\text{m}$ and $458 \mu\text{m}$ and a Pe of between 394 and 822 for the six experiments [Table 6.6]. L and Pe are lowest for Estailades which has a high specific surface area and highest for Portland which has the lowest porosity (and thus the highest U_{av}). At these high Péclet numbers fresh reactant is readily available throughout the core since the spatially averaged advection is much faster than diffusion.

Table 6.6 Computed flow and reaction parameters for times 0, ~60, ~120 and ~240 min for section 6.3.

Time [min]	Property	Experiment 1: Ketton pH 3.6	Experiment 2: Ketton pH 3.1	Experiment 3: Estailades pH 3.6	Experiment 4: Estailades pH 3.1	Experiment 5: Portland pH 3.6	Experiment 6: Portland pH 3.1
0							
	absolute permeability (direct simulation) [m ²]	4.42 × 10 ⁻¹²	4.81 × 10 ⁻¹³	5.17 × 10 ⁻¹⁴	1.53 × 10 ⁻¹⁴	9.52 × 10 ⁻¹⁶	1.25 × 10 ⁻¹⁶
	image measured porosity ϕ_{CT} []	0.161	0.110	0.137	0.102	0.086	0.087
	image measured specific surface area S [m ⁻¹]	6.86 × 10 ³	7.41 × 10 ³	1.03 × 10 ⁴	1.25 × 10 ⁴	7.82 × 10 ³	8.60 × 10 ³
	calculated L [m]	4.58 × 10 ⁻⁴	4.24 × 10 ⁻⁴	3.04 × 10 ⁻⁴	2.51 × 10 ⁻⁴	4.01 × 10 ⁻⁴	3.65 × 10 ⁻⁴
	calculated Pe [] [eq 6.1]	5.03 × 10 ²	6.81 × 10 ²	3.94 × 10 ²	4.36 × 10 ²	8.22 × 10 ²	7.45 × 10 ²
	calculated Da [] using batch reaction rate [eq 6.11]	4.70 × 10 ⁻⁵	1.02 × 10 ⁻⁴	4.33 × 10 ⁻⁵	1.02 × 10 ⁻⁴	2.46 × 10 ⁻⁵	7.80 × 10 ⁻⁵
	calculated PeDa []	2.36 × 10 ⁻²	6.93 × 10 ⁻²	1.71 × 10 ⁻²	4.46 × 10 ⁻²	2.02 × 10 ⁻²	5.81 × 10 ⁻²
	calculated reaction rate r_{eff} [mol.m ⁻² .s ⁻¹] [eq 6.13]	6.71 × 10 ⁻⁵	4.57 × 10 ⁻⁵	3.5 × 10 ⁻⁵	1.85 × 10 ⁻⁵	8.48 × 10 ⁻⁵	2.71 × 10 ⁻⁵
60							
	absolute permeability (direct simulation) [m ²]	1.26 × 10 ⁻¹¹	4.28 × 10 ⁻¹²	5.88 × 10 ⁻¹³	7.33 × 10 ⁻¹⁴	6.31 × 10 ⁻¹²	1.59 × 10 ⁻¹¹
	image measured porosity ϕ_{CT} []	0.201	0.159	0.166	0.145	0.145	0.133
	image measured specific surface area S [m ⁻¹]	7.83 × 10 ³	8.94 × 10 ³	1.06 × 10 ⁴	1.39 × 10 ⁴	8.86 × 10 ³	9.38 × 10 ³
	calculated L [m]	4.01 × 10 ⁻⁴	3.52 × 10 ⁻⁴	2.95 × 10 ⁻⁴	2.26 × 10 ⁻⁴	3.54 × 10 ⁻⁴	3.35 × 10 ⁻⁴
	calculated Pe [] [eq 6.1]	3.52 × 10 ²	3.92 × 10 ²	3.15 × 10 ²	2.75 × 10 ²	4.33 × 10 ²	4.44 × 10 ²
	calculated Da [] using batch reaction rate [eq 6.11]	6.17 × 10 ⁻⁵	1.55 × 10 ⁻⁴	5.45 × 10 ⁻⁵	1.53 × 10 ⁻⁴	4.40 × 10 ⁻⁵	1.27 × 10 ⁻⁴
	calculated PeDa []	2.18 × 10 ⁻²	6.07 × 10 ⁻²	1.72 × 10 ⁻²	4.21 × 10 ⁻²	1.93 × 10 ⁻²	5.62 × 10 ⁻²
	calculated reaction rate r_{eff} [mol.m ⁻² .s ⁻¹] [eq 6.13]	6.74 × 10 ⁻⁵	1.71 × 10 ⁻⁵	2.59 × 10 ⁻⁵	1.07 × 10 ⁻⁵	2.89 × 10 ⁻⁵	1.44 × 10 ⁻⁵

Table 6.6 (cont) Computed flow and reaction parameters for times 0, ~60, ~120 and ~240 min for section 6.3.

120							
	absolute permeability (direct simulation) [m ²]	5.39×10^{-11}	2.17×10^{-11}	4.03×10^{-11}	5.50×10^{-12}	5.66×10^{-11}	7.98×10^{-11}
	image measured porosity ϕ_{CT} []	0.270	0.190	0.217	0.210	0.164	0.145
	image measured specific surface area S [m ⁻¹]	8.81×10^3	9.17×10^3	1.16×10^4	1.39×10^4	8.96×10^3	9.27×10^3
	calculated L [m]	3.57×10^{-4}	3.42×10^{-4}	2.72×10^{-4}	2.62×10^{-4}	3.50×10^{-4}	3.39×10^{-4}
	calculated Pe [] [eq 6.1]	2.34×10^2	3.20×10^2	2.22×10^2	1.90×10^2	3.78×10^2	4.13×10^2
	calculated Da [] using batch reaction rate [eq 6.11]	9.06×10^{-5}	1.92×10^{-4}	7.57×10^{-5}	2.39×10^{-4}	5.09×10^{-5}	1.39×10^{-4}
	calculated $PeDa$ []	2.12×10^{-2}	6.14×10^{-2}	1.68×10^{-2}	4.55×10^{-2}	1.93×10^{-2}	5.76×10^{-2}
	calculated reaction rate r_{eff} [mol.m ⁻² s ⁻¹] [eq 6.13]	3.27×10^{-5}	1.78×10^{-5}	7.01×10^{-6}	4.26×10^{-6}	5.77×10^{-6}	3.57×10^{-6}
240							
	absolute permeability (direct simulation) [m ²]	2.01×10^{-10}	1.04×10^{-10}	1.45×10^{-10}	6.44×10^{-11}	2.52×10^{-10}	1.47×10^{-10}
	image measured porosity ϕ_{CT} []	0.339	0.214	0.253	0.237	0.186	0.150
	image measured specific surface area S [m ⁻¹]	9.67×10^3	9.41×10^3	1.20×10^4	1.43×10^4	9.19×10^3	1.43×10^4
	calculated L [m]	3.25×10^{-4}	3.34×10^{-4}	2.63×10^{-4}	2.20×10^{-4}	3.38×10^{-4}	3.42×10^{-4}
	calculated Pe [] [eq 6.1]	1.69×10^2	2.76×10^2	1.84×10^2	1.64×10^2	3.30×10^2	4.04×10^2
	calculated Da [] using batch reaction rate [eq 6.11]	1.26×10^{-4}	2.24×10^{-4}	9.28×10^{-5}	2.80×10^{-4}	5.95×10^{-5}	1.44×10^{-4}
	calculated $PeDa$ []	2.13×10^{-2}	6.18×10^{-2}	1.70×10^{-2}	4.61×10^{-2}	1.96×10^{-2}	5.84×10^{-2}
	calculated reaction rate r_{eff} [mol.m ⁻² s ⁻¹] [eq 6.13]	3.76×10^{-5}	8.71×10^{-6}	9.61×10^{-6}	4.26×10^{-6}	5.74×10^{-6}	1.16×10^{-6}

It has been proposed Compton et al. [102] and Peng et al. [52] that in an entirely surface controlled reaction regime of $\text{pH} < 4$, calcite dissolution kinetics can be modelled as a first order heterogeneous reaction with the equation:

$$r_{exp} = k\alpha_{H^+} \quad (6.16)$$

where r_{exp} is the batch reaction rate, k is the reaction rate constant and α_{H^+} is the activity of H^+ which is equal to $10^{-\text{pH}}$. Using the r_{exp} at our experimental conditions (10 MPa and 50°C) measured by Peng et al. (2015) at our experimental conditions and a pH 3.1 of $8.1 \times 10^{-4} \text{ mol.m}^{-2}.\text{s}^{-1}$ we can calculate r_{exp} at pH 3.6 to be $2.56 \times 10^{-4} \text{ mol.m}^{-2}.\text{s}^{-1}$: we use these values to estimate Da for the experiments in Table 6.6.

We can then use dynamic imaging to assess the accuracy of this predicted reaction rate by observing the evolution of the porosity throughout the experiment. As Da and $PeDa \ll 1$, the reaction rate is slow compared to both the advection and diffusion rates. We then use the change in overall porosity to estimate the average effective reaction rate [$\text{mol.m}^{-2}.\text{s}^{-1}$] for each image time-step (see section 6.1).

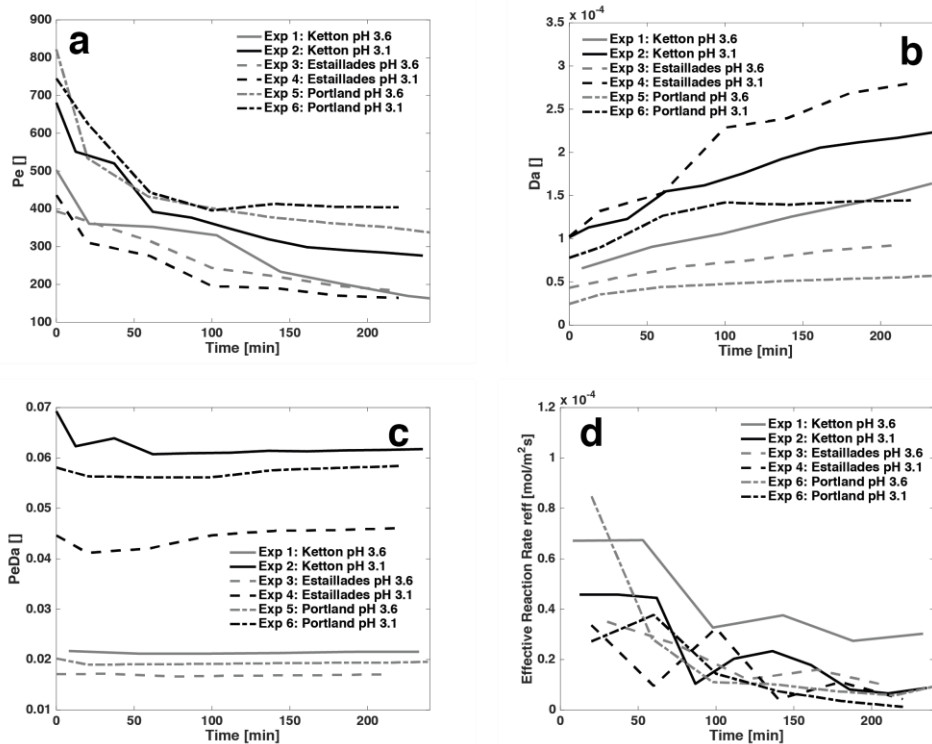


Figure 6.21 (a) Péclet number (Pe), (b) Damköhler number (Da), (c) Péclet-Damköhler number ($PeDa$), and (d) effective reaction rates (r_{eff}) for each experiment through time.

Figure 6.21 depicts the evolution of Pe , Da , $PeDa$, and r_{eff} for each experiment. The Pe [Figure 6.21a] decreases with time for each experiment with the largest Pe decrease in the samples with the most dissolution and the sharpest Pe decrease in the samples with the most heterogeneity. Conversely Da [Figure 6.21b] has a general increase with all experiments with the greatest increase in experiment 4 and the smallest in experiments 3 & 5. Thus, the $PeDa$ [Figure 6.21c] have a small dip at the beginning of reaction for experiments 2-6 and but remains relatively constant at later times for all experiments.

The image-measured effective reaction rate declines with time for all experiments, but remains the highest for experiment 1. Experiments 2, 4, & 6 conducted at pH 3.1 have slightly higher initial reaction rates than the experiments conducted at pH 3.6, but with the exception of experiment 1 where the reaction rate remains high, the reaction rates decline sharply at later times.

Network extraction [Table 6.7] indicates that the number of initial pores and throats are greatest in the Portland samples, while the average pore radius and throat diameter are greatest in the Ketton samples. The coordination number (representing the connectivity) is highest initially for the Estailades samples and lowest for the Ketton samples, which have very large pores.

Table 6.7 Network properties for the initial images in each experiment.

Property	Exp 1: Ketton pH 3.6	Exp 2: Ketton pH 3.1	Exp 3: Estailades pH 3.6	Exp 4: Estailades pH 3.1	Exp 5: Portland pH 3.6	Exp 6: Portland pH 3.1
number of pores	1268	2431	7380	9523	16451	16918
number of throats	2356	3468	12061	15769	10140	13514
average pore radius [m] (volume-weighted)	8.39×10^{-5}	4.76×10^{-5}	5.65×10^{-5}	2.79×10^{-5}	3.61×10^{-5}	3.05×10^{-5}
average throat radius [m] (volume-weighted)	3.50×10^{-5}	1.92×10^{-6}	1.48×10^{-6}	8.79×10^{-6}	1.67×10^{-5}	1.29×10^{-5}
pore-throat contraction ratio (volume-weighted)	0.32	0.31	0.27	0.32	0.28	0.28
average coordination number	6.71	5.04	14.04	7.02	8.12	4.50

Figure 6.22 depicts the calcium concentration and pH measured from effluent samples. The concentration of Ca^{2+} [Figure 6.22a] is measured using an ICP-MS from effluent samples taken during the experiment. We observe the highest Ca^{2+} concentration initially for experiment 1 which then declines slightly through time. In experiments 2 - 6, the Ca^{2+} concentration starts high (and is higher with a lower injected pH), declines sharply and then remains relatively steady as the experiment continues.

The pH is computed using the geochemical equations found in Leal et al. [237] using the Ca^{2+} concentration in the effluent as input and assumes that the brine remains fully saturated with CO_2 . As expected, the pH follows the same trends as the Ca^{2+} concentration with the highest steady values for experiment 1 and lower values

for experiments 2-6. Notably, however, the pH is higher than that of the injected brine. It is highest for Ketton, then Estailades and then Portland, indicating different amounts of transport and reaction in the experiments: this explains why injection pH is not a good predictor of the behaviour for different rocks. The effluent pH is consistent with the ordering of effective reaction rates, Figure 6.21(d): where the reaction is faster, there the pH in the effluent is higher.

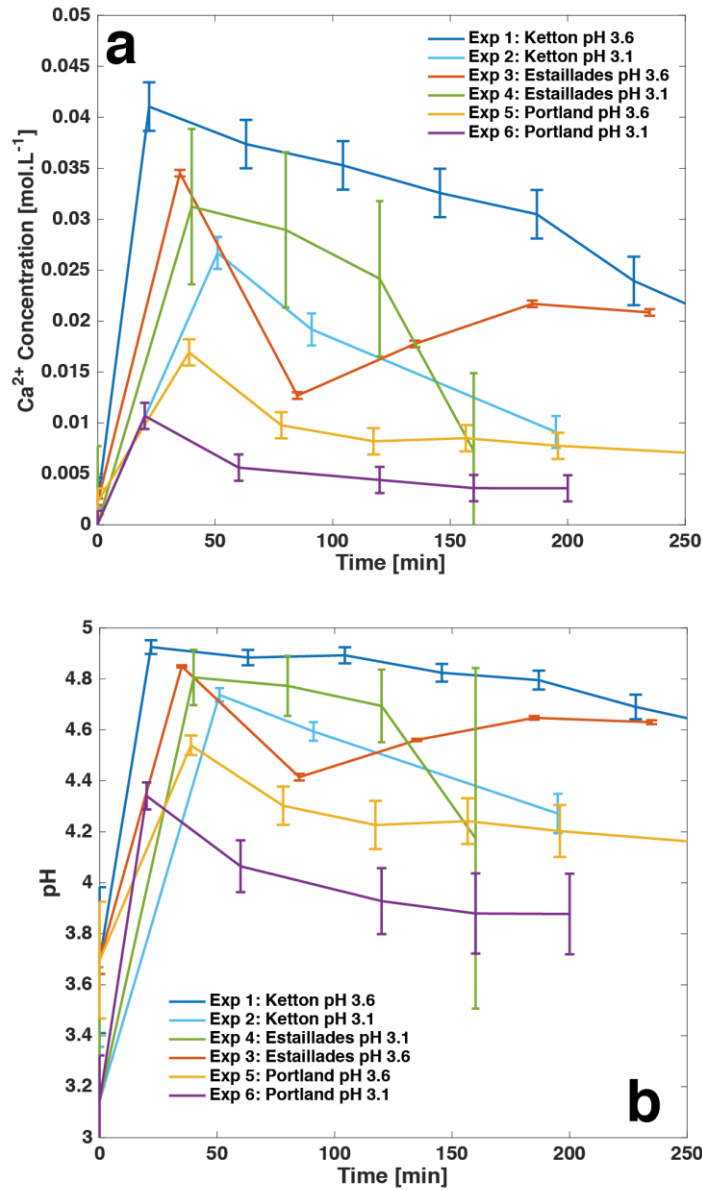


Figure 6.22 (a) Ca²⁺ concentration [mol.L⁻¹] measured in effluent and (b) pH as calculated from Ca²⁺ concentration by the method presented in Leal et al. [240] versus time [min]. The error bars represent the standard error of the concentration and pH values.

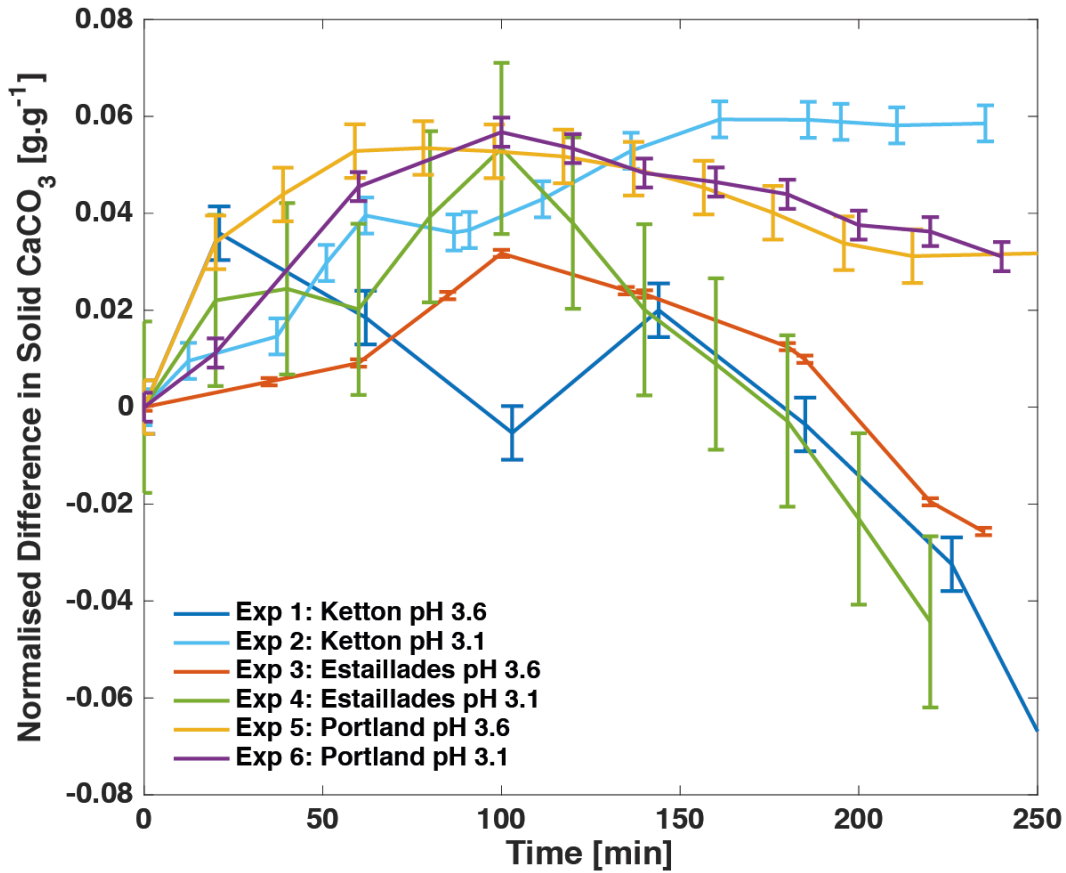


Figure 6.23 A comparison of effluent measured and CT observed fluid-solid reaction plotted as the difference in dissolved solid CaCO_3 versus time calculated using Eq. 6.17.

We then compare the mass of dissolved solid predicted from the effluent sample to the mass of dissolved solid observed by μ -CT. The normalised difference, Figure 6.23, is found from:

$$\Delta\text{CaCO}_{3(s)\#} \text{normalised} = \frac{\text{CaCO}_{3\text{effluent}\#} - \text{CaCO}_{3(s)\text{CT}\#}}{\text{CaCO}_{3\text{effluent}\#}} \quad (6.17)$$

where the mass of solid calcium carbonate remaining in the sample is predicted by effluent analysis by subtracting the cumulative mass of calcium measured in the effluent samples from the mass of calcium carbonate in the initial CT image (time zero) at each time step:

$$\begin{aligned}
CaCO_{3_{effluent\#}} &= CaCO_{3_{(s)_{CT\ time=0}}} \\
&- \frac{M_{calcite}}{M_{Ca^{2+}}} \sum_{i=0}^{i=\#} ([Ca^{2+}]_{effluent} - [Ca^{2+}]_{reactor}) F \Delta t_i
\end{aligned} \tag{6.18}$$

where t is time [s], F is the flowrate [$m^3.s^{-1}$], $M_{Ca^{2+}}$ is the molecular mass of Ca^{2+} , $M_{calcite}$ is the molecular mass of calcite, and $\#$ is the effluent sample number and $CaCO_{3_{(s)_{CT}}}$ is the total mass of solid calcium carbonate in the core calculated from the initial CT scan. Here the concentrations are measured in $moles.m^{-3}$.

The total mass of calcium carbonate is calculated at each time from the CT images with:

$$CaCO_{3_{(s)_{CT_t}}} = (1 - \phi_{total_t}) \rho_{calcite} \pi d^2 h \tag{6.19}$$

where d is the core radius h is the total core length and $\rho_{calcite}$ is the density of calcite. We observe that there is an agreement between the CT observed dissolution and those predicted by effluent analysis to within 6%. Most of the time the difference is positive, indicating that effluent analysis may be missing some of the dissolution. This could be due to small particles that are left behind when the effluent sample is transferred from the sampling syringe into test tubes for ICP-MS analysis or slightly differing dissolution rates in the unimaged portions of the core.

Moreover, we can use the pH measured in the experiment and equation 5 to compare the image-measured reaction rate and assess whether batch-measured effective reaction rates can be used to predict pore scale effective reaction rates from effluent-measured pH [Table 6.8]. We use the values of pH calculated from the effluent Ca^{2+} concentration and image-measured r_{eff} values from ~ 180 minutes which is when we observe that the rate of reaction has reached a quasi-equilibrium state for all experiments. The surface area used in our r_{eff} calculations is the image-measured surface area. Peng [46] found that the geometric surface area of a cleaved piece of calcite mineral was accurate to within 0.2% for calculating batch reaction rates. We find that the values of pH calculated from the effluent Ca^{2+} concentration are a reasonably good predictor of image-observed reaction rate to within a factor of two for experiments 1 and 3. However, as reactive flow complexity increases and the dissolution regime changes from uniform to channelling the prediction becomes less accurate. Experiments 2 and 4 are predicted to have an effective reaction rate that is 6 times higher than those observed and experiment 5 and 6 are predicted to be 18 times higher. Had we used the injected pH the discrepancies would have been even higher, with an over-estimate of likely rate by up to a factor of 100.

Table 6.8 Image measured vs. pH predicted reaction rates at time ~180 minutes. The error represents the standard error of the effluent calcium content.

Experiment #	Image observed r_{eff} [mol.m ⁻² s ⁻¹] [eq 6.12]	Effluent Calculated pH	Effluent Calculated r_{exp} [mol.m ⁻² s ⁻¹] [eq 6.16]
Experiment 1: Ketton pH 3.6	3.27×10^{-5}	4.80 ± 0.04	$1.6 \times 10^{-5} \pm 1.4 \times 10^{-6}$
Experiment 2: Ketton pH 3.1	8.09×10^{-6}	4.27 ± 0.08	$5.5 \times 10^{-5} \pm 9.2 \times 10^{-6}$
Experiment 3: Estailades pH 3.6	1.59×10^{-5}	4.65 ± 0.01	$2.3 \times 10^{-5} \pm 5.3 \times 10^{-7}$
Experiment 4: Estailades pH 3.1	1.10×10^{-5}	4.17 ± 0.67	$6.8 \times 10^{-5} \pm 5.4 \times 10^{-5}$
Experiment 5: Portland pH 3.6	3.57×10^{-6}	4.20 ± 0.10	$6.4 \times 10^{-5} \pm 1.3 \times 10^{-5}$
Experiment 6: Portland pH 3.1	7.46×10^{-6}	3.88 ± 0.16	$1.4 \times 10^{-4} \pm 4.2 \times 10^{-5}$

We believe that discrepancy between predicted and measured reaction rates is due to flow limitations in removing reaction products from the rock surface. Figure 6.24 depicts the interplay between flow and transport processes during uniform dissolution and channel formation. During uniform dissolution [Figure 6.24a] the flow velocity distribution is relatively narrow and the majority of the pore space experiences relatively high velocities. Thus, the reaction products are efficiently moved away from the surface of the grains and are swept away down the advective flow streamlines. This causes the reaction to be relatively uniform and the measured effluent pH to be high, as the Ca²⁺ concentration in the effluent is representative of the pore fluid. This also implies that for these samples the resolution of μ -CT scanning adequately captures the surface area available for reaction in the surface-reaction-controlled regime. However during channelling [Figure 6.24b], the velocity distribution spans many orders of magnitude and there are many regions of the pore space that do not experience fast flow. The Ca²⁺ cations are then less easily removed from these diffusive regions and are effectively trapped and cause local pH rise (and thus less reaction) in the slow pore space regions. The majority of the injected reactive fluid, however, moves through the centre of the fast flow paths without encountering or reacting with the rock grains except on the channel walls. Thus, during uniform dissolution the effluent pH measurement is indicative of the average pore space reaction and in channelling the effluent pH measurement is only a measure of the reaction within the fast flow paths.

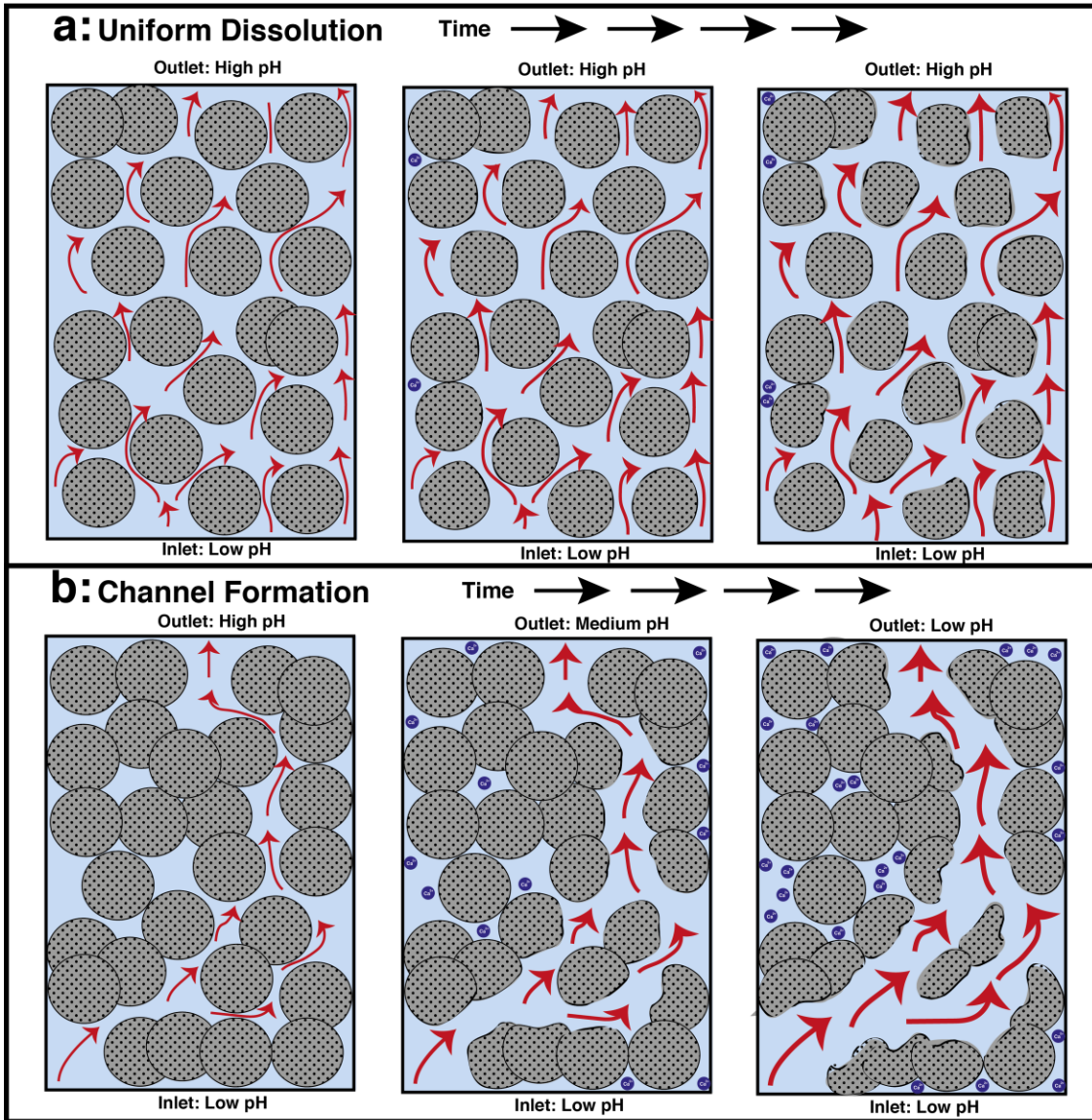


Figure 6.24 A schematic of the flow and transport processes through time during (a) uniform dissolution and (b) channel formation. Rock grains (grey circles) are dissolved in advectively-dominated regions of fast flow (red arrows). Ca^{2+} ions (dark blue circles) are slow to move out of the diffusive regions of the pore space.

6.3.4 Conclusions

We have found that the initial brine pH and initial pore structure have a clear influence on the reaction-induced development of porosity and permeability at the pore scale. We observe uniform dissolution in a homogenous carbonate at an injection pH of 3.6 and channelling at pH 3.1 and high initial pore-space heterogeneity. Additionally in heterogeneous samples we see faster channelling with increasing heterogeneity and decreasing pH of the injected brine. We find that effluent pH is a reasonably good predictor of effective reaction rate during uniform dissolution. However, pH is a poor predictor of the effective reaction rate during channelling, but can be used to help identify dissolution regime with a lower effluent pH being more likely to be caused by channelized flow. Moreover, we observe that the overall reaction rates are up to 18 times lower than batch reaction rates at the effluent pH due to transport and flow limitations at the fluid/solid interface.

Bench-top x-ray microtomography coupled with a reservoir condition flow apparatus and effluent sampling provides an accessible experimental tool that is adaptable to many applications. Our method integrates experiment and modelling to explore the dynamics of reservoir condition reactive flow at the micron scale.

7 Conclusions and Future Work

7.1 Conclusions

This thesis presents a novel methodology for non-invasive dynamic imaging of reaction in porous media at representative subsurface conditions using x-ray microtomography. This research has focussed on developing a collection of techniques for analysing a range of pore-scale dissolution behaviour that has focused on three experimental datasets:

- 1) Laboratory *in situ* dynamic imaging of reaction in a homogeneous carbonate.
- 2) Fast synchrotron *in situ* dynamic imaging of reaction in two heterogeneous carbonates at multiple flow conditions.
- 3) Laboratory *in situ* dynamic imaging of reaction in three carbonates at multiple reactive conditions.

For each of these datasets a suite of image processing workflows was developed to analyse the images for properties such as surface area, porosity, and grain size. Pore-scale models were used to extract key petrophysical properties such as connectivity, permeability, and velocity distributions. Furthermore, dimensionless numbers were defined to look at the evolving flow and reactive state of the system in response to dissolution.

First, we used x-ray micro-tomography to investigate dynamic pore structure evolution *in situ* at temperatures and pressures representative of underground reservoirs and aquifers. We found an approximate doubling of porosity with only a 3.6% increase in surface area to volume ratio measured from the images. We used pore-scale direct simulation and network modeling on the images quantify an order of magnitude increase in permeability and an appreciable alteration of the velocity field. We studied the uniform reaction regime, with dissolution throughout the core. However, at the pore scale, we saw variations in the degree of dissolution with an overall reaction rate, which was approximately 16 times lower than estimated from batch measurements using the injected pH. This work implies that in heterogeneous rocks, pore-scale transport of reactants limits dissolution and can reduce the average effective reaction rate by an order of magnitude.

We then use fast synchrotron tomography to investigate the impact of initial pore structure and velocity field heterogeneity on the dynamics of fluid/solid reaction at high Péclet numbers (fast flow) and low Damköhler number (relatively slow reaction rates). The dynamic changes in porosity, permeability, and reaction rate were examined using image analysis and flow modelling. We found that, depending on initial pore structure and flow conditions, the porosity can either increase uniformly through time along the length of the samples, or may exhibit a spatially and temporally varying increase that is attributed to channel formation, a

process that is distinct from wormholing. The dissolution regime was structure-dependent: Estailades with a higher porosity showed more uniform dissolution, while the lower porosity Portland experienced channel formation. The effective reaction rates were up to two orders of magnitude lower than those measured on a flat substrate with no transport limitations, indicating that the transport of reactant and product is severely hampered away from fast flow channels.

Finally, we explore the impact of brine acidity and initial pore structure on the dynamics of fluid/solid reaction at high Péclet numbers (fast flow) and low Damköhler number (relatively slow reaction rates) with the inclusion of effluent analysis using a laboratory μ -CT scanner. The images were binarized, used as inputs into flow simulations, and analysed for dynamic changes in porosity, permeability, and reaction rate. Additionally, the effluent samples were used to verify the image-measured porosity changes. We found that initial brine acidity and pore structure determine the type of dissolution. This is either uniform where the porosity increases evenly both spatially and temporally, or channelling where the porosity increase is concentrated in preferential flow paths. Ketton, which has a relatively homogeneous pore structure, dissolved uniformly at the higher pH and showed more channelized flow at lower pH. In increasingly complex carbonates, channelized flow was observed at both acidities with the channel forming faster at lower pH. We find that effluent pH is a reasonably good predictor of effective reaction rate during uniform dissolution. However, pH is a poor predictor of the effective reaction rate during channelling, but can be used to help identify dissolution regime with a lower effluent pH being more likely to be caused by channelized flow. Moreover, we observe that the overall reaction rates are up to 18 times lower than batch reaction rates at the effluent pH due to transport and flow limitations at the fluid/solid interface.

7.2 Future work

While the methodology presented in this thesis has been used to study pore-scale reaction, it can be applied to many other fields of research in both single and multiphase flow in porous media. Additionally, the dynamic image datasets provided by this work can be used in the calibration and verification of pore-scale reactive transport models that can then confidently be applied to a large range of other uses.

Moreover this work represents only the tip of the iceberg when exploring the impact of heterogeneity and flow and transport conditions on reaction dynamics. Carbonate rocks vary considerably in both physical and chemical complexity. The methodologies developed in this thesis must be applied to many more rocks at the complete natural range of conditions to develop the knowledge base for distilling the controlling reaction mechanisms [149] for upscaling.

In many injection scenarios, the flow dynamics are not a single-phase problem and have not only scCO₂, but oil and organic contaminants that change the way reactive fluid behaves in the system. The methodologies developed in this thesis can

be combined with other methodologies (e.g. [177, 204]) to look at multiphase reaction under an abundance of conditions applicable to a range of storage options.

One outstanding issue in this work is how the dissolution regimes observed at the pore scale can be upscale to the core and ultimately reservoir scale. The channelling regime has thus far not been observed even on the core (~cm) scale. Experiments that compare scales under the same reactive conditions would be valuable in the upscaling effort.

In conclusion, this work represents only one of the first applications that are accessible with reservoir condition dynamic tomography. Both imaging technology and data science are advancing at a fantastic pace. Thus, there is great potential of these techniques to elucidate novel scale-independent means of describing flow in porous media.

8. References

- [1] Schlumberger. Carbonate Reservoirs: Meeting unique challenges to maximize recovery. 2007.
- [2] Jouzel J, V Masson-Delmotte, O Cattani, G Dreyfus, S Falourd, G Hoffmann, et al. Orbital and millennial Antarctic climate variability over the past 800,000 years. *Science*. 317 (2007) 793-6.
- [3] Lüthi D, M Le Floch, B Bereiter, T Blunier, J-M Barnola, U Siegenthaler, et al. High-resolution carbon dioxide concentration record 650,000–800,000 years before present. *Nature*. 453 (2008) 379-82.
- [4] Petit J-R, J Jouzel, D Raynaud, NI Barkov, J-M Barnola, I Basile, et al. Climate and atmospheric history of the past 420,000 years from the Vostok ice core, Antarctica. *Nature*. 399 (1999) 429-36.
- [5] Siegenthaler U, TF Stocker, E Monnin, D Lüthi, J Schwander, B Stauffer, et al. Stable carbon cycle–climate relationship during the late Pleistocene. *Science*. 310 (2005) 1313-7.
- [6] Keeling CD, TP Whorf. Atmospheric CO₂ records from sites in the SIO air sampling network. *Trends: a compendium of data on global change*. (2005) 16-26.
- [7] Tans P, R Keeling. Mauna Loa CO₂ monthly mean data. NOAA/ESRL and Scripps Institution of Oceanography) Available at <ftp://aftp.cmdl.noaa.gov/products/trends/co.2> (2013).
- [8] Metz B, O Davidson, H De Coninck, M Loos, L Meyer. IPCC, 2005: IPCC special report on carbon dioxide capture and storage. Prepared by Working Group III of the Intergovernmental Panel on Climate Change. Cambridge, United Kingdom and New York, NY, USA, 442 pp. (2005).
- [9] Wigley TM, R Richels, JA Edmonds. Economic and environmental choices in the stabilization of atmospheric CO₂ concentrations. (1996).
- [10] Ehrlich PR, AH Ehrlich. *The population explosion*. Simon and Schuster New York, 1990.
- [11] Association IE. *World Energy Outlook, 2012*.
- [12] Finley M. *BP statistical review of world energy. BP technical report 2013*.
- [13] Stern NH, HMs Treasury. *Stern Review: The economics of climate change*. HM treasury London, 2006.
- [14] Mitigation CC. *IPCC special report on renewable energy sources and climate change mitigation*. (2011).
- [15] Davis SJ, K Caldeira, HD Matthews. Future CO₂ emissions and climate change from existing energy infrastructure. *Science*. 329 (2010) 1330-3.
- [16] Lackner KS. A guide to CO (2) sequestration. *Science*. 300 (2003) 1677.
- [17] Lackner KS, CH Wendt, DP Butt, EL Joyce, DH Sharp. Carbon dioxide disposal in carbonate minerals. *Energy*. 20 (1995) 1153-70.
- [18] Lackner KS. Carbonate chemistry for sequestering fossil carbon. *Annu Rev Energy Env*. 27 (2002) 193-232.
- [19] Vandeginste V, NL Rafiuddin, A Peskin. Three-dimensional reconstruction of diagenetic geobodies for geological carbon dioxide storage. *Int J Greenh Gas Con*. 42 (2015) 319-28.

- [20] Wollenweber J, SA Alles, A Kronimus, A Busch, H Stanjek, BM Krooss. Caprock and overburden processes in geological CO₂ storage: An experimental study on sealing efficiency and mineral alterations. *Greenhouse Gas Control Technologies* 9. 1 (2009) 3469-76, doi: 10.1016/j.egypro.2009.02.138.
- [21] Pruess K, J Garcia. Multiphase flow dynamics during CO₂ disposal into saline aquifers. *Environ Geol.* 42 (2002) 282-95, doi: 10.1007/s00254-001-0498-3.
- [22] Nordbotten JM, MA Celia, S Bachu. Injection and storage of CO₂ in deep saline aquifers: Analytical solution for CO₂ plume evolution during injection. *Transport Porous Med.* 58 (2005) 339-60, doi: 10.1007/s11242-004-0670-9|10.1007/s11242-004-0670-9.
- [23] Bachu S. Review of CO₂ storage efficiency in deep saline aquifers. *Int J Greenh Gas Con.* (2015), doi: 10.1016/j.ijggc.2015.01.007.
- [24] Mohamed IM, J He, M Mahmoud, HA Nasr-El-Din. Effects of Pressure, CO₂ Volume, and the CO₂ to Water Volumetric Ratio on Permeability Change during CO₂ Sequestration. Abu Dhabi International Petroleum Exhibition and Conference. Society of Petroleum Engineers2010.
- [25] Izgec O, B Demiral, H Bertin, S Akin. CO₂ injection into saline carbonate aquifer formations I: laboratory investigation. *Transport Porous Med.* 72 (2008) 1-24.
- [26] Lucia FJ. Carbonate reservoir characterization: an integrated approach. Springer Science & Business Media, 2007.
- [27] Lasaga AC. Kinetic theory in the earth sciences. Princeton University Press, 2014.
- [28] Grigg RB, BJ McPherson, RK Svec. Laboratory and model tests at reservoir conditions for CO₂-brine-carbonate rock systems interactions. prepared for The Second Annual Conference on Carbon Capture and Sequestration Conference. Citeseer2003. pp. 5-8.
- [29] Mohamed IM, HA Nasr-El-Din. Formation Damage Due to CO₂ Sequestration in Deep Saline Carbonate Aquifers. SPE International Symposium and Exhibition on Formation Damage Control. Society of Petroleum Engineers2012.
- [30] Birkholzer JT, JP Nicot, CM Oldenburg, QL Zhou, S Kraemer, K Bandilla. Brine flow up a well caused by pressure perturbation from geologic carbon sequestration: Static and dynamic evaluations. *Int J Greenh Gas Con.* 5 (2011) 850-61, doi: 10.1016/j.ijggc.2011.01.003.
- [31] Baines SJ, RH Worden. The long-term fate of CO₂ in the subsurface: natural analogues for CO₂ storage. Geological Society, London, Special Publications. 233 (2004) 59-85.
- [32] Thomas D, S Benson. Natural CO₂ fields as analogs for geologic CO₂ storage. Carbon Dioxide Capture for Storage in Deep Geologic Formations-Results from the CO₂ Capture Project: Vol 2-Geologic Storage of Carbon Dioxide with Monitoring and Verification. (2015) 687.
- [33] Boyd AD. Connections between community and emerging technology: Support for enhanced oil recovery in the Weyburn, Saskatchewan area. *Int J Greenh Gas Con.* 32 (2015) 81-9.
- [34] Qureshi F, O Gharbi, P Julien. The Interpretation of Permeability Changes During Acid Injection In Carbonates: A New Integrated Methodology. Abu Dhabi International Petroleum Exhibition and Conference. Society of Petroleum Engineers2015.

- [35] Kuuskraa V, M Wallace. CO₂-EOR set for growth as new CO₂ supplies emerge. *Oil & Gas Journal*. 112 (2014) 92-.
- [36] Safari A, F Rashidi, E Kazemzadeh, A Hassani. Determining optimum acid injection rate for a carbonate gas reservoir and scaling the result up to the field conditions: A case study. *Journal of Natural Gas Science and Engineering*. 20 (2014) 2-7.
- [37] Freitag NP. Chemical Reaction Mechanisms That Govern Oxidation Rates During In-Situ Combustion and High-Pressure Air Injection. SPE Heavy Oil Conference-Canada. Society of Petroleum Engineers 2014.
- [38] Sayed MAI, HA Nasr-El-Din. Reaction Rate of Emulsified Acids and Dolomite. SPE International Symposium and Exhibition on Formation Damage Control. Society of Petroleum Engineers 2012.
- [39] Williams B, M Whiteley. Hydrofluoric acid reaction with a porous sandstone. *Society of Petroleum Engineers Journal*. 11 (1971) 306-14.
- [40] Kaszuba JP, DR Janecky, MG Snow. Carbon dioxide reaction processes in a model brine aquifer at 200 C and 200 bars: implications for geologic sequestration of carbon. *Appl Geochem*. 18 (2003) 1065-80.
- [41] Kaszuba JP, DR Janecky, MG Snow. Experimental evaluation of mixed fluid reactions between supercritical carbon dioxide and NaCl brine: Relevance to the integrity of a geologic carbon repository. *Chem Geol*. 217 (2005) 277-93, doi: 10.1016/j.chemgeo.2004.12.014|10.1016/j.chemgeo.2004.12.014.
- [42] Duan Z, R Sun, C Zhu, I-M Chou. An improved model for the calculation of CO₂ solubility in aqueous solutions containing Na⁺, K⁺, Ca²⁺, Mg²⁺, Cl⁻, and SO₄²⁻. *Mar Chem*. 98 (2006) 131-9.
- [43] Chang Y-B, BK Coats, JS Nolen. A compositional model for CO₂ floods including CO₂ solubility in water. Permian Basin Oil and Gas Recovery Conference. Society of Petroleum Engineers 1996.
- [44] Duan Z, R Sun. An improved model calculating CO₂ solubility in pure water and aqueous NaCl solutions from 273 to 533 K and from 0 to 2000 bar. *Chem Geol*. 193 (2003) 257-71.
- [45] Peng C, JP Crawshaw, GC Maitland, JM Trusler, D Vega-Maza. The pH of CO₂-saturated water at temperatures between 308K and 423K at pressures up to 15MPa. *J Supercrit Fluid*. 82 (2013) 129-37, doi: 10.1016/j.supflu.2013.07.001.
- [46] Peng C. Chemical Interactions between Carbon Dioxide Acidified Aqueous Fluids and Carbonate Minerals: Imperial College London; 2015.
- [47] Nordahl K, PS Ringrose. Identifying the representative elementary volume for permeability in heterolithic deposits using numerical rock models. *Mathematical geosciences*. 40 (2008) 753-71.
- [48] Bear J. Dynamics of Fluids in Porous Media. Courier Dover Publications, 1972.
- [49] Bijeljic B, P Mostaghimi, MJ Blunt. Insights into non-Fickian solute transport in carbonates. *Water Resour Res*. 49 (2013) 2714-28.
- [50] Mostaghimi P, MJ Blunt, B Bijeljic. Computations of absolute permeability on micro-CT images. *Mathematical Geosciences*. 45 (2013) 103-25.

- [51] Span R, W Wagner. A new equation of state for carbon dioxide covering the fluid region from the triple-point temperature to 1100 K at pressures up to 800 MPa. *J Phys Chem Ref Data*. 25 (1996) 1509-96.
- [52] Peng C, JP Crawshaw, GC Maitland, JM Trusler. Kinetics of calcite dissolution in CO₂-saturated water at temperatures between (323 and 373) K and pressures up to 13.8 MPa. *Chem Geol*. 403 (2015) 74-85, doi: 10.1016/j.chemgeo.2015.03.012.
- [53] Carroll JJ, JD Slupsky, AE Mather. The solubility of carbon dioxide in water at low pressure. *J Phys Chem Ref Data*. 20 (1991) 1201-9.
- [54] Covington AK, R Bates, R Durst. Definition of pH scales, standard reference values, measurement of pH and related terminology (Recommendations 1984). *Pure Appl Chem*. 57 (1985) 531-42.
- [55] Bachu S, WD Gunter, EH Perkins. AQUIFER DISPOSAL OF CO₂ - HYDRODYNAMIC AND MINERAL TRAPPING. *Energy Convers Manage*. 35 (1994) 269-79, doi: 10.1016/0196-8904(94)90060-4.
- [56] Kaszuba JP, DR Janecky, MG Snow. Carbon dioxide reaction processes in a model brine aquifer at 200 degrees C and 200 bars: implications for geologic sequestration of carbon. *Appl Geochem*. 18 (2003) 1065-80, doi: Doi 10.1016/S0883-2927(02)00239-1.
- [57] Emberley S, I Hutcheon, M Shevalier, K Durocher, WD Gunter, EH Perkins. Geochemical monitoring of fluid-rock interaction and CO₂ storage at the Weyburn CO₂-injection enhanced oil recovery site, Saskatchewan, Canada. *Energy*. 29 (2004) 1393-401, doi: 10.1016/j.energy.2004.03.073.
- [58] Gherardi F, TF Xu, K Pruess. Numerical modeling of self-limiting and self-enhancing caprock alteration induced by CO₂ storage in a depleted gas reservoir. *Chem Geol*. 244 (2007) 103-29, doi: 10.1016/j.chemgeo.2007.06.009.
- [59] Cantucci B, G Montegrossi, O Vaselli, F Tassi, F Quattrocchi, EH Perkins. Geochemical modeling of CO₂ storage in deep reservoirs: The Weyburn Project (Canada) case study. *Chem Geol*. 265 (2009) 181-97, doi: 10.1016/j.chemgeo.2008.12.029.
- [60] Carroll S, Y Hao, R Aines. Geochemical detection of carbon dioxide in dilute aquifers. *Geochem Trans*. 10 (2009), doi: 10.1186/1467-4866-10-4.
- [61] Bacci G, A Korre, S Durucan. An experimental and numerical investigation into the impact of dissolution/precipitation mechanisms on CO₂ injectivity in the wellbore and far field regions. *Int J Greenh Gas Con*. 5 (2011) 579-88, doi: 10.1016/j.ijggc.2010.05.007.
- [62] Gharbi O. Fluid-Rock Interactions in Carbonates: Applications to CO₂ storage. London, UK: Imperial College London; 2014.
- [63] Galster H. pH measurement: fundamentals, methods, applications, instrumentation. VCH, 1991.
- [64] Spycher N, K Pruess. A phase-partitioning model for CO₂-brine mixtures at elevated temperatures and pressures: application to CO₂-enhanced geothermal systems. *Transport Porous Med*. 82 (2010) 173-96.
- [65] Wunsch A, AK Navarre-Sitchler, J Moore, JE McCray. Metal release from limestones at high partial-pressures of CO₂. *Chem Geol*. In Review (2013).
- [66] Moore J, M Adams, R Allis, S Lutz, S Rauzi. Mineralogical and geochemical consequences of the long-term presence of CO₂ in natural reservoirs: an example

- from the Springerville–St. Johns Field, Arizona, and New Mexico, USA. *Chem Geol.* 217 (2005) 365-85.
- [67] Rosenbauer RJ, T Koksalan, JL Palandri. Experimental investigation of CO₂–brine–rock interactions at elevated temperature and pressure: implications for CO₂ sequestration in deep-saline aquifers. *Fuel Process Technol.* 86 (2005) 1581-97.
- [68] Palandri JL, RJ Rosenbauer, YK Kharaka. Ferric iron in sediments as a novel CO₂ mineral trap: CO₂–SO₂ reaction with hematite. *Appl Geochem.* 20 (2005) 2038-48.
- [69] Rimmelé G, V Barlet-Gouédard, O Porcherie, B Goffé, F Brunet. Heterogeneous porosity distribution in Portland cement exposed to CO₂-rich fluids. *Cem Concr Res.* 38 (2008) 1038-48.
- [70] Lin H, T Fujii, R Takisawa, T Takahashi, T Hashida. Experimental evaluation of interactions in supercritical CO₂/water/rock minerals system under geologic CO₂ sequestration conditions. *Journal of Materials Science.* 43 (2008) 2307-15.
- [71] Suto Y, L Liu, N Yamasaki, T Hashida. Initial behavior of granite in response to injection of CO₂-saturated fluid. *Appl Geochem.* 22 (2007) 202-18.
- [72] Birkholzer JT, QL Zhou, CF Tsang. Large-scale impact of CO₂ storage in deep saline aquifers: A sensitivity study on pressure response in stratified systems. *Int J Greenh Gas Con.* 3 (2009) 181-94, doi: 10.1016/j.ijggc.2008.08.002|10.1016/j.ijggc.2008.08.002.
- [73] Li ZW, MZ Dong, SL Li, S Huang. CO₂ sequestration in depleted oil and gas reservoirs - caprock characterization and storage capacity. *Energy Convers Manage.* 47 (2006) 1372-82, doi: 10.1016/j.enconman.2005.08.023.
- [74] Giorgis T, M Carpita, A Battistelli. 2D modeling of salt precipitation during the injection of dry CO₂ in a depleted gas reservoir. *Energy Convers Manage.* 48 (2007) 1816-26.
- [75] Hurter S, D Labregere, J Berge. Simulations of dry-out and halite precipitation due to CO₂ injection. *AGU Fall Meeting Abstracts2007.* pp. 08.
- [76] Pruess K, N Müller. Formation dry - out from CO₂ injection into saline aquifers: 1. Effects of solids precipitation and their mitigation. *Water Resour Res.* 45 (2009).
- [77] Bandura AV, SN Lvov. The ionization constant of water over wide ranges of temperature and density. *J Phys Chem Ref Data.* 35 (2006) 15-30.
- [78] Wolf-Gladrow DA, RE Zeebe, C Klaas, A Körtzinger, AG Dickson. Total alkalinity: The explicit conservative expression and its application to biogeochemical processes. *Mar Chem.* 106 (2007) 287-300.
- [79] Manov GG, RG Bates, WJ Hamer, S Acree. Values of the Constants in the Debye—Hückel Equation for Activity Coefficients1. *J Am Chem Soc.* 65 (1943) 1765-7.
- [80] Helgeson HC, DH Kirkham. Theoretical prediction of the thermodynamic behavior of aqueous electrolytes at high pressures and temperatures; II, Debye-Huckel parameters for activity coefficients and relative partial molal properties. *Am J Sci.* 274 (1974) 1199-261.
- [81] Waters JF, FJ Millero. The free proton concentration scale for seawater pH. *Mar Chem.* 149 (2013) 8-22.
- [82] Bates RG, AK Vihh. Determination of pH: theory and practice. *J Electrochem Soc.* 120 (1973) 263C-C.

- [83] Bethke C. Geochemical reaction modeling: Concepts and applications. Oxford University Press, 1996.
- [84] Parkhurst DL. User's guide to PHREEQC: A computer program for speciation, reaction-path, advective-transport, and inverse geochemical calculations. (1995).
- [85] Kinniburgh D, D Cooper. PhreePlot: Creating graphical output with PHREEQC. (2011).
- [86] Millero FJ. The physical chemistry of natural waters. Pure Appl Chem. 57 (1985) 1015-24.
- [87] Stillinger FH. Theory and molecular models for water. Adv Chem Phys. 31 (1975) 10.
- [88] Rapaport D. Hydrogen bonds in water: Network organization and lifetimes. Mol Phys. 50 (1983) 1151-62.
- [89] Chen S, J Teixeira. Structure and dynamics of low-temperature water as studied by scattering techniques. Adv Chem Phys. 64 (1986).
- [90] Delleur JW. The handbook of groundwater engineering. CRC press, 2006.
- [91] Alkattan M, EH Oelkers, J-L Dandurand, J Schott. Experimental studies of halite dissolution kinetics, 1 The effect of saturation state and the presence of trace metals. Chem Geol. 137 (1997) 201-19.
- [92] Barrett W, W Wallace. Studies of NaCl-KCl Solid Solutions. I. Heats of Formation, Lattice Spacings, Densities, Schottky Defects and Mutual Solubilities1, 2. J Am Chem Soc. 76 (1954) 366-9.
- [93] Morse JW, RS Arvidson. The dissolution kinetics of major sedimentary carbonate minerals. Earth-Sci Rev. 58 (2002) 51-84.
- [94] Lasaga AC. Chemical kinetics of water - rock interactions. Journal of Geophysical Research: Solid Earth (1978–2012). 89 (1984) 4009-25.
- [95] Morse JW, FT Mackenzie. Geochemistry of sedimentary carbonates. (1990).
- [96] Busenberg E, L Plummer. A comparative study of the dissolution and crystal growth kinetics of calcite and aragonite. Studies in diagenesis. US Geol. Surv. Bull1986. pp. 139-68.
- [97] Wollast R. Rate and mechanism of dissolution of carbonates in the system CaCO₃-MgCO₃. IN: Aquatic Chemical Kinetics: Reaction Rates of Processes in Natural Waters Environmental Science and Technology Series John Wiley & Sons, New York 1990 p 431-445 6 fig, 1 tab, 26 ref. (1990).
- [98] Sjöberg E. A fundamental equation for calcite dissolution kinetics. Geochim Cosmochim Acta. 40 (1976) 441-7.
- [99] Plummer L, T Wigley, D Parkhurst. The kinetics of calcite dissolution in CO₂-water systems at 5 degrees to 60 degrees C and 0.0 to 1.0 atm CO₂. Am J Sci. 278 (1978) 179-216.
- [100] Ennis-King J, L Paterson. Engineering aspects of geological sequestration of carbon dioxide. SPE Asia Pacific Oil and Gas Conference and Exhibition. Society of Petroleum Engineers2002.
- [101] Freeze RA, JA Cherry, C JA. Groundwater, 1979.
- [102] Compton RG, KL Pritchard, PR Unwin. The dissolution of calcite in acid waters: mass transport versus surface control. Freshwat Biol. 22 (1989) 285-8.

- [103] Chou L, RM Garrels, R Wollast. Comparative study of the kinetics and mechanisms of dissolution of carbonate minerals. *Chem Geol.* 78 (1989) 269-82.
- [104] Temam R. Navier-Stokes equations: theory and numerical analysis. American Mathematical Soc., 2001.
- [105] Whitaker S. Flow in porous media I: A theoretical derivation of Darcy's law. *Transport Porous Med.* 1 (1986) 3-25.
- [106] Fetter CW, C Fetter Jr. Contaminant hydrogeology. Prentice hall Upper Saddle River, NJ, 1999.
- [107] Gramling CM, CF Harvey, LC Meigs. Reactive transport in porous media: A comparison of model prediction with laboratory visualization. *Environ Sci Technol.* 36 (2002) 2508-14.
- [108] Ott H, K de Kloe, M van Bakel, F Vos, A van Pelt, P Legerstee, et al. Core-flood experiment for transport of reactive fluids in rocks. *Rev Sci Instrum.* 83 (2012) 084501, doi: 10.1063/1.4746997.
- [109] Hart DJ, KR Bradbury, DT Feinstein. The vertical hydraulic conductivity of an aquitard at two spatial scales. *Ground Water.* 44 (2006) 201-11, doi: 10.1111/j.1745-6584.2005.00125.x|10.1111/j.1745-6584.2005.00125.x.
- [110] Siirila ER, AK Navarre-Sitchler, RM Maxwell, JE McCray. A quantitative methodology to assess the risks to human health from CO₂ leakage into groundwater. *Adv Water Resour.* 36 (2012) 146-64.
- [111] Atchley AL, RM Maxwell, AK Navarre-Sitchler. Using streamlines to simulate stochastic reactive transport in heterogeneous aquifers: Kinetic metal release and transport in CO₂ impacted drinking water aquifers. *Adv Water Resour.* (2012).
- [112] Atchley AL, R Maxwell, A Navarre-Sitchler. Human health risk assessment of CO₂ leakage into overlying aquifers using a stochastic, geochemical reactive transport approach. *Environ Sci Technol.* (2013).
- [113] Blunt MJ, B Bijeljic, H Dong, O Gharbi, S Iglauer, P Mostaghimi, et al. Pore-scale imaging and modelling. *Adv Water Resour.* 51 (2013) 197-216.
- [114] Walter A, E Frind, D Blowes, C Ptacek, J Molson. Modeling of multicomponent reactive transport in groundwater: 1. model development and evaluation. *Water Resour Res.* 30 (1994) 3137-48.
- [115] Tartakovsky AM, P Meakin, TD Scheibe, RME West. Simulations of reactive transport and precipitation with smoothed particle hydrodynamics. *J Comput Phys.* 222 (2007) 654-72.
- [116] Luquot L, P Gouze. Experimental determination of porosity and permeability changes induced by injection of CO₂ into carbonate rocks. *Chem Geol.* 265 (2009) 148-59, doi: 10.1016/j.chemgeo.2009.03.028.
- [117] Bird RB, WE Stewart, EN Lightfoot. Transport phenomena. 1960. Madison, USA. (1960).
- [118] Sahimi M. Flow and Transport Through Porous Media and Fractured Rock. VCH, Weinheim 1995.
- [119] Fredd CN, HS Fogler. Influence of transport and reaction on wormhole formation in porous media. *AIChE J.* 44 (1998) 1933-49, doi: doi:10.1002/aic.690440902.

- [120] Luquot L, O Rodriguez, P Gouze. Experimental Characterization of Porosity Structure and Transport Property Changes in Limestone Undergoing Different Dissolution Regimes. *Transport Porous Med.* 101 (2014) 507-32.
- [121] Daccord G, R Lenormand. Fractal patterns from chemical dissolution. *Nature.* 325 (1987) 41-3.
- [122] Daccord G, R Lenormand, O Lietard. Chemical dissolution of a porous medium by a reactive fluid—I. Model for the “wormholing” phenomenon. *Chem Eng Sci.* 48 (1993) 169-78.
- [123] Daccord G, O Lietard, R Lenormand. Chemical Dissolution of a Porous-medium by a Reactive Fluid .2. Convection vs Reaction, Behavior Diagram. *Chem Eng Sci.* 48 (1993) 179-86, doi: 10.1016/0009-2509(93)80294-z.
- [124] Gouze P, L Luquot. X-ray microtomography characterization of porosity, permeability and reactive surface changes during dissolution. *J Contam Hydrol.* 120 (2011) 45-55.
- [125] Maheshwari P, R Ratnakar, N Kalia, V Balakotaiah. 3-D simulation and analysis of reactive dissolution and wormhole formation in carbonate rocks. *Chem Eng Sci.* 90 (2013) 258-74, doi: 10.2118/171731-PA.
- [126] Kang Q, D Zhang, S Chen. Simulation of dissolution and precipitation in porous media. *Journal of Geophysical Research: Solid Earth (1978–2012).* 108 (2003).
- [127] Golfier F, C ZARCONI, B Bazin, R Lenormand, D Lasseux, M QUINTARD. On the ability of a Darcy-scale model to capture wormhole formation during the dissolution of a porous medium. *J Fluid Mech.* 457 (2002) 213-54.
- [128] Hung K, A Hill, K Sepehrnoori. A mechanistic model of wormhole growth in carbonate matrix acidizing and acid fracturing. *Journal of petroleum technology.* 41 (1989) 59-66.
- [129] Fredd C, S Fogler. Influence of Transport and Reaction on Wormhole Formations in Porous Media. *AIChE.* 44 (1998), doi: 10.1002/aic.690440902.
- [130] Cohen CE, D Ding, M Quintard, B Bazin. From pore scale to wellbore scale: Impact of geometry on wormhole growth in carbonate acidization. *Chemical Engineering Science.* 63 (2008) 3088-99.
- [131] Arvidson RS, IE Ertan, JE Amonette, A Luttge. Variation in calcite dissolution rates:: A fundamental problem? *Geochim Cosmochim Acta.* 67 (2003) 1623-34.
- [132] Alkattan M, EH Oelkers, J-L Dandurand, J Schott. An experimental study of calcite and limestone dissolution rates as a function of pH from– 1 to 3 and temperature from 25 to 80 C. *Chem Geol.* 151 (1998) 199-214.
- [133] Lund K, HS Fogler, C McCune, J Ault. Acidization—II. The dissolution of calcite in hydrochloric acid. *Chem Eng Sci.* 30 (1975) 825-35.
- [134] Noiriél C, D Bernard, P Gouze, X Thibault. Hydraulic properties and microgeometry evolution accompanying limestone dissolution by acidic water. *Oil & gas science and technology.* 60 (2005) 177-92.
- [135] Ziauddin ME, E Bize. The Effect of Pore Scale Heterogeneities on Carbonate Stimulation Treatments. *SPE Middle East Oil and Gas Show and Conference.* Society of Petroleum Engineers 2007.
- [136] Bryant SL, KE Thompson. Theory, modeling and experiment in reactive transport in porous media. *Current opinion in colloid & interface science.* 6 (2001) 217-22.

- [137] White SP, GJ Weir, WM Kissling. Numerical Simulation of CO₂ Sequestration in Natural CO₂ Reservoirs on the Colorado Plateau. Industrial Research Ltd., 2001.
- [138] White SP, GJ Weir, WM Kissling. Numerical simulation of CO₂ sequestration in natural CO₂ reservoirs on the Colorado Plateau. Proceedings of First National Conference on Carbon Sequestration, Washington, DC2001.
- [139] Swoboda-Colberg NG, JI Drever. Mineral dissolution rates in plot-scale field and laboratory experiments. *Chem Geol.* 105 (1993) 51-69, doi: 10.1016/0009-2541(93)90118-3.
- [140] Steefel CI, DJ DePaolo, PC Lichtner. Reactive transport modeling: An essential tool and a new research approach for the Earth sciences. *Earth Planet Sci Lett.* 240 (2005) 539-58.
- [141] Steefel C, C Appelo, B Arora, D Jacques, T Kalbacher, O Kolditz, et al. Reactive transport codes for subsurface environmental simulation. *Computational Geosciences.* 19 (2015) 445-78.
- [142] White AF, SL Brantley. The effect of time on the weathering of silicate minerals: why do weathering rates differ in the laboratory and field? *Chem Geol.* 202 (2003) 479-506.
- [143] Hayes JM, JR Waldbauer. The carbon cycle and associated redox processes through time. *Philosophical Transactions of the Royal Society of London B: Biological Sciences.* 361 (2006) 931-50.
- [144] Maher K. The dependence of chemical weathering rates on fluid residence time. *Earth Planet Sci Lett.* 294 (2010) 101-10.
- [145] Noiriél C, L Luquot, B Madé, L Raimbault, P Gouze, J Van Der Lee. Changes in reactive surface area during limestone dissolution: An experimental and modelling study. *Chem Geol.* 265 (2009) 160-70.
- [146] Mitchell AC, K Dideriksen, LH Spangler, AB Cunningham, R Gerlach. Microbially enhanced carbon capture and storage by mineral-trapping and solubility-trapping. *Environ Sci Technol.* 44 (2010) 5270-6.
- [147] Fredd C. Dynamic model of wormhole formation demonstrates conditions for effective skin reduction during carbonate matrix acidizing. SPE Permian Basin Oil and Gas Recovery Conference. Society of Petroleum Engineers2000.
- [148] Singurindy O, B Berkowitz. Flow, dissolution, and precipitation in dolomite. *Water Resour Res.* 39 (2003).
- [149] Noiriél C, CI Steefel, L Yang, D Bernard. Effects of pore-scale precipitation on permeability and flow. *Adv Water Resour.* (2015).
- [150] Singurindy O, B Berkowitz. Evolution of hydraulic conductivity by precipitation and dissolution in carbonate rock. *Water Resour Res.* 39 (2003).
- [151] Menke W. Geophysical data analysis: discrete inverse theory. Academic press, 2012.
- [152] Mettler Jr FA, PW Wiest, JA Locken, CA Kelsey. CT scanning: patterns of use and dose. *J Radiol Prot.* 20 (2000) 353.
- [153] Ritman EL. Micro-computed tomography-current status and developments. *Annu Rev Biomed Eng.* 6 (2004) 185-208.

- [154] Ellis B, C Peters, J Fitts, G Bromhal, D McIntyre, R Warzinski, et al. Deterioration of a fractured carbonate caprock exposed to CO₂ - acidified brine flow. *Greenhouse Gases: Science and Technology*. 1 (2011) 248-60.
- [155] Smith MM, Y Sholokhova, Y Hao, SA Carroll. Evaporite caprock integrity: An experimental study of reactive mineralogy and pore-scale heterogeneity during brine-CO₂ exposure. *Environ Sci Technol*. 47 (2012) 262-8.
- [156] Lamy - Chappuis B, D Angus, Q Fisher, C Grattoni, BW Yardley. Rapid porosity and permeability changes of calcareous sandstone due to CO₂ - enriched brine injection. *Geophys Res Lett*. 41 (2014) 399-406.
- [157] Flannery BP, HW Deckman, WG Roberge, KL D'AMICO. Three-dimensional X-ray microtomography. *Science*. 237 (1987) 1439-44.
- [158] Berg S, H Ott, S Klapp, A Schwing, R Neiteler, N Brussee, et al. Multiphase Flow in Porous Rock imaged under dynamic flow conditions with fast X-ray computed micro-tomography. *EGU General Assembly Conference Abstracts2013*. pp. 5544.
- [159] Wildenschild D, AP Sheppard. X-ray imaging and analysis techniques for quantifying pore-scale structure and processes in subsurface porous medium systems. *Adv Water Resour*. 51 (2013) 217-46.
- [160] Raeini AQ, MJ Blunt, B Bijeljic. Modelling two-phase flow in porous media at the pore scale using the volume-of-fluid method. *J Comput Phys*. 231 (2012) 5653-68, doi: 10.1016/j.jcp.2012.04.011.
- [161] Mostaghimi P, B Bijeljic, MJ Blunt. Simulation of flow and dispersion on pore-space images. *SPE Annual Technical Conference and Exhibition, Italy doi2012*.
- [162] Bijeljic B, A Raeini, P Mostaghimi, MJ Blunt. Predictions of non-Fickian solute transport in different classes of porous media using direct simulation on pore-scale images. *Phys Rev E*. 87 (2013) 013011, doi: 10.1103/PhysRevE.87.013011.
- [163] Raeini AQ, B Bijeljic, MJ Blunt. Numerical modelling of sub-pore scale events in two-phase flow through porous media. *Transport Porous Med*. 101 (2014) 191-213.
- [164] Buffiere J-Y, E Maire, J Adrien, J-P Masse, E Boller. In situ experiments with X ray tomography: an attractive tool for experimental mechanics. *Experimental mechanics*. 50 (2010) 289-305.
- [165] Qajar J, N Francois, CH Arns. Microtomographic Characterization of Dissolution-Induced Local Porosity Changes Including Fines Migration in Carbonate Rock. *SPE Journal*. 18 (2013) 545-62.
- [166] Qajar J. *Reactive Flow in Carbonate Cores via Digital Core Analysis: The University of New South Wales; 2012*.
- [167] Iglauer S, A Paluszny, CH Pentland, MJ Blunt. Residual CO₂ imaged with X - ray micro - tomography. *Geophys Res Lett*. 38 (2011).
- [168] Andrew M, B Bijeljic, MJ Blunt. Pore - scale imaging of geological carbon dioxide storage under in situ conditions. *Geophys Res Lett*. 40 (2013) 3915-8.
- [169] Andrew M, B Bijeljic, MJ Blunt. Pore-scale imaging of trapped supercritical carbon dioxide in sandstones and carbonates. *Int J Greenh Gas Con*. 22 (2014) 1-14, doi: 10.1016/j.ijggc.2013.12.018.
- [170] Andrew M. *Reservoir-Condition Pore-Scale Imaging of Multiphase Flow*. London: Imperial College London; 2015.

- [171] Carroll S, Y Hao, M Smith, Y Sholokhova. Development of scaling parameters to describe CO₂-rock interactions within Weyburn-Midale carbonate flow units. *Int J Greenh Gas Con.* 16 (2013) S185-S93.
- [172] Smith MM, Y Sholokhova, Y Hao, SA Carroll. CO₂-induced dissolution of low permeability carbonates. Part I: Characterization and experiments. *Adv Water Resour.* 62 (2013) 370-87, doi: 10.1016/j.advwatres.2013.09.008.
- [173] Hao Y, M Smith, Y Sholokhova, S Carroll. CO₂-induced dissolution of low permeability carbonates. Part II: Numerical modeling of experiments. *Adv Water Resour.* 62 (2013) 388-408, doi: 10.1016/j.advwatres.2013.09.009.
- [174] Luquot L, P Gouze. Experimental determination of porosity and permeability changes induced by injection of CO₂ into carbonate rocks. *Chem Geol.* 265 (2009) 148-59.
- [175] Gharbi O, B Bijeljic, E Boek, MJ Blunt. Changes in Pore Structure and Connectivity Induced by CO₂ Injection in Carbonates: A Combined Pore-Scale Approach. *Energy Procedia.* 37 (2013) 5367-78.
- [176] Berg S, H Ott, SA Klapp, A Schwing, R Neiteler, N Brussee, et al. Real-time 3D imaging of Haines jumps in porous media flow. *Proc Natl Acad Sci USA.* 110 (2013) 3755-9, doi: 10.1073/pnas.1221373110.
- [177] Andrew M, H Menke, MJ Blunt, B Bijeljic. The Imaging of Dynamic Multiphase Fluid Flow Using Synchrotron-Based X-ray Microtomography at Reservoir Conditions. *Transport Porous Med.* (2015) 1-24, doi: 10.1007/s11242-015-0553-2.
- [178] Armstrong R, H Ott, A Georgiadis, M Rucker, S Berg. Pore-scale displacement processes and relaxation dynamics in multiphase flow imaged at sub-second temporal resolution. *AGU Fall Meeting Abstracts2014.* pp. 0756.
- [179] Noiriel C, P Gouze, B Made. 3D analysis of geometry and flow changes in a limestone fracture during dissolution. *J Hydrol.* 486 (2013) 211-23, doi: 10.1016/j.jhydrol.2013.01.035.
- [180] Noiriel C, P Gouze, D Bernard. Investigation of porosity and permeability effects from microstructure changes during limestone dissolution. *Geophys Res Lett.* 31 (2004).
- [181] Noiriel C. Resolving time-dependent evolution of pore-scale structure, permeability and reactivity using X-ray microtomography. *Rev Mineral Geochem.* 80 (2015) 247-85.
- [182] Lambert J-H. *JH Lambert, ... Photometria, sive de Mensura et gradibus luminis, colorum et umbrae. sumptibus viduae E. Klett, 1760.*
- [183] Beer A. Bestimmung der Absorption des rothen Lichts in farbigen Flüssigkeiten. *Annalen der Physik und Chemie.* 86 (1852) 78-88.
- [184] Bouguer P. *Essai d'Optique, sur la gradation de la lumiere. Claude Jombert, 1729.*
- [185] Reed SJB. *Electron microprobe analysis and scanning electron microscopy in geology. Cambridge University Press, 2005.*
- [186] Radon J. 1.1 über die bestimmung von funktionen durch ihre integralwerte längs gewisser mannigfaltigkeiten. *Classic papers in modern diagnostic radiology.* 5 (2005).
- [187] ASTM. *Standard Guide for Computed Tomography (CT) Imaging. ASTM1992.* pp. 690-713.

- [188] Chao A. Handbook of accelerator physics and engineering. World scientific, 1999.
- [189] Luchini P, H Motz. Undulators and free-electron lasers. Oxford University Press, USA, 1990.
- [190] Archie GE. Classification of carbonate reservoir rocks and petrophysical considerations. AAPG Bulletin. 36 (1952) 278-98.
- [191] Lønøy A. Making sense of carbonate pore systems. AAPG bulletin. 90 (2006) 1381-405.
- [192] Choquette PW, LC Pray. Geologic nomenclature and classification of porosity in sedimentary carbonates. AAPG bulletin. 54 (1970) 207-50.
- [193] Cantrell DL, RM Hagerty. Microporosity in arab formation carbonates, Saudi Arabia. GeoArabia. 4 (1999) 129-54.
- [194] American Association of Petroleum Geologists. 2016.
- [195] Münch B, P Trtik, F Marone, M Stampanoni. Stripe and ring artifact removal with combined wavelet—Fourier filtering. Opt Express. 17 (2009) 8567-91.
- [196] Schlüter S, A Sheppard, K Brown, D Wildenschild. Image processing of multiphase images obtained via X - ray microtomography: A review. Water Resour Res. 50 (2014) 3615-39, doi: 10.1002/2014WR015256.
- [197] Iassonov P, T Gebrenegus, M Tuller. Segmentation of X - ray computed tomography images of porous materials: A crucial step for characterization and quantitative analysis of pore structures. Water Resour Res. 45 (2009).
- [198] Ataman E, V Aatre, K Wong. Some statistical properties of median filters. Acoustics, Speech and Signal Processing, IEEE Transactions on. 29 (1981) 1073-5.
- [199] Buades A, B Coll, J-M Morel. A non-local algorithm for image denoising. Computer Vision and Pattern Recognition, 2005 CVPR 2005 IEEE Computer Society Conference on. 2 (2005) 60-5.
- [200] Buades A, B Coll, J-M Morel. Nonlocal image and movie denoising. Int J Comput Vision. 76 (2008) 123-39, doi: 10.1007/s11263-007-0052-1.
- [201] Li W. Mutual information functions versus correlation functions. J Stat Phys. 60 (1990) 823-37.
- [202] Lanczos C. An iteration method for the solution of the eigenvalue problem of linear differential and integral operators. United States Governm. Press Office, 1950.
- [203] Burger W, MJ Burge. Digital image processing: an algorithmic introduction using Java. Springer Science & Business Media, 2009.
- [204] Ott H, S Oedai. Wormhole formation and compact dissolution in single - and two - phase CO₂ - brine injections. Geophys Res Lett. 42 (2015) 2270-6, doi: 10.1002/2015GL063582.
- [205] Sheppard AP, RM Sok, H Averdunk. Techniques for image enhancement and segmentation of tomographic images of porous materials. Physica A. 339 (2004) 145-51.
- [206] Poludniowski G, G Landry, F DeBlois, P Evans, F Verhaegen. SpekCalc: a program to calculate photon spectra from tungsten anode x-ray tubes. Physics in medicine and biology. 54 (2009) N433.
- [207] Poludniowski GG. Calculation of x-ray spectra emerging from an x-ray tube. Part II. X-ray production and filtration in x-ray targets. Med Phys. 34 (2007) 2175-86.

- [208] Poludniowski GG, PM Evans. Calculation of x-ray spectra emerging from an x-ray tube. Part I. Electron penetration characteristics in x-ray targets. *Med Phys.* 34 (2007) 2164-74.
- [209] El-Maghraby R, C Pentland, S Iglauer, M Blunt. A fast method to equilibrate carbon dioxide with brine at high pressure and elevated temperature including solubility measurements. *J Supercrit Fluid.* 62 (2012) 55-9, doi: 10.1016/j.supflu.2011.11.002.
- [210] Menke HP, B Bijeljic, M Blunt. Reservoir Condition Imaging of Reactive Transport in Heterogeneous Carbonates Using Fast Synchrotron Tomography – Effect of Initial Pore structure and Flow Conditions. *Chem Geol.* 428 (2016) 15-26, doi: 10.1016/j.chemgeo.2016.02.030.
- [211] Sakata K, N Yamada, R Midorikawa, JC Wirfel, DL Potter, AGG Martinez. Inductively coupled plasma mass spectrometer and method. Google Patents2001.
- [212] Pokrovsky OS, SV Golubev, J Schott, A Castillo. Calcite, dolomite and magnesite dissolution kinetics in aqueous solutions at acid to circumneutral pH, 25 to 150 C and 1 to 55 atm pCO₂: new constraints on CO₂ sequestration in sedimentary basins. *Chem Geol.* 265 (2009) 20-32.
- [213] Dong H, MJ Blunt. Pore-network extraction from micro-computerized-tomography images. *Phys Rev E.* 80 (2009) 036307, doi: 10.1103/PhysRevE.80.036307.
- [214] Tanino Y, MJ Blunt. Capillary trapping in sandstones and carbonates: Dependence on pore structure. *Water Resour Res.* 48 (2012).
- [215] Menke HP, B Bijeljic, MG Andrew, MJ Blunt. Dynamic Three-Dimensional Pore-Scale Imaging of Reaction in a Carbonate at Reservoir Conditions. *Environ Sci Technol.* 49 (2015) 4407-14, doi: 10.1021/es505789f.
- [216] Banner JL, GN Hanson. Calculation of Simultaneous Isotopic and Trace-Element Variations during Water-Rock Interaction with Applications to Carbonate Diagenesis. *Geochim Cosmochim Acta.* 54 (1990) 3123-37, doi: Doi 10.1016/0016-7037(90)90128-8.
- [217] Mayer KU, EO Frind, DW Blowes. Multicomponent reactive transport modeling in variably saturated porous media using a generalized formulation for kinetically controlled reactions. *Water Resour Res.* 38 (2002) 13-1--21, doi: Artn 1174 Doi 10.1029/2001wr000862.
- [218] McLeod HO. Matrix acidizing. *Journal of Petroleum Technology.* 36 (1984) 2,055-2,69.
- [219] Herzog H, K Caldeira, J Reilly. An issue of permanence: Assessing the effectiveness of temporary carbon storage. *Clim Change.* 59 (2003) 293-310, doi: 10.1023/A:1024801618900.
- [220] Metz B, O Davidson, H De Coninck, M Loos, L Meyer. Carbon dioxide capture and storage. IPCC Geneva, Switzerland, 2005.
- [221] Langmuir D, P Hall, J Drever. *Aqueous Environmental Geochemistry.* (1997).
- [222] Marland G, K Fruit, R Sedjo. Accounting for sequestered carbon: the question of permanence. *Environmental Science & Policy.* 4 (2001) 259-68, doi: 10.1016/S1462-9011(01)00038-7.

- [223] Daccord G, O Lietard, R Lenormand. Chemical dissolution of a porous medium by a reactive fluid—II. Convection vs reaction, behavior diagram. *Chem Eng Sci.* 48 (1993) 179-86.
- [224] Navarre - Sitchler A, CI Steefel, L Yang, L Tomutsa, SL Brantley. Evolution of porosity and diffusivity associated with chemical weathering of a basalt clast. *Journal of Geophysical Research: Earth Surface* (2003–2012). 114 (2009).
- [225] Li L, CA Peters, MA Celia. Upscaling geochemical reaction rates using pore-scale network modeling. *Adv Water Resour.* 29 (2006) 1351-70, doi: 10.1016/j.advwatres.2005.10.011.
- [226] Berkowitz B. Characterizing flow and transport in fractured geological media: A review. *Adv Water Resour.* 25 (2002) 861-84.
- [227] Tribollet A, C Godinot, M Atkinson, C Langdon. Effects of elevated pCO₂ on dissolution of coral carbonates by microbial euendoliths. *Global Biogeochem Cycles.* 23 (2009).
- [228] Daccord G, E Touboul, R Lenormand. Carbonate acidizing: toward a quantitative model of the wormholing phenomenon. *SPE Production Engineering.* 4 (1989) 63-8.
- [229] Gouze P, L Luquot. X-ray microtomography characterization of porosity, permeability and reactive surface changes during dissolution. *J Contam Hydrol.* 120-21 (2011) 45-55, doi: 10.1016/j.jconhyd.2010.07.004.
- [230] Molins S, D Trebotich, L Yang, JB Ajo-Franklin, TJ Ligoeki, C Shen, et al. Pore-scale controls on calcite dissolution rates from flow-through laboratory and numerical experiments. *Environ Sci Technol.* 48 (2014) 7453-60.
- [231] Lai P, S Krevor. Pore-scale heterogeneity in the mineral distribution and reactive surface area of porous rocks. *Chem Geol.* (2015).
- [232] Siddhartha Seth S, NR Morrow. Efficiency of the Conversion of Work of Drainage to Surface Energy for Sandstone and Carbonate. (2007).
- [233] Lai P, S Krevor. Pore scale heterogeneity in the mineral distribution and surface area of Berea sandstone. *Energy Procedia.* 63 (2014) 3582-8.
- [234] Pereira Nunes J, B Bijeljic, M Blunt. Pore-scale simulation of carbonate dissolution in micro-CT images. in review. *J Geophys Res.* (2015).
- [235] Szymczak P, A Ladd. Wormhole formation in dissolving fractures. *Journal of Geophysical Research: Solid Earth* (1978–2012). 114 (2009).
- [236] Daccord G, R Lenormand, O Lietard. Chemical Dissolution of a Porous-Medium by a Reactive Fluid .1. Model for the Wormholing Phenomenon. *Chem Eng Sci.* 48 (1993) 169-78, doi: 10.1016/0009-2509(93)80293-y.
- [237] Leal AM, MJ Blunt, TC LaForce. A robust and efficient numerical method for multiphase equilibrium calculations: Application to CO₂-brine-rock systems at high temperatures, pressures and salinities. *Adv Water Resour.* 62 (2013) 409-30.
- [238] OPENFOAM, The open source CFD toolbox. 2011.
- [239] Raeini AQ, MJ Blunt, B Bijeljic. Direct simulations of two-phase flow on micro-CT images of porous media and upscaling of pore-scale forces. *Adv Water Resour.* 74 (2014) 116-26.

[240] Leal AM, MJ Blunt, TC LaForce. Efficient chemical equilibrium calculations for geochemical speciation and reactive transport modelling. *Geochim Cosmochim Acta*. 131 (2014) 301-22.

Appendix 1 – Permissions

Figure 1.2:

Order Completed

Thank you very much for your order.

This is a License Agreement between Hannah Menke ("You") and Elsevier ("Elsevier"). The license consists of your order details, the terms and conditions provided by Elsevier, and the [payment terms and conditions](#).

[Get the printable license.](#)

License Number	3765260404234
License date	Dec 10, 2015
Licensed content publisher	Elsevier
Licensed content publication	Chemical Geology
Licensed content title	An Improved model calculating CO2 solubility in pure water and aqueous NaCl solutions from 273 to 533 K and from 0 to 2000 bar
Licensed content author	Zhenhao Duan,Rui Sun
Licensed content date	14 February 2003
Licensed content volume number	193
Licensed content issue number	3-4
Number of pages	15
Type of Use	reuse in a thesis/dissertation
Portion	figures/tables/illustrations
Number of figures/tables/illustrations	1
Format	both print and electronic
Are you the author of this Elsevier article?	No
Will you be translating?	No
Original figure numbers	Figure 5
Title of your thesis/dissertation	Reservoir Condition Pore-Scale Imaging of Reaction
Expected completion date	Jan 2016
Estimated size (number of pages)	150
Elsevier VAT number	GB 494 6272 12
Permissions price	0.00 USD
VAT/Local Sales Tax	0.00 USD / 0.00 GBP
Total	0.00 USD

Figure 1.3 & Figure 2.6:

12/10/2015

Spinal: Chemical Interactions Between CO₂ Acidified Aqueous Fluids and Carbonate Minerals

Title: Chemical Interactions Between CO₂ Acidified Aqueous Fluids and Carbonate Minerals. Author(s): Peng, Cheng. Item Type: Thesis or dissertation. Abstract: The chemical interactions between carbon dioxide (CO₂) acidified aqueous fluids and carbonate minerals were studied at elevated temperature and pressure conditions for the purposes of modelling fluid flow and reactive transport in carbonate reservoir formations. Experimental measurements were made of the rate of dissolution of carbonate mineral samples in acidified brines, with specific focus on the reaction rate in the surface reaction controlled regime. Another key outcome of this study was the experimental measurement of pH for CO₂ acidified aqueous systems within the context of the data requirements of the oil and gas industry. Some studies have also conducted on the equilibrium constants of carbonate dissolution reactions. Three novel pieces of experimental apparatus were used to perform the experimental measurements, each designed to accommodate the corrosive CO₂-acidified reservoir fluids at high-temperature, high-pressure reservoir conditions. A newly designed and constructed batch dissolution reactor system, consisting of three vessels, implemented the rotating disc technique to study carbonate dissolution process without the impact of mass transfer effects. A newly designed and constructed high-pressure pH measurement system used an electrometric technique to quantify the impacts of dissolved CO₂ on the acidity of the aqueous solution. An in-situ Micro-Raman reactor apparatus used Raman spectroscopy to examine the equilibrium concentration of bicarbonate ions. All three systems were fully calibrated and validated before being applied to conduct systemic measurements with variation of temperature, pressure, salinity and minerals. The pH measurements for CO₂-saturated water in the pressure range from (0.28 to 15.3) MPa and temperatures from (308.3 to 423.2) K were conducted first. Commercially-available pH and Ag/AgCl electrodes were used together with a high pressure equilibrium vessel operating under conditions of precisely controlled temperature and pressure. The results of the study indicate that pH decreases along an isotherm in proportion to $-\log_{10}(x)$, where x is the mole fraction of dissolved CO₂. An empirical equation has been developed to represent the present results with an uncertainty of ± 0.06 pH units. We also compare our results with a new chemical equilibrium model and find agreement to within 0.1 pH unit. The pH measurements were further extended to a CO₂-saturated aqueous NaCl solution. A new strategy is proposed to calibrate the pH electrodes by using the Pitzer model to quantify the salt effects. Measurements were carried out at temperatures between (308 and 373) K and at pressures up to 15.4 MPa for NaCl solutions with concentrations of (1, 3, 5) mol·kg⁻¹. The pH is found to increase with increase of pressure, decrease of temperature and increase of NaCl concentration. An empirical equation correlating pH with CO₂ solubility has been proposed with an uncertainty of ± 0.08 pH units. Comparisons of the experimental data with two thermodynamic simulation packages using different aqueous electrolyte models suggest that the Pitzer model provides reasonably accurate predictions, although further improvements at higher NaCl concentrations would be desirable. New experimental data have been measured for carbonate mineral dissolution rates in CO₂-saturated aqueous system and the dissolution kinetics have been determined using the pH model derived in this study. Calcite dissolution rates in CO₂-saturated water at pressures ranging from (6.0 to 13.8) MPa and temperatures from (323 to 373) K were first measured. The rate of calcite dissolution in HCl(aq) at temperatures from (298 to 353) K was also measured. The impact of mineral sample surface morphology was investigated and the results suggest that at far-from-equilibrium conditions, the measured calcite dissolution rate is independent of the dislocation density due to the development of a dynamic steady-state pattern of etch pits. The results also indicate that the calcite dissolution rates under surface-reaction-controlled conditions increase with increase of temperature and CO₂ partial pressure. A kinetic model incorporating both pH and the activity of CO₂(aq) has been developed to represent the dissolution rates found in this study. We report correlations for the corresponding reaction rate constants based on the Arrhenius equation and the activation energies so determined are in reasonable agreement with the literature. The dissolution rate studies were then carried out for two other carbonate minerals, dolomite and magnesite, using pure mineral crystals. Dissolution experiments were conducted in CO₂-saturated water and HCl(aq) systems at similar temperature, pressure and pH conditions compared to the calcite experiments. The results indicate that the dissolution rates of

<http://spinal.imperial.ac.uk/handle/10044/124811>

1/2

12/10/2015

Spinal: Chemical Interactions Between CO₂ Acidified Aqueous Fluids and Carbonate Minerals

dolomite and magnesite also increase with increase of temperature and CO₂ partial pressure. The dissolution kinetics of both minerals can be modelled as a single first-order heterogeneous reaction for both the HCl system and the (CO₂ + H₂O) system. It was also noticed that dolomite dissolves in a stoichiometric manner, which greatly reduced the complexity in modelling. Finally, the dissolution rate investigations were extended to two different reservoir analogue samples (Limestone and Chalk) to validate the reaction kinetics models proposed in this project for reservoir samples. Significant efforts were made to estimate the true reactive surface area. Good agreement has been observed between the experimentally-measured dissolution rates of the reservoir analogue samples and the data calculated using the reaction kinetics model established in this project. It is concluded that the kinetic models and the associated parameters derived in this project can be incorporated into reservoir simulators to provide more accurate reactive transport simulations for future large scale CCS projects. Finally, Raman spectroscopy was used to probe the chemical equilibrium constants of carbonate dissolution reactions by measuring the equilibrium bicarbonate concentration (HCO₃⁻). The utilisation of a new calibration procedure has enabled in-situ, non-invasive and non-destructive, online quantitative fluid-rock interaction studies for carbonate-CO₂-brine systems. Both calcite and magnesite were studied in CO₂ acidified H₂O and 1 M NaCl systems at three temperatures from (297 to 373) K and pressures of 7 MPa and 15 MPa. Several geochemical simulators using different aqueous electrolyte models were used and were able to achieve various degrees of success in predicting the equilibrium HCO₃⁻ concentration in comparison with the experimental values. Overall, the Pitzer model demonstrates the widest applicability and highest accuracies for CO₂ acidified aqueous system. The present work was carried out as part of the Qatar Carbonates and Carbon Storage Research Centre (QCCSRC) program. It provided extensive mineral dissolution rates and pH data that can be used to characterise the chemical interactions between CO₂-acidified aqueous fluids and carbonate minerals relevant to oil- and gas-field applications. The results of this study should facilitate more rigorous modelling of reactive transport and fluid flow in the design and optimisation of enhanced oil recovery and carbon storage processes. Areas in which the research might be extended, both through further experimental studies and improved modelling, have been identified. Content Version: Open Access. Issue Date: Feb-2015. Date Awarded: Apr-2015. URI: <http://hdl.handle.net/10044/124811>. Advisor: Maitland, Geoffrey. Trustee, Martin. Sponsor/Funder: Qatar Carbonates and Carbon Storage Research Centre. Department: Chemical Engineering. Publisher: Imperial College London. Qualification Level: Doctoral. Qualification Name: Doctor of Philosophy (PhD). Appears in Collections: Chemical Engineering PhD theses

Figure 2.2:

Copyright Clearance Center **RightsLink®** Home Account Info Help Live Chat

Title: Total alkalinity: The explicit conservative expression and its application to biogeochemical processes

Author: Dieter A. Wolf-Gladrow, Richard E. Zeebe, Christine Klaas, Arne Körtzinger, Andrew G. Dickson

Publication: Marine Chemistry

Publisher: Elsevier

Date: July 2007

Logged in as:
Hannah Menke
Account #:
3000901821
LOGOUT

Copyright © 2007 Published by Elsevier B.V.

Order Completed

Thank you very much for your order.

This is a License Agreement between Hannah Menke ("You") and Elsevier ("Elsevier"). The license consists of your order details, the terms and conditions provided by Elsevier, and the [payment terms and conditions](#).

[Get the printable license.](#)

License Number	3843640208178
License date	Apr 07, 2016
Licensed content publisher	Elsevier
Licensed content publication	Marine Chemistry
Licensed content title	Total alkalinity: The explicit conservative expression and its application to biogeochemical processes
Licensed content author	Dieter A. Wolf-Gladrow, Richard E. Zeebe, Christine Klaas, Arne Körtzinger, Andrew G. Dickson
Licensed content date	July 2007
Licensed content volume number	106
Licensed content issue number	1-2
Number of pages	14
Type of Use	reuse in a thesis/dissertation
Portion	figures/tables/illustrations
Number of figures/tables/illustrations	1
Format	both print and electronic
Are you the author of this Elsevier article?	No
Will you be translating?	No
Original figure numbers	Fig. 2
Title of your thesis/dissertation	Reservoir Condition Pore-Scale Imaging of Reaction
Expected completion date	Jan 2016
Estimated size (number of pages)	150
Elsevier VAT number	GB 494 6272 12
Permissions price	0.00 GBP
VAT/Local Sales Tax	0.00 GBP / 0.00 GBP
Total	0.00 GBP

ORDER MORE...

CLOSE WINDOW

Figure 2.5: License Details

Thank you very much for your order.


This is a License Agreement between Hannah Menke ("You") and Elsevier ("Elsevier"). The license consists of your order details, the terms and conditions provided by Elsevier, and the [payment terms and conditions](#).

[Get the printable license.](#)

License Number	3765251022263
License date	Dec 10, 2015
Licensed Content Publisher	Elsevier
Licensed Content Publication	Chemical Engineering Science
Licensed Content Title	3-D simulation and analysis of reactive dissolution and wormhole formation in carbonate rocks
Licensed Content Author	P. Maheshwari,R.R. Ratnakar,N. Kalia,V. Balakotaiah
Licensed Content Date	7 March 2013
Licensed content volume number	90
Licensed content issue number	n/a
Number of pages	17
Type of Use	reuse in a thesis/dissertation
Portion	figures/tables/illustrations
Number of figures/tables/illustrations	2
Format	both print and electronic
Are you the author of this Elsevier article?	No
Will you be translating?	No
Original figure numbers	Figure 4, Figure 5
Title of your thesis/dissertation	Reservoir Condition Pore-Scale Imaging of Reaction
Expected completion date	Jan 2016
Estimated size (number of pages)	150
Elsevier VAT number	GB 494 6272 12
Price	0.00 USD
VAT/Local Sales Tax	0.00 USD / 0.00 GBP
Total	0.00 USD

Figure 2.7:





[Home](#)
[Account Info](#)
[Help](#)


Title: Dynamic Model of Wormhole Formation Demonstrates Conditions for Effective Skin Reduction During Carbonate Matrix Acidizing

Conference Proceedings: SPE Permian Basin Oil and Gas Recovery Conference

Author: C.N. Fredd, Schlumberger Oilfield Services et al

Publisher: Society of Petroleum Engineers

Date: 2000
2000. Society of Petroleum Engineers

Logged in as:
Hannah Menke
Account #: 3000901821

[LOGOUT](#)

Order Completed

Thank you very much for your order.

This is a License Agreement between Hannah Menke ("You") and Society of Petroleum Engineers ("Society of Petroleum Engineers"). The license consists of your order details, the terms and conditions provided by Society of Petroleum Engineers, and the [payment terms and conditions](#).

[Get the printable license.](#)

License Number	3843640827200
License date	Apr 07, 2016
Licensed content publisher	Society of Petroleum Engineers
Licensed content publication	SPE Proceedings
Licensed content title	Dynamic Model of Wormhole Formation Demonstrates Conditions for Effective Skin Reduction During Carbonate Matrix Acidizing
Licensed content author	C.N. Fredd, Schlumberger Oilfield Services et al
Licensed content date	2000
Type of Use	Thesis/Dissertation
Requestor type	academic/educational
SPE member	no
Format	print and electronic
Portion	figures/tables/images
Number of figures/tables/images	1
Will you be translating?	no
Distribution	10
Order reference number	None
Title of your thesis / dissertation	Reservoir Condition Pore-Scale Imaging of Reaction
Expected completion date	Jan 2016
Estimated size (number of pages)	150
Billing Type	Invoice
Billing address	Hannah Menke Imperial College London South Kensington Campus London, United Kingdom SW7 2AZ Attn: Hannah Menke
Total	9.56 GBP

Figure 5.4 and 5.8:

Title:	Reservoir Condition Pore Scale Imaging of Multiphase Flow using X-Ray Microtomography
Author(s):	Andrew, Matthew (/browse?type=author&value=Andrew%2C+Matthew)
Item Type:	Thesis or dissertation
Abstract:	This thesis presents the first method for the imaging of multiple fluid phases at conditions representative of subsurface flow by the use of X-ray micro-CT, focussing on four principal applications: (1) Capillary Trapping; (2) Ganglion Snap-off and remobilization; (3) Contact angle measurement; and (4) Dynamic phenomena associated with CO ₂ drainage. Firstly the pore-scale arrangement of CO ₂ after drainage and imbibition was imaged in three carbonates and two sandstones. In each sample substantial amounts of CO ₂ were trapped, showing that residual trapping can be used to locally immobilise CO ₂ . The size distributions of larger residual ganglia obey power law distributions with exponents broadly consistent with percolation theory, over two orders of magnitude. To examine snap-off in more detail residual CO ₂ was imaged at high resolution in a single carbonate. The capillary pressures of residual ganglia were found to be inversely proportional to the radius of the largest restriction surrounding each ganglion. The remobilization of residual ganglia was assessed using a reformulation of both the capillary and Bond numbers, finding the majority of ganglia in this system were remobilized at reformulated capillary numbers of around 1. Thirdly this thesis presents the first method for the measurement of in-situ contact angle at realistic conditions by the use of micro-CT, applied to a single carbonate sample at 50oC and 10 MPa. Contact angles ranging from 35o to 55o were observed, indicating that the CO ₂ -brine-carbonate system is weakly water-wet. Finally, we use fast synchrotron-based X-ray micro-CT to examine drainage into a brine saturated carbonate. The equilibrium capillary pressure change associated with drainage events is not sufficient to explain the accompanying snap-off, showing that dynamic forces can have a persistent impact on the pattern and sequence of the drainage process.
Content Version:	Open Access
Publication Date:	Nov-2014
Date Awarded:	Mar-2015
URI:	http://hdl.handle.net/10044/1/24915 (http://hdl.handle.net/10044/1/24915)
Advisor:	Bijeljic, Branko (/browse?type=author&value=Bijeljic%2C+Branko) Blunt, Martin (/browse?type=author&value=Blunt%2C+Martin)
Sponsor/Funder:	Imperial College London (/browse?type=author&value=Imperial+College+London)
Department:	Earth Science & Engineering
Publisher:	Imperial College London
Qualification Level:	Doctoral
Qualification Name:	Doctor of Philosophy (PhD)

perial.ac.uk:8443/handle/10044/1/24915

Pag

ir Condition Pore Scale Imaging of Multiphase Flow using X-Ray Microtomography

07/04/2011

Appears in
Collections: Earth Science and Engineering PhD theses (/handle/10044/1/1233)

Items in Spiral are protected by copyright, with all rights reserved, unless otherwise indicated.



(<http://creativecommons.org/licenses/by-nc-nd/3.0/>)

Section 6.1

Dynamic Three-Dimensional Pore-Scale Imaging of Reaction in a Carbonate at Reservoir Conditions

Hannah P. Menke*, Branko Bijeljic, Matthew G. Andrew, and Martin J. Blunt

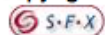
Qatar Carbonates and Carbon Storage Research Centre, Department of Earth Science and Engineering, Imperial College London, London SW7 2AZ, U.K.

Environ. Sci. Technol., 2015, 49 (7), pp 4407–4414

DOI: 10.1021/es505789f

Publication Date (Web): March 4, 2015

Copyright © 2015 American Chemical Society



*E-mail: h.menke12@imperial.ac.uk.

ACS AuthorChoice - This is an open access article published under a Creative Commons Attribution (CC-BY) License, which permits unrestricted use, distribution and reproduction in any medium, provided the author and source are cited.

Section 6.2



RightsLink®

Creative Commons Attribution License (CC BY)

This article is available under the terms of the [Creative Commons Attribution License \(CC BY\)](#). You may copy and distribute the article, create extracts, abstracts and new works from the article, alter and revise the article, text or data mine the article and otherwise reuse the article commercially (including reuse and/or resale of the article) without permission from Elsevier. You must give appropriate credit to the original work, together with a link to the formal publication through the relevant DOI and a link to the Creative Commons user license above. You must indicate if any changes are made but not in any way that suggests the licensor endorses you or your use of the work.

Permission is not required for this type of reuse.

CLOSE WINDOW

Copyright © 2016 [Copyright Clearance Center, Inc.](#) All Rights Reserved.
Comments? We would like to hear from you. E-mail us at customercare@copyright.com